FACULTY OF SCIENCES
Department of Astrophysics, Geophysics and Oceanography UR SPHERES
Groupe Infra-Rouge de Physique Atmosphérique et Solaire (GIRPAS)

First MAX-DOAS observations of tropospheric NO_2 and H_2CO in Central Africa: impact on air quality and validation of the TROPOMI satellite instrument

Thesis submitted for the partial fulfilment of the requirements for the academic degree of Philosophiae Doctor in Sciences at University of Liège (College in Space Sciences)

by
Rodriguez Yombo Phaka

Academic year 2023-2024

Jury Members:

Name	Function	Institution
Bernard Tychon	President	University of Liège, Belgium
Louis François	Secretary	University of Liège, Belgium
Emmanuel Mahieu	Promotor	University of Liège, Belgium
Jean-Pierre Mbungu Tsumbu	Co-promotor	University of Kinshasa, DRCongo
Richard Bopili Mbotia Lepiba	Examiner	University of Kinshasa, DRCongo
Alexis Merlaud	Examiner	Royal Belgian Institute for Space Aeronomy, Belgium
Gaia Pinardi	Examiner	Royal Belgian Institute for Space Aeronomy, Belgium

Acknowledgment of Funding:
This research received partial funding from the Belgian Science Policy Office (BELSPO) under the KinAERO project and the EQUATOR (Emission QUantification of Atmospheric tracers in the Tropics using ObseRvations from satellites, 2021–2025) project. Additionally, support was provided by the Commission de la Coopération au Développement (ARES-CCD) of the Académie de Recherche et d'Enseignement Supérieur. This support was managed at the Université de Liège by the Centre pour le Partenariat et la Coopération au Développement (PACODEL). The funding from UR SPHERES of the Université de Liège also contributed to this research.

« Discovery consists of seeing what everybody has seen and thinking what nobody has thought. »
Albert Szent-Gyorgyi 1937.

ACKNOWLEDGEMENTS

The research undertaken in this thesis was conducted in three different institutions: the Royal Belgian Institute for Space Aeronomy (BIRA-IASB), the University of Kinshasa (UniKin), and the University of Liège. My acknowledgments are first addressed to the entire scientific and academic bodies of these three institutions, followed by others without whom it would have been challenging for me to complete this academic journey.

At BIRA-IASB, my gratitude is primarily directed towards Gaia Pinardi. Thanks to the KinAERO project initiated in 2016, of which she was the main coordinator, I obtained my initial funding. This allowed me to pursue my DEA(Diplôme d'Etudes approfondies) in a field that introduced me to atmospheric sciences, data analysis techniques, and the principles of scientific writing. Gaia has consistently been present, available to guide me, engage in discussions, and provide advice on both social and professional levels. My sincere thanks also go to Alexis Merlaud, a researcher at BIRA-IASB, whose unwavering support has been invaluable since the beginning of my academic journey, starting from the Master's degree to the Ph.D. His precision in scientific writing significantly contributed to my improvement, and his insightful advice deepened my understanding of fundamental concepts crucial for interpreting my results. Alexis has not only been an essential mentor but also a generous financial supporter, contributing to the well-being of my small family. In addition to his mentorship, Alexis played a central role in the design and installation of instruments in Kinshasa. His generous provision of various electronic components for my laboratory at UniKin, ranging from diodes to transistors, integrated circuits, LEDs, and much more, was crucial. Furthermore, he provided low-cost sensors for local air quality monitoring, along with a spectrometer that continues to be a crucial tool in my personal experiments. Alexis introduced me to the use of QGIS, and his clear explanations of the physical principles applied to instruments, as well as to the physics and chemistry of the atmosphere, have been of great utility. His writing style, evident in his articles and thesis, has been a major source of inspiration for my scientific work.

My gratitude also extends to Michel Van Roozendael, the head of the UV-Vis group at BIRA-IASB, where a significant portion of this work was conducted. I am fortunate to benefit from the guidance of this prominent figure in DOAS worldwide. Despite his extensive experience, he has always been humble and straightforward in explanations, never hesitating to offer assistance. His guidance and interactions have been invaluable. He generously covered a significant portion of my stay in Belgium during the final months of my thesis from his personal reserves when I had no resources. It is also thanks to his expertise that the H_2CO analyses were greatly improved, leading to anticipated results; Annex E is largely due to his mentorship. I am truly grateful for everything he has done. Jenny Stavrakou and Jean-François Müller, researchers in the BIRA-IASB modeling group, also provided financial support from their team in the EQUATOR project, which resulted in the publication of one of my articles. They have contributed significantly to my

understanding of models, interpretation, and discussions. Their support extended even to the social aspect through their compassion, availability, and advice. Jenny always knew how to use kind words to motivate me, especially in the final phase of submitting my last article for the thesis. I also thank Isabelle De Smedt, a researcher in the UV-Vis group, for providing me with the satellite data set for H_2CO and for her availability to exchange and answer all the questions I had for understanding the satellite product. I also thank Ermioni Dimitropoulou and François Hendrick for their availability in terms of exchanges and for providing stratospheric model data and NO_2 data. Thanks also to Nuno Pereira, a researcher at BIRA-IASB, for his generosity, kindness, and especially his contribution to troubleshooting the instrument in Kinshasa during his family visit. I would also like to thank Caroline Fayt for making the QDOAS software available to me, which was a great help in analysing spectra. Martina Friedrich deserves appreciation for providing access to the FRM_4DOAS framework and offering valuable insights into the interpretation of geophysical products.

At UniKin, I express gratitude to all the professors in the Department of Physics and Technology for their moral support and academic guidance. Special thanks to Professor Mbungu Tsumbu for his scientific guidance. It is thanks to his connections that I had the opportunity to meet researchers from BIRA-IASB, allowing me to enter the atmospheric research field. He also fought tirelessly to secure the ARES scholarship that enabled me to start the thesis. His rigorous methods of analysis and interpretations, although sometimes challenging to grasp, allowed me to develop a critical mindset for understanding physical concepts in general. His pedagogical methodology has always inspired me in teaching. He is also the co-supervisor of this thesis. Thank you very much, dear mentor. My thanks also go to Professor Richard Bobili, whom I consider a father figure, for his strategic advice and social, moral, and professional support. I cannot forget Professor Ernest Kakudji, the first person to believe in me and motivate me to pursue scientific research. His encouragement, both morally and professionally, has always been present. Special thanks also to Professor Holenu Mangenda, my wedding sponsor, for his constant scientific and spiritual support.

In Liège, my thanks go directly to Professor Emmanuel Mahieu, my thesis advisor, who is undoubtedly the best academic mentor I have ever known. He possesses all the qualities necessary to guide a student to success. Not only does he provide excellent guidance in terms of science, but he also does his best to provide professional mentorship. His advice and support leave an indelible mark on his students. Special mention to his wife, "Maman" Diane Zender, who also serves as the secretary of the laboratory where I worked (Groupe Infra-Rouge de Physique Atmosphérique et Solaire GIRPAS/ULiège). She has the ability to turn any sorrow into a smiling happiness. A heartfelt thank you to Maxime Pignon, whose extensive experience in Python programming significantly enhanced my coding skills. Despite his busy schedule during the final year of his thesis, Maxime generously provided valuable insights, especially in debugging lengthy codes, contributing significantly to my progress. I extend my gratitude to Professor Louis Francois for his guidance in the thesis committee and his willingness to serve as a jury member. Special thanks to Professor Bernard Tychon for agreeing to chair the thesis committee. Lastly, a big thank you to my office mate, Irène Pardos Cantos, the coordinator for doctoral students in Space Sciences, for her invaluable moral and technical support throughout the process.

Finally, I conclude these acknowledgments by expressing my gratitude to my family, both biological and spiritual, and close friends. My parents, Papa Yombo and Maman Laurence Mambu, continue to provide unwavering support in my academic journey, and my siblings, especially Maman Mymy Makota, have been invaluable allies. A special ac-

knowledgment to Mama Catherine Kiwaka Muilu, my wife, for her unwavering support throughout the challenges of my doctoral training and, most importantly, for blessing me with two beautiful, kind, and intelligent children, Alexia-Elia Yombo and Flavour Yombo, who are the fruits of my endeavors and the source of my strength. I am also thankful to Djibi Buenimio, my best friend, for diligently maintaining the instruments in Kinshasa during my absences. Papa Guylain Mbundu, my surrogate father in Belgium, deserves my appreciation for hosting and caring for me. Gratitude extends to Mama Kiambi, Mr. Magloire, Papa Phili, Maman Elie Kitenge, Papa Noro Nsungu, Julvancy Nsumbu, Charmant Mayukuta Pete—wonderful friends considered as family—for their generosity and various forms of assistance over the years, Professor Daniel M. Westervelt (University's Lamont Doherty Earth Observatory in Palisades) for his review of this manuscript, Rosein Waba for her financial support during challenging times and her encouraging words, PhD candidate Hugues Museba for technical writing advice, Professor Kenny Kale Sayi for his valuable strategic guidance, Professor Maliki for his assistance and encouraging words and Adnam Lumbu (Rest in peace), a true friend whom I lost during this doctoral training, which was a profound shock for me. Lastly, I extend my thanks to colleagues, Max Seke, Ivan Kikunga, Hipolite Ditona, Jean-Jacke Mafuta, Benoit Pongo, Mawete Thiery, John Luabania, Léon Eyumu, Wilfrid Lutete, Andrien Banwitiya, Gilbert Mbuyamba, and all other unsung heroes who may find here the expression of our sincere appreciation.

GENERAL SUMMARY

The research presented in this thesis focuses on the issue of air pollution in Central Africa. The deterioration of air quality in this region has been prominently observed, as evidenced by various recent studies. Based on satellite observations, these recent studies have identified significant peaks in nitrogen dioxide, formaldehyde, and aerosol pollution. Initial interpretations point to biogenic emissions from the extensive forests in the region, subject to various challenges related to biomass burning, forest fires for agricultural land preparation, as well as charcoal production widely used as an energy source and for cooking by a large part of the local population. Validating such hypotheses requires ground-level observations to understand the situation on the ground and contribute to the validation of satellite data and model simulations. Unfortunately, Africa remains significantly undersampled compared to other parts of the world, with a near absence of ground measurement stations in Central Africa and a lack of regulation.

In this context, this thesis focuses on the operationalization and implementation of a remote sensing instrument to measure specific pollutants. We installed an instrument based on the the Differential Optical Absorption Spectroscopy (DOAS) technique in Kinshasa. After processing the recorded spectra from May 2017 to July 2021, a database of NO_2, H_2CO, and Aerosol optical depth (AOD), strong indicators of air pollution in the region, was established. Observations reveal significant pollution from these molecules in Kinshasa and its surroundings, with high tropospheric column values observed during the dry season. Daily cycles have also been identified, showing elevated values around noon. The database also facilitated the initial validation of the TROPOMI instrument aboard the S5P satellite. This validation demonstrated good agreement between TROPOMI and ground observations, using a realistic a priori profile for local conditions, with a median bias of around 10% for both compounds (NO_2 and H_2CO).

Another aspect of this thesis involved evaluating the performance of the GEOS-Chem model, a chemistry-transport model simulating pollution in the study area. This evaluation is crucial to determine the extent to which the model can accurately replicate real atmospheric conditions in the Kinshasa region and its surroundings. The preliminary results indicate that simulations including biomass burning emissions inventory align remarkably well with TROPOMI observations, while those without accounting for biomass burning exhibit a non-cyclical seasonal behavior. The impact of biomass burning is particularly pronounced, especially during the dry season for NO_2 pollution and throughout the year for H_2CO.

The overall results of this thesis confirm significant pollution from NO_2 and H_2CO in Kinshasa and its surroundings. TROPOMI satellite products align well with ground observations, taking into account the a priori measured by the ground instrument. The impact of biomass burning is strongly significant in the observed pollution. Recommen-

dations are made to deepen studies by installing more ground instruments in different cities in the sub-region and to use these results to raise awareness and encourage local authorities to implement control and regulation measures.

RESUME GENERAL

Les travaux exposés dans cette thèse se concentrent sur la problématique de la pollution de l'air en Afrique centrale. La dégradation de la qualité de l'air dans cette région a été particulièrement remarquée, comme le démontrent diverses études récentes. Basées sur des observations par satellite, ces études ont identifié des pics significatifs de dioxyde d'azote (NO_2), de formaldéhyde (H_2CO) et de pollution par les aérosols. Les premières interprétations pointent vers des émissions biogéniques issues des vastes forêts de la région, confrontées à divers défis liés à la combustion de biomasse, aux incendies de forêt pour la préparation des terres agricoles, ainsi qu'à la production généralisée de charbon de bois utilisé comme source d'énergie pour la cuisson par une grande partie de la population locale. La validation de telles hypothèses nécessite des observations au niveau du sol pour comprendre la situation réelle sur le terrain et contribuer à la validation des données satellitaires et des simulations de modèles. Malheureusement, l'Afrique reste significativement sous-échantillonnée par rapport à d'autres parties du monde, avec une quasi-absence de stations de mesure au sol en Afrique centrale et un manque de réglementation.

Dans ce contexte, cette thèse se focalise sur l'opérationnalisation et la mise en œuvre d'un instrument de télédétection destiné à mesurer des polluants spécifiques. Un instrument basé sur la technique de la Spectroscopie d'Absorption Différentielle Optique (DOAS) a été installé à Kinshasa. Après le traitement des spectres enregistrés de mai 2017 à juillet 2021, une base de données de NO_2, H_2CO, et de l'épaisseur optique des aérosols (AOD), des indicateurs significatifs de la pollution de l'air dans la région, a été établie. Les observations révèlent une pollution significative par ces molécules à Kinshasa et dans ses environs, avec des valeurs élevées de colonne troposphérique observées pendant la saison sèche. Des cycles journaliers ont également été identifiés, montrant des valeurs maximales autour de midi. La base de données a en outre facilité la validation initiale de l'instrument TROPOMI à bord du satellite S5P. Cette validation a démontré une bonne concordance entre TROPOMI et les observations au sol, une fois prise en compte des corrections basées sur l'utilisation de profils mesurés par MAX-DOAS comme information a priori dans le produit TROPOMI. Le biais médian trouvé entre les observations TROPOMI et les mesures au sol est d'environ 10% pour les deux composés (NO_2 et H_2CO).

Un autre volet de cette thèse a consisté à évaluer la performance du modèle GEOS-Chem, un modèle de transport chimique permettant de simuler la pollution dans la zone d'étude. Cette évaluation est cruciale pour déterminer dans quelle mesure le modèle peut reproduire avec précision les conditions atmosphériques réelles dans la région de Kinshasa et ses environs. Les résultats préliminaires indiquent que les simulations incluant l'inventaire des émissions de combustion de biomasse s'alignent remarquablement bien avec les observations de TROPOMI, tandis que celles qui ne tiennent pas compte de la combustion de biomasse ne présentent pas de maximu saisonier significatif. L'impact de la combustion de biomasse est particulièrement prononcé, surtout pendant la saison sèche

pour la pollution au NO_2 et tout au long de l'année pour le H_2CO.

Les résultats globaux de cette thèse confirment une pollution significative au NO_2 et au H_2CO à Kinshasa et dans ses environs résultant majoritairement de la combustion de la biomasse. Des recommandations sont formulées afin d'approfondir les études en déployant davantage d'instruments au sol dans diverses villes de la sous-région. Ces résultats devraient servir à sensibiliser et inciter les autorités locales à mettre en place des mesures de contrôle et de régulation.

Contents

List of Figures

List of Tables

Acronym List

AOD Aerosol Optical Depth

AMF Air Mass Factor

AERONET Aerosol Robotic Network

AK Averaging Kernel

ATBD Algorithm Theoretical Basis Document

BIRA-IASB Royal Belgian Institute for Space Aeronomy

CCD Charge-coupled device

CTM Chemistry Transport Model

COV Volatile Organic Compounds

CCAC Climate and Clean Air Coalition

DRC Democratic Republic of Congo

dof degrees of freedom

DOAS Differential Optical Absorption Spectroscopy

dSCD differential slant column densitie

ECMWF European Centre for Medium-Range Weather Forecasts

ESA European Space Agency

HEMCO Harmonized Emissions Component

FRM$_4$DOAS Fiducial Reference Measurements for Ground-Based DOAS

GEOS-Chem Goddard Earth Observing System Chemistry model

GHG greenhouse gase

GIRPAS Groupe Infra-Rouge de Physique Atmosphérique et Solaire

GMAO Global Modeling and Assimilation Office

GFED Global Fire Emissions Database

IHME Institute for Health Metrics and Evaluation

IPCC Intergovernmental Panel on Climate Change

LIDORT Linearized Discrete Ordinate Radiative Transfer

MAX-DOAS Multi-Axis Differential Optical Absorption Spectroscopy

MMF Mexican MAX-DOAS Fit

M-L Levenberg-Marquart

NDACC Network for the Detection of Atmospheric Composition Change

NASA National Aeronautics and Space Administration

NMVOC non-methane volatile organic compounds

OECD Organisation for Economic Co-operation and Development

OMI Ozone Monitoring Instrument

OEM Optimal Estimation Method

RTM Radiative Transfer Model

RTE Radiative Transfer Equation

ppb parts per billion

SZA Solar Zenithal Angle

SCD Slant Column Density

TROPOMI Tropospheric Monitoring Instrument

TOA Top of Atmosphere

UN United Nations

UNEP United Nations Environment Programme

UniKin University of Kinshasa

ULiège University of Liège

UV ultraviolet

UV-Vis ultraviolet-visible

VOC Volatile Organic Compounds

VCD Vertical Column Density

VLIDORT Vector Linearized pseudo-spherical Discrete Ordinate Radiative Transfer

VMR Volume Mix Ratio

WHO World Health Organization

Chapter 1

GENERAL INTRODUCTION

1.1 ISSUE AND RESEARCH QUESTION

The growing problem of air pollution in Africa, especially in urban areas, and its repercussions on health and the environment, have been largely neglected or even forgotten in many African countries (CCAC, 2023). In spite of the alarming reports from independent organizations and foreign researchers underscoring a significant rise in premature deaths linked to air pollution in Africa (see for example : Fisher et al. (2021), Babatola (2018), OECD (2014), IHME (2015)), and the projection of a substantial increase in concentrations over the next decade for pollutants such as NO_2 and aerosols (Liousse et al., 2014), the situation remains low prioritized in some countries. It is worth noting that there is limited knowledge regarding the precise extent to which anthropogenic pollutant emissions are exacerbated by natural processes, such as Saharan dust storms and forest fires. This lack of understanding makes it difficult to determine whether these combined factors lead to more severe consequences for human health in Africa compared to regions like Western Europe (OECD (2014), Knippertz et al. (2015)).

Regarding regulations and air pollution control, many African countries suffer from a severe lack of legislative measures and adequate monitoring systems IHME (2022). Global networks, such as the Network for the Detection of Atmospheric Composition Change (NDACC), which install ground-based instruments worldwide, have established very few stations in Africa, leaving the continent largely underrepresented compared to other regions of the world. While satellite observations and computer models can be used to study this issue, ground-based measurements are essential for a comprehensive understanding of air pollution. Additionally, these models and satellite data rely on ground-based measurements for validation.

The Democratic Republic of Congo (DRC), the largest country in Central Africa, is not exempt from the problem of air pollution. Due to its location in the heart of the Congo Basin, a vast forested area, the DRC experiences forest fires related to agriculture and charcoal production, as a significant portion of the Congolese population heavily relies on charcoal for cooking. These emissions, once released into the atmosphere, can travel great distances, affecting even areas beyond the country's borders. Recent publications have shown that the atmosphere in Bujumbura is influenced by biogenic (Volatile Organic Compounds (VOC)) emissions originating from intensive biomass burning agricultural

activities and forest fires in the south/southeastern region (Gielen et al., 2017). Several other studies based on satellite observations confirm that the DRC is strongly affected by H_2CO emissions (see for example De Smedt et al. (2015), De Smedt et al. (2021)).

In major Congolese cities, such as Kinshasa, the capital, additional anthropogenic sources of pollution, such as old cars and motorcycles, expose urban populations to high pollution levels, as reported by the McFarlane et al. (2021). Unfortunately, no Congolese city, including Kinshasa, has an air quality monitoring system (Katoto and Coauthors, 2019), severely limiting the availability of data necessary for researchers to address this issue, raise public awareness, and propose control and regulatory solutions to local authorities. This thesis focuses on the issue of data availability in Kinshasa. It is a question that involves both technical and scientific aspects: the establishment of an initial database of pollutants requires technical skills related to instrumentation and data processing, while the initial assessments and studies based on these ground measurements require scientific expertise. The success of this initiative has been made possible through a close collaboration between the UniKin, the BIRA-IASB and the University of Liège (ULiège).

1.2 REASEARCH OBJECTIVES

In this thesis, we pursue three main objectives: (1) The operationalization and installation of the first atmospheric observation instrument in the city of Kinshasa. (2) Participation in the validation process of the TROPOMI instrument on board the S5P satellite. (3) Evaluation of the performance of the GEOS-Chem [1] chemistry and transport model in the Kinshasa area and its surroundings.

1.2.1 The operationalization and installation of the first atmospheric observation instrument in the city of Kinshasa.

The primary objective of this thesis is to provide the city of Kinshasa and its surrounding area with a high-performance professional instrument capable of filling the data gap concerning atmospheric pollutants. Faced with budgetary constraints that hindered the acquisition of a professional commercial instrument, the intended option was to participate in the development and testing of an optical atmospheric remote sensing instrument. Once the instrument's testing was successfully completed, the plan was to install it in Kinshasa and proceed with accurate spectroscopic measurements of the pollutant absorbers present in Kinshasa's atmosphere. By doing so, the goal was to establish an initial database of tropospheric NO_2 and H_2CO profiles and vertical tropospheric columns in Kinshasa and its vicinity. A first Multi-Axis Differential Optical Absorption Spectroscopy (MAX-DOAS)[2] database in this poorly documented area could allow the first in-depth studies on tropospheric pollution of these two target molecules in this thesis. This objective is part of the broader vision of transferring knowledge and technology from the more developed countries to those of the Global South, which is in line with the perspective and vision of the project funding this thesis. This project aims to strengthen the scientific capacities of countries in the South and promote scientific independence.

[1] GEOS-Chem : Goddard Earth Observing System Chemistry model (see chapter 7)
[2] Multi-Axis Differential Optical Absorption Spectroscopy : see chapter 3

1.2.2 Participation in the validation process for the TROPOMI satellite instrument.

The TROPOMI instrument aboard the Sentinel-5 Precursor satellite launched in October 2017 underwent extensive calibration and algorithm testing during the commissioning phase , and a first data set (O_3, NO_2, and CO) was already publicly available since July 2018. Formaldehyde was part of a second distribution from September 2018. Dedicated measurement campaigns to validate TROPOMI data are an important data quality control. The participation of the Kinshasa station for H_2CO is of great importance due to its location, in the vicinity of VOC sources. Satellite instruments face challenges in capturing pollution hotspots in large cities due to various issues such as low vertical sensitivity near the surface, the use of unrealistic a priori information in the product retrieval process, and difficulties related to visibility conditions like aerosol presence and clouds. The profiles measured by the Kinshasa instrument would be used as a priori information for the correction of existing products, thus contributing to the validation process. Satellite observations have revealed that the highest concentrations of H_2CO in the world are located in these remote and challenging-to-access regions, encompassing tropical forests such as the Amazon, Central African, and Indonesian rainforests. Therefore, it is crucial to conduct measurements and undertake a comprehensive study of H_2CO in Central Africa. This initiative will not only be pivotal in validating the TROPOMI instrument but will also contribute to enhancing the existing dataset.

1.2.3 Evaluation of performance of the GEOS-Chem model around the city of Kinshasa.

The third objective of this thesis is to assess the performance of the GEOS-Chem model, a global-scale atmospheric chemistry and transport model. This evaluation holds paramount importance as it aims to determine to what extent the model can accurately replicate real atmospheric conditions in the Kinshasa region and its surroundings. This understanding is crucial for obtaining an accurate depiction of air quality in this area, particularly in light of the limitations of ground-based atmospheric monitoring. By evaluating the GEOS-Chem model, we can further refine the model's input data, such as emission inventories, which will contribute to an improved comprehension of air pollution in this region. For instance, this evaluation will enable us to analyze whether the study area is impacted by specific emissions sources, such as biomass burning, and how these emissions affect air quality.

1.3 DISSERTATION STRUCTURE

In addition to the introduction and the conclusions, this manuscript is divided into 7 distinct chapters. Chapter 2 provides some descriptive elements of the atmosphere and prepares the reader to address questions related to air pollution, with a particular focus on the situation in Africa in general and the DRC in particular. Chapter 3 is a comprehensive description of the tools and methods used for data processing. It begins with an in-depth description of the central instrument used in this study, followed by an exploration of the theories surrounding the recorded spectra and the data processing tools used throughout this thesis. Chapter 4 is dedicated to presenting the satellite data that have been used in this thesis. This chapter details the satellite missions, the instruments onboard for

measuring the studied pollutants, as well as the techniques for retrieving tropospheric vertical columns. Chapters 5 and 6 then focus on presenting the two key articles published in connection with the research conducted in this thesis. These chapters are presented as they were published online, without any modifications.

Finally, Chapter 7 delves into the theories surrounding the GEOS-Chem model and showcases the various results obtained from the simulations of this model.

Chapter 2

EARTH'S ATMOSPHERE AND AIR QUALITY IN AFRICA

The following chapter presents the theoretical framework in which this thesis is embedded. The aim is to present in a simple way the theoretical concepts of the Earth's atmosphere, air pollution and the issue of air quality in Africa. The objective is to prepare the reader to understand the terms and concepts related to atmospheric sciences used throughout this manuscript.

2.1 EARTH'S ATMOSPHERE

Atmosphere is the term used to describe the gravitationally bound envelope of compressible gases around a planet (Seigneur, 2018). Planets of sufficient mass such as Venus, Earth, Mars and the giant planets have atmospheres around them. On Earth, the atmosphere is the basis for life as we know it. Seen from space, the edge of the atmosphere is a thin halo of dark blue light on a curved horizon (Figure 3.13). Without this gaseous envelope around the Earth, many things would be possible, neither making fire, nor hearing sounds, nor even doing simple things like drinking with a straw.

The Earth's atmosphere protects us from external aggression. It acts as a shield against meteorites and space debris, which enter our atmosphere by the thousands of tons every day before burning up. One of its components, called ozone (O_3), acts as a natural sunscreen, filtering out the sun's ultraviolet rays that are bad for our health. This is why it is essential to protect this ozone layer simply to protect our lives.

The atmosphere also transports air and dust particles around our planet. It therefore acts as a reservoir, storing water vapour that produces clouds, rain and snow. It is therefore at the origin of the meteorological phenomena involved in the survival of species. Its influence on the various heat flows entering and leaving the earth helps to maintain an average temperature of 15°C on the earth's surface (see 2.3.3). It also serves as a reservoir for natural substances as well as for emissions resulting from human activity. In this "storehouse", physical and chemical actions and reactions take place, most of which can alter our climate or weather systems. In short, the atmosphere is arguably the most important ingredient for our survival on planet earth.

Figure 2.1: The Earth's atmosphere seen from outside the Earth. Adapted from `https://www.gettyimages.be/detail/foto/view-of-planet-earth-royalty-free-beeld/155149307`.

2.1.1 Chemical composition of the Earth's atmosphere

Table 2.1: Principal gases of dry air (Lutgens and Tarbuck, 2001)

constituent	Percent by volume
Nitrogen (N_2)	78.084
Oxygen (O_2)	20.946
Argon (Ar)	0.934
Carbone dioxyde (CO_2)	0.036
Neon (Ne)	0.00182
Helium (He)	0.000524
Methane (CH_4)	0.00015
Crypton (Cr)	0.000114
Hydrogen (H_2)	0.00005

The Earth's atmosphere, the layer surrounding our planet, is composed mainly of molecular nitrogen (N_2) and molecular oxygen (O_2) in proportions of about 78% and 21%, respectively. Argon is present at less than 1%. Carbon dioxide (CO_2) is present at about 400 ppm (parts per million), i.e. 0.04%. The water vapor is on average 1% with however a great spatio-temporal variability. The true values in percentage and in concentration (ppm) are shown in diagram 1 and in table 2.1 according to Lutgens and Tarbuck (2001).

2.1.2 Atmospheric pressure

Atmosphere is a gas that can be considered as a perfect gas at the pressures observed in the Earth's atmosphere. The law of perfect gas applies therefore:

$$PV = nRT \tag{2.1}$$

In equation 2.1, P represents atmospheric pressure, V symbolizes the volume of air under consideration, T denotes temperature, n represents the quantity of moles of air contained in the studied volume, and finally, R represents the ideal gas constant[1]. Atmospheric pressure arises from the gravitational effect exerted by the planet on the gaseous components that make up our atmosphere. As a result, it gradually decreases with altitude. This relationship is expressed by the hydrostatic equation, as indicated in equation 2.2, with z=0 representing the Earth's surface.

$$dP(z) = -\rho_{\mathrm{a}} g dz \tag{2.2}$$

Where z represents altitude (in meters), P is the pressure , ρ is the density, and g is the constant gravitational acceleration. For an incompressible fluid ($\rho_{\mathrm{a}}(z)$ = constant), we observe a linear variation of pressure with altitude. The atmosphere is composed of a gas and is therefore a compressible fluid (its density increases with pressure). The density can be calculated using the expression 2.3.

$$\rho_{\mathrm{a}} = M_{\mathrm{air}} \frac{n}{V} = \frac{M_{\mathrm{air}} P(z)}{RT(z)} \tag{2.3}$$

Where M_{air} represents the average molar mass of air, which is a weighted average of the molar masses of various components of air (0.029 kg.mole^{-1} for dry air). Therefore, the density of dry air is 1.185 kg.m^{-3} at 1 atm and 25°C. By substituting $\rho_{\mathrm{a}}(z)$ into the hydrostatic equation, we obtain:

$$\frac{dP(z)}{P(z)} = -\frac{dz}{H} \tag{2.4}$$

with

$$H = \frac{RT(z)}{M_{\mathrm{air}} g} \tag{2.5}$$

H represents a quantity homogenous with respect to altitude. It is referred to as the height scale, and its interpretation becomes clearer when integrating the differential equation in which it appears, considering the boundary condition at the lower limit $P(z = 0) = P_0$. And we can deduce:

$$P(z) = P(0) \exp\left(- \int_0^z \frac{M_{\mathrm{air}} g}{RT(z)} \, dz \right) \tag{2.6}$$

The equation 2.6 plays a significant role in understanding the vertical structure of the atmosphere's pressure. This equation, known as the barometric formula, describes how atmospheric pressure changes with altitude. It shows that pressure decreases exponentially with increasing altitude (see Figure 2.2).

[1] (R=8.314 J.mol^{-1}.K^{-1})

2.1.3 Vertical structure

The vertical structure of the atmosphere refers to how the different layers of Earth's atmosphere are organized based on altitude. This arrangement is the outcome of various physical and chemical processes occurring in the atmosphere due to variations in temperature, pressure, density, chemical composition, and other environmental factors. The vertical structure of the atmosphere is typically divided into several primary layers, each with its own distinct characteristics. The most commonly recognized layers, starting from the Earth's surface and extending into space, include: the troposphere, stratosphere, mesosphere, thermosphere, and exosphere, each characterized by unique properties and behaviors (See Figure 2.2). Understanding this structure is crucial for meteorology, atmospheric chemistry, satellite operations, and more.

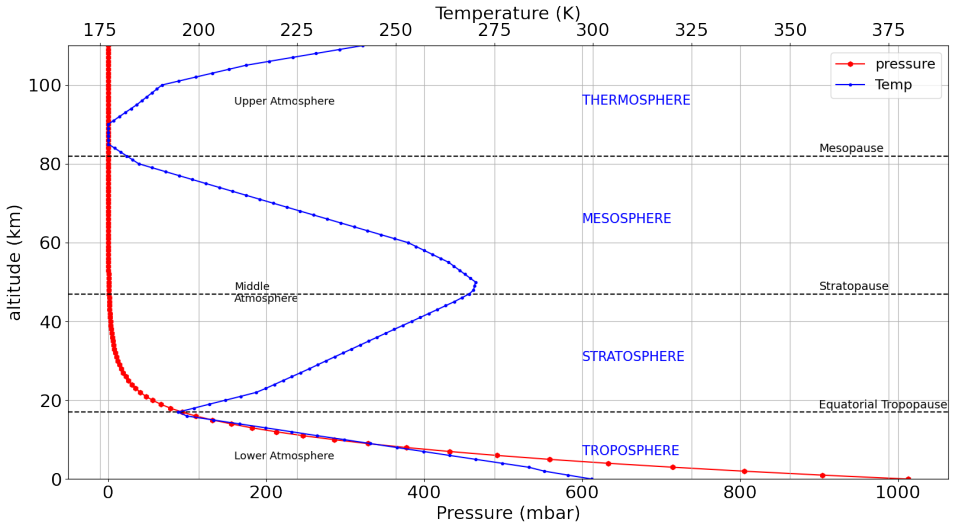

Figure 2.2: Tropical Temperature and pressure profile of the standard Earth atmosphere. Data from Anderson et al. (1986).

The troposphere is the layer closest to Earth's surface, extending to an altitude of approximately 8 to 17 kilometers (lower at the poles and higher at the equator). It comprises about three-quarters of the total mass of the atmosphere. This layer is where most meteorological phenomena occur, including cloud formation, precipitation, and temperature variations. The boundary between the troposphere and the stratosphere is known as the tropopause. The tropopause can be defined based on thermal considerations, where it is the altitude at which the vertical temperature profile starts to reverse, transitioning from decreasing to increasing temperature with altitude. It can also be defined chemically, where it is the altitude at which ozone concentrations increase (Seigneur, 2018).

Above the tropopause lies the stratosphere, extending to about 50 kilometers in altitude. In this layer, temperatures increase with altitude due to the presence of ozone, creating an ozone layer that absorbs a significant portion of the sun's ultraviolet radiation. The stratopause is the transitional region between the stratosphere and the mesosphere, characterized by relatively constant temperatures. As oxygen and ozone concentrations decrease to a point where they no longer significantly contribute to warming, the vertical temperature profile starts to decrease with altitude in the region known as the mesosphere, extending to an altitude of approximately 50 to 85 kilometers. In this layer, the atmosphere hosts the region where meteors burn up upon entering Earth's atmosphere. The

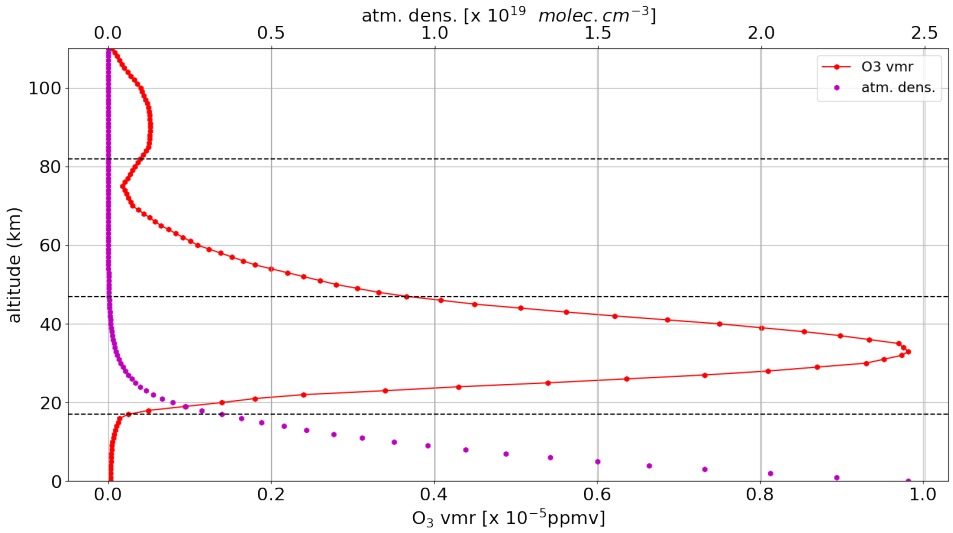

Figure 2.3: Tropical air density (in molec cm^{-3}) and ozone (in ppmv : parts per million by volume) profile of the standard Earth atmosphere. Data from Anderson et al. (1986).

mesopause marks the boundary between the mesosphere and the thermosphere, characterized by relatively low temperatures.

The uppermost layer is called the thermosphere, which includes the ionosphere where solar radiation leads to ionizing reactions, producing gaseous ions. The thermosphere extends to about 100 kilometers. Beyond this, there are the exosphere and the magnetosphere. The boundary between the atmosphere and interplanetary space is typically considered to be within the thermosphere, at around 100 kilometers in altitude, and is referred to as the Kármán line. At this altitude, the atmosphere is extremely thin, no longer behaving like a fluid. Molecules have few interactions with each other, and those with sufficient kinetic energy can escape Earth's gravitational field and journey into space (Seigneur, 2018).

2.2 SUN-ATMOSPHERE INTERACTION

The interaction between the Sun and Earth's atmosphere is a fundamental process that impacts numerous aspects of our environment. This interaction forms the basis for several key phenomena, including solar radiation, ozone formation, atmospheric circulation, optical phenomena, and climatic effects.

2.2.1 Solar radiation

Solar radiation, originating from the sun, is a crucial climatic variable that plays a fundamental role in sustaining life on Earth. In addition to providing light, it carries a wide range of wavelengths, following the principles of blackbody radiation. The spectrum of solar radiation spans from gamma rays and X-rays to microwaves and radio waves[2], with a particularly critical segment between 300 nm (ultraviolet rays) and 3000 nm (infrared)

[2]gamma-ray (10 fm to 1 pm), X-ray (1 pm to 10 nm), ultraviolet (10–380 nm), visible (380–780 nm), infrared (780 nm to 1 mm), microwave (1–15 mm), and radio wavelengths (0.1 mm to 100 mnm)

playing a significant role in our well-being and our environment. In the realm of human health, exposure to ultraviolet (UV) rays, with wavelengths ranging from 280 nm to 400 nm, affects various life forms directly or indirectly, impacting quality of life (Webb et al., 2002). For instance, UV radiation facilitates the synthesis of vitamin D, essential for bone growth. Conversely, prolonged exposure can lead to skin cancer and contribute to cataracts (Hess et al., 1998; Wang et al., 2012). Plants rely on solar radiation for their growth, converting solar energy into chemical energy through photosynthesis. This radiation absorbed by plants is termed photosynthetically active radiation and falls within wavelengths of 400 nm to 700 nm. As solar radiation enters Earth's atmosphere, certain wavelengths are absorbed by molecules present, enabling ground-based spectroscopic analysis. This data is pivotal in determining the chemical composition (abundance of atmospheric gases contributing to climate studies and air quality monitoring). A precise knowledge of the solar spectrum holds significant relevance for various disciplines and fields, including astronomy, astrophysics, solar physics, atmospheric science, remote sensing and its applications, solar energy, materials science, and medical science (Meftah et al., 2023).

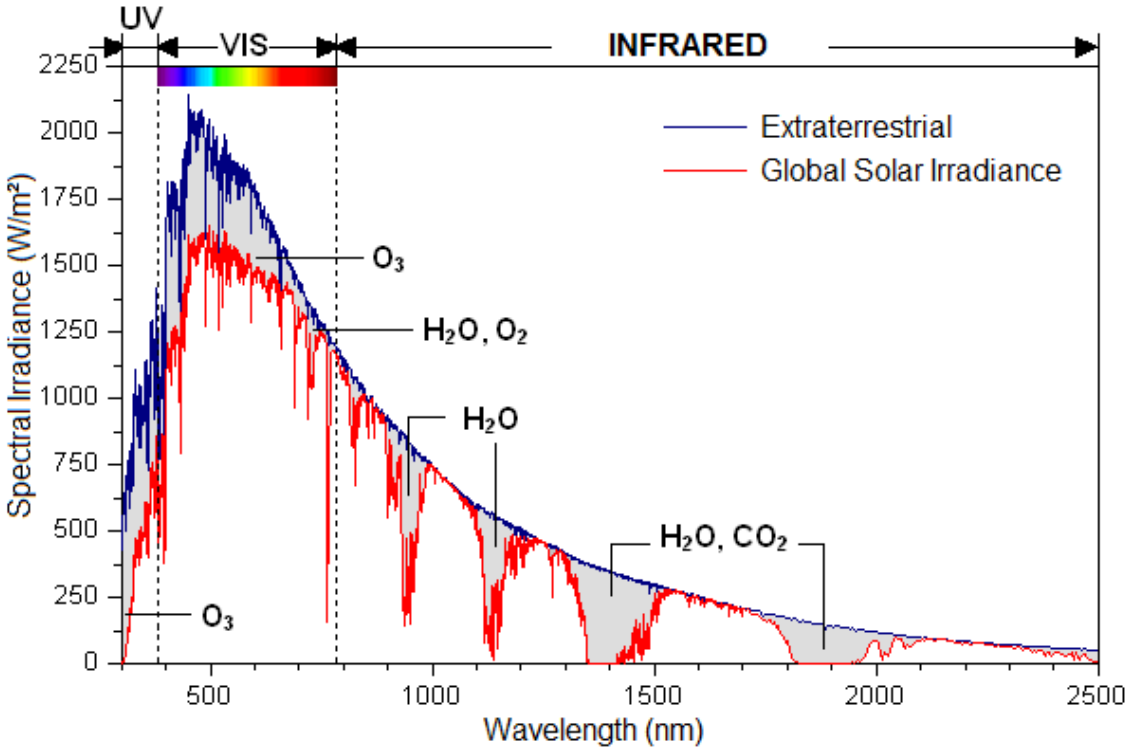

Figure 2.4: Solar spectrum (Dornelles et al., 2011).

Analysis of the solar spectrum (figure 2.4) provides a valuable window for exploring not only the Sun's atmosphere[3], but also that of the Earth, paving the way for a deeper understanding of solar physics, atmospheric chemistry, and their complex interactions.

Solar radiation reaching the Earth's surface is partly absorbed by the planet, while a portion is scattered and radiated back into space. However, the amount of absorbed energy varies with latitude, with greater absorption at the equator compared to the poles due to the higher presence of water vapor in the equatorial and tropical atmospheres than at

[3]Among the most prominent absorption lines characterizing the solar atmosphere are the Fraunhofer lines, which are a set of well-known absorption lines in the solar spectrum: [1]. For probing the chromosphere (the Mg II line at 280.27 nm, the ionized calcium K line at 393.4 nm, the H-alpha line at 656.28 nm). [2]. To study the solar photosphere: silicon lines at 390.55 nm, neutral iron line at 543.5 nm. [3]. For probing information on the upper layers of the solar atmosphere: Sodium line at 589.6 nm.

other latitudes. Additionally, the presence of snow and ice in polar regions leads to higher surface reflectivity, resulting in less radiative energy absorption by the Earth in polar and boreal zones. These phenomena, primarily associated with the water cycle (evaporation in the tropics with latent heat release and the presence of ice and snow in polar regions), create a thermal energy differential between the equator (or generally tropical regions) and polar regions, hence the atmospheric circulation phenomenon (Seigneur, 2018).

2.2.2 Atmospheric circulation

The Earth's atmosphere is in constant motion due to differences in temperature, pressure and humidity around the globe. These differences create pressure and temperature gradients that cause air to move. The Earth's rotation also influences atmospheric circulation, creating phenomena such as prevailing winds and atmospheric currents. The Earth's rotation induces an atmospheric flow to veer to the East in the Northern Hemisphere and to the west in the Southern Hemisphere. These shifts are a consequence of the Coriolis force[4] (Seigneur, 2018). Three distinct zones of wind circulation exist between the equator and each pole (Figure 2.5):

(1). The first zone, known as the Hadley Cell, extends from the equator to 30 degrees north and south. Here, steady winds blow from the northeast in the Northern Hemisphere and from the southeast in the Southern Hemisphere—these are the trade winds. Sailors have long relied on this region of consistent winds for transoceanic voyages.

(2). The second zone is situated at mid-latitudes and is characterized by transient low-pressure systems beneath generally westward-flowing upper-level winds. This is referred to as the Ferrel Cell.

(3). The third zone comprises the polar cells, located respectively north and south of the 60th parallel, with surface circulation generally from the east.

In equatorial regions, significant convection processes occur, leading to substantial precipitation. Conversely, at the edges of these convection cells, deserts are found, partly due to the decrease in relative humidity as temperature rises. The circulation of the Hadley cells, both in the Northern and Southern Hemispheres, varies with the seasons. However, the Intertropical Convergence Zone (ITCZ), located near the equator, acts as a barrier limiting the exchange of air between the two hemispheres. Beyond the 60-degree latitudes, the polar cells essentially replicate the circulation pattern of the Hadley cells. The Ferrel cell, rotating in the opposite direction due to the Coriolis effect, is responsible for the westerly winds observed at mid-latitudes and plays a crucial role in the overall dynamics of atmospheric circulation.

This variability influences how these chemical compounds are transported within the atmosphere and distributed across the globe. Based on their varying lifetimes, which can range from hours to several decades from one species to another, some of these species remain confined to the lower atmospheric layer at regional or global scales, while others can travel long distances and impact remote regions far from their emission sources. Therefore,

[4]The Coriolis force, is a fictitious force caused by the rotation of the Earth. It leads to the apparent deflection of moving objects to the right in the Northern Hemisphere and to the left in the Southern Hemisphere. This force has an impact on ocean currents, winds, and various movements on Earth.

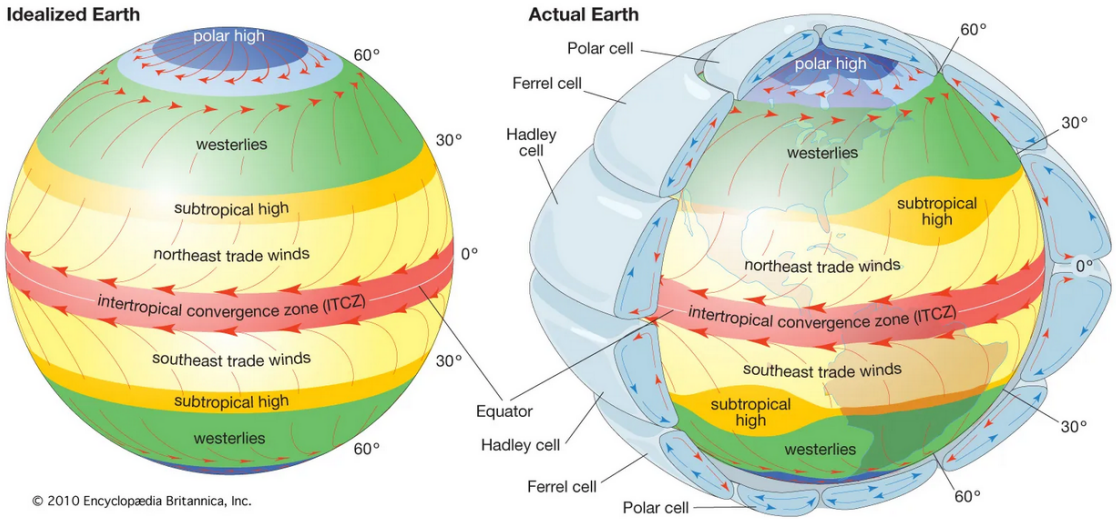

Figure 2.5: Illustration of the general patterns of atmospheric circulation over an idealized Earth with a uniform surface on the left and the actual Earth on the right. It encompasses both horizontal and vertical aspects of atmospheric circulation in the depiction of the actual Earth from Ferrel (2010).

understanding atmospheric circulation is crucial for deciphering the spatial distribution of these chemical species.

2.3 ATMOSPHERIC POLLUTION

2.3.1 General considerations

Some gases and particles present in the atmosphere can have adverse effects on human health, ecosystems, infrastructure, and atmospheric visibility, categorizing them as atmospheric pollutants. It is important to note that certain chemical substances, although initially harmless when present in the atmosphere, can become pollutants after deposition on the ground, following transformations in other environments, or through their gradual accumulation in the food chain (Seigneur, 2018).

Air pollution has a long history, dating back to the use of fire, which emitted pollutants into poorly ventilated environments and posed health risks (Hardy et al., 2012). The 19th-century industrial revolution also resulted in significant emissions of air pollutants due to the combustion of fossil fuels. In the 1950s, a new form of pollution emerged in Los Angeles, linked to the formation of ozone, particularly during the summer months, due to chemical reactions in the atmosphere involving Volatile Organic Compounds (COV). This was exacerbated by the use of large vehicles in the city's sprawling layout and the presence of industries such as power plants, refineries, and port activities, emitting other harmful compounds. The 1970s witnessed forest damage in Europe and North America attributed to acid rain resulting from the deposition of sulfuric and nitric acids (Odén, 1967, 1968; Martin and Barber, 1984). These observations hinted at the existence of another form of pollution, as atmospheric deposition of acidic species like sulfuric acid (H_2SO_4) and nitric acid (HNO_3) significantly altered the chemical balance of soils and

surface waters (Likens and Bormann, 1974). More recently, diesel particles have been classified as carcinogenic by the International Agency for Research on Cancer (IARC) of the World Health Organization (WHO) (WHO; Benbrahim-Tallaa et al. (2012)), and pollutants like ozone have harmful effects not only on human health but also on vegetation, leading to significant economic losses in agriculture (Rich, 1964).

2.3.2 Type of atmospheric pollutants

Atmospheric pollution involves various aspects. Some are of global nature due to the long lifespan of involved chemical compounds, such as climate change from greenhouse gase (GHG)s[5] and stratospheric ozone layer depletion. Others primarily concern the lower atmosphere, impacting Earth's surface. Pollution can occur at local, regional, or global scales, with short (hours) or long (years) durations (see Figure 2.6). Certain atmospheric pollutants are emitted directly, while others form through chemical or physical processes, arising from gases or particles. These include primary pollutants, emitted directly, and secondary pollutants, formed in the atmosphere from chemical precursors.

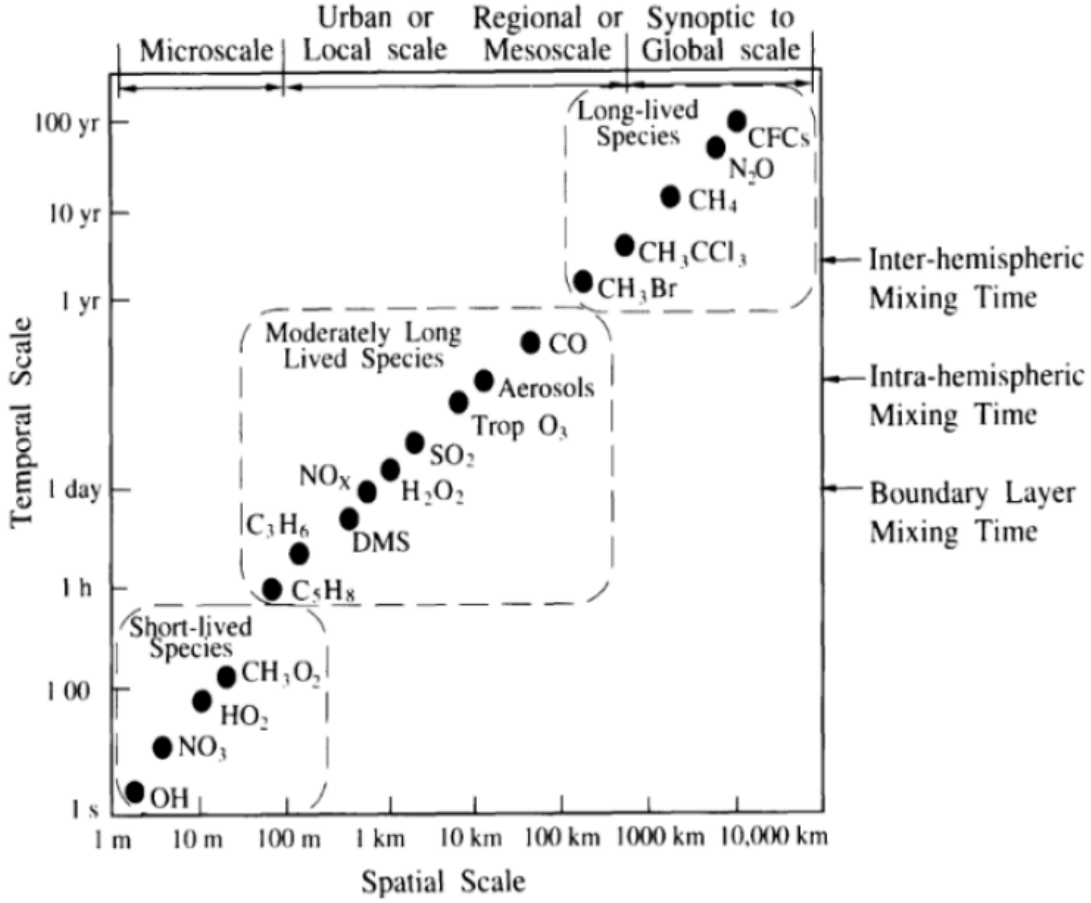

Figure 2.6: Duration and Range of Atmospheric Component Transport (Seinfeld and Pandis, 1997).

Though not all precursors of secondary pollutants are inherently harmful to health or the

[5]Greenhouse gases (GHGs) include carbon dioxide (CO_2), methane (CH_4), nitrous oxide (N_2O), ozone (O_3), water vapor (H_2O), chlorofluorocarbons (CFCs), hydrofluorocarbons (HFCs), perfluorinated hydrocarbons (PFCs), sulfur hexafluoride (SF6), and nitrogen trifluoride (NF3). They are produced by various human activities and influence climate change by trapping heat in the atmosphere.

environment, they are generally considered pollutants due to their contribution to atmospheric pollution. Some pollutants have effects directly tied to their air concentrations, while others result from deposition on land surfaces and their transport and transformation in non-atmospheric environments, such as surface waters or soils (Seigneur, 2018). The sources of these pollutants can either be natural or associated with human activities.

2.3.3 Climate change and air pollution

Climate change is a major issue related to the atmosphere, differing from air pollution near the Earth's surface due to spatial and temporal scale differences. Climate change is primarily caused by greenhouse gases that persist in the atmosphere for extended periods. In contrast, air pollution exhibits considerable variability in both time and space, with rapid responses between emissions and their impact on air quality. Although distinct, there are connections between climate change and air pollution. Some atmospheric pollutants contribute to climate change, while climate change can influence air pollution. Recognizing these connections is crucial for effectively addressing environmental issues, emphasizing the importance of identifying all emissions from a source to avoid inadvertently contributing to another problem.

The Earth's climate is influenced by the presence of GHGs that retain a portion of the infrared radiation emitted by the Earth in the atmosphere. Consequently, they help maintain an average surface temperature of around 15°C, whereas it would be approximately -19°C without them (Seigneur, 2018). Climate change arises from an increase in GHG concentrations, either through the rise in natural GHG concentrations like CO_2 or the introduction of new gases into the atmosphere, such as halocarbons. Since 1988, the Intergovernmental Panel on Climate Change (IPCC) has been tasked with summarizing the state-of-the-art scientific knowledge about climate change, its causes, the involved processes, and potential consequences through regularly published reports.

According to the IPCC, assessing the impact of factors influencing the climate on the energy balance of the coupled Earth/atmosphere system is measured by radiative forcing. Radiative forcing is defined as the difference between the received and emitted radiative energy by a given system (R.K. Pachauri and L.A. Meyer, 2014). Figure 2.7 illustrates the radiative forcing resulting from emissions of various GHGs and their precursors.

As mentioned earlier, some atmospheric pollutants have a direct or indirect impact on climate change. Among gases, O_3, for example, is a GHG and a significant pollutant. However, its lifespan is short as it is reactive (can be destroyed by photolysis and react with other gases like nitrogen oxides and alkenes) and deposits relatively easily on surfaces. Therefore, any action taken to reduce the consequences of O_3 has an immediate effect on its radiative forcing (Jacob and Winner, 2009).

Other air pollutants play various roles in climate change, including producing GHGs, generating particles, and producing oxidants that affect the lifespan of certain GHGs. Pollutants like CO, NO_x, and VOCs are precursors to O_3, so their emissions contribute to radiative forcing. These precursors also produce hydroxyl radicals (OH), which oxidize CH_4 (Jacob and Winner, 2009). Therefore, an increase in OH radicals due to CO, NO_x, and/or VOC emissions leads to a decrease in CH_4 concentration, resulting in a negative contribution to radiative forcing. NO_x, VOCs, SO_2, and ammonia (NH_3) are precursors to particulate matter (nitrate, organic, sulfate, and ammonium, respectively). Particles

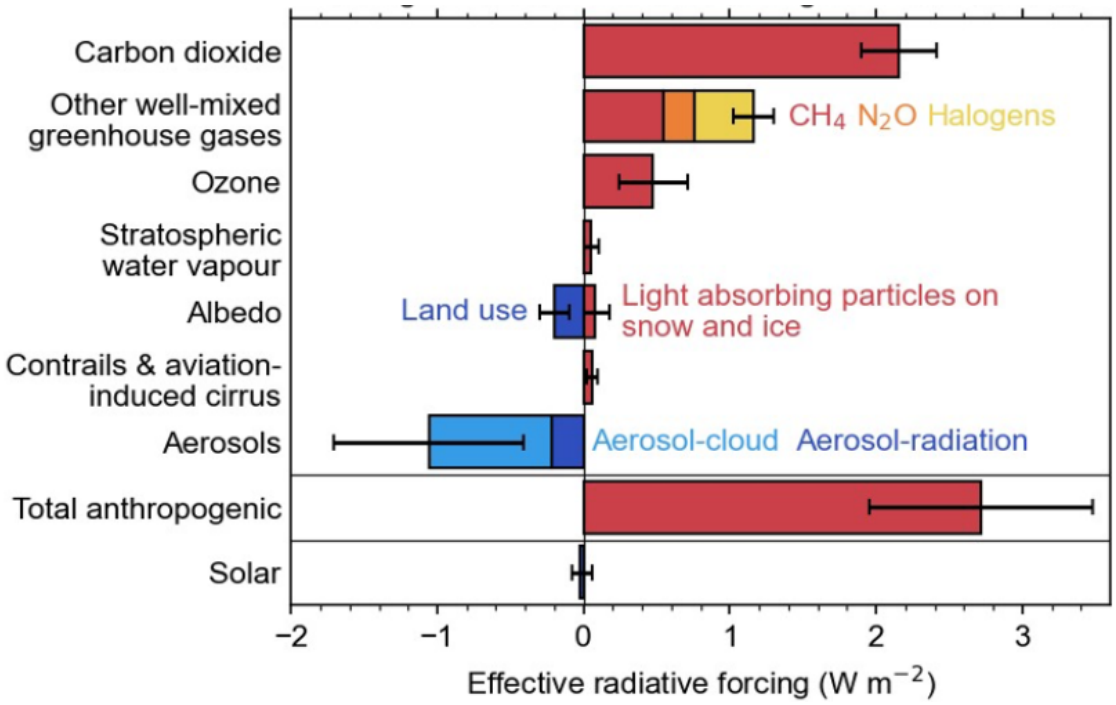

Figure 2.7: Change in effectire radiative forcing from 1750 to 2019(IPCC, 2001)

.

primarily have a negative forcing effect, except for black carbon (BC or elemental carbon), which absorbs radiation and, consequently, warms the atmosphere (Shen et al., 2017). The effects of particles on climate are complex and require a thorough characterization of their physicochemical and optical properties (Boucher, 2012).

Without atmospheric pollution, global warming would have been more pronounced (Seigneur, 2018). However, it's essential to note that the primary GHG (CO_2) is the main product of combustion, and combustion processes are the source of many pollutants and precursors such as NO_x, CO, VOCs, SO_2, and particles. In the subsequent section, we delve into the underlying principles of pollutant formation, with a specific focus on the study's pollutants: NO_2, H_2CO, and aerosols. We will elaborate on their origins, transformations, and removal processes.

2.3.4 Tropsheric nitrogen dioxide

Nitrogen dioxide (NO_2) and nitric oxide (NO), often collectively referred to as nitrogen oxides ($NO_x = NO + NO_2$), are trace gases of significant importance within the Earth's atmosphere, present in both the troposphere and the stratosphere. Their introduction into the atmosphere results from both human activities, such as the combustion of fossil fuels and biomass, and natural processes, including microbiological processes occurring in soils, wildfires, and electrical discharges (thunder)(Seinfeld and Pandis, 1998). Approximately 95% of NO_x emissions are in the form of NO (Saleem et al., 2022). During daylight hours, in the presence of sunlight, a photochemical process involving ozone (O_3) rapidly converts NO to NO_2 (and vice versa), making NO_2 a robust indicator of nitrogen oxide concentrations (Solomon, 1999; Jacob, 1999).

In the troposphere, NO_2 plays a pivotal role in addressing air quality concerns, as it has

a direct impact on human health, as noted by the WHO in 2003. Additionally, NO_x serve as essential precursors for tropospheric O_3 formation, as demonstrated by studies such as Sillman et al. (1990), and they influence OH concentrations, thus shortening the lifespan of CH_4, as exemplified in research by Fuglestvedt et al. (1999).

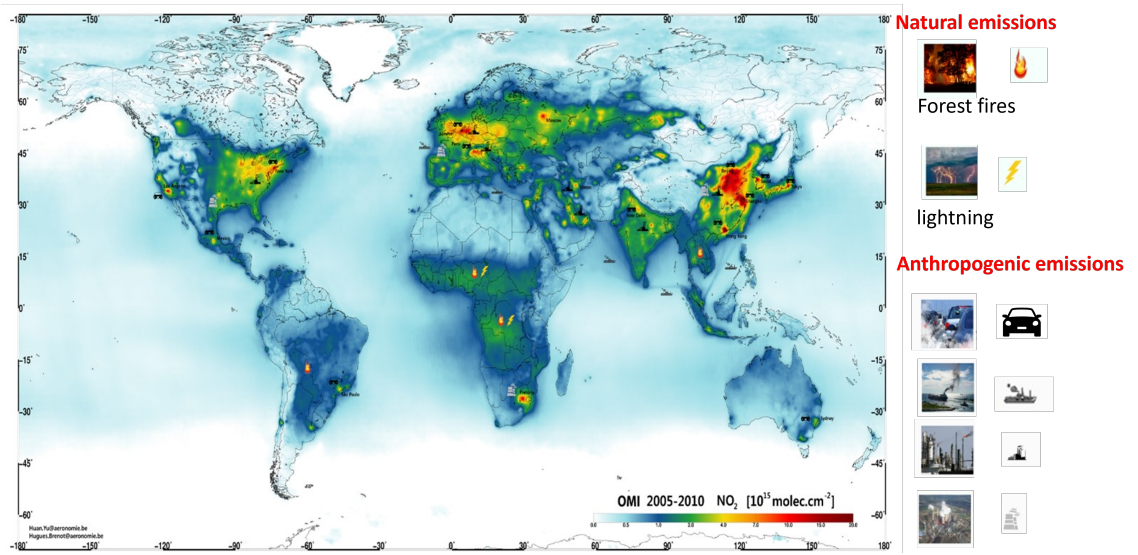

Figure 2.8: Global map of average NO_2 concentration extracted from OMI measurements during the period 2005-2010. Adapted from `https://uv-vis.aeronomie.be/news/20141027/`

While NO_2 is a minor greenhouse gas on its own, its indirect effects on global climate change are likely more significant. This is primarily attributed to a presumed net cooling effect, primarily driven by increased aerosol concentrations resulting from nitrate formation from nitrogen oxides and heightened oxidant levels, as observed by Shindell et al. (2009). The deposition of nitrogen compounds holds great importance concerning eutrophication, as outlined by Dentener et al. (2003). Eutrophication [6] represents the ecosystem's response to the introduction of substances like nitrates and phosphates. Negative environmental consequences include oxygen depletion in water, leading to reductions in fish and other aquatic populations de Vries (2021). In the lower troposphere, the lifespan of NO_x is typically less than a day, depending on location and season. These short lifetimes mean that NO_2 remains relatively close to its source, making easier the detection of NO_x emissions from space. Figure 2.8 illustrates the global distribution of NO_2 from 2005 to 2010, as observed from space by the OMI instrument aboard the AURA satellite. The map also highlights various types of potential emission sources that impact NO_2 levels worldwide. It is evident that heavily industrialized cities experience significant NO_2 concentrations, with pronounced peaks attributed to industrial activity and traffic. Conversely, tropical regions show a moderate impact, albeit with natural emissions such as forest fires and lightning, as indicated by the symbols on the map.

2.3.5 Formaldehyde

Formaldehyde (H_2CO) plays a critical role as an intermediate gas in nearly all oxidation processes involving non-methane volatile organic compounds (NMVOC), ultimately

[6] Eutrophication is characterized by excessive plant and algae growth due to the high availability of nutrients. The algae that thrive on these nutrients absorb large quantities of oxygen.

leading to the formation of carbon dioxide (CO_2), as highlighted by Seinfeld and Pandis (2006). NMVOCs, in conjunction with NO_x, carbon monoxide (CO), and methane (CH_4), rank among the primary precursors of tropospheric ozone. Additionally, NMVOCs contribute to the production of secondary organic aerosols and influence the concentrations of hydroxyl radicals (OH), which serve as the primary tropospheric oxidant, as noted in Hartmann et al. (2013).

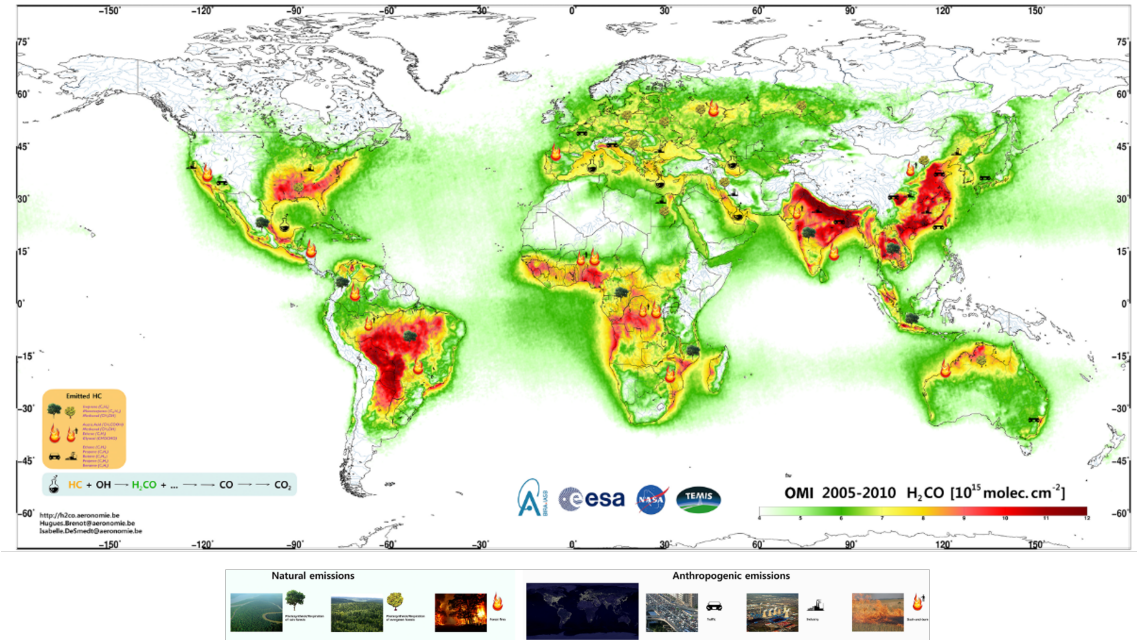

Figure 2.9: Global map of average H_2CO concentration extracted from OMI measurements during the period 2005-20010. Adapted from `https://uv-vis.aeronomie.be/news/20141027/`

H_2CO primarily originates from the oxidation of CH_4 in the remote atmosphere. Nevertheless, over continental regions, the oxidation of larger NMVOCs emitted by vegetation, wildfires, vehicular traffic, and industrial sources leads to significant localized increases in formaldehyde levels, as exemplified by Stavrakou et al. (2009c). Given its relatively short lifespan, a few hours, formaldehyde concentrations in the atmospheric boundary layer can be directly linked to emissions of short-lived volatile organic compounds, many of which cannot be observed directly from space. Furthermore, formaldehyde observations provide valuable insights into the chemical oxidation processes within the atmosphere, including the chemical production of CO from CH_4 and NMVOCs. Seasonal and interannual variations in the distribution of formaldehyde are primarily driven by temperature changes (which affect vegetation emissions), occurrences of wildfires, and alterations in anthropogenic activities (Stavrakou et al., 2009a).

2.4 AIR QUALITY IN AFRICA

Africa is currently facing, and will continue to face in the future, significant adverse effects resulting from human-induced environmental changes, such as climate change as reported by the IPCC (2021), as well as air pollution, as indicated in Babatola (2018). It is estimated that each year, more than one million people in Africa prematurely lose their lives due to exposure to indoor and outdoor air pollution, as documented by the

research of Fisher et al. (2021). Additionally, development in many African regions is particularly vulnerable to the consequences of climate change, as emphasized in the report of IPCC (2021). Recent research highlights the growing issue of air pollution in Africa. An Organisation for Economic Co-operation and Development (OECD) report, revealed a staggering 36 % increase in premature deaths attributed to air pollution between 1990 and 2013 (OECD, 2014). Furthermore, findings from Liousse's research indicate that urban air quality in Africa, particularly characterized by concentrations of NO_2 and aerosols, is anticipated to significantly worsen over the next decade (Liousse et al., 2014). With the ongoing urbanization across the continent, anthropogenic emissions stemming from the combustion of biomass are projected to undergo a substantial surge (Liousse et al., 2014). In 2019, air pollution was responsible for 691,000 premature deaths among infants and children under the age of 5 worldwide, with a staggering 56 percent of these tragic child fatalities, totaling 385,000, occurring on the African continent IHME (2022). The African continent boasts a wide climatic diversity, ranging from the arid regions of the north, predominantly Sahara-dominated, to the semi-arid zones of the Sahel, acting as a transitional area between the desert and the savanna and tropical rainforest regions further south. The annual movements of the Intertropical Convergence Zone have a pronounced impact on precipitation patterns in tropical and subtropical regions, resulting in distinct dry and wet seasons across many African nations (Giannini et al., 2008). This diverse climate exerts a significant influence on air quality, affecting both particulate matter (PM) and gas pollutants. For instance, countries experiencing distinct dry and wet seasons exhibit pronounced seasonal variations in PM levels, with higher concentrations during the dry season (Engelbrecht et al., 2001; Petkova et al., 2013).

The pressing development challenges that Africa faces, impacting air quality and climate change, are interconnected with factors like urbanization, economic growth, demographic shifts, poverty, and healthcare (CCAC, 2023).

2.4.1 Urbanization impact on air quality

Africa is currently experiencing unprecedented urban growth, ranking as the world's fastest-growing urban region. From a mere 15% urban population in 1960, this figure surged to 40% by 2010, with projections indicating a likely surpassing of 60% by 2050 (UN, 2018). This swift urbanization not only holds significant environmental and climatic implications but transforms expanding African cities into high-risk zones for climate change impacts, amplifying challenges related to poverty, informality, social exclusion, and governance. Projections reveal a notable increase in urban population exposure to extreme heat, rising from 2 billion person-days annually between 1985 and 2005 to a projected 45 billion person-days by the 2060s, with West Africa facing the highest exposure (Pörtner et al., 2022).

An observable outcome accompanying this urbanization surge is the emergence of slums around many African cities. Driven by factors such as population growth, rural-to-urban migration, a scarcity of affordable housing, weak governance, and the impacts of conflicts, natural disasters, and climate change (UN-Habitat, 2018), more than 60% of Africa's urban dwellers currently reside in these slums. This concentration includes vulnerable groups, such as those with preexisting illnesses, the unemployed, and the elderly (Godfrey and Tunhuma, 2020).

Population growth and urbanization have also spurred increased vehicle ownership, insuffi-

cient infrastructure development, densely populated areas, and service delivery challenges encompassing electricity access and waste management (Amegah, 2020). In numerous urban areas, especially informal settlements, residents rely on solid fuels for cooking and heating. The limited municipal capacity for waste collection leads to illegal waste dumping and open-air burning, compounding environmental problems. If prevailing trends persist, Africa is on track to become the world's leading region in total waste production due to population growth and rapid urbanization (UNEP, 2020).

In light of the challenges stemming from population growth and poverty in Africa, effective urbanization management is imperative. Poor air quality, unpreparedness of cities for increased populations, and the consequences of extreme weather events, such as the heat island effect and floods resulting from inadequate drainage systems, pose serious health and safety risks (Freire et al., 2014).

2.4.2 Agriculture impact on air quality

Agriculture, as a crucial sector, is responsible for environmental issues, including human health concerns arising from exposure to ammonia, hydrogen sulfide, toxic organic compounds, pesticides, and airborne particulate matter (Aneja et al., 2009). It also contributes to climate change through its greenhouse gas emissions and aerosols. Biomass burning, driven by agricultural practices like post-harvest burning for fertilization and pest control, predominantly results from human activities (Bauer et al., 2019). In many African countries, the practice of forest burning is common, primarily for land preparation in agriculture and protection against predators. Farmers burn forested areas to free up fertile land for essential food crops. However, this traditional method can lead to environmental issues such as biodiversity loss, soil degradation, and greenhouse gas emissions (Brink, 2021; Shukla et al., 2019). Additionally, forest burning is also employed to deter harmful wildlife, but it can disrupt natural ecosystems and wildlife populations. Land plays a critical role as both a source and sink of greenhouse gas emissions, making it a crucial factor in climate change mitigation strategies (Shukla et al., 2019). Several studies, primarily based on satellite observations and models, provide evidence that seasonal biomass burning is considered a significant source of pollution in Africa, leading to emissions of black carbon and volatile organic compounds (e.g., Marais and Wiedinmyer (2016b); De Smedt et al. (2015)). In sub-Saharan Africa, 60% of greenhouse gas emissions originate from slash-and-burn agriculture, a practice involving the cutting and burning of natural vegetation to clear land for cultivation (Bornman et al., 2017). Local authorities and conservation organizations should collaborate closely to promote sustainable agricultural practices and environmentally friendly predator management strategies. This collaborative approach aims to balance the needs of local communities with the preservation of natural resources while minimizing negative impacts on biodiversity.

2.4.3 Energy use impact on air quality

The African continent holds substantial potential for the development of clean and renewable energy sources, such as hydroelectricity, solar, and wind power. It possesses one of the world's richest solar resources, yet only holds 1% of the installed global solar photovoltaic capacity. Despite this, Africa's electricity generation primarily relies on thermal power plants, with over 80% of the total production coming from these sources, including

coal-fired power plants in South Africa and oil-fired units in Nigeria and North Africa (Karekezi, 2002; IEA, 2019). In 2018, nearly half of Africa's population, approximately 600 million people, lacked access to electricity, while around 80% of African businesses frequently experienced power interruptions, resulting in economic losses (IEA, 2019). Another significant challenge lies in the realm of cooking, where biomass, such as firewood and charcoal, remains the primary energy source for many communities, with over 70% of the population relying on it. This has substantial environmental and health implications (World Bank 2014; IEA (2019)). Marais and Wiedinmyer (2016b) suggest that human-induced pollution in Africa primarily stems from dispersed and inefficient combustion sources, attributed to limited access to electricity and the proliferation of outdated motorcycles and cars. The same study reveals that in Africa, between 2006 and 2013, the production and utilization of charcoal, gasoline, and diesel for motorcycles, cars, and generators increased at a faster rate than the use of firewood as an energy source.

In summary, coal-fired thermal power plants and the use of charcoal for cooking have a significant impact on air quality in Africa, contributing to significant public health and environmental issues. Transitioning to cleaner and more sustainable energy sources is crucial to mitigate these detrimental effects and improve air quality in the region.

Figure 2.10: Illustration of some scenes influencing air quality in Africa

2.4.4 Precariousness, economic disparities impact on air quality

The relationship between poverty and air quality is intricate and multifactorial, and it can vary depending on geographical and economic contexts. However, there are several mechanisms through which poverty can influence air quality, and vice versa. It is essential to underscore the economic precarity that Africa is grappling with. The United Nations Conference on Trade and Development (UNCTD, 2021) reported that in 2019, 478 million people were living in extreme poverty in Africa. Moreover, it estimated that in 2021, 490 million people in Africa were living below the poverty threshold of 1.90 USD per day in purchasing power parity, which is 37 million more people than initially projected before the pandemic (UNCTD, 2021). These issues can have a significant impact on air quality, especially in the following aspects:

1. Access to Clean Energy: As previously mentioned, impoverished populations often

have limited access to clean energy sources, compelling them to use solid fuels like wood, charcoal, and biomass for cooking and heating. Millions of Africans live below the international poverty line.

2. Housing Conditions: These same individuals living in poverty are more likely to reside in substandard housing, often poorly ventilated and overcrowded, exacerbating indoor air quality by promoting pollutant concentration.

3. Mobility: Impoverished populations often have fewer mobility options and are more likely to use less clean modes of transportation, such as old, polluting vehicles or overcrowded public transport, contributing to outdoor air pollution. In Africa, many people rely on old buses emitting exhaust fumes as their means of transportation, often enduring long hours in traffic jams, further exposing them to air pollution.

4. Awareness: Addressing air quality issues requires raising awareness among the population because it's challenging for local authorities to tackle a problem that the public doesn't consider a significant concern. Effective awareness campaigns, starting with education, are crucial. Notably, there is a shortage of scientists working in the field of air quality and climate change in Africa. The few scientists interested in this domain often lack adequate funding and resources to conduct their research effectively.

2.4.5 Control and regulation

Controlling and regulating air quality is of paramount importance in safeguarding public health and the environment. Government authorities and environmental agencies closely monitor air pollution levels, measuring the concentration of pollutants such as fine particulate matter, nitrogen oxides, sulfur dioxide, and volatile organic compounds. These measurements are crucial for assessing compliance with established air quality standards, identifying sources of pollution, and developing policies to reduce harmful emissions. Stringent regulations are in place to control industrial emissions, vehicle emissions, as well as heating and cooking practices.

These regulations are often established at the national and regional levels, but there are also international agreements in place to manage air pollution on a global scale, as is the case for global environmental issues such as the depletion of the stratospheric ozone layer and climate change. Among the major international agreements related to air pollution are the 1987 Montreal Protocol for the elimination of CFCs[7], the 2001 Stockholm Convention for the reduction of persistent organic pollutants, the 2013 Minamata Convention for the reduction of mercury emissions, the 1999 Gothenburg Protocol for the reduction of regional emissions of nitrogen oxides, sulfur dioxide, ammonia, and volatile organic compounds, as well as the 2015 Paris Agreement for the reduction of greenhouse gas emissions. While most of these international agreements target long-lived atmospheric pollutants with global impacts on the environment and health, the Gothenburg Protocol focuses on pollutants with regional effects (Seigneur, 2018). This highlights the need for an international approach to harmonize regulations, implement public policies, and monitor the effects of emission reductions, even at the regional level. Regulations related to air pollution in Africa vary from one country to another and are often influenced by national environmental standards and policies. Nevertheless, the majority of African nations do not possess comprehensive national air quality regulations, which includes several highly

[7]CFCs, or chlorofluorocarbons, are a class of chemical compounds containing chlorine, fluorine, and carbon.

populated countries like the Democratic Republic of the Congo, Egypt, and Ethiopia. In reality, only 17 African countries have implemented legal frameworks that incorporate air quality standards. These nations are Algeria, Benin, Burkina Faso, Côte d'Ivoire, Egypt, Eswatini, Gambia, Ghana, Kenya, Mauritius, Morocco, Mozambique, Nigeria, Rwanda, Senegal, South Africa, and the United Republic of Tanzania (IHME, 2022).

Additionally, modern air quality monitoring utilizes a combination of ground-based surveillance networks and satellite-based systems to provide comprehensive coverage and data for informed decision-making. Raising public awareness about air quality issues and promoting environmentally responsible behaviors also play a pivotal role in improving air quality and protecting the health of the population.

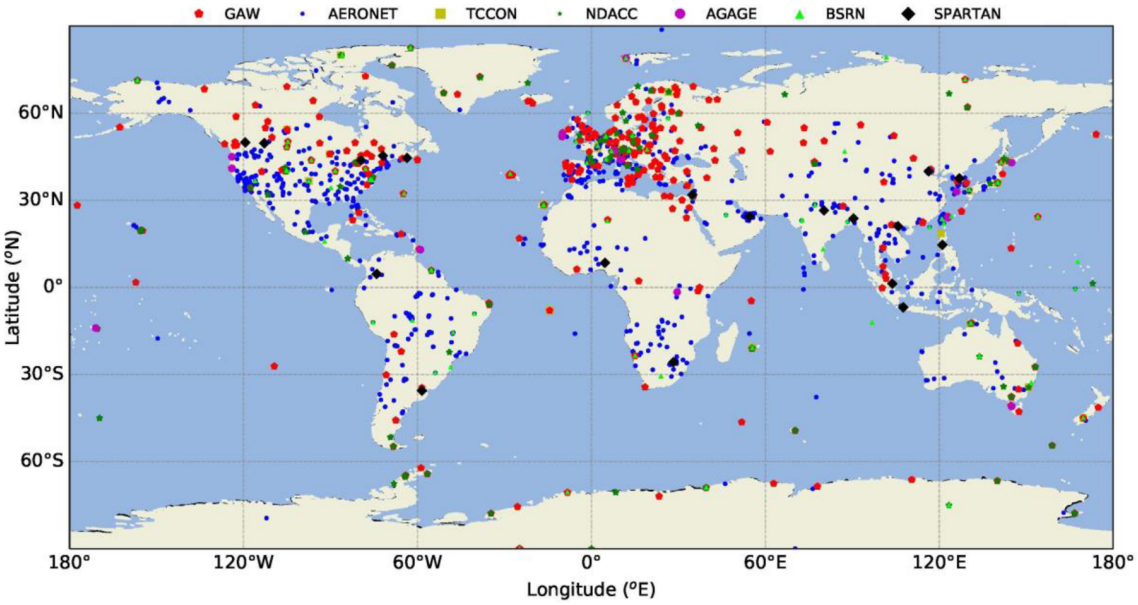

Figure 2.11: Networks of worldwide measurements with considerable underrepresentation in Africa (Paton-Walsh et al., 2022).

Several atmospheric monitoring networks exist worldwide, playing a crucial role in gathering essential data on air quality and atmospheric composition. Among these networks are for example the International Network for the NDACC, encompassing approximately 70 stations distributed globally, contributing to the monitoring of various atmospheric pollutants and gases[8]. Additionally, the European Monitoring and Evaluation Programme (EMEP)[9] focuses on air quality monitoring in Europe, especially concerning transboundary pollutants. AIRNow in the United States provides real-time air quality data across the country, while Aerosol Robotic Network (AERONET) measures the distribution of atmospheric aerosols on a global scale[10]. These networks, among others, collaborate to monitor atmospheric pollutants, assess trends, and provide critical data to inform air quality policies and protect human health and the environment.

Despite the presence of these few ground-level air quality monitoring networks, Africa remains significantly undersampled compared to other regions of the world. Indeed, the number of monitoring stations in Africa is substantially lower than in other continents (Figure 2.11[11]). For some networks, it is even concerning to note that there are no stations

[8] https://www.dwd.de/EN/research/international_programme/ndacc/ndacc_node.html
[9] https://www.emep.int/
[10] https://aeronet.gsfc.nasa.gov/
[11] GAW : Global Atmosphere Watch, AERONET: AErosol RObotic NETwork, TCCON: Total Carbon Column

installed in Africa. This data collection gap greatly limits the possibilities for in-depth scientific studies in the field of air quality on the continent.

While satellite measurements and simulation models may be available, ground-level measurements remain essential for a comprehensive understanding of local atmospheric pollution phenomena. However, many African countries do not have such networks, making air quality monitoring and control particularly challenging in these regions. The establishment of more extensive monitoring networks in Africa remains a priority to better understand and mitigate air pollution issues. Thanks to independently funded initiatives such as AfriqAir, AirQo, and the Clean Air Monitoring and Solutions Network (CAMS-Net), we are witnessing the emergence of monitoring stations (Low-cost), albeit with limited financial resources, that are already capable of monitoring PM2.5 levels. This trend is particularly evident in countries like Ethiopia, Kenya, Rwanda, and Uganda (IHME, 2022). In 2020, we witnessed the official launch of air quality management plans in major African capitals like Cairo in Egypt and Addis Ababa in Ethiopia. While these plans are still in progress, they already demonstrate a strong commitment from the authorities of these countries to combat and improve air quality in their capitals, thus enabling residents to better cope with the existing high levels of pollution (IHME, 2022).

South Africa undoubtedly stands out as the African country most well-positioned and equipped for air quality control. The country already has its own air quality monitoring network (`https://saaqis.environment.gov.za/`), and in 2021, it formally solidified its commitment to a low-carbon economy. Additionally, a recent court ruling in South Africa recognized air pollution as a violation of constitutional rights, potentially paving the way for future actions aimed at enhancing air quality. South Africa also possesses a comprehensive document that guides air quality management in the country, providing clear regulatory requirements, including the identification of priority areas for air quality improvement.

In summary of this section on air pollution in Africa, we can conclude that ambient air pollution is on the rise across the continent. Without deliberate intervention, it is expected to increase morbidity and mortality rates, reduce economic productivity, hinder human capital development, and impede overall development. Given that many African countries are still in the early stages of development, they have the opportunity to implement robust solutions to combat this destructive menace. This includes establishing effective monitoring systems for tracking and facilitating control, transitioning to clean energy sources to reduce reliance on fossil fuels, and implementing regulations for aging vehicles and transportation equipment. In essence, adopting effective environmental management policies is crucial.

2.4.6 Biogenic emissions in the Democratic Republic of Congo (DRC)

DRC is one of the largest countries in Africa, ranking second in terms of land area after Algeria and third in terms of population after Egypt[12]. This vast country faces issues related to air quality degradation, similar to other African nations grappling with the aforementioned challenges.

Observing Network, NDACC: Network for the Detection of Atmospheric Composition Change, AGAGE: Advanced Global Atmospheric Gases Experiment, BSRN: Baseline Surface Radiation Network, and SPARTAN: Surface Particulate Matter Network

[12]In 2019, the population of the DRC was 95,784,841 people `https://www.populationdata.net/pays/republique-democratique-du-congo/`

It is essential to emphasize that the DRC occupies a central position within the Congo Basin, where 54 % of the forested area of this basin is located within its borders Mayaux et al. (2013) (see Figure. 2.12). This forested area within the Congo Basin is exposed to multiple sources of pollutants, due to agricultural activities and the increasing demand for charcoal for cooking. According to the United Nations (UN) report, the DRC ranks second after Ethiopia in terms of household use of cooking fuels, whether it be wood, charcoal, or crop residues (UN, 2022). This forested region emits significant amounts of pollutants, which are directly observable from satellites, as evidenced by recent research.

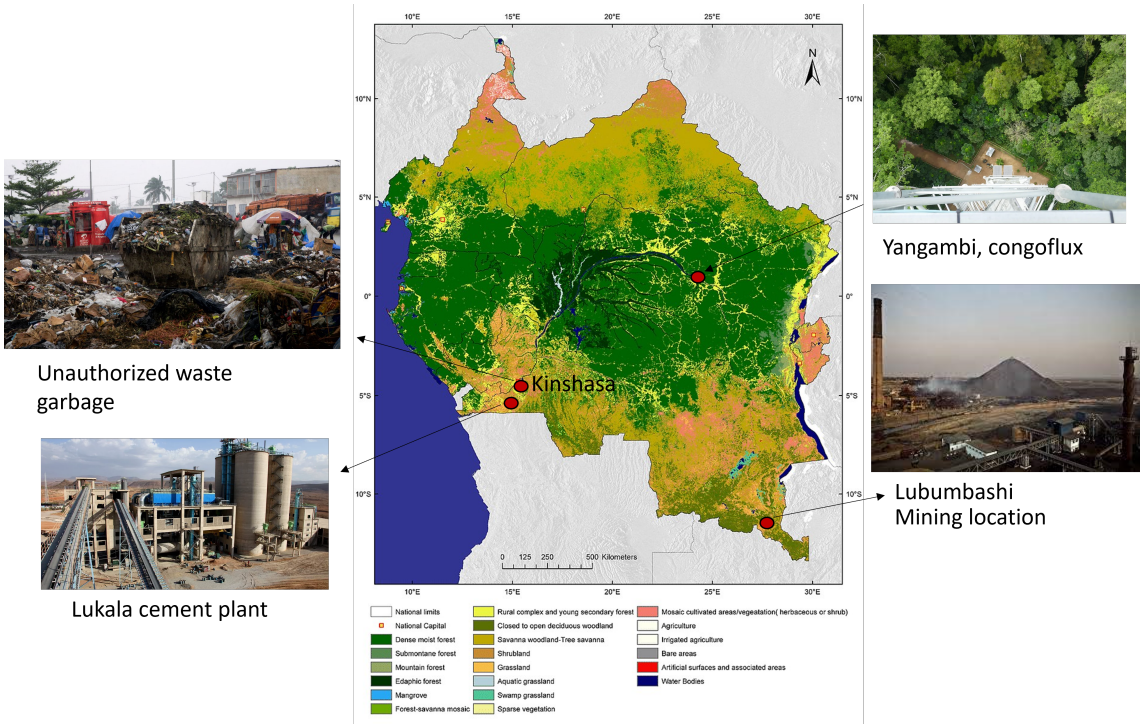

Figure 2.12: Stratification Map of Forests in the Democratic Republic of Congo and some illustrations of the country's industrial sites (Lukala, Lubumbashi), the Yangambi site where the congoflux hole is located and an illustration of a wild garbage dump in Kinshasa.. Adapted from Verhegghen et al. (2012)

For example, De Smedt et al. (2015) found that H_2CO column hotspots associated with vegetation fires in the region are among the highest in the world. Measurements in Bujumbura (Burundi) using the MAX-DOAS technique, have shown that the local atmospheric composition is influenced by biogenic VOC emissions from the south/southeastern region, even though this site is relatively far away from emission sources, located further west in the Democratic Republic of Congo Gielen et al. (2017). In addition, the DRC has a volcano in the East which also happens to be an important source of SO_2, a species that strongly influences air quality. A recent study by the BIRA-IASB team in the RESIST project (study of Nyamuragira and Nyiragongo volcanoes, SO_2 measurements from satellites and a UV camera) shows the presence of peak SO_2 concentrations in the study area[13].

Most major cities in the DRC are facing rapid population growth, accompanied by an increase in anthropogenic activities, including road traffic. In some industrial cities like

[13]BIRA-IASB, internal communication, 2015

Lubumbashi[14], Kimpese-Lukala[15], and Moanda[16], the effects of air quality degradation have become nearly visible to the naked eye, primarily due to the lack of monitoring and control policies. A recent study presented by Martínez-Alonso et al. (2023) highlights inter-annual trends in NOx emissions derived from TROPOMI data that are strongly correlated with mining production throughout the mining area of the DRC, including cities like Kolwezi, Lumwana, and Lubumbashi. Despite these alarming findings regarding air quality degradation, the country as a whole still lacks, to this day, regulatory measures concerning air quality control. There are few articles[17] scattered among other regulatory texts governing the forestry code, civil aviation and environmental protection in general. While the latest report by CCAC (2023) suggests that efforts are being made by the Ministry of Environment and Sustainable Development of the DRC to plan measures aimed at improving access to adequate sanitation services, unfortunately, these measures primarily focus on municipal waste management, maintenance of drainage canals, rivers, and waste collection points. In 2012, the country installed a tower equipped with instruments for precise and continuous monitoring of GHGs exchanges between the atmosphere and the ecosystem in the Congo Basin forest[18]. This was part of a large-scale project funded by the European Union aimed at promoting sustainable participatory management of the Yangambi Biosphere Reserve[19]. It's worth noting that this project primarily focuses on climate-related aspects rather than air quality. Thus far, no policies have been established regarding air quality monitoring systems, tracking, and control.

Kinshasa, the capital of the DRC, is a rapidly expanding metropolis with a population of 12 million in 2016, expected to reach 20 million by 2030 UN (2016). Unfortunately, like many other large cities in Central Africa, Kinshasa faces significant air pollution challenges (McFarlane et al., 2021). The city is witnessing a surge in the number of motorcycles, mostly older vehicles, and its road infrastructure is poorly managed and largely unpaved. Additionally, the fuel quality in the region is poor due to the presence of fuel sold by individual brokers who acquire their products through unofficial networks from neighboring countries[2021]. Kinshasa is also surrounded by the vast forests of the Congo Basin, and a majority of its population relies on charcoal for cooking. A recent study conducted by Vohra et al. (2022), based on satellite observations, has revealed substantial annual increases in NO_2 levels in several major African megacities, including Kinshasa, due to emerging anthropogenic sources. Despite these alarming pollution trends, the absence of regular monitoring hampers the development of effective policies aimed at improving air quality. Nonetheless, effectively addressing an issue like air pollution necessitates a comprehensive understanding of the phenomenon, which can vary significantly from one region to another. This understanding hinges on the collection of data primarily aimed at conducting studies that, in turn, inform strategies for the prevention and management of

[14]Lubumbashi, the second-largest city in the Democratic Republic of the Congo in terms of population and economic significance, serves as the headquarters for several major Congolese companies, including GECAMINES (General Company of Mines and Quarries).

[15]Kimpese and Lukala are two major cities in the DRC that host cement companies. Emissions from the cement plant in these cities result in visible dry deposits that can be seen with the naked eye..

[16]Moanda is a coastal city located on the shores of the Atlantic Ocean, housing the oil companies of the DRC.

[17]Loi no10/014 du 31 décembre 2010 relative à l'aviation civile, Loi no 011/2002 du 29 Août 2002, portant code forestier, Loi no11/009 du 09 juillet 2011 portant principes fondamentaux relatifs à la protection de l'environnement

[18]`https://www.congo-biogeochem.com/congoflux`

[19]At the pinnacle of this tower, which offers a vantage point above the forest canopy, measurements are taken at a 15 Hz frequency to assess the concentrations of different greenhouse gases (CO_2, H_2O, N_2O and CH_4). Additionally, wind speed and direction are also monitored.

[20]https://www.publiceye.ch/en/publications/detail/dirty-diesel-1-1

[21]Public Eye collected samples at the pump in eight countries (Angola, Benin, Congo Brazzaville, Côte d'Ivoire, Ghana, Mali, Senegal, and Zambia) and found that the sulfur content in fuels is up to 378 times higher than the allowed levels in Europe.

Figure 2.13: Current atmospheric pollutant measurement station located on the rooftop of the Faculty of Sciences at the University of Kinshasa. On the left, the MODULAIR instrument for surface measurements, installed in May 2023, and on the right, the MAX-DOAS instrument, the foundation of this thesis, installed since November 2019. The MAX-DOAS instrument enables measurements at various elevation angles, facilitating the extraction of vertical profiles of trace gases in the UV-Vis range.

pollution peaks.

Since 2017, the University of Kinshasa has established a fruitful collaboration with the BIRA-IASB in Belgium to set up the first observation station in Kinshasa. This station serves as the basis for the current study. Additionally, the Kinshasa School of Public Health has also succeeded, through its collaboration with Columbia University, in installing several low-cost fixed stations in various locations throughout the city, enabling the measurement of suspended particulate matter in the air[22]. Since May 2023, we have a total of four operational instruments in Kinshasa, dedicated to monitoring surface pollutants and analyzing vertical profiles of certain trace gases.

It is important to emphasize that these advancements are the result of active collaboration between local scientists and foreign universities, primarily focused on training the next generation of academics. It should be noted that these initiatives do not receive substantial support from local or national authorities. Thus far, these efforts remain confined to the city of Kinshasa, and there are still no similar measurement systems in place in other cities within the country.

2.5 CHAPTER PARTIAL CONCLUSION

In summary, this chapter is divided into two main sections. The first section provides an overview of fundamental aspects of the Earth's atmosphere, starting with its chemical

[22]Ecole de santé Publique de Kinshasa, in collaboration with Columbia University(Lamont-Doherty Earth Observatory), has installed three low-cost PM measurement instruments at three strategic locations in Kinshasa: Kintambo Magasin Crossroad, UPN Crossroad, and the US Embassy in Kinshasa

composition and various physicochemical characteristics. The two molecules under study, NO_2 and H_2CO, are introduced briefly, including their emission processes, formation, and transformation, leading to the production of other compounds, which are referred to as precursors. Their impacts on human health and the environment are also discussed.

The second section is dedicated entirely to the issues of air pollution, with a strong focus on the current state of this problem in Africa, particularly in Central Africa, where this study is conducted. It is states that Africa is significantly affected by deteriorating air quality due to rapid population growth, widespread use of non-clean energy sources such as charcoal for cooking, forest fires for agriculture preparation, and the presence of many old vehicles and motorcycles. This crisis has a particularly severe impact on vulnerable populations and has been highlighted by recent reports and research from organizations such as the WHO, the UN, and Climate and Clean Air Coalition (CCAC). It is also shown that only a few African countries have implemented effective strategies to combat this issue. The majority of countries lack air quality regulations and monitoring systems. This problem is further exemplified in the last part of the chapter, focusing on the case of the DRC, a vast country at the heart of the Congo Basin. Despite the severe air quality deterioration in its capital, a major metropolis, there is no air quality monitoring network or relevant regulatory framework in place to address the issue.

Chapter 3

TOOLS AND METHODS

This chapter introduces the equipment utilized for the measurements conducted in Kinshasa, outlining its hardware and software components, the calibration through the extensive MAX-DOAS instrument of the BIRA-IASB, its installation in Kinshasa, and ultimately, the display of the recorded spectra. It also presents the tools used in the processing of the measurements made, the analysis and the interpretation.

3.1 INSTRUMENTAL SETUP

In the context of this thesis, we used two complementary instrument versions. The first version, referred to as the "simplified" version, operates under a fixed observation geometry (at an elevation angle of 35 degrees and at zenith) and was active from May 2017 to November 2019. The second version, operating with variable elevation angle geometry, has been running from November 2019 to the present day.

Both of these instrument versions are based on the DOAS technique and were developed at the BIRA-IASB/UV-Visible Group. Each version consists of two main components: the scanning unit, responsible for collecting scattered light, and the acquisition-control unit, housing a spectrometer and a computer for recording and storing measurements. These two components are interconnected through an optical fiber and a data connection cable. Each of these aspects will be briefly described in the following sections.

3.1.1 The scanner

For the first version of the instrument, we utilized a scanner based on a commercial motorized mount called NexStar (see Figure 3.1). The NexStar mount, manufactured by Celestron, was originally designed to facilitate the observation of stars, planets, and other celestial objects using an automated pointing system commonly known as the GoTo system. In our particular application, which did not involve star observation, we removed the optical component of the instrument and replaced it with an interface piece that secured an optical fiber. Since the motorized NexStar mount is an electromechanical module controlled by programmable electronics to perform orientation movements, we took advantage of this feature to interface the system with a computer. On this computer, we installed a program that allowed us to command the telescope either from its original

console (hand control) or from the computer itself, enabling us to take measurements at various elevation angles.

This system proved to be less efficient because it required us to climb onto the roof of the Faculty of Science with all the heavy equipment and remain in place to take measurements. Therefore, the system depended on the presence of the operator at the observation site (see Figure 3.7, panel a), and under certain adverse weather conditions, measurements could not be conducted. These limitations led us to restrict measurements for extended periods to a fixed position (35° and zenith), which motivated us to replace the old version of the instrument with an automated scanner.

Figure 3.1: Motorized mount for version 1 of the MAX-DOAS instrument installed on the roof of Faculty of Science of UniKiN.

In the second version of the instrument, the scanning apparatus consists of a hermetically sealed metal Aluminium enclosure , safeguarding the internal components from water and insect intrusion (see Figure 3.2). This construction is vital to ensure extended measurement periods even in challenging conditions, as highlighted by Galle et al. (2010); Hönninger et al. (2004). The enclosure measures 22×14×8 cm^3 and is mounted on a 45° inclined support. Scattered light enters the main compartment through a fused silica window (in quartz) and strikes a flat elliptical mirror with a minor axis 26.97 mm coated with enhanced aluminum. This mirror is attached to a HITEC servomotor (HS-7985MG) that scans between the horizon and zenith at various angles above the horizon (0°, 1°, 2°, 3°, 4°, 5°, 6°, 7°, 8°, 15°, 30°, 45°, 88°). The reflected light from the mirror is then directed onto a fused silica plano-convex lens with a diameter (D) of 25 mm and a focal length (f) of 50 mm. This lens focuses the light onto an optical fiber, facilitating its transfer to the acquisition-control unit. At each mirror position, light is accumulated for 50 seconds, resulting in a total scan time of about 10 minutes. The motor is governed by an ARDUINO electronic board, featuring a USB port for communication with the acquisition-control unit. The theoretical field of view (FOV) of the optical system is 0.66° (see B1, calculated using Equation 3.1 (Merlaud, 2013), taking into account a fiber diameter (d) of 600 μm. All internal components of the enclosure have been mounted on an anodized aluminum support (black-colored plate) to prevent reflections from any extraneous light

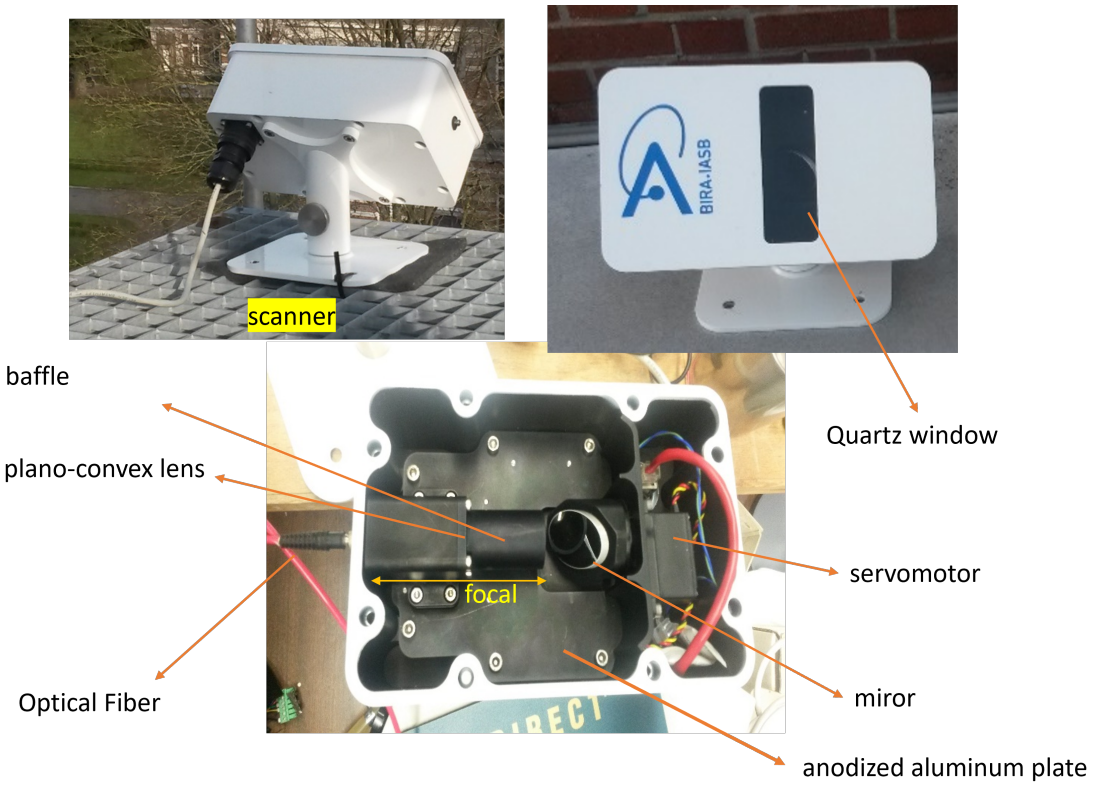

Figure 3.2: Kinshasa MAX-DOAS instrument optical head.

sources (straylight).

$$FOV = 2 \arctan \frac{2d}{2f} \tag{3.1}$$

3.1.2 The acquisition–control unit

For the first version of the instrument, the data acquisition system included a spectrometer connected to an optical fiber, with this configuration directly connected to a computer running the Windows operating system. The computer was equipped with software designed for controlling the Nexstar mount and capturing spectra in ASCII format. The specifications of the spectrometer and optical fiber remained unchanged from those used in the second version of the instrument, as described in table 3.1.

In the second version of the instrument, the second part of the instrument is also comprised of a metallic housing (Enclosures : nominal height = 300m, nominal width = 300m and nominal depth = 150 m), which receives the collected light through the optical fiber and directs it towards the UV–Vis spectrometer ((AvaSpec-ULS2048XL-USB2)[3]. This commercial spectrometer is designed with a symmetric crossed Czerny-Turner configuration, incorporates a diffraction grating (1200 lines per millimeter), and features a 50 µm wide slit. It is capable of recording spectra in the wavelength range of 280 to 550 nm, with a resolution of 0.7 nm (full width at half maximum) with a focal length of 75 mm.

[3]https://cdn.specpick.com/images/photonics/43_45_avaspec_uls2048xl_sensline_high_uv_and_nir_sensitivity_back_thinned_ccd_spectrometer.pdf

Table 3.1: The main technical characteristics of the Avantes UV-Vis AvaSpec-ULS2048XL-USB2 Fiber Optic Spectrometer.

Parameters	**characteristics**
Optical Bench	Symmetrical Czerny-Turner, 75 mm focal length
Wavelength range	200 – 550 nm
Resolution	0.7 nm
Slit, Grating	50µW, 1200 L/mm
Stray light	$< 0.3\%$
Sensitivity (counts/µW per ms int. time)	250,000 counts
UV Quantum efficiency	60% (200-300nm)
Detector	Back-thinned CCD[1] image sensor 2048 pixels
Signal/Noise	450:1
AD converter	16 bit, 1 MHz
Integration time	1.82 ms – 60 sec
Interface	USB 2.0 high speed
Sample speed with on-board averaging	2.09 ms / scan
Data transfer speed	1.82 ms / scan (USB2)
Digital IO	HD-26 connector, 2 Analog in, 2 Analog out, 3 Digital in, 12 Digital out, trigger, synchronization
Power supply	Default USB power, 450 mA Or with SPU2[2] external 12VDC, 200 mA
Dimensions, weight	175 x 110 x 44 mm (1 channel), 855 grams

For detection, it utilizes a Charge-coupled device (CCD) detector array consisting of 2048 pixels, and its integration time can be adjusted within a range of 1.82 ms to 60 sec.

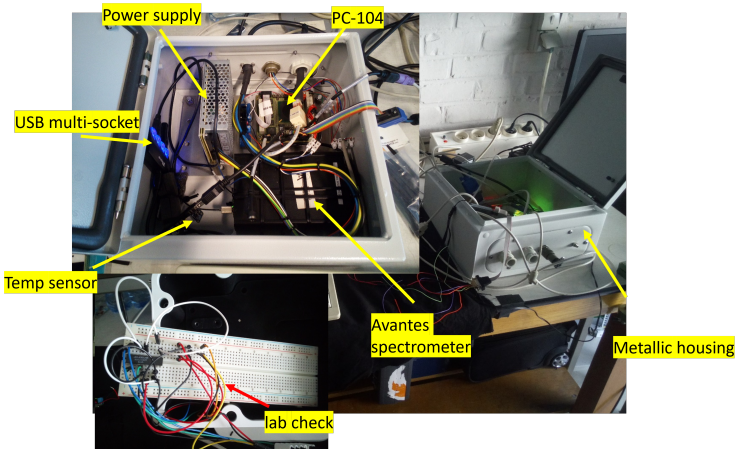

Figure 3.3: Internal part of the acquisition and control system for the second version of the MAX-DOAS instrument.

To monitor the temperature and to detect excessive thermal elevation, a temperature measurement system has been installed. This system comprises a type temperature sensor (BMP180 : -40°C to 85°C with ±1.0°C accuracy) controlled by an ARDUINO electronic board. Additionally, a cooling fan is integrated into the housing to ensure proper cooling.

Within this housing, a Linux-based PC-104 modular industrial microcomputer standard (96×90 mm) is installed. This computer manages the servo motor of the instrument's optical head and is responsible for acquiring spectra from the spectrometer. The voltage regulation system is integrated due to the fact that the control unit is powered by a 220V/AC supply. A C++ program, the flowchart of which is provided in Figure 3.5, is implemented on the PC104 computer, controlling the entire system. Figure 3.4 provides the overall diagram of the instrument, along with a schematic description of the interconnections between different components of the instrument.

It is worth noting that the descriptions provided in the preceding lines concern exclusively the second version of the instrument, as it is considered an improvement over the first version and was installed to replace the latter. The first version consisted of the same type of spectrometer, directly connected to a Windows-operating computer. An optical fiber with identical characteristics was also used for the collection of scattered light. The details of this initial instrument can be found in the article by Yombo Phaka et al. (2021).

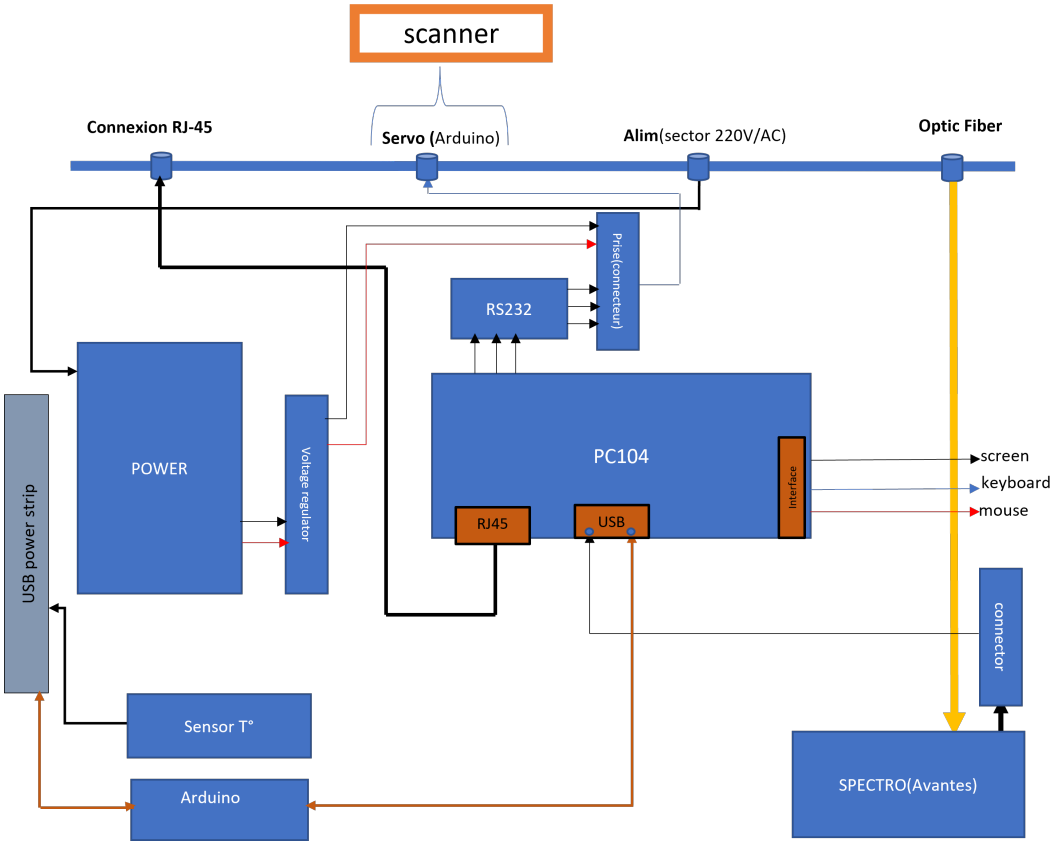

Figure 3.4: MAX-DOAS Kinshasa Instrumental setup.

3.1.3 Installation instrument in Kinshasa

After development at BIRA-IASB, the two versions of the MAX-DOAS instrument in Kinshasa, known as the Kin-AeroDOAS system, were tested and validated before being installed in Kinshasa. The test consisted in comparing the measurements provided by the latter with those of the large MAX-DOAS instrument of the NDACC network operational at BIRA-IASB. To this end, the Kin-AeroDOAS system and the large MAX-DOAS instrument at BIRA-IASB were placed side-by-side to operate under the same atmospheric

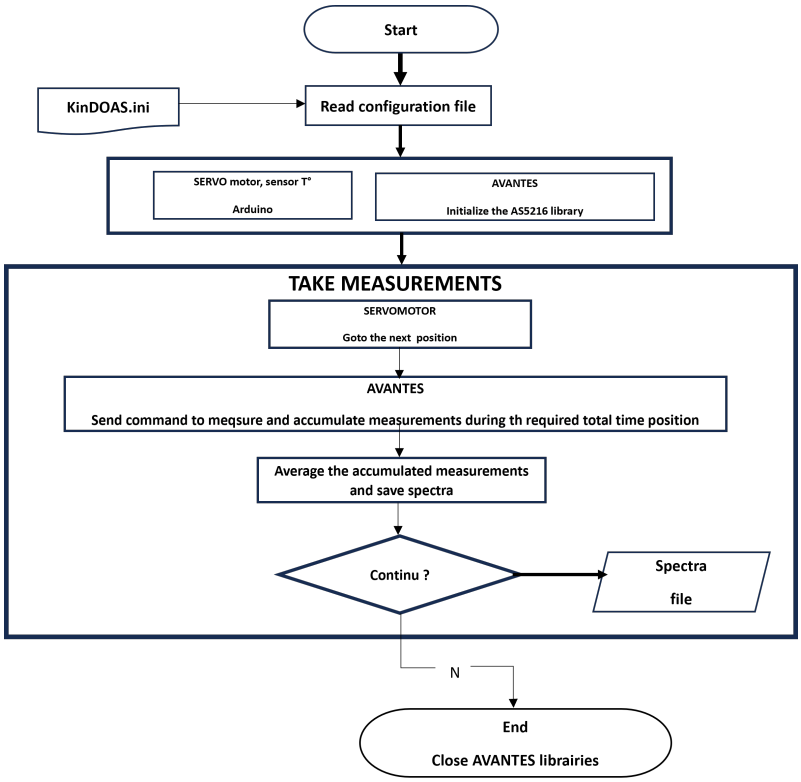

Figure 3.5: The flowchart process of the Kinshasa MAX-DOAS acquisition software.

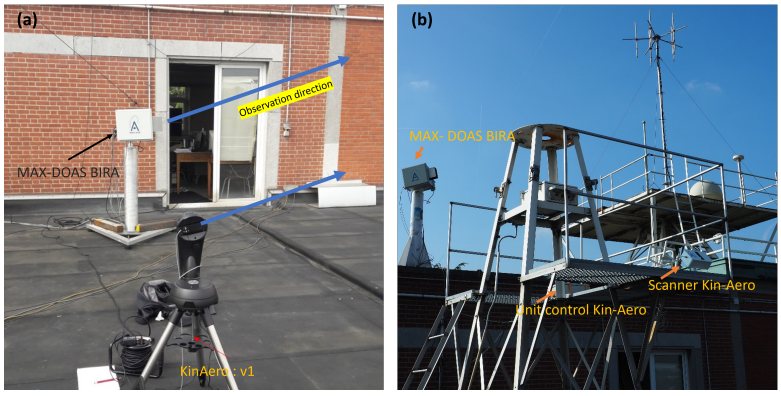

Figure 3.6: Test installation at BIRA-IASB: BIRA MAX-DOAS and KinAERO measurements

and logistical conditions (Figure 3.6). The results of these comparisons, in terms of dSCD (see appendix C), showed a correlation of 89 % and a slope of around 1. This result gave us confidence that the system was performing well and could be used in a different environment.

3.1.4 Measured spectrum

The spectrum measured by the MAX-DOAS instrument in Kinshasa consists of 2048 data points (see Figure 3.8), corresponding to the number of pixels on its onboard linear detector. The amplitude of the recorded signal depends on the amount of light (number of photons) reaching each pixel per unit of time.

Figure 3.7: Installation of the instrument in Kinshasa. (panel a, b: MAX-DOAS measurement with version 1) (panel a, b: scanner on the roof of UniKin's Faculty of Science and the control and command unit : version 2)

The quality of the recorded signal depends on several essential parameters, including light intensity, integration time, detector sensitivity, detector stability, calibration, signal-to-noise ratio, and the measurement environment.

Light intensity plays a central role in the quality of measurements. Adequate light intensity is imperative to ensure accurate and reliable data. Low-light conditions, such as during rain or the presence of dark clouds, can pose challenges. In such situations, count values for low intensities can drop below 600 counts [4]. Effectively managing variations in light intensity is crucial, and the integration time parameter determines the duration during which the detector measures light, directly impacting data quality.

Detector sensitivity to light within the spectral range of interest is crucial. A highly sensitive detector can detect low-intensity light signals, which is essential for applications that require the detection of very faint light levels. The Avantes spectrometer, known for its high sensitivity, is frequently used in the scientific community for optical atmospheric remote sensing applications, especially for measuring trace gas pollution (e.g :Chan et al. (2020b); Roșu et al. (2021)).

Detector stability over time, as well as its linearity of response, are critical considerations. Stability ensures consistent and reproducible measurements over time. The Avantes spectrometer has demonstrated exceptional stability, even in demanding environmental conditions, such as dust, heat, and humidity. Since its installation in Kinshasa in 2017, no instability has been observed.

Accurate detector calibration is a critical factor in ensuring measurement precision. Calibration corrects variations and signal distortions. Additionally, signal filtering and processing techniques enhance data quality by eliminating noise and unwanted artifacts. This calibration involves testing the spectrometer with spectral lamps and verifying the alignment of spectral lines with known wavelengths.

[4]The term "count" refers to a unit of measurement used to quantify the number of events or detections recorded by a detector. In the context of light or radiation detection, "count" typically represents the number of photons or particles detected by a detector during a specific time period.

Finally, the signal-to-noise ratio (SNR) is an essential parameter for reducing interference and improving data quality. A high SNR indicates that there is much more signal than noise, which is desirable as it signifies better detection quality. A low SNR means that the noise is comparable to or even greater than the signal, which can lead to lower-quality data. The Signal refers to the electrical signals generated by the CCD array in response to incident light. These signals are generated when photons of light strike the pixels of the CCD array, creating an electrical charge proportional to the light intensity. On the other hand, "noise" refers to unwanted fluctuations or disturbances in the electrical signals. Noise can have various sources, such as thermal noise, electronic noise, background noise, and more.

For a perfect detector, the noise, often referred to as "shot noise," depends solely on a single source, which is created by the fundamental nature of light itself and is therefore independent of the detector's quality. For such a perfect detector measuring N photons, its signal-to-noise ratio(shot noise) is determined by $\sqrt{N}$, which analytically describes it as a Poisson distribution on the number of detected photons (N) (Maître, 2016).

However, when working with non-perfect sensors like CCDs, two additional sources of noise may come into play: dark noise and read noise. Dark noise arises from thermally generated electrons within the CCD and also follows a Poisson distribution. It can be reduced by cooling the detector, as seen in high-powered detectors. For such detectors, the signal-to-noise ratio for a CCD is expressed in Equation 3.2.

$$SNR = \frac{IQ_E t}{\sqrt{IQ_E t + Dt + N_r^2}} \tag{3.2}$$

In equation 3.2, we utilize the following variables: I represents the incident photon flux (in photons per pixel per second), QE stands for quantum efficiency of the detector, t denotes the integration time (in seconds), D represents the dark current value, and Nr is the read noise (expressed in electrons rms per pixel). In practical scenarios, when the signal level is sufficiently high, shot noise often becomes the dominant factor compared to the other two sources. In such instances, the measurement is referred to as being "photon-noise limited" (Maître, 2016). In this study, the dark current correction for the recorded spectra is performed using the ozone cutoff principle, which occurs between 292 nm and 294 nm. Within this wavelength interval, ozone absorbs all incoming light, which means that any signal present in this spectral range is directly associated with the noise related to the dark current. Consequently, this correction is applied in the analysis of each measured spectrum.

3.2 DIFFERENTIAL OPTICAL ABSORPTION SPECTROSCOPY (DOAS)

3.2.1 DOAS historical background

The technique used to analyse the measurements made with the instrument used in this thesis is DOAS. DOAS is one of the atmospheric probing techniques that allows the derivation of column abundances of trace species from measurements of electromagnetic radiation in a specified interval. In the 1970s, Brewer et al. (1973) made the first atmospheric measurements of NO_2 using the first ideas of DOAS. Noxon (1975) and Platt

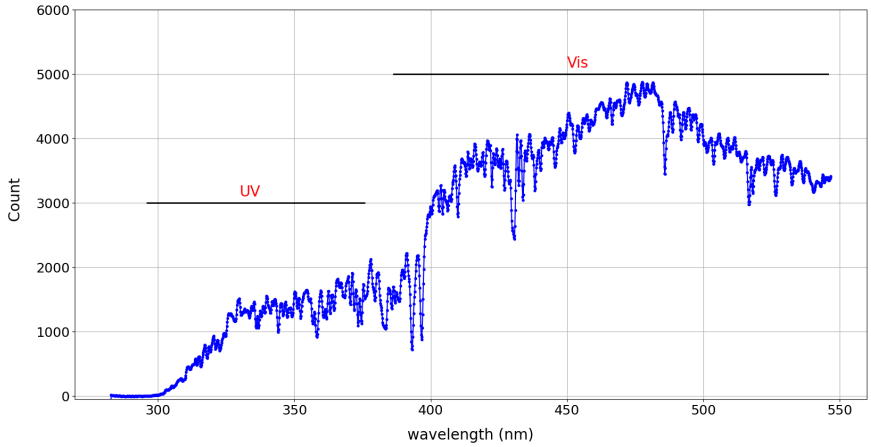

Figure 3.8: A typical spectrum measured by the MAX-DOAS instrument in Kinshasa. Two spectral bands are present: UV and Visible. The spectrum consists of 2048 data points on the x-axis, corresponding to the number of pixels on the linear detector of the spectrometer.

et al. (1979, 1980) further developed this technique and it is now in widespread use in the scientific community. With the advent of the photodiode array detector and the CCD array detector, which allows simultaneous measurement at many wavelengths, the use of DOAS has expanded considerably. The advantages and limitations of DOAS are briefly outlined in Section 3.3.

3.2.2 DOAS Light scattering

Light scattering is a term for physical processes involving the interaction of light and matter. In the framework of the DOAS technique, it is based on the Beer-Lamber law as illustrated in Figure3.9. Indeed, the spectrum recorded by the acquisition system represents the intensity of the light as a function of the wavelength as captured by the detector. For a single molecular species along the optical path (Figure3.9), the Beer-Lambert law states that the intensity of the detected light depends on the concentration of the molecular species and can be expressed as follows:

$$I(\lambda) = I_0(\lambda) exp(-L\sigma(\lambda)c) \tag{3.3}$$

where $I_0(\lambda)$ is the initial intensity, $I(\lambda)$ is the intensity of the radiation after passing through a thickness L of an absorber of uniform concentration c, $\sigma(\lambda)$ is the effective cross-section of that absorber. If the optical path length L is known, the concentration c of the molecular species along the optical path can be calculated by the expression :

$$c = \frac{D}{\sigma(\lambda)L} \tag{3.4}$$

$$D = \ln(\frac{I_0(\lambda)}{I(\lambda)}) \tag{3.5}$$

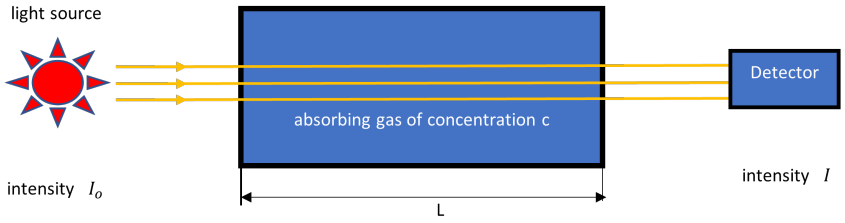

Figure 3.9: Illustration of the Beer-Lamber law.

Equation. 3.5, which features the parameter D referred to as optical thickness, proves readily applicable within laboratory settings with a prior understanding of cross-sections (see Fig. 3.10 somes cross-sections) as well as the optical path traversed by the photon across the sample. However, in atmospheric conditions, this expression necessitates certain adjustments to accommodate the intricate nature of the phenomenon along the optical trajectory, such as:

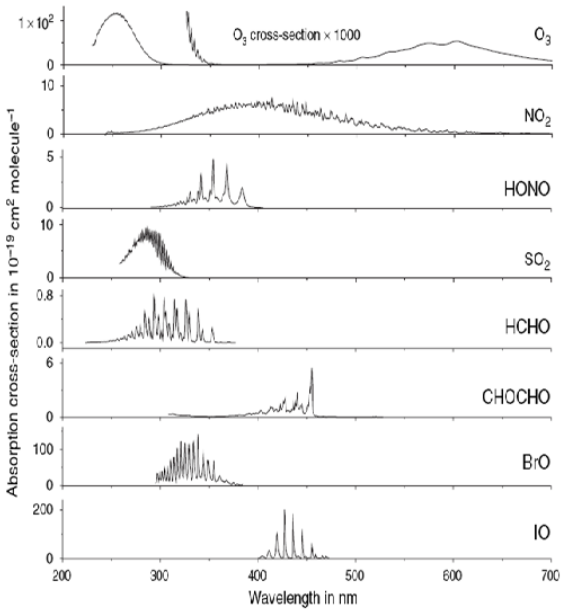

Figure 3.10: The different cross sections of some trace gases measured in the laboratory in the UV-Visible wavelength range (Platt and Stutz, 2008).

(1). The trajectory of light is not straight as it would be in controlled laboratory conditions. The light captured by the instrument undergoes multiple scattering events, which cannot be predetermined and are contingent upon observational geometry and atmospheric characteristics. For instance, aerosols induce varied alterations to the light path based on their dimensions (Petty, 2006).

(2). Numerous absorbers coexist. Their absorption spectra not only exhibit potential overlaps but also their concentrations exhibit variability with altitude.

(3). The light source, i.e., the sun, displays absorption features even prior to entering the atmosphere. These Fraunhofer lines emerge from atomic absorptions (H, Mg, Ca, etc.) within the solar atmosphere. Furthermore, barring satellite instruments,

direct measurement isn't feasible, given our observations occur within the absorbing medium. Consequently, the reduction in sunlight intensity dispersed within the atmosphere is far more intricate than depicted in Equation. 3.5.

(4). The instrument's transmissivity (comprising mirrors, CCD grids, retroreflectors, etc.) also diminishes the light intensity detected by the sensor. Turbulence contributes to the broadening of the light beam, impacting the received intensity as well (Platt and Stutz, 2008).

By formulating the Beer-Lambert equation while accounting for these considerations, the intensity of detected light, inclusive of N absorbers, can be expressed as follows:

$$I(\lambda) = I_0(\lambda)A(\lambda, T, p)exp - \int [\sum_{n=1}^{N} \sigma_{\mathrm{i}}(\lambda, s)c_{\mathrm{i}}(s) + \sigma_{\mathrm{Mi}}\rho_{\mathrm{Mi}}(\lambda, s) + \sigma_{\mathrm{Ray}}\rho_{\mathrm{Ray}}(\lambda, s)]ds \quad (3.6)$$

where $\mathrm{I}_0(\lambda)$ and $\mathrm{I}(\lambda)$ are respectively the intensities of direct sunlight at the Top of Atmosphere (TOA) without extinction and the scattered fraction measured by the instrument. $\sigma(\lambda)$ represents the effective cross-sections of the various absorbers present in the atmosphere. σ_{Mi} and σ_{Ray} are Rayleigh and Mi scattering cross-section, ρ_{Mi} and ρ_{Ray} are concentration of Mi and Rayleigh scatterers. A is the factor due to instrumental phenomena and atmospheric turbulence. The integral is carried along the optical path of the light measured in the atmosphere. For many absorbers, the ultraviolet-visible (UV-Vis) cross-section varies only slightly with temperature and pressure under atmospheric conditions. Assuming that the effective cross-section is a constant that depends only on wavelength, the optical thickness of a given absorber "i" in a spectrum of scattered light can be expressed as :

$$\tau(\lambda) = \int \sigma_{\mathrm{i}}(\lambda)c_{\mathrm{i}}(s)ds = \sigma_{\mathrm{i}}(\lambda) \int c_{\mathrm{i}}(s)ds \quad (3.7)$$

This leads to the definition of the Slant Column Density (SCD) of the species i (in molecules cm^{-2}) as:

$$SCD_{\mathrm{i}} = \int_0^{TOA} c_{\mathrm{i}}(s)ds \quad (3.8)$$

TOA means the Top of Atmosphere, assuming instrument is on the ground. SC_{i} does represent a concentration of the species measured, but along the optical path of the measurement ((Merlaud, 2013)). By integrating Rayleigh and Mie scattering, the intensity of the light detected can be expressed as follows:

$$I(\lambda) = I_0(\lambda)A(\lambda, T, p)exp - [\sum \sigma_{\mathrm{i}}(\lambda, s)SCD_{\mathrm{i}}(s) + \tau(\lambda)_{\mathrm{M}}(\lambda) + \tau(\lambda)_{\mathrm{R}}(\lambda)] \quad (3.9)$$

$\tau(\lambda)_{\mathrm{M}}$ and $\tau(\lambda)_{\mathrm{R}}$ represent the Mie and Rayleigh extinction coefficients respectively. Given the wavelength dependence of scattering ($\sigma_{\mathrm{Ray}} \approx \lambda^{-4}$ and $\sigma_{\mathrm{Mi}} \approx \lambda^{-1+..1}$)((Rayleigh, 1871; Mie, 1908)), the Mie and Rayleigh extinction coefficients can be smoothed and represented by polynomials ($\sum_{j=1}^{M} p_{\mathrm{i}}\ \lambda^j$), equation 3.6 can be written as :

$$I(\lambda) = I_0(\lambda) exp[-\sum_{n=1}^{N} \sigma_{\mathrm{i}}(\lambda, s) SCD_{\mathrm{i}}(s) - \sum_{j=1}^{M} p_{\mathrm{i}} \lambda^j] \tag{3.10}$$

By taking the logarithm of two sides, the Eq. 3.10 can be converted into the following linear equation and we return to the form of Equation. 3.5, taking into account the complex phenonomenes of light absorption and scattering by the air molecule. We then find the fundamental DOAS equation as :

$$D = \ln(\frac{I_0(\lambda)}{I(\lambda)}) = \sum_{n=1}^{N} \sigma_{\mathrm{i}}(\lambda, s) SCD_{\mathrm{i}}(s) + \sum_{j=1}^{M} p_{\mathrm{i}} \lambda^j \tag{3.11}$$

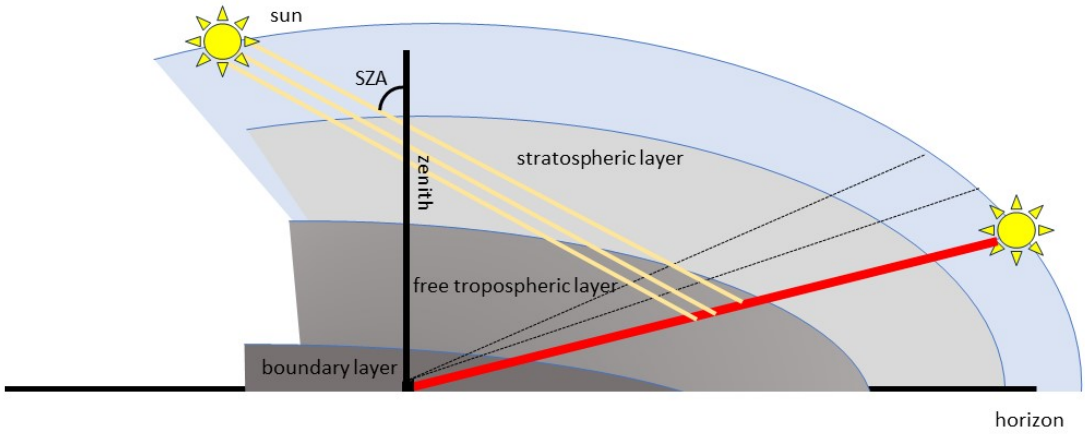

Figure 3.11: Optical path of sunlight at noon and horizons.

In practice, the intensity (I_0) cannot be directly measured from within the atmosphere and is thus inherently uncertain. To address this, a reference spectrum is employed, captured at a low Solar Zenithal Angle (SZA), preferably at zenith (around noon), to minimize the absorption of trace gases. Employing a reference spectrum consequently facilitates the computation of dSCD, which are differentials relative to this reference spectrum (Hönninger et al., 2004), as per Equation 3.12.

$$dSCD = SCD - SCD_{\mathrm{ref}} \tag{3.12}$$

Equation. 3.11 essentially constitutes a system of equations featuring N + M + 1 unknowns, which needs to be solved across all the relevant wavelengths. In this study, we employed the QODAS program developed at BIRA-IASB to process our acquired spectra, thereby generating the dSCDs.

3.3 DOAS limitations

The DOAS method, like other pollution detection techniques, presents both advantages and limitations that might prompt consideration of alternative methods[5]. The primary strengths of this technique include its ability to (1) provide real-time measurements of various tracer gas species using a single instrument (Platt and Perner, 1980), (2) offer a more representative average value over a long distance compared to a single measurement at a monitoring point (Edner et al., 1993), (3) effectively monitor a wide area from a single station, as illustrated in this study, and (4) reduce the frequency of instrumental calibration needs. Additionally, spectroscopic instruments are well-suited for automation, allowing continuous measurements without the need for oversight by DOAS(Edner et al., 1993).

Despite its numerous advantages, DOAS also presents somes limitations, including: (1) its effectiveness and functionality are limited to weak absorbers like NO_2, H_2CO, SO_2 and BrO due to the assumption of an optical path that must be independent of the concentration of the targeted pollutant (assumption of a thin atmosphere). (2) The challenge of extracting geophysical quantities for molecules with strong absorption features in the same spectral window of interest (interferences), as is the case, for example, with H_2CO and O_3 in the UV. (3) Sensitivity to atmospheric conditions, such as temperature variations (temperature-dependent cross-section). In addition, there are instrumental limitations, requiring favorable observation conditions, such as clear skies to maximize the number of photons reaching the detector.

3.4 DOAS retrieval

3.4.1 QDOAS theory

The program QDOAS (Danckaert and Fayt, 2017) is based on the Marquardt-Levenberg (M-L) technique. It fits the data to the absorption model derived from the Beer-Lambert law, using linear and non-linear regression methods. The fitting is performed on a small wavelength band adapted to a chosen absorber, and consists in solving a coupled problem involving a linear and a non-linear part. The non-linearity of Equation 3.11 is introduced with the consideration of parameters such as "the shift", "stretch" and "offset". Shift represent small wavelength shifts $\Delta(\lambda)$ between spectra I and I_0 and are taken into account by introducing the appropriate shift and stretch parameters as shown in Equation 3.13

$$\ln\left(\frac{I(\lambda-\Delta(\lambda))-offset(\lambda)}{I_0(\lambda)}\right)+\sum_{n=1}^{N}\sigma_{\mathrm{i}}(\lambda,s)SCD_{\mathrm{i}}(s)+\sum_{j=1}^{M}p_{\mathrm{j}}\lambda^{j}=0 \tag{3.13}$$

To recover the SCDs, the QDOAS sofware performs a least-squares fit of the measurement data to equation Eq. 3.13. As this is a nonlinear mutliple-variable problem, the fit is performed using the M-L algorithm. Note that the parameters known in this expression and which must be introduced as inputs into the QDOAS program are: the cross-sections

[5]Other pollutant measurement techniques include: Lidar Remote Sensing: Lidar (Light Detection and Ranging), Mass Spectrometry (Mass spectrometers), Passive Sampling, Fine Particle Measurements, In Situ Chemical Measurements (Specific Gas Analyzers), Fourier Transform Spectroscopy Detection, ..

of the molecules concerned, a low degree polynomial to take into account the contributions of the large bands to atmospheric attenuation (Rayleigh and Mie scattering) and other pseudo-effective cross-sections taking into account the Ring effect or instrument subsampling effects. The "Ring Effect" results from the filling-in effect on Fraunhofer lines originating from the rotational Raman scattering of oxygen and nitrogen molecules (Chance and Spurr, 1997). In DOAS analysis, a synthetic spectrum is introduced into QDOAS to correct for this filling-in effect.

3.4.2 QDOAS : M-L solution

The Marquardt algorithm combines the Gauss-Newton method and the gradient descent method to fit a nonlinear model to measured data more efficiently and robustly. The Gauss-Newton method is used when the parameters are close to the optimal solution, as it approximates the non-linear model by a linear model and allows rapid updates. On the other hand, the gradient descent method is used when the parameters are far from the solution, as it follows the direction of the gradient to converge faster. The algorithm alternates between these methods to optimize the fit of the model to the data in different situations. In QDOAS, the M-L algorithm is used to determine parameter values that minimize the sum of weighted squares (Eq. 3.14), thus ensuring optimal model fit to measured data (optical depth).

$$F(\overrightarrow{\alpha}) = \frac{1}{2}\sum_{k=1}^{K}[\frac{f^k(\overrightarrow{a})}{\nu^k}]^2 = \frac{1}{2}\sum_{k=1}^{K}[\frac{\ln(I^k(\overrightarrow{a}) + \sum_{i=1}^{N}\sigma_{\mathrm{ik}}SCD_{\mathrm{i}} + \sum_{j=1}^{M}p_{\mathrm{j}}\lambda_{\mathrm{k}}^{j} - \ln(I_0^k)}{\nu^k}]^2 \tag{3.14}$$

In Equation 3.14, $\overrightarrow{\alpha}$ represents the vector containing all fitted parameters, $\overrightarrow{a}$ the vector of parameters such as shift, stretch and offset of the measured spectrum and ν the standard error on the measurements. Full details of the M-L algorithm can be found in (Marquard et al., 2000), here we will show just the various stages as developed in QDOAS. These steps can be summarized in 3 points:

(1). Initialization: The algorithm starts by providing an initial estimate of the model parameters. These parameters determine the shape of the mathematical model used to fit the data. In QDOAS, this is done by providing the program with some initial values of parameters such as shift and stretch, enabling the initial value of SCD to be calculated analytically.

(2). Residual calculation (ε): For each data point, calculate the difference between the actual value and the value predicted by the model using the current parameters. This produces a set of residuals, representing the difference between the actual data and the model for each point. At each iteration, the new parameters are determined from the old ones and the program recalculates the sum of F.

$$\varepsilon = F^{old} - F^{new} \tag{3.15}$$

(3). Verification of convergence and results: Check whether the model parameters have converged to an optimal solution by comparing the new values with the old ones. If the difference is less than a predefined threshold, the algorithm is considered to

have converged. Dynamically adjust the regularization parameter λ to facilitate algorithm convergence. In QDOAS, the algorithm is considered to have converged to a solution when the difference between two successive F values is less than 10^{-3} or 10^{-4} (Danckaert and Fayt, 2017).

3.4.3 Errors On Slant Column Densities

The uncertainties on the extracted dSCDs after adjustment will therefore strongly depend on the sensitivity of the F-square sum and measurement noise. Theoretically, the covariance matrix is a statistical tool for quantifying the relationships between different parameters and their uncertainties. When the fit is complete, QDOAS generally provides the covariance matrix associated with the fitted parameters, by the inverse of the Hessian of the sum of the covariance matrix, evaluated at the fitted values of the parameters as follows :

$$\sum \overrightarrow{\alpha} = \chi^2 H^{-1} \tag{3.16}$$

Where H is the Hessian matrix given by the expression :

$$H_{pq} = \sum_{k=1}^{K} \frac{\partial^2 f^k}{\partial_{\alpha_p}} \frac{\partial^2 f^k}{\partial_{\alpha_q}} \frac{1}{(\nu^k)^2} \tag{3.17}$$

Equation 3.16 and Equation 3.17 are used when individual measurement errors ν_k are not available, or when the user has chosen not to weight the fit according to instrumental errors. In this case, the weight matrix W is simply the identity matrix. As a result, the mean square error on the measurements ν^k can be estimated by the reduced χ^2, which corresponds to the sum of the squares of the residuals divided by the number of degrees of freedom in the fit.

$$\chi^2 = \frac{\sum_{k=1}^{K} (f^i)^2}{M - N} \tag{3.18}$$

When QDOAS determines column density errors, it is crucial to consider the limitations of the statistical model used. The uncertainties of the fitted parameters depend on this model, which assumes independent measurement errors following a normal distribution. However, errors of adjustment or missing elements in the model may underestimate the true uncertainty. Residuals after fitting or a high χ^2 indicate a poor fit. Furthermore, the uncertainties calculated do not take into account errors in effective cross-sections Danckaert and Fayt (2017).

3.4.4 Application to NO_2 and H_2CO

Before embarking on the analysis of the gathered spectra, the careful selection of the optimal wavelength range for the target absorber proves imperative. This involves scrutinizing the effective cross-sections for all participating absorbers in the analysis. Ideally, a spectral window should be chosen in which the absorption related to the specific species

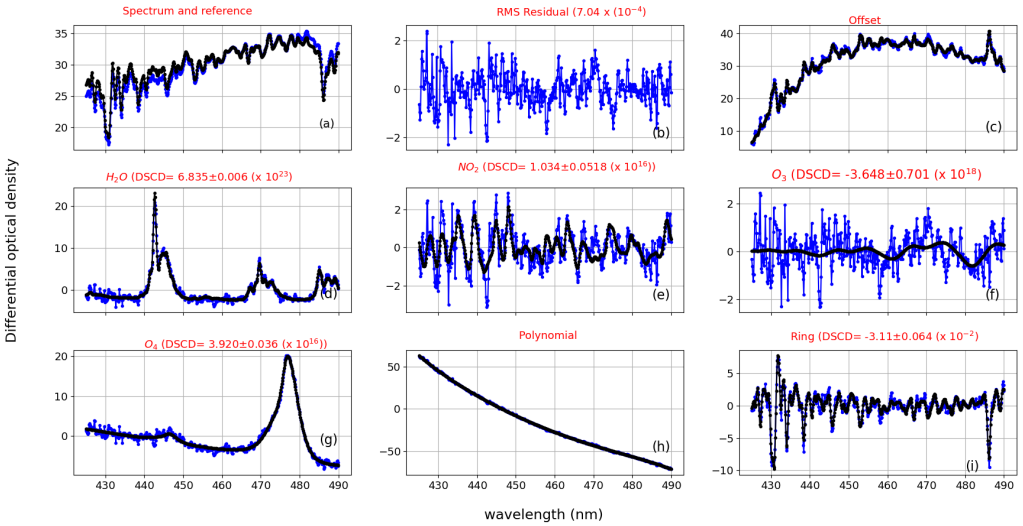

Figure 3.12: An illustration of a NO_2 DOAS fit is provided for a spectrum recorded at 10:23 UT on April 17, 2020. In the plot, the black lines represent molecular cross-sections that have been scaled to match the detected absorptions observed in the measured spectrum (indicated by the blue lines).

Table 3.2: QDOAS parameters for the retrieval of NO_2, O_4Vis, H_2CO dSCDs

Parameters	NO_2/O_4Vis (425-490nm)	H_2CO (325-360nm)
Calibration	Chance and Kurucz (2010a)	
NO_2	Vandaele et al. (1996), 220K and 298K	
O_3	Serdyuchenko et al. (2014), 223K and 243K	
H_2O	Rothman et al. (2010), 293K	
H_2CO		Meller and Moortgat (2000), 293K
BrO		Fleischmann et al. (2004), 223K
O_4	Thalman and Volkamer (2013a), 293K (and 203K for NO_2/O_4Vis)	
Ring effect	Chance and Spurr (1997)	
Polynomial order	5	
Offset order	2	1

under consideration is at its maximum, while concurrently mitigating the influence of other molecules. In this study, the DOAS fitting was executed within the spectral interval of 425-490 nm for NO_2, and 325-360 nm for H_2CO. Other species, including O_3, H_2O, and O_4, also manifest pronounced absorption features and thus merit inclusion within the QDOAS analysis.

To counteract the slowly varying elastic contributions (Rayleigh, Mie) that shift with wavelength, a fifth-degree polynomial is introduced. Furthermore, a synthetic Ring spectrum is introduced to correct for the "filling" effect on the Fraunhofer lines, commonly known as the Ring effect. The parameters and cross-sections adopted from the QDOAS analysis are documented in Table 6.1. Figure 3.12 illustrates an example of the DOAS fitting for nitrogen dioxide (NO_2) performed using the QDOAS program. In the figure, the black lines represent molecular cross sections that have been adjusted based on the absorptions detected in the measured spectrum (indicated by the blue lines). The values

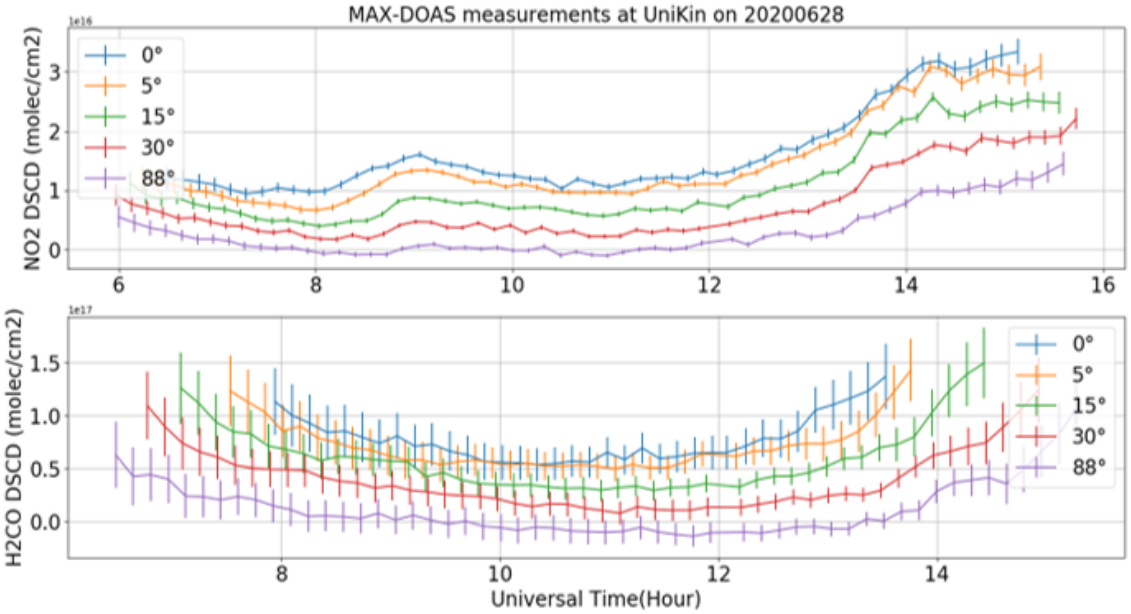

Figure 3.13: Example of dSCDs.

of the recovered dSCD for each molecular cross section are displayed in red next to the name of each sub-panel. This representation highlights how the molecular cross sections are fitted to the observed data to determine the slant columns of NO_2 in the atmosphere.

Figure 3.13 presents an illustration of the evolution of dSCDs for NO_2 and NO_2 retrieved from measurements taken over an entire day. The various curves are stacked on top of each other according to the elevation angles at which the measurements were made. It is evident that dSCDs obtained at lower elevation angles exhibit significantly higher values compared to those recorded at higher elevation angles. This feature arises due to the longer optical path traveled by light at lower elevation angles (Figure 3.11).

Furthermore, the dSCDs curves exhibit a distinctive "U" shape, which is closely tied to the variation in solar zenith angle throughout the day. Solar zenith angle is maximal at sunrise and sunset, while reaching its minimum around local noon. This dependency on solar zenith angle is reflected in the dSCDs, thus explaining the observed "U" shape. To mitigate the influence of solar angle and observation geometry, the dSCD are converted into Vertical Column Density (VCD)s (see equation 3.20), a geophysical quantity commonly employed for comparisons with satellite data and atmospheric models. This conversion enables the acquisition of more stable and comparable information, independent of observational geometry parameters. It is worth noting that for molecules contributing to both the troposphere and stratosphere, such as NO_2, the obtained dSCDs represent the sum of these two components. In the context of tropospheric applications of these dSCDs, the stratospheric contribution can be derived from these dSCDs during the twilight period when the photon's light path becomes more extensive in the stratosphere compared to the troposphere (e.g. Van Roozendael and Hendrick (2012)). In the scope of this study, for the analysis of our measurements collected from 2017 to 2019 with the initial version of the instrument, which was unable to achieve solar zenith angles close to 90°, stratospheric dSCDs were derived from simulations using the UVspec/DISORT-RRTM model (Mayer and Kylling, 2005) coupled with the photochemical box model PSCBOX (Errera and Fonteyn, 2001).

3.5 AIR MASS FACTOR

The absorption of trace gases as measured by a ground-based spectrometer is significantly dependent on the trajectories followed by photons during their passage through the atmosphere. Therefore, an accurate description of radiative transfer within the atmosphere is essential in order to conduct proper analysis and interpretation of measurements (Platt and Stutz, 2008).

Consequently, the Air Mass Factor (AMF) emerges as a variable aimed at quantifying the atmospheric path length that light or electromagnetic radiation must traverse to reach an observer from a light source or target. The AMF is influenced by various atmospheric parameters such as air density, altitude, atmospheric pressure, trace gas concentration, pressure, temperature, profiles of strong absorbers, and aerosols (including clouds). In the literature, the concept of the AMF has been utilized to assist in interpreting zenith-scattered light observations (e.g., Solomon et al. (1987); Perliski and Solomon (1993)). This factor is defined as the ratio of dSCD to the VCD, which is further described in Equation. 3.20 (Hönninger et al., 2004). The VCD, represente the concentration of trace gases, denoted as c(z), integrated along the vertical path through the atmosphere.

$$VCD = \int_0^{TOA} c(z)dz \tag{3.19}$$

$$AMF(\lambda, \theta, \alpha, \phi) = \frac{dSCD(\lambda, \theta, \alpha, \phi)}{VCD} \tag{3.20}$$

With θ representing the solar zenith angle, α denoting the elevation angle, and ϕ being the azimuthal angle defined as the angle between the telescope direction and the sun.

For the sake of simplicity, it is sometimes necessary to employ a geometric approximation to calculate the AMF directly. This approximation takes into account only the elevation and SZA, assuming a single scattering event as depicted in Figure. 3.14. Therefore, for this geometric approximation, the AMF can be calculated using Equation. 3.21 (Hönninger et al., 2004).

$$dSCD = VCD[a\frac{1}{\sin\alpha} + (1+a)\frac{1}{\cos\theta}] \tag{3.21}$$

It is worth noting that in practical applications, this simplification comes with disadvantages and limitations[6], prompting the need for more robust methods that account for atmospheric conditions and the mentioned observational geometry parameters. These robust methods involve the utilization of radiative transfer models, as discussed in the subsequent paragraph.

[6]Not only is it an approximation that only considers single scattering, but at angles close to 90°, the value of the AMF tends towards infinity

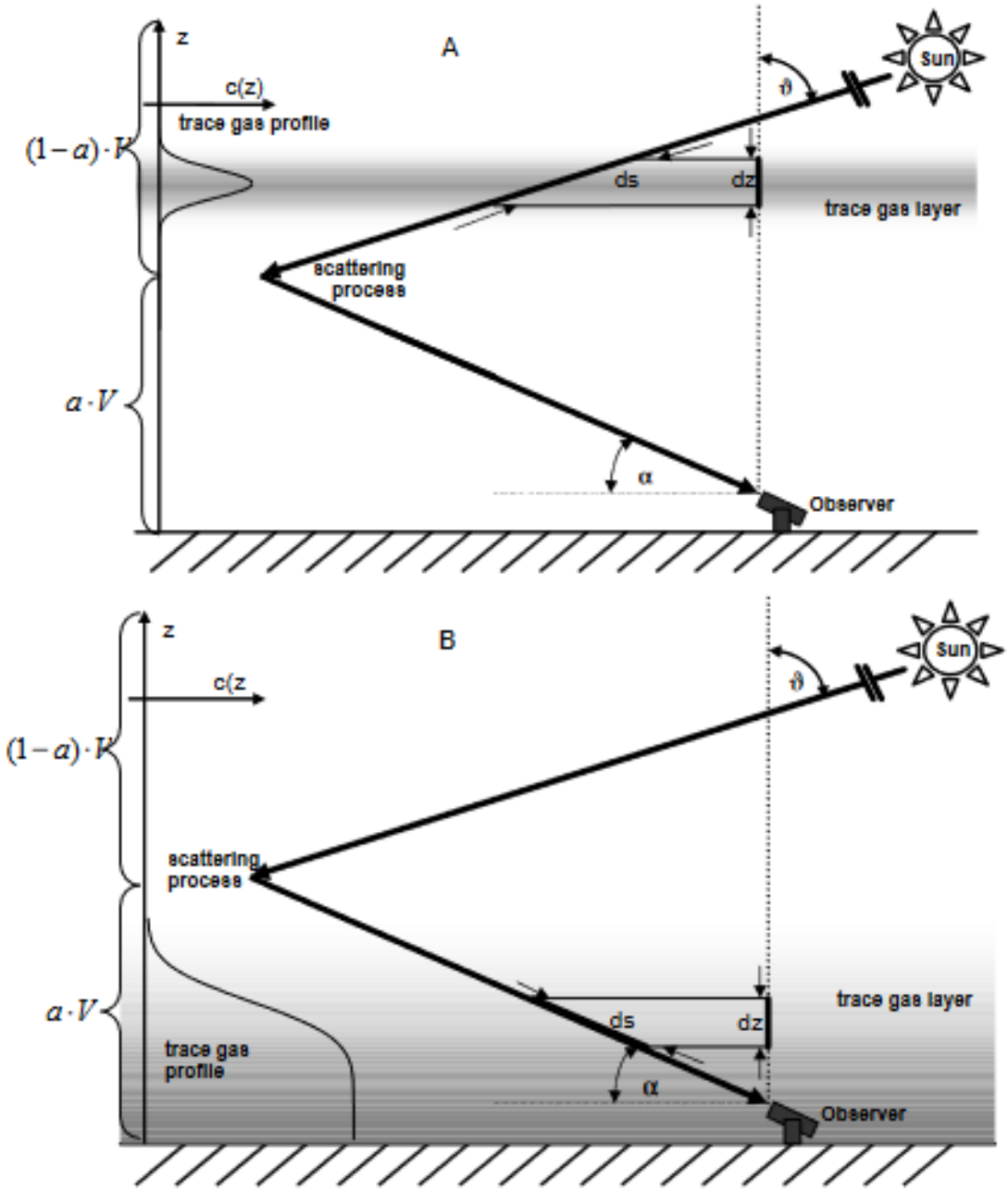

Figure 3.14: Estimation of the air mass factor is performed using the geometric approximation for: (A) the scenario where the trace gas is located in a higher (stratospheric) layer and (B) for a situation near the surface (Hönninger et al., 2004).

3.6 RADIATIVE TRANSFERT MODELS

A Radiative Transfer Model (RTM) is generally a program (computer code) whose purpose is to numerically solve the radiative transfer equation. For the sake of clarity, we will begin by introducing the processes involved in modeling UV-Vis radiation, including phenomena such as absorption and scattering during atmospheric traversal, as well as surface albedo. This will lead us to present the radiative transfer equation.

3.6.1 Absorption

Absorption refers to the reduction in incident energy resulting from a chemical or thermal reaction. Let's revisit the example in Figure. 3.9, but this time considering that the monochromatic incident radiation falls at an angle $\cos\theta$ through a thickness z, across a uniformly distributed absorbing gas. The relationship between the intensity of incident radiation I_0 and the intensity of transmitted radiation I, following the Beer-Lambert law presented in Equation. 3.5, can be expressed as:

$$I = I_0 e^{-\tau(\lambda,z)/\cos\theta} \tag{3.22}$$

3.6.2 Scattering

When a narrow beam of light interacts with matter, its direction of propagation can be altered, leading to a phenomenon known as scattering. This interaction can cause the light beam to change direction multiple times, which is referred to as multiple scattering. Consequently, the light can even be directed back, termed as retroreflection. The process of scattering is influenced by various factors, such as the size of particles or molecules and the wavelength of light. The Θ scattering angle in spherical geometry is established through the equation Equation. 3.23 (Liou, 2002), considering both the incident radiation arriving from (θ', ϕ') and the radiation scattering towards (θ, ϕ)

$$\cos\Theta = \cos\theta'\cos\theta + \sin\theta'\sin\theta\sin(\phi - \phi') \tag{3.23}$$

For particles much smaller than the wavelength, Rayleigh scattering (Rayleigh, 1871) prevails, with uniform distribution in both forward and backward directions. This applies to gases like nitrogen and oxygen. Scattering efficiency, is wavelength-dependent (λ^{-4}), explaining sky color; shorter wavelengths (blue, violet) scatter more. For larger particles, Lorenz-Mie scattering (Frisvad and Kragh, 2019; Mie, 1908) takes over, primarily involving aerosols and cloud particles. Main scattering direction is predominantly forward.

In the process of scattering, radiation gets dispersed in multiple directions, necessitating the characterization of its angular distribution. To accomplish this, a dimensionless parameter called the phase function $\mathrm{P}(\cos\Theta)$ is introduced. This parameter can also be understood as the probability that a photon traveling in the direction $\Omega'(\theta', \phi')$ scatters towards the direction $\Omega(\theta, \phi)$. By definition, the phase function is normalized:

$$1 = \int_0^{2\pi}\int_0^{\pi} \frac{P(\cos\Theta)}{4\pi} d\Theta d\phi \tag{3.24}$$

For non-polarized photons scattered by air molecules, Rayleigh theory yields the phase function described in equation. 3.25. This function can also be expressed as a sum of Legendre polynomials P_l, as given in equation. 3.26.

$$P(\Theta) = \frac{3}{4}(1 + \cos^2\Theta) \tag{3.25}$$

$$P(\cos\Theta) = \sum_{l=1}^{N} \omega_l P_l \cos\Theta \tag{3.26}$$

In an alternative manner, the expansion coefficient wl is defined as:

$$\omega_l = \frac{2l+1}{2} \int_{-1}^{1} P \cos\Theta P_l \cos\Theta d\cos\Theta \tag{3.27}$$

In equation. 3.27, when $l = 0$, ω_0 equals 1, aligning with the normalization definition of the phase function as in equation 3.24. Upon setting $l = 1$, the outcome is the first moment of the phase function, termed the asymmetry factor g, as defined in equation. 3.28. Figure 3.15 presents diverse phase functions related to particles of varying sizes.

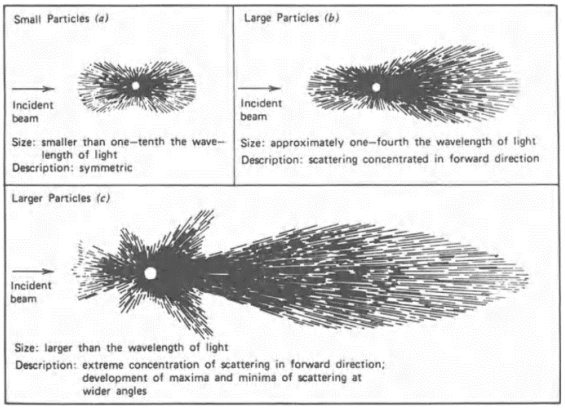

Figure 3.15: Phase functions related to particles of varying sizes Hide (1977).

$$g = \frac{1}{2} \int_{-1}^{1} P(\Theta) \cos\Theta d\cos\Theta \tag{3.28}$$

This factor, g, offers insight into the scattering of directional tendencies:

- g = +1 indicates complete forward scattering.
- g = -1 indicates complete backward scattering.
- g = 0 denotes symmetric scattering, such as Rayleigh scattering.

In practical terms, absorption and scattering occur simultaneously. The single scattering albedo (ω_0) is utilized to measure the proportion of scattering within the total extinction. This parameter is defined as the ratio of the scattering cross-section (σ_{sca}) to the extinction cross-section (σ_{ext}), where the latter encompasses the combined cross-sections of both scattering σ_{sca} and absorption (σ_{abs}).

$$\omega_0 = \frac{\sigma_{\text{sca}}}{\sigma_{\text{ext}}} = \frac{\sigma_{\text{sca}}}{\sigma_{\text{abs}} + \sigma_{\text{sca}}} \tag{3.29}$$

3.6.3 The radiative transfer equation

The Radiative Transfer Equation (RTE) is a differential-integral equation that models the propagation of radiation within an atmospheric medium subject to scattering, absorption, and/or emission. The purpose of studying this equation is to calculate luminances and radiative fluxes as they would be measured by an instrument, given a specific atmospheric state. Luminance represents the energy emitted or transferred in a specific direction, per unit of surface area and time. This paragraph RTE is inspired by the doctoral work of Lamy (2018) and Merlaud (2013).

Considering an energy flux propagating in the direction $\Omega = (\theta, \phi)$ through a plane-parallel atmosphere with an optical thickness of $d\tau$, we can refer to Chandrasekhar (1960) to define the monochromatic RTE. This equation describes the propagation of luminance L through a medium characterized by a single scattering albedo ω_0, a phase function P, and an extinction coefficient σ_{ext} as :

$$\mu \frac{dL(\tau, \Omega)}{d\tau} = L(\tau, \Omega) - S(\tau, \Omega) \tag{3.30}$$

where :

$$\mu = \cos\theta \tag{3.31}$$

The source term S, which encompasses Radiative Diffusion from Ω' to Ω, Thermal Radiative Transfer (Q), and Direct Incident Flux, is expressed as per equation 3.32.

$$\begin{aligned} S = \frac{\omega_0}{4\pi} \int_0^{2\pi} d\phi' \int_{-1}^{1} P(\tau, \Omega, \Omega') d\mu' + Q(\tau, \Omega) \\ + \frac{\omega_0 I_0}{4\pi} P(\Omega, \Omega') e^{-\tau/\mu_0} \end{aligned} \tag{3.32}$$

Alternatively, Q is defined as:

$$Q(\tau, \Omega) = (1 - \omega_0) B(T, \tau) \tag{3.33}$$

$B(T, \tau)$ represents the radiance emitted by a black body of temperature T. By combining the source terms, equation 3.30 can be reformulated as equation 3.34, representing the equation for radiative transfer in the transport of radiation within a narrow atmospheric layer with uniform optical properties.

$$\begin{aligned} \mu \frac{dL(\tau, \Omega)}{d\tau} = L(\tau, \Omega) \\ - \frac{\omega_0}{4\pi} \int_0^{2\pi} d\phi' \int_{-1}^{1} P(\tau, \mu, \phi, \mu', \phi') L(\tau, \mu', \phi') d\mu' \\ - (1 - \omega_0) B(T, \tau) - \frac{\omega_0 I_0}{4\pi} P(\Omega, \Omega') e^{-\tau/\mu_0} \end{aligned} \tag{3.34}$$

It's worth noting that in the context of modeling radiation within the UV-Visible spectral range, equation 3.34 can indeed be solved without simultaneously considering thermal and solar radiative transfer. This is due to the non-overlapping nature of the solar and

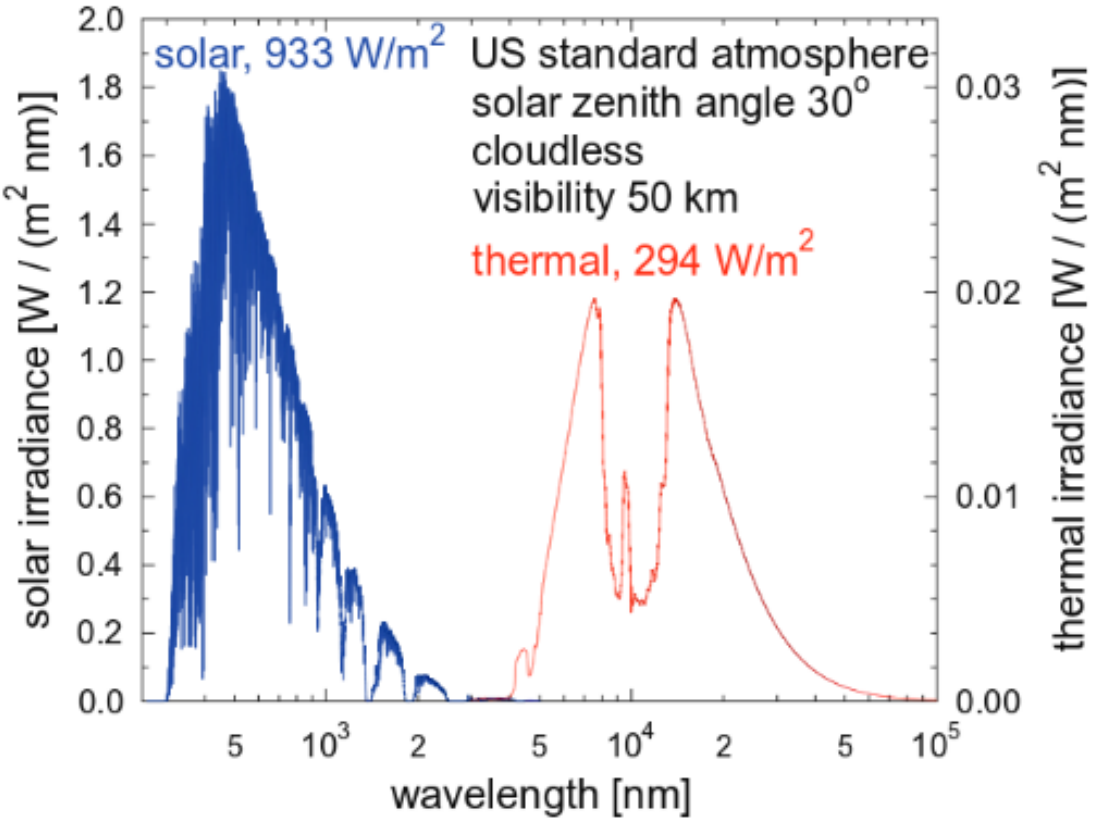

Figure 3.16: Solar and terrestrial irradiance (Mayer, 2009).

terrestrial irradiance spectra; they do not coincide 3.16. The equation 3.34 is an integro-differential equation, the solution of which is complex and requires the use of numerical models. Existing models employ various mathematical techniques for resolution. Generally, these techniques are based on dividing the atmosphere into homogeneous parallel plane layers and include additional corrections to account for its sphericity. For example, the Discrete Ordinates Radiative Transfer (DISORT) method (Laszlo et al., 2016; Chandrasekhar, 1960) ; the Linearized Discrete Ordinate Radiative Transfer (LIDORT) model (Spurr et al., 2001), which provides an analytical expression for the model's Jacobians; or the "Doubling-Adding" method (de Haan et al., 1987). Figure 3.17 depicts a schematic of the various inputs and outputs utilized in the utilization of a radiative transfer code, along with its different outputs. In this thesis, we employed the radiative transfer code named VLIDORT (Spurr, 2013), the description of which is provided in the following paragraph.

3.6.4 VLIDORT Radiative Transfer Code

VLIDORT, developed in Fortran 90, models radiation in the UV-visible range. It simulates the Stokes vector components (I, Q, U, V)[7] to account for radiation polarization using discrete ordinate method (Spurr, 2013). The goal is to describe photon flow, considering wave properties using Stokes formalism (I, Q, U, V). Here, I represents the light intensity,

[7]The Stokes vector components, I, Q, U, and V, are vital in characterizing polarized light. I represents the total intensity of light, whereas Q and U measure linear polarizations at different angles. Q signifies the difference in intensity between horizontal and vertical linear polarizations, while U quantifies the 45-degree linear polarization. V represents circular polarizations.

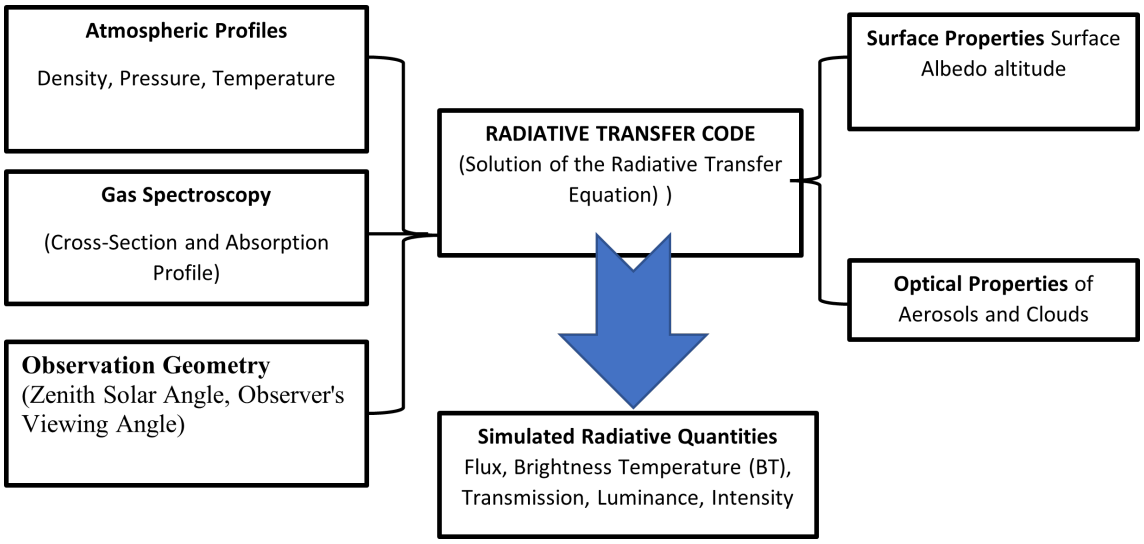

Figure 3.17: Illustrative Diagram of Various inputs and outputs in the Utilization of a Radiative Transfer Code.

V signifies circular polarization intensity, and $L = Q + iU$ denotes linear polarization intensity. Despite sunlight being unpolarized, due to random orientation of polarization states, its polarization changes in the atmosphere due to scattering processes. VLIDORT handles multiple scattering, including polarized light, and uses the pseudo-spherical approximation for solar radiation attenuation in curved atmospheres. VLIDORT employs Rayleigh scattering for air and Mie scattering for aerosols (Spurr, 2013).

The VLIDORT program calculates SCD and AMF for atmospheric components based on simulated intensities. If x represents one of these absorbers (such as H_2CO, NO_2), its slant column density is evaluated using equation 3.35 where I_{sca} represents scattered intensity, I_0 is the intensity without absorber x, and σ_{x} is the cross-section of absorber x with respect to wavelength. In the case where VCD_{x} represents the VCD of x, and is directly computed using the absorber's partial profile, its AMF_{calc} is determined by equation 3.36.

$$SCD_{\text{calc}} = \frac{ln\frac{I_0}{I_{\text{sca}}}}{\sigma_{\text{x}}} \tag{3.35}$$

$$AMF_{\text{calc}} = \frac{SCD_{\text{calc}}}{VCD_x} \tag{3.36}$$

Table 3.3 presents the parameters employed to calculate the AMFs showcased in Figure 3.18, used during the initial phase of our observations in Kinshasa, spanning from May 2017 to November 2019. Given that observations were conducted at both 90 and 35° elevation angles, AMF calculations with VLIDORT were conducted for both these elevation angles. The AMF was thus computed with respect to the solar zenith angle. Considering the significant aerosol impact at the Kinshasa site, as depicted in MODIS TERRA's observation (Figure 5.2.2), sensitivity tests for visibility were also conducted as part of this study.

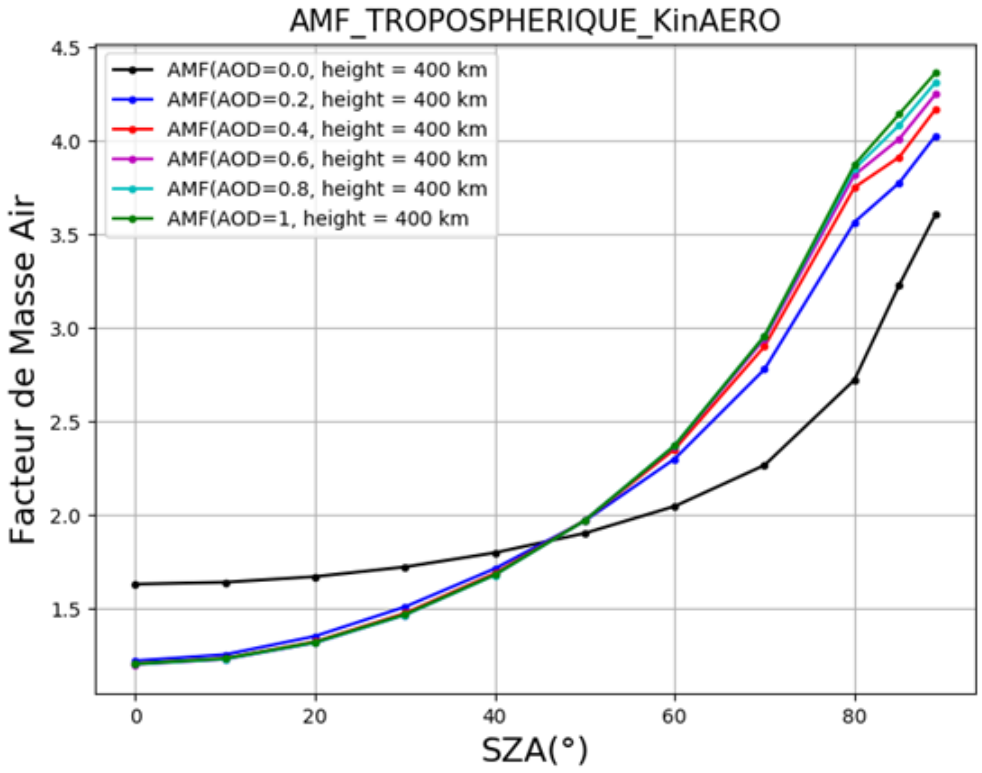

Figure 3.18: Investigating the Impact of Aerosols, Profile Assumptions, and Surface Albedo on Tropospheric NO_2 AMFs Modeled with the Radiative Transfer Model VLIDORT. Exploring Changes in Different Aerosol Optical Depths (AODs) as a Function of SZA

3.7 INVERSE PROBLEM

When atmospheric parameters such as temperature, pressure, or concentrations of various constituents can be directly determined through in situ measurements, the inversion problem does not arise. However, the need for global measurements has led to the development of remote sensing and the processing of such data to indirectly retrieve local quantities of interest. This transition from measured quantities to desired parameters requires solving an inverse problem. For instance, in the case of atmospheric spectra, signals recorded by remote sensing instruments depend on factors like temperature in different layers, pressure, and concentration ratios of chemical species in the atmosphere. To obtain this physical information, an inversion model of spectra must be developed to determine vertical concentration profiles of atmospheric constituents (Chailleux, 2018; Ferreira, 2005). The content presented in this section has been influenced by the works of Ferreira (2005); Lamoulie (1998) and we have also incorporated the notations introduced by Rodgers (1976).

This approach, illustrated in figure 3.19 for nitrogen dioxide and formaldehyde profile inversion, involves using diverse input data to reverse the vertical profiles of these molecules based on instrument observations. Crucial inputs encompass spectroscopic particulars, atmospheric metrics such as pressure and temperature profiles, details regarding aerosols, cloud and surface albedo, apriori profile and a comprehensive instrument model characterizing its properties. Achieving a successful inversion hinges on suppositions such as local

Table 3.3: Configuration Parameters for VLIDORT Simulation

Parameters	**characteristics**
Climatology	
Temperature and pressure profile	European Centre for Medium-Range Weather Forecasts (ECMWF)[8] reanalyses Climatology
Physico-Chemical Parameters	
Air density	GEOS-Chem simulation
NO_2 profile	GEOS-Chem simulation
Wavelength	477.0 nm
O_4 cross-section	6.5×10^{-46} molec/cm^2: (Hermans and Coauthors, 2003)
NO_2 cross-section	4.5×10^{-19} molec/cm^2 : (Vandaele et al., 1998), 298K
Aerosol optical depth	0 to 1 (in intervals of 0.2)
Anisotropy coefficients	0.68
Single scattering albedo	0.98
Surface albedo	0.06
Geometric and Geographic Parameters	
Solar zenith angle	0 to 90 (in steps of 10)
Relative azimuth angle	31
observation (elevation angle)	35° and 90°
Instrument altitude	0.4km
Extraction Grid	
Number of sublayers	64
Extraction grid	The distribution of retrieval grid layers is not equidistant. The grid consists of 64 layers extending up to 60 km.

thermodynamic equilibrium and ideal gas behavior for elements within the atmosphere.

3.7.1 Forward model

The direct model, denoted as f, represents a mathematical formulation that simulates the relationship between various input parameters, collectively represented as x, and the corresponding output state y and ϵ represents the difference between the calculated and measured spectra. This model, along with the input parameters, produces an estimated output state $\widehat{y}$. The primary goal of the inversion process is to determine the optimal set of input parameters x that yields a simulated output state $\widehat{y}$ closely aligned with the actual measured state y.

$$y = f(x, b) + \epsilon \tag{3.37}$$

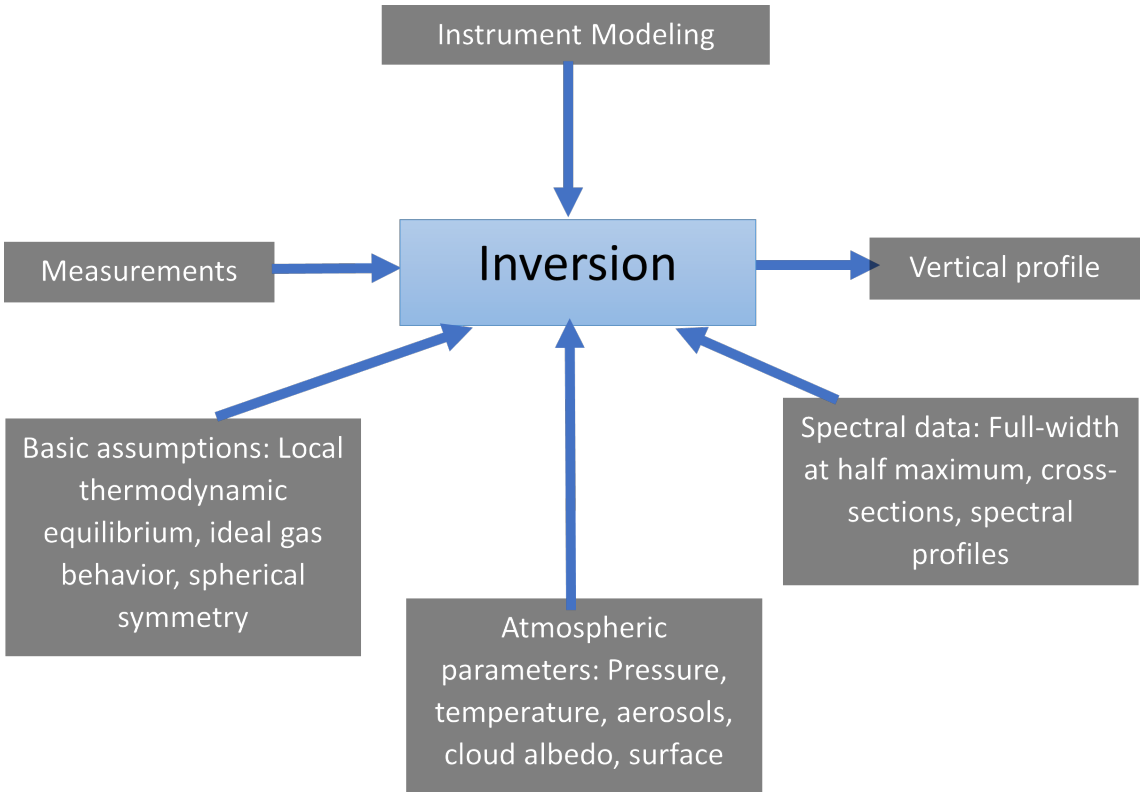

Figure 3.19: Inversion Process

Before proceeding with the inversion, initial values are provided to the direct model. These include an a priori estimate, denoted as x_a, for the state vector x, and a corresponding a priori estimate b for the parameters not being inverted. Subsequently, the direct model equation 3.37 is linearized to account for the deviation from these initial estimates:

$$y = f(x_\mathrm{a}, \widehat{b}) + \frac{\partial f}{\partial x}(x - x_\mathrm{a}) + \frac{\partial f}{\partial b}(b - \widehat{b}) \tag{3.38}$$

Where $\frac{\partial f}{\partial x}$ represents the sensitivity of the model to the state vector x, also known as the weighting function or Jacobian matrix K_x, and $\frac{\partial f}{\partial b}$ denotes the sensitivity of the model to the parameter b, or Jacobian matrix K_b.

3.7.2 Inverse model

In the context of a model inversion, the goal is to find an estimate of the state vector $\widehat{x}$ that closely approximates the measured value x. This is achieved using a measurement y and a prior estimation of parameters b:

$$\widehat{x} = R(y, \widehat{b}) = R((x; b) + \epsilon, \widehat{b}) \tag{3.39}$$

By linearizing this equation equation 3.39 again around the prior estimate of the state vector x_a and the parameters b, we obtain:

$$\widehat{x} = R[f(x_{\mathrm{a}}, \widehat{b}) + K_{\mathrm{x}}(x - x_{\mathrm{a}}) + K_{\mathrm{b}}(b - \widehat{b}) + \epsilon, \widehat{b}] \tag{3.40}$$

Finally, by linearizing with respect to the measured state vector y:

$$\widehat{x} = R[f(x_{\mathrm{a}}, \widehat{b})] + G_{\mathrm{y}}[K_{\mathrm{x}}(x - x_{\mathrm{a}}) + K_{\mathrm{b}}(b - \widehat{b}) + \epsilon] \tag{3.41}$$

Here, $G_{\mathrm{y}} = \frac{\partial R}{\partial y}$ represents the gain matrix of the inverse model, and $K_{\mathrm{b}}(b - \widehat{b}) + \epsilon = \epsilon_y$ denotes the total measurement error relative to the direct model. Using $AK = G_{\mathrm{y}}K_{\mathrm{x}} = \frac{\partial \widehat{x}}{\partial x}$, the matrix of averaging kernels (AK), we can rephrase the equation as follows:

$$\widehat{x} = R[f(x_{\mathrm{a}}, \widehat{b})] + AK(x - x_{\mathrm{a}}) + G_{\mathrm{y}}\epsilon_{\mathrm{y}} \tag{3.42}$$

3.7.3 Averaging Kernel

To better understand the crucial role of the Averaging Kernel (AK) matrix in an inversion method, let's assume that the model is ideally characterized, meaning that $R[f(x_{\mathrm{a}}, \widehat{b})] = x_{\mathrm{a}}$. In this case, equation 3.42 simplifies to:

$$\widehat{x} = (AK)x + (I - AK)x_{\mathrm{a}} + G_{\mathrm{y}}\epsilon_{\mathrm{y}} \tag{3.43}$$

Where I represents the identity matrix. Thus, in an ideal scenario where $G_{\mathrm{y}}K_{\mathrm{x}}$ tends to 0, the AK matrix becomes equivalent to the identity matrix. This implies that all the information comes from the measurements, and we have $x = \widehat{x}$. The AK matrix therefore reflects the sensitivity of the estimated state to the true state, providing insights into the quality of the inversion performed. The matrices AK express the relationship between the retrieved profile $\widehat{x}$ and the true atmospheric profile x through the following equation:

$$\widehat{x} = x_{\mathrm{a}} + AK(x - x_{\mathrm{a}}) + G_{\mathrm{y}}\epsilon_{\mathrm{y}} \tag{3.44}$$

Based on equation 3.44, retrieving each profile point involves averaging the entire actual profile, weighted by the row of matrix AK associated with the altitude of the retrieved profile point. In an ideal observational setup, matrix A would be equivalent to the identity matrix. However, in reality, the retrieved profile only reflects a smoothed perception of the true profile. Another important characterization parameter, derived from matrix AK, is the degrees of freedom (dof)s of the signal. It allows estimating the amount of independent pieces of information that can be obtained from the measurements. This number is determined by calculating the trace of matrix AK (Rodgers, 2000).

Figure 3.20 illustrates an example of AK estimates derived from the MAX-DOAS observations of the instrument in Kinshasa. It can be observed that the vertical sensitivity is higher in the lowermost layers near the ground, decreasing up to an altitude of approximately 3 km. The examination of the AKs for NO_2 in Figure 3.20 suggests that the inversions are sensitive to layers from the surface up to 1-3 km. The corresponding number of dofs is approximately 3 (panel a: AK NO_2) and 1 (panel b: AK H_2CO), meaning that there are about 3 independent pieces of information in the measurements. The various other parameters that contributed to the determination of this AK matrix are detailed in section 3.8.

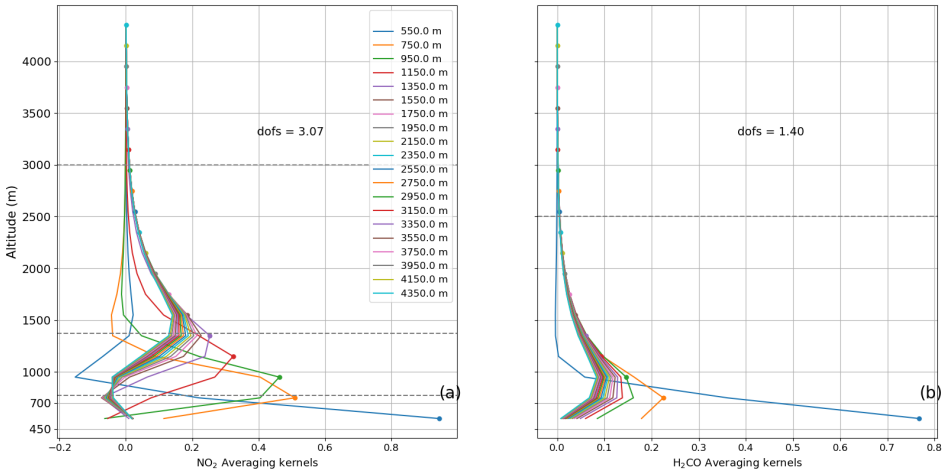

Figure 3.20: Typical example of Averaging kernel of NO_2 (a) and H_2CO (b) retrievals for Kinshasa MAX-DOAS measurements. The dotted horizontal lines in each sub-panel represent the layers according to the information extracted after inversion (depending on the number of degrees of freedom, 3 layers for NO_2 and 1 layer for H_2CO)

3.7.4 Iterative inversion problem solution

In line with (Rodgers, 2000), solving an inversion problem involves minimizing the discrepancies between the actual measurements y and those simulated by the direct model $f(x)$. This also entails reducing the disparities between the state vector x and its prior estimate x_a, while considering the error covariance matrices associated with the measurements (S_ϵ) and the prior estimate (S_a) (see equation 3.45.

$$|||y-f(x)|||^2_{S_\epsilon^{-1}} + |||x-x_a|||^2_{S_a^{-1}} = (y-f(x))^T S_\epsilon^{-1}(y-f(x)) + (x-x_a)^T S_a^{-1}(x-x_a) \quad (3.45)$$

However, in order to mitigate the error introduced by the non-linearity of $f(x)$, it becomes necessary to employ an iterative minimization approach (see equation 3.46). Here, superscript T denotes transposed; superscript $^{-1}$ denotes the inverse.

$$x_{i+1} = x_i + (K_i^T S_\epsilon^{-1} K_i + S_a^{-1})^{-1} \left(K_i^T S_\epsilon^{-1}(y - f(x_i)) - S_a^{-1}(x_i - x_a)\right) \quad (3.46)$$

Similarly, with i denoting the iteration index and Ki representing the Jacobian at the ith iteration, the gain matrix and AK matrix are derived in equations 3.47 and 3.48, respectively.

$$G_y = (K^T S_\epsilon^{-1} K + S_a^{-1})^{-1} K^T S_\epsilon^{-1} \quad (3.47)$$

$$AK = (K^T S_\epsilon^{-1} K + S_a^{-1})^{-1} K_i^T S_\epsilon^{-1} K \quad (3.48)$$

Indeed, by employing the covariance matrices (S_ϵ) and (S_a) along with the Jacobian, we can compute the AK matrices, which provide insights into the measurement quality. Furthermore, the gain matrix G_y is crucial for estimating various errors associated with the retrieval of the state vector.

In this thesis, we used the FRM$_4$DOAS project (`https://frm4doas.aeronomie.be/`, last access: 10 July 2023)), which includes the code implementing the mathematical solutions described in the previous section. This tool is elaborated on in the following section.

3.8 FRM$_4$DOAS PROJECT

The FRM$_4$DOAS is a global project funded by the European Space Agency (ESA) with the aim of harmonizing and standardizing the data retrieval from MAX-DOAS instruments within the International Network for the NDACC. It incorporates community-based algorithms for automated, high-quality processing. Two MAX-DOAS retrieval algorithm are employed: MAPA (Beirle et al., 2019), based on parameterizing the retrieval profile, and Mexican MAX-DOAS Fit (MMF) (Friedrich et al., 2019), an Optimal Estimation Method (OEM). Both have been extensively tested and validated using synthetic data (Frieß et al., 2019) as well as real data (Tirpitz et al., 2021; Karagkiozidis et al., 2022).

It is important to mention that throughout this thesis, we primarily utilized MMF due to its coherence with the Aerosol Optical Depth (AOD) measurements obtained from the MODIS-TERRA instrument. Currently, within the framework of FRM$_4$DOAS, MAPA is predominantly employed as a quality control tool, but it does not provide averaging kernels. Owing to a sampling effect, the use of MAPA as a quality check, mainly for H_2CO, introduces a bias in the statistics. Higher VCDs are more likely to be excluded, leading to discrepancies between MAPA and MMF. Therefore, in the following section, we will solely describe the MMF approach, outlining the specific steps employed for retrieving profiles from our measurements. For more details on the choice of MMF, refer to Chapter6.

3.8.1 MMF inversion algorithm

The MMF is an inversion software designed for interpreting MAX-DOAS measurements. Its development took place at the Universidad Nacional Autónoma de México (UNAM) from 2013 to 2015. Throughout 2017, MMF underwent enhancements and further refinements at both UNAM and the BIRA-IASB.

The retrieval of profiles x for both aerosol and trace-gas, as implemented in MMF, is based on the formalism developed in equations 3.46. Initially, the vertical profiles of aerosol extinction are obtained for every MAX-DOAS scan based on the detected oxygen dimer O_4 dSCDs. The vertical profile of O_4 is well-known and nearly constant (it varies with the square of the O_2 monomer concentration), allowing O_4 dSCD measurements to provide information about the vertical distribution of aerosols (Wagner et al., 2004; Frieß et al., 2006). To achieve this, by using the radiative transfer model VLIDORT, which is the forward model in MMF ($f(x)$), along with the vector of O_4 dSCDs (y), we can retrieve the desired aerosol profile using a non-linear iterative approach based on a Gauss-Newton or Levenberg-Marquart (M-L) minimization scheme. From the resulting aerosol profile, the gas profiles are deduced using an OEM for optically thin absorbers like NO_2 and

H_2CO, given that their measured dSCDs depend linearly on the concentrations in each profile layer (FRM4DOAS ATBD, 2017).

$$y = \begin{pmatrix} DSCD_{\alpha=0^\circ} \\ DSCD_{\alpha=1^\circ} \\ . \\ . \\ . \\ DSCD_{\alpha=88^\circ} \end{pmatrix} \tag{3.49}$$

The a-priori profiles in terms of Volume Mix Ratio (VMR) in parts per billion (ppb) or in terms of number densities, along with the values of g and w, are provided through input files. Additionally, a temperature-pressure profile must also be provided. An uncertainty covariance matrix (S_a for the specified a-priori profile is calculated using equation 3.50.

$$S_{\mathrm{ai,j}} = \sqrt{S_{\mathrm{ai,i}} S_{\mathrm{aj,i}} exp^{-ln(2)\frac{h_\mathrm{i}-h_\mathrm{j}}{c_\mathrm{l}}}} \tag{3.50}$$

The matrix AK of weighting functions indicating the sensitivity of the differential slant column abundances for each SZA to a change in the vertical profile is calculated using equation 3.51. h_i and h_j are the altitudes of ith and jth levels.

$$K = \frac{(K_0^\alpha I_\mathrm{g}^{zen} I_\mathrm{g}^\alpha I_0^{zen} + I_0^\alpha K_\mathrm{g}^{zen} I_\mathrm{g}^\alpha I_0^{zen} - I_0^\alpha I_\mathrm{g}^{zen} K_\mathrm{g}^\alpha I_0^{zen} - I_0^\alpha I_\mathrm{g}^{zen} I_\mathrm{g}^\alpha K_0^{zen})}{(I_0^\alpha I_\mathrm{g}^{zen} I_\mathrm{g}^\alpha I_0^{zen} \sigma(\lambda))} \tag{3.51}$$

With I_0^α and K_0^α being the intensity and Jacobian of the simulation at various elevation angles without gas absorption, I_g^{zen} and K_g^{zen}, the intensity and Jacobian with gas absorption towards the zenith, and I_g^α K_g^α the intensity (Jacobian) with gas absorption towards the desired angle, the dSCD is also calculated using the same quantities via equation 3.52.

$$dSCD = \frac{log(\frac{I_0^\alpha I_\mathrm{g}^{zen}}{I_\mathrm{g}^\alpha I_0^{zen}})}{\sigma(\lambda)} \tag{3.52}$$

It's worth noting that the a priori profiles, as well as the temperature-pressure profile, are provided on a given altitude grid through input files and internally interpolated onto the simulation grid. This simulation grid contains specifications regarding the number of layers used as the retrieval grid, starting from the surface, and this is also defined via an input file.

In the context of this thesis, an exponential decay profile with a scale height of 1 km was used as the a priori profile. The retrieval grid was defined with a height grid of 200 m spacing up to 4 km, and an ECMWF climatology from 1995 to 2016 was employed for the temperature-pressure profile (FRM4DOAS ATBD, 2017). Figure 3.21 provides a typical illustration of inversion results for retrieved gas and aerosol profiles using the MMF method.

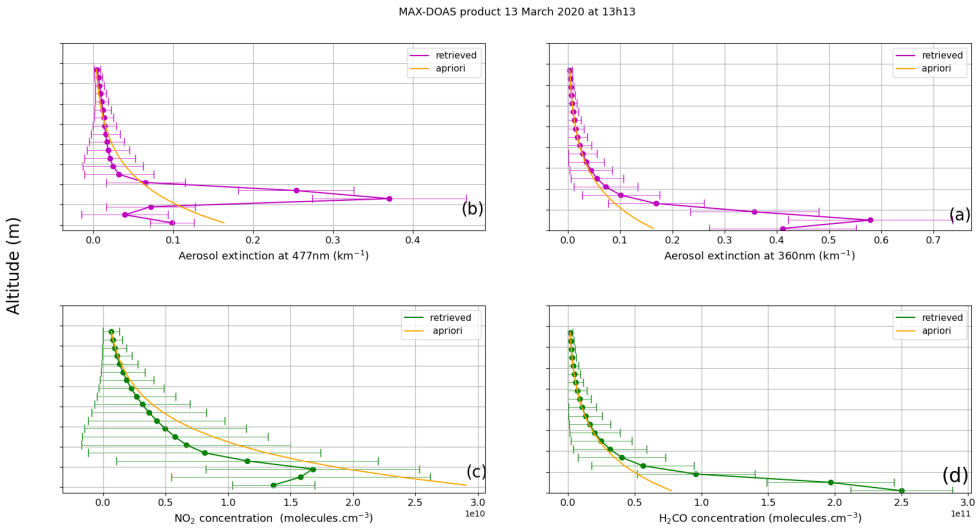

Figure 3.21: Example of MMF retrieved profiles around 13h13 **UT!** of 1 March 2020 from the Kinshasa measurements. The NO_2 and H_2CO profiles are represented in panels (c) and (d), respectively. Likewise, extinction profiles at 360 nm and 477 nm are represented in panels (a) and (b). The orange curves in the right subpanels are the a priori profiles. The horizontal bars represent the uncertainty on the retrieved profiles.

3.8.2 Estimation of errors in data retrieval

Based on Rodgers (2000), the total error associated with the retrieved profile using the OEM consists of three main components:

1. The error resulting from the smoothing of the true profile, referred to as the smoothing error (S_s).
2. The error arising from random and systematic errors in the measurements made (S_m).
3. The error due to systematic inaccuracies in the direct model used (S_f).

Smoothing error (S_s), in the field of atmospheric data retrieval, is a crucial component of the total error associated with determining an atmospheric profile from raw measurements. It arises when efforts are made to obtain a profile that is smoother and less noisy than the true atmospheric profile. This regularization is necessary to generate more stable results, but it often comes at the cost of losing some details compared to the actual profile. Therefore, the smoothing error quantifies the difference between the retrieved profile and the true atmospheric profile, which is a consequence of algorithmic choices and regularization parameters employed during the data retrieval process. It can be characterized by the covariance matrix as given in Equation 3.53 (Rodgers, 2000).

$$S_s = (AK - I)S_x(AK - I)^T \tag{3.53}$$

The covariance matrix S_x represents the statistical variability of the true profile, while the AK matrix expresses the averaging kernels associated with the data retrieval process. In

parallel, the identity matrix I comes into play in calculations. The matrix S_x accounts for interactions between trace gas concentrations at different altitude levels by incorporating off-diagonal terms. Initially, S_x is often chosen to be similar to matrix S_a, serving as an initial estimate.

The error resulting from random and systematic errors in the measurements made (S_m) corresponds to the variability in measurements caused by unpredictable and systematic factors. Random errors stem from unpredictable fluctuations in measurements, while systematic errors result from constant biases or deviations in measurement instruments. This error encompasses both random fluctuations and systematic biases that can affect the collected data. It is calculated using the expression 3.54 as outlined in Rodgers (2000).

$$S_m = G_y S_\epsilon G^T \tag{3.54}$$

S_ϵ represents the measurement error covariance matrix, and G_y is the matrix of contribution functions, expressing how the retrieved profile responds to variations in the measured trace gas column abundances (see equation 3.47). The S_ϵ matrix is configured with diagonal elements, each corresponding to the statistical errors associated with the DOAS fitting.

The error related to the forward model parameters, denoted as S_f, represents the retrieval error arising from uncertainties associated with the parameters of the forward model. The matrix S_f is computed using the expression 3.55, as defined by Rodgers (2000).

$$S_f = G_y K_b S_b K_b^T G_y^T \tag{3.55}$$

K_b represents the reactivity of the forward model to variations in the forward model parameters b, and S_b is the covariance matrix of these parameters. Calculating S_f is a complex task due to the large number of parameters involved in the forward model. Thus, in FRM_4DOAS, the S_f matrix for trace gas profiling is obtained using the uncertainty on retrieved aerosol profiles, which generally serves as the primary error source related to the forward model parameters. This uncertainty is estimated through sensitivity tests, as demonstrated in previous studies such as Clemer et al. (2010); Hendrick et al. (2014); Wang et al. (2017).

Chapter 4

SATELLITE DATASETS

This chapter presents a brief theoretical description of the satellite instruments whose data have been used in this thesis. These instruments are OMI and TROPOMI. We will describe the essential elements of these instruments, their measurement geometry, the measurements, a brief description of the code for inversion from spectra to geophysical quantities and their vertical sensitivities.

4.1 OMI and TROPOMI Missions

The OMI and TROPOMI are backscattered radiation observation instruments of Earth, installed on the Aura and the Sentinel-5 Precursor (S5P) satellites, respectively. The Aura spacecraft is part of a long-term Earth Observing System (EOS) National Aeronautics and Space Administration (NASA) mission, launched on July 15, 2004, from Vandenberg Air Force Base in California Levelt et al. (2006), while S5P ESA-Copernicus platform was launched on October 13, 2017, from the Plesetsk Cosmodrome in Russia [1] Veefkind et al. (2016).

In addition to the two instruments OMI and TROPOMI, the two satellites also carry other types of instruments such as the Microwave Limb Sounder (MLS), the High-Resolution Dynamics Limb Sounder (HIRDLS), and the Tropospheric Emission Spectrometer (TES). Aura and S5P operate on a heliosynchronous polar orbit with an inclination of 98.2 degrees, with an equatorial crossing in the afternoon at 13:45 (ascending node), allowing it to complete 14 orbits per day, a altitudes of 705 km and 824 km for Aura and S5P, respectively de Graaf et al. (2016); Veefkind et al. (2016).

The Copernicus Sentinel-5 Precursor mission addresses the need to bridge the data gap in global atmospheric data products between the conclusion of SCIAMACHY/Envisat [2] in April 2012. The OMI/AURA mission, and the upcoming Copernicus Sentinel-4 and Sentinel-5 missions, is built upon the concept of capturing the complete spectrum in the ultraviolet, visible, and near-infrared (UV/VIS/NIR) regions, enabling the simultaneous extraction of columns for multiple trace gases from a single air sample.

[1] https://sentinels.copernicus.eu/web/sentinel/missions/sentinel-5p
[2] Scanning Imaging Absorption Spectrometer for Atmospheric Chartography Instruments

4.1.1 OMI Instrument description

The central component of the OMI instrument is a ultraviolet-visible spectrometer equipped with two-dimensional CCD detectors operating in "push-broom" mode. The overall instrument configuration (including the optical assembly, optical bench, detector modules, electronic unit, and interface adaptor module) can be referenced in Levelt et al. (2006). The first dimension of the detectors (780 pixels) is dedicated to capturing spectral information, while the second dimension (576 pixels) is used for spatial information. OMI employs a wide field of view (114°) that is focused onto the two-dimensional detector using an innovative optical design. The spectral resolution of the Vis channel is 0.63 nm.

OMI records backscattered solar radiation in the spectral range of 270 to 500 nm using two distinct channels: UV (270-365 nm) and VIS (365-500 nm). With this broad spectral coverage, OMI can measure key components of air quality, including NO_2, H_2CO, CHOCHO, SO_2, BrO, OClO, and aerosol characteristics. It is also capable of distinguishing between different types of aerosols, such as smoke, dust, and sulfates.

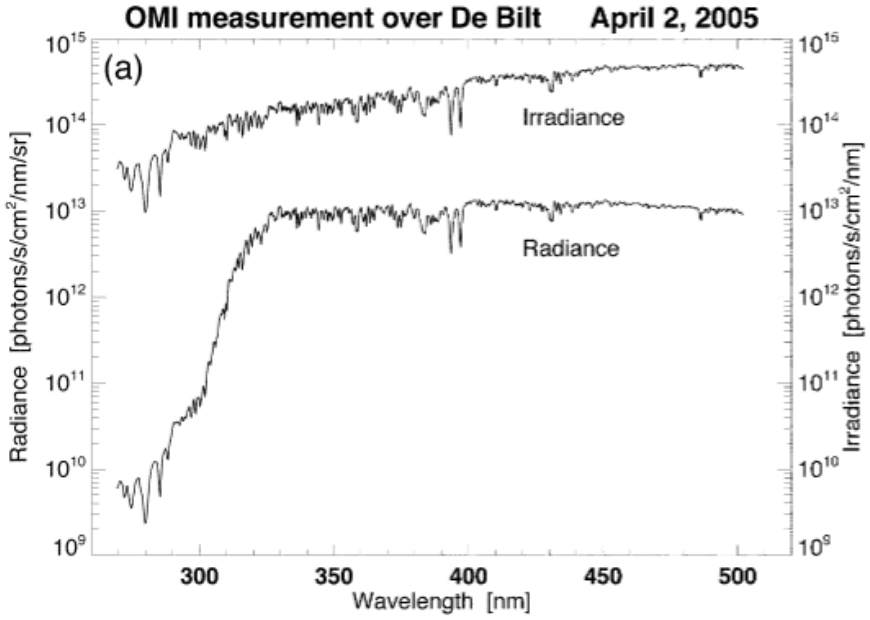

Figure 4.1: OMI solar irradiance and Earth radiance spectrum above the Netherlands on a cloudless day (Levelt et al., 2006).

OMI offers three observation modes: the global measurement mode, the spatial zoom-in measurement mode, and the spectral zoom-in measurement mode. In the global measurement mode, OMI samples the entire swath of 2600 km in the wavelength range of 270 to 500 nm with a spatial resolution of 13 km x 24 km at nadir, an average of eight detector elements (Levelt et al., 2006). The spatial zoom-in mode reduces the ground pixel size to 13 km x 12 km for the UV-2 and VIS channels and 13 km x 24 km for the UV-1 channel while maintaining the full wavelength range. The spectral zoom-in mode retains the swath width but limits the wavelength range to 306-432 nm.

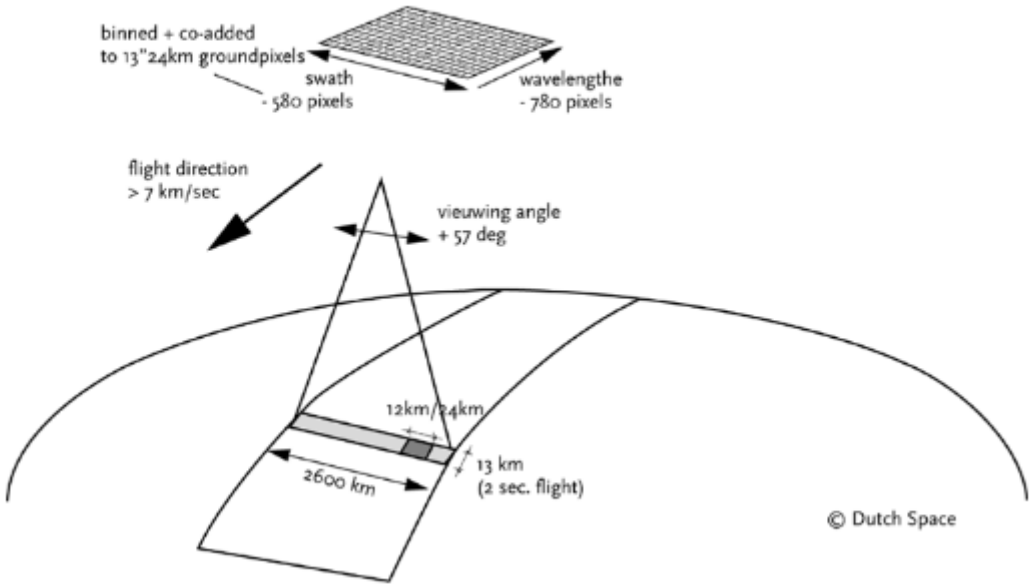

Figure 4.2: OMI measurment principle (Veefkind et al., 2012).

4.1.2 TROPOMI Instrument description

Similary to OMI, the driving component of the TROPOMI instrument is the nadir-viewing hyperspectral push-broom spectrometer, known as TROPOMI, which measures radiation in the UV, visible, and IR spectral regions, enabling the measurement of various atmospheric components such as H_2CO, SO_2, O_3, CO, CH_4, as well as aerosol and cloud properties (Veefkind et al., 2012; van Geffen et al., 2020b). Its two-dimensional CCD detector captures spectra across a swath width of approximately 2600 km in approximately 450 viewing directions simultaneously in about 1 second, as illustrated in Figure 4.3. This results in ground pixel sizes of roughly 3.5 km $\times$ 7 km in the middle of the swath. Since August 5, 2019, the ground pixel size has been reduced to about 3.5 km $\times$ 5.5 km through shorter along-track averaging of only 0.84 seconds. With 4173 along-track scanlines, this leads to approximately 1.88 million ground pixels per orbit. With orbit times of 100 minutes and a wide swath, TROPOMI achieves nearly global coverage with equator crossing times at around 13:30 local time. These advancements make it a more sophisticated instrument than its predecessor OMI, with significantly improved resolution, allowing for a more precise capture of ground-level pollution information.

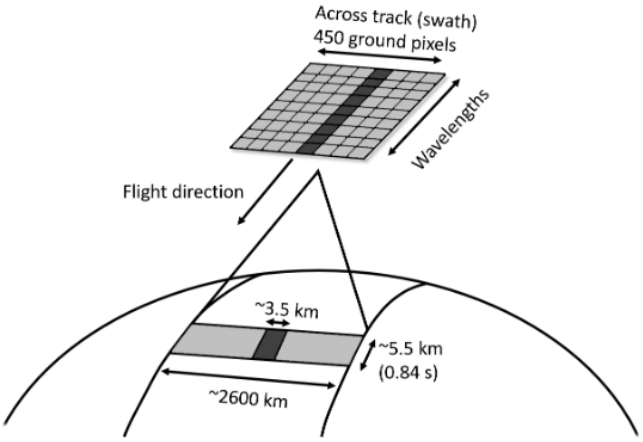

Figure 4.3: TROPOMI measurment principle (Levelt et al., 2006).

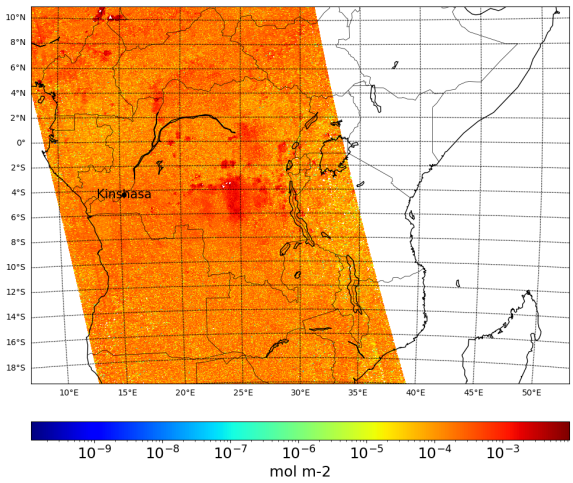

Figure 4.4: Illustration of a typical TROPOMI orbit, covering the Democratic Republic of Congo for the day of May 13, 2020.The color scale is marked according to the H_2CO VCD shown on the map. $1\,\mathrm{mol/m^2} = 6,022 \times 10^{15}\,\mathrm{molécules/cm^2}$.

4.2 NO_2 retrieval algorithm for OMI and TROPOMI

4.2.1 Retrieval algorithm overview

The OMI and TROPOMI data products are obtained using various retrieval techniques that draw upon the experience gained from similar instruments like TOMS[3], SBUV[4], GOME[5], and SCIAMACHY[6]. There are roughly five major retrieval techniques, including

[3]TOMS : Total Ozone Mapping Spectrometer (TOMS) : NASA satellite instrument `https://eospso.nasa.gov/missions/total-ozone-mapping-spectrometer-earth-probe`

[4]SBUV : Solar Backscatter Ultraviolet Radiometer `https://www.ospo.noaa.gov/Products/atmosphere/sbuv.html`

[5]GOME : Global Ozone Monitoring Experiment (GOME) : ESA satellite instrument `https://earth.esa.int/eogateway/instruments/gome`

[6]SCIAMACHY : SCanning Imaging Absorption spectroMeter for Atmospheric CartograpHY : ESA satellite instrument `https://earth.esa.int/eogateway/instruments/sciamachy`

the TOMS-type retrieval (for ozone column and SO_2), the DOAS-type retrieval (for O_3, NO_2, cloud pressure, H_2CO, OClO, and BrO), optimal estimation methods (for ozone profiles), Raman scattering (for cloud pressure), and retrievals based on radiance variations over long wavelength ranges (for aerosols). Each of these techniques relies differently on performance of satellite and calibration, depending on its spectral characteristics and stability (Levelt et al., 2006).

4.2.2 Satellite DOAS approach

The procedure used for NO_2 product recovery by OMI or TROPOMI is based on the DOAS technique explained in Chapter 3. The process involves three primary steps executed for each Level-1b spectrum:

1. Retrieving the total slant column density (SCD) for the target gas from the Level-1b radiance and irradiance spectra measured by OMI or TROPOMI using a fit DOAS method detailed in Chapter 3. Note that this step is valid for both molecules (NO_2 or H_2CO).
2. Separating SCD into a stratospheric part (SCD_{strat}) and a tropospheric part (SCD_{trop}) based on assimilated data information. It should be noted that this second step is solely performed for molecules that have a stratospheric contribution, such as NO_2, for example. However, for H_2CO, this step is not executed within the algorithm.
3. Converting the tropospheric slant column density into tropospheric vertical column density (VCD_{trop}).

The entirety of the steps, as per the procedure explained, is well depicted in Figure 4.5, and Equation 4.1) formalizes the determination of the retrieved tropospheric VCD_{trop}.

$$VCD_{trop} = \frac{SCD - SCD_{strato}}{AMF_{trop}} \tag{4.1}$$

4.2.3 SCD retrieval algorithm

In this initial stage of the DOAS algorithm involving SCD determination, the process is carried out in accordance with the DOAS technique by fitting the R_{meas} function (reflectance spectrum), which is the ratio of measured terrestrial radiance I_λ and solar irradiance data $E_0(\lambda)$ to the modelled R_{mod} spectrum. This adjustment is applied to data collected within a specific wavelength range known as the fitting window, which needs to be optimized for each trace gas separately. A polynomial function (last term of the equation 4.2), serving as a high-pass filter, is employed to accommodate gradual variations in scattering and absorption across wavelengths, such as surface reflection and scattering by molecules, aerosols, and clouds (contribution of elastic scattering to the differential absorption signatures). The satellite DOAS equation can be expressed as:

$$\ln(R_{\text{meas}}) = -\sum_{i=1}^{N} \sigma_{\text{i}}(\lambda, s) SCD_{\text{i}}(s) - \sum_{j=1}^{M} p_{\text{i}} \lambda^j \tag{4.2}$$

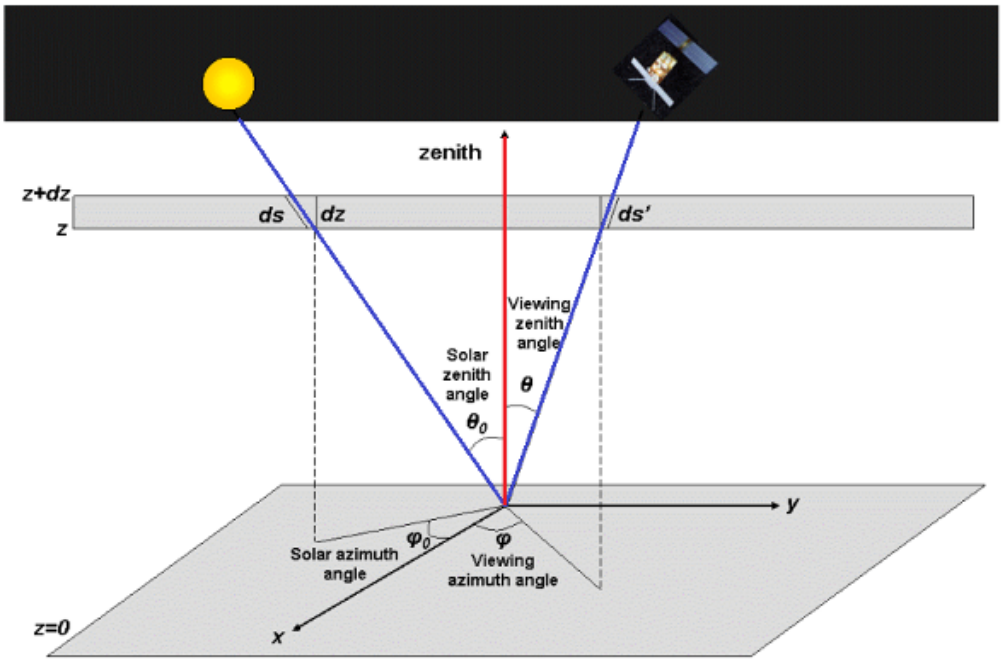

Figure 4.5: Diagram of satellite radiation measurement and geometry in a planar atmosphere. The blue lines delineate the optical path associated with the slant column density (initial stage of the DOAS algorithm). The red line pertains to the vertical column density (third stage of the DOAS algorithm). `https://sentinels.copernicus.eu/web/sentinel/technical-guides/sentinel-5p/level-2/doas-method`

$\sigma_i(\lambda)$ represents the absolute cross-section ($i = 1, \ldots, N_i$; e.g., NO_2, O_3, etc. see table 4.1), SCD_i denotes the total slant column amount of molecule i and R_{meas} reflectance spectrum given in the equation 4.3 (van Geffen et al., 2022b). The satellite DOAS retrieval utilizes a reference spectrum derived from extraterrestrial solar sources, which exclusively includes Fraunhofer structures without any Earth atmospheric absorptions. This enables the retrieval of absolute SCDs. The R_{meas} expression is given by the expression 4.3.

$$R_{\text{meas}}(\lambda) = \frac{\pi I(\lambda)}{\mu_0 E_0(\lambda)} \tag{4.3}$$

Is important to specify that E_0 and I are captured by the same detector row and provided on the identical wavelength grid. Additionally, $\mu_0 = \cos(\theta_0)$ is the cosine of the solar zenith angle. The DOAS spectral fitting is conducted for all satellite ground pixels with $\theta_0 < 88°$, ensuring no potential issue from the division by μ_0 in Equation 4.3. The DOAS spectral fitting aims to determine the optimal modeled reflectance spectrum, $R_{\text{mod}}(\lambda)$, by minimizing the chi-squared merit function (4.4), striving for the smallest possible differences between the observed and modeled reflectance spectrum (van Geffen et al., 2022b).

$$\chi^2 = \frac{1}{n_\lambda} \sum_{i=1}^{n_\lambda} \left(\frac{R_{\text{meas}}(\lambda_i) - R_{\text{mod}}(\lambda_i)}{\Delta R_{\text{meas}}(\lambda_i)} \right)^2 \tag{4.4}$$

The magnitude of χ^2 is a measure for the goodness of the fit. Another indicator for the fit's quality is the root-mean-square (RMS) error, which is defined as follows:

Table 4.1: Spectral NO_2 fitting parameter settings for OMI-QA4ECV, and TROPOMI (van Geffen et al., 2020a, 2022b).

Parameters	**OMI**	**TROPOMI**
Fitting window	405–465 nm nm	405-465 nm
Reference spectrum E_0	Annual mean (2005) solar reference	Daily solar reference
Polynomial	4th-order	5th-order
Included cross section		
O_3	Bogumil et al. (2000) at 243 K	Serdyuchenko et al. (2014) at 223 K
NO_2	Vandaele et al. (1998)	Vandaele et al. (1998) at 220 K
O_4	Thalman and Volkamer (2013b) at 293 K	Thalman and Volkamer (2013b) at 293 K
H_2O(liquid)	Pope and Fry (1997)	Pope and Fry (1997)
H_2O (vapor)	Rothman et al. (2013)	Rothman et al. (2013)
Ring Effect	Chance and Spurr (1997)	Chance and Spurr (1997)
high-resolution solar reference	Dobber et al. (2008)	(Chance and Kurucz, 2010b)
Intensity Offset correction	constant	not included
Type of DOAS fit	Optical density fit (Danckaert and Fayt, 2017)	Intensity (Van Geffen et al., 2015)
Minimisation method	Levenberg-Marquardt	Optimal estimation

$$\mathrm{RRMS} = \sqrt{\frac{1}{n_\lambda}\sum_{i=1}^{n_\lambda}\left(R_{\mathrm{meas}}(\lambda_i) - R_{\mathrm{mod}}(\lambda_i)\right)^2} \tag{4.5}$$

The specific details of $R_{\mathrm{mod}}(\lambda)$ and the approach to minimize differences between this simulated reflectance and the measured reflectance slightly vary depending on the techniques applied for retrievals in TROPOMI and OMI (van Geffen et al., 2020a). For TROPOMI, for instance, the formulation of R_{mod} is provided by 4.6 (van Geffen et al., 2022b).

$$R_{\mathrm{mod}}(\lambda) = P(\lambda)\cdot\exp\left[-\sum_{i=1}^{N}\sigma_{\mathrm{i}}(\lambda,s)SCD_{\mathrm{i}}(s)\right]\cdot\left(1 + C_{\mathrm{ring}}\frac{I_{\mathrm{ring}}(\lambda)}{E_0(\lambda)}\right) \tag{4.6}$$

C_{ring} stands for the Ring fitting coefficient, $I_{\mathrm{ring}}(\lambda)$ is the synthetic Ring spectrum. The Ring spectrum delineates the differential spectral signature arising from inelastic Raman scattering of incoming sunlight by N_2 and O_2 molecules.

4.2.4 Separating stratospheric NO_2 (SCD_{strat})

The total SCD extracted from the adjustments detailed in the previous paragraph encompasses both tropospheric and stratospheric contributions. To exclusively extract the tropospheric contribution from this total SCD, knowledge of the stratospheric contribution is imperative. However, direct measurements of NO_2 within the stratosphere (collocated limb measurements) remain unavailable. To address this, an assimilation-based approach using slant columns' NO_2 data in a three-dimensional model is employed.

The fundamental concept of data assimilation involves regularly updating a three-dimensional coupled troposphere-stratosphere NO_2 distribution simulation with available measurement data. Studies such as those conducted by Hendrick et al. (2012) have demonstrated a strong correlation between satellite retrievals using data assimilation to estimate stratospheric NO_2 columns (GOME, SCIAMACHY, and GOME-2) and on-site measurements at the Jungfraujoch station, showcasing the effectiveness of data assimilation systems in estimating NO_2 concentrations in the stratosphere. This process aims to ensure that the CTM simulation of the stratospheric NO_2 column closely aligns with TROPOMI slant columns over regions known for their low or absent tropospheric NO_2 (e.g. over the Pacific Ocean: Van Geffen et al. (2015)). A concise theoretical and algorithmic explanation of this method, as implemented by instruments like TROPOMI, is outlined in the van Geffen et al. (2022b). The Chemistry Transport Model (CTM) utilized for OMI is the three-dimensional chemical transport model TM5-MP (Williams et al., 2017). This model provides comprehensive global data with 34 atmospheric layers and a grid resolution of 1°× 1°(longitude × latitude). It relies on the ECMWF ERA-Interim meteorological re-analysis (Dee et al., 2011) and is updated every 3 hours through interpolation of intermediate time period data. Model outputs include the NO_2 profile, temperature profile (in K), hybrid pressure levels (in Pa), and a tropopause layer index to differentiate between the stratosphere and troposphere. For TROPOMI, the TM5-MP is used to calculate the stratospheric vertical column density (VCD_{strat}). The SCD_{strat} is then determined using AMF_{strat} according to equation 4.7.

$$SCD_{\text{strat}} = VCD_{\text{strat}} \cdot AMF_{\text{strat}} \tag{4.7}$$

4.3 H_2CO retrieval algorithm for OMI and TROPOMI

For the retrieval of the H_2CO product from spectral observations, the DOAS algorithm is employed primarily in two steps. The first step involves determining the slant column density derived from the measured reflectance spectrum. Secondly, an air mass factor (AMF) is determined for converting the slant column into a vertical column. In addition to these two steps, a third step involves an additional correction due to the reference spectrum. (De Smedt et al., 2018) provides a detailed description of the formaldehyde retrieval algorithm, with successive adaptations documented in the S5P product Algorithm Theoretical Basis Document (ATBD). In accordance with De Smedt et al. (2021), the tropospheric vertical column is deduced from Equation 4.8.

$$VCD = \frac{SCD_s - SCD_{s,0}}{AMF} + VCD_0 \tag{4.8}$$

.

Where VCD are the tropospheric vertical, SCD_s the slant column density, AMF the tropospheric air mass factor and (SCD_s, VCD_0), the values used for the reference sector correction (see section 4.3.2).

4.3.1 H_2CO SCD retrieval

Detecting H_2CO in terrestrial radiations poses challenges due to its lower optical density compared to other UV-Vis spectrum absorbers like NO_2 and O_3 (De Smedt et al., 2018). Spectral interferences with gases such as O_3 and BrO further complicate its detection. Ozone absorptions reduce the number of photons reaching lower atmospheric layers, while Rayleigh and Mie scattering restrict reflected radiation (De Smedt et al., 2018). To optimize retrieval, reduce noise, and address these interference and scattering phenomena, a trade-off has to be established between these effects and instrument characteristics (TROPOMI HCHO ATBD, 2021).

Table 4.2: Spectral H_2CO fitting parameter settings for TROPOMI (TROPOMI HCHO ATBD, 2021).

Parameters	**Characteristics**
Fitting window	328.5-359 nm
Reference spectrum E_0	Average of radiances, per row, selected in the equatorial Pacific within the last 5 valid days
Polynomial	5th-order
Included cross section	
H_2CO	Meller and Moortgat (2000) at 298 K
O_3	Serdyuchenko et al. (2014) at 293 K
BrO	Thalman and Volkamer (2013b) at 293 K
NO_2	Vandaele et al. (1998) at 220 K
O_4	Thalman and Volkamer (2013b) at 293 K
Ring Effect	Chance and Spurr (1997)
Non-linear O_3 absorption effect	(Puk̄ite et al., 2010)
Intensity Offset correction	Linear offset

The table provides details about the parameters used for the DOAS adjustment, specifically detailing two wavelength intervals. One interval, ranging from 328.5 to 359 nm, encompasses six zones where the gas BrO absorbs light, aiding in reducing its connection with H_2CO, thus decreasing the noise in the retrieved slant columns. The second interval, covering 328.5 to 346 nm, is utilized to avoid biases associated with O_4's influence, as O4 also absorbs light around 360 nanometers. These intervals respectively utilize the values of BrO slant columns for effective decorrelation. They include the cross-sections of O_3 at 223K and 243K, NO_2, BrO, and O_4 in the adjustment, along with correction for the Ring effect.

Additionally, to counter the strong ozone absorption at wavelengths below 336 nm, the method introduced by Puk̄ite et al. (2010) is applied, considering the variability of the ozone column within the adjustment window. This method allows for improved handling of

ozone absorption, reducing the underestimation of H_2CO slant columns while maintaining the attractive features of DOAS in terms of performance.

4.3.2 H_2CO reference sector correction

In the DOAS fitting for H_2CO retrieval, the reference spectrum ($SCD_{s,0}$) is derived from measurements made over the Pacific Ocean (from 5° S to 5° N in latitude and from 180 to 140° W in longitude). The choice of this region is based on the assumption that the background column of H_2CO observed over remote oceanic areas is solely due to methane oxidation, a factor that can be easily managed with the model. Hence, the use of such a reference spectrum requires correction due to this methane oxidation to account for the residual H_2CO signal in the reference spectra. As per De Smedt et al. (2018), this correction is provided by equation 4.9.

$$VCD_0 = \frac{AMF_0}{AMF} \times VCD_{0,model} \tag{4.9}$$

AMF_0 represents the air mass factor in the reference area, while $VCD_{0,model}$ is derived from the TM5 model in the reference region.

4.4 Satellite Air Mass Factor retrieval algorithm

The air mass factor is defined by the expression 3.20, as seen in Chapter 3, representing the ratio between the slant optical depth and the vertical optical depth of a specific absorber, based on the primary assumption of the DOAS approach that considers an optically thin atmosphere. Consequently, the average path of scattered photons is assumed to be independent of the wavelength within the relatively narrow spectral range selected for the fitting.

However, this formulation changes when considering the troposphere due to scattering by air molecules, clouds, and aerosols leading to complex light paths dependent on altitude. It disentangles the measurement sensitivity dependent on altitude from the vertical profile shape of the species of interest. Consequently, the tropospheric air mass factor can be expressed as the sum of altitude-dependent air mass factors ($ml(\mathbf{b})$), weighted by the partial columns ($x_{a,l}$) of the pre-defined vertical profile in each vertical layer, from the surface to the tropopause index (equation 4.10 (Boersma et al., 2004)).

$$AMF = \frac{\sum_l m_l(\mathbf{b}) x_{a,l}.c_l}{\sum_l x_{a,l}} \tag{4.10}$$

In this context, cl represents the temperature correction factor utilized to accommodate the temperature sensitivity of NO_2 cross-sections. It's important to note that this Air Mass Factor (AMF) is contingent on several variables, such as wavelength, Solar Zenith Angle (SZA), Relative Azimuth Angle (RAA), surface albedo, surface pressure, cloud fraction, cloud albedo, cloud top pressure, and elevation-dependent surface pressure. For NO_2, the AMF is computed at 437.5 nm, while for H2CO, it is determined at 340 nm, employing the VLIDORT radiative transfer model (Spurr et al., 2001). The a priori NO_2 profile

and surface pressure used for AMF calculations are derived from the three-dimensional chemical transport model TM5-MP (Williams et al., 2017).

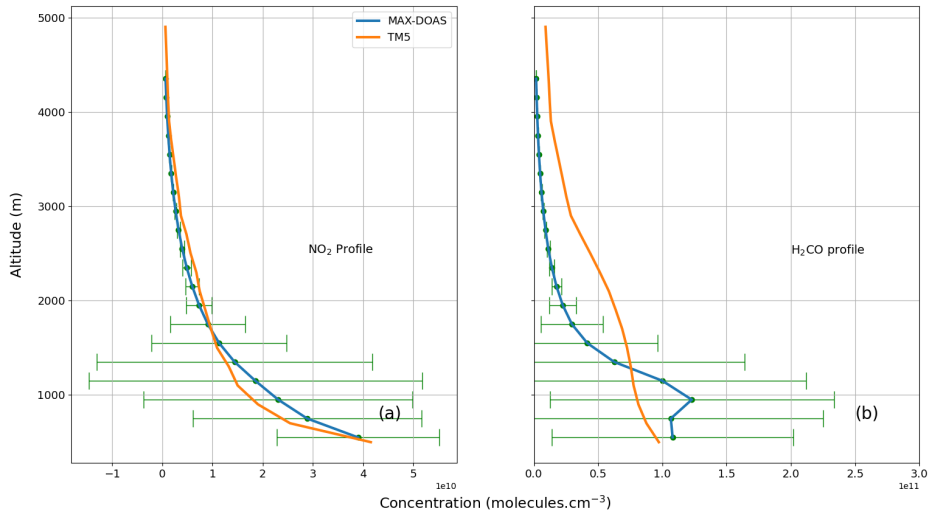

Figure 4.6: Typical profiles for TM5 and MAX-DOAS. These profiles are the medians obtained over a 4-month period from May 15 to September 15, 2020, corresponding to the dry season in Kinshasa.

Surface albedo is derived from the monthly OMI albedo climatology, with a spatial resolution of 1° × 1°, using the minimum Lambertian equivalent reflectivity (LER) (Kleipool et al., 2008). Surface elevation is sourced from GMTED2010 data[7], which offer a uniform spatial resolution of 30 arc seconds. During AMF calculations, scattering weights are interpolated based on observation conditions and the pressure grid of the a priori profile.

A representation of NO_2 and H_2CO profiles derived from the TM5 model is provided in Figure 4.6, complemented by median profiles measured by MAX-DOAS in Kinshasa during the dry season of 2020. In panel a, it is observed that the NO2 profiles retrieved by MAX-DOAS are quite close to those from the TM5 model. However, for H_2CO, significant differences between the two median profiles can be noticed. This substantial discrepancy in the profile constitutes one of the main sources of errors in satellite product retrieval, extensively discussed in Chapter 6.

4.5 Vertical sensitivity

The vertical sensitivity of satellites is a critical factor in understanding and interpreting data provided by these spacecraft. Satellite-derived data typically represents a weighted average of all contributions from the atmosphere to the signal observed by the satellite instrument. AMFs used to convert SCD to VCD strongly depend on the assumed shape of the a priori trace gas profile. They take into account the measurement's sensitivity to gaz concentrations at different altitudes, with adjustments based on the assumed shape of the a priori profile to obtain the vertical column. As described in Chapter 3, Section 2, the AK plays a key role in assessing this vertical sensitivity. To compute the DOAS

[7]https://www.usgs.gov/coastal-changes-and-impacts/gmted2010

AK for total column observations of optically thin absorbers, the following formula is used (Eskes and Boersma, 2003) :

$$AVK(l) = \frac{amf_l}{AMF} \tag{4.11}$$

where amf_l represents the altitude-dependent air mass factor, and AMF denotes the

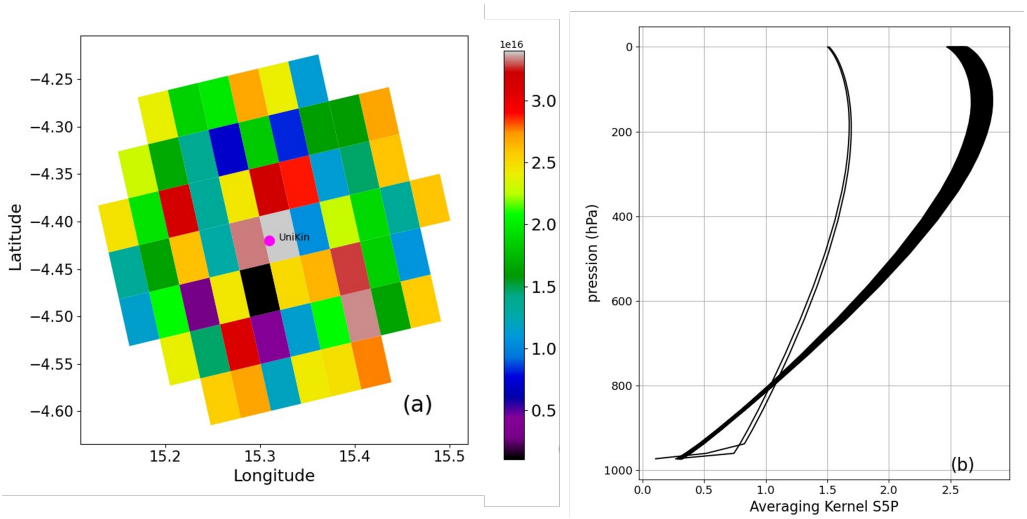

Figure 4.7: The H_2CO Column TROPOMI pixels selected within a 20 km radius around UniKin, above Kinshasa for 30 March 2020 (panel a). The corresponding AKs for each selected pixel (Panel b). Two of these pixels exhibit a cutoff at 800 hPa due to the presence of clouds (Boersma et al., 2004)

tropospheric air mass factor. It consists of 34 layers corresponding to the 34 vertical grid levels of the TM5 model and is provided alongside retrieval data, accompanied by the error budget for each individual pixel. For example, Figure 4.7 illustrates 61 AK vectors corresponding to 61 pixels located above Kinshasa. Low AK values, typically below 1, are observed in the early layers, ranging from 0 to 3 km in altitude, indicating limited satellite sensitivity near the surface. This reduced sensitivity is largely attributed to the profile's shape, as previously noted during AMF calculations. In contrast, Figure 4.6 compares TM5 model profiles with those obtained by MAX-DOAS. Unlike satellites, MAX-DOAS instruments exhibit much higher sensitivity near the surface (see MAX-DOAS AK, Chapter 3).

In this study, one of the objectives was to compare observations from these two instruments, following the approach outlined by (Boersma et al., 2004). To address the challenge posed by the apparent low satellite sensitivity near the surface, we utilized MAX-DOAS profiles in conjunction with satellite AK. A detailed analysis of these comparisons is presented in Chapter 7.

4.6 Impact of clouds and aerosols

Characterizing the scattering of light by clouds and aerosols is an important aspect of atmospheric remote sensing, as it significantly influences how satellites and observational instruments measure reflectance. When retrieving tropospheric columns of NO_2 or H_2CO,

special consideration must be given to the treatment of these two parameters. As illustrated in Figure 4.7, two pixels affected by clouds are shown, as indicated by the cutoffs at 800 hPa. When using the data, for example, for comparisons with other ground-based instruments, a filtering process is applied to these pixels affected by clouds. We briefly provide some insights into the treatment of these parameters in the retrieval of OMI and TROPOMI data.

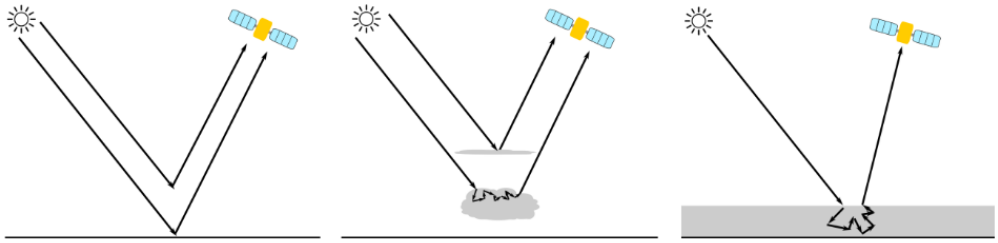

Figure 4.8: [Possible light paths for satellite observations: clear sky (left), cloudy (middle), aerosols (right). Based on John P. Burrows (2011).

In Figure 4.8, an illustration presents three different scenarios for the path of solar light, influenced by cloud and aerosol conditions before being reflected and captured by the satellite. On the left, the scene depicts a clear sky without clouds or aerosols near the surface, ensuring an undisturbed path of light. In the middle, the situation is characterized by the presence of clouds in both upper and lower tropospheric layers, resulting in a significant elongation of the optical path compared to the first scenario. In the third case, on the right, the path of light is influenced by the presence of aerosols near the ground.

Clouds reduce the sensitivity of measurements by blocking some of the photons, especially towards the lower layers, particularly the base of the clouds and the surface. Conversely, aerosols cause multiple scattering of light, thereby increasing sensitivity within the aerosol layer and above it due to a higher probability of scattering (amplification/albedo effect), but decreasing sensitivity below the aerosol layer due to masking effects. In the presence of highly absorbing aerosols, sensitivity is further reduced within the aerosol layer. Therefore, the overall impact of clouds and aerosols depends on their specific characteristics, vertical distribution, solar zenith angle, observation geometry, wavelength, and surface reflectivity. Sensitivity can either increase or decrease compared to clear sky conditions, depending on these factors (John P. Burrows, 2011; Chimot et al., 2016; Leitão et al., 2010).

4.7 Clouds correction

The correction of the cloud-related effects in satellite product retrievals is carried out by considering the parameters known as cloud fraction and cloud pressure. "Cloud fraction (c_f)" is a measure used in the field of satellite remote sensing to assess the proportion of the Earth's surface currently covered by clouds. It is a numerical value that indicates what portion of the area observed by a satellite is cloud-covered at a given time.

$$c_f = \frac{R_{TOA} - R_s}{R_c - R_s} \tag{4.12}$$

Rs and Rc represent the surface and cloud reflectances, respectively, obtained through

modeling. R_{TOA} represents the measured reflectance at top-of-atmosphere (TOA) at λ_c, which is equal to 440 nm for NO2. These parameters are taken into account in the calculation of the Air Mass Factor (AMF), using the independent pixel approximation (Cahalan et al., 1994; Martin et al., 2002), assuming that the AMF is a linear combination of a cloudy-sky AMF (M_{cl}) and a clear-sky AMF (M_{cr}):

$$AMF = \omega M_{cl} + (1 + \omega) M_{cl}, \tag{4.13}$$

Using M_{cl}, the air mass factor described in Equation 4.10, with the cloud surface treated as a Lambertian reflector and with m_l=0 for layers below the cloud top pressure c_p, where ω represents the radiance cloud fraction given in Equation 4.14.

$$\omega = \frac{c_f R_c}{(1 - c_f) R_c + c_f R_s} \tag{4.14}$$

Algorithms aimed at retrieving information about clouds are generally based on the assumption that both the surface and clouds act as Lambertian reflectors. They utilize reflectance spectra from the oxygen absorption band O_2, located around 760 nm, to determine cloud pressure and effective cloud fraction. This approach is based on the understanding that clouds have a more significant impact on reflectance in the oxygen O_2 absorption band than aerosols. Among these algorithms, you can find the ICFA (Initial Cloud Fitting Algorithm), FRESCO (Fast REtrieval Scheme for Clouds from the Oxygen A-band), SACURA (Semi-Analytical CloUd Retrieval Algorithm), the Optical Cloud Recognition Algorithm (OCRA) and the Retrieval of Cloud Information using Neural Networks(ROCINN) algorithm (`https://sentinel.esa.int/documents/247904/2476257/Sentinel-5P-TROPOMI-ATBD-Clouds`).

In the context of OMI, where O_2 A-band measurements are not available, the DOAS approach is used for the retrieval of O_2-O_2 slant columns, which are then compared to simulated Look-Up Table (LUT) entries to derive the effective fraction and cloud-top pressure. For the OMI QA4ECV product, the algorithm is based on the O_2-O_2 absorption feature around 477 nm and assumes a fixed cloud albedo of 0.8 (version 2.0, Veefkind et al. (2016). As for TROPOMI, the OCRA/ROCINN-CRB algorithm Loyola et al. (2018) is used for cloud processing.

4.8 Products used for OMI and TROPOMI

In this section, we provide a simplified overview of various product versions utilized in this thesis. The aim is to briefly outline some technical specifics that differentiate these products.

4.8.1 Data product-version history

After the satellite launch, the initial data types are typically classified into three levels. Firstly, Level-0 products encompass raw satellite telemetry data, arranged in chronological order without temporal overlap. This includes sensor data from the spectrometers,

addressing both atmospheric measurements and calibration. Additionally, it incorporates engineering data (e.g., housekeeping [8]), satellite ancillary data (e.g., position, attitude), and acquisition metadata essential for ground processing and monitoring tasks. Level 0 data is not made publicly available (`https://sentinels.copernicus.eu/web/sentinel/missions/sentinel-5p/data-products`, last accessed on November 2, 2023).

Subsequently, Level-1B products contain geolocated and radiometrically corrected top-of-the-atmosphere Earth radiances across all spectral bands, along with solar irradiances[9].

Finally, Level-2 products consist of geolocated information such as total columns of ozone, sulfur dioxide, nitrogen dioxide, carbon monoxide, formaldehyde, and methane. They also include geolocated tropospheric ozone columns, vertical ozone profiles, and information on clouds and aerosols (e.g., absorbing aerosol index and aerosol layer height). User documentation for these products is accessible in the ATBD.

Regarding processing, three types are distinguished: Near Real Time (NRT), Offline (OFFL), and Reprocessing (RPRO). For NRT processing, product availability must be within 3 hours after detection. Total columns of various gases, vertical ozone profiles, cloud and aerosol information are provided in NRT.

For OFFL processing, data availability depends on the product. Currently planned delivery times include approximately 12 hours after detection for Level-1B products, and about 5 days for methane, tropospheric ozone, and total nitrogen dioxide columns (van Geffen et al., 2022b).

A final category is RPRO, which involves reprocessing dependent on changes over time, either due to minor algorithm bugs or major changes such as the adoption of a different crucial parameter, like the a priori profile. This may also include a different treatment of cloud products. Reprocessing activities are not bound by time constraints (`https://sentinels.copernicus.eu/web/sentinel/missions/sentinel-5p/data-products`, last accessed on November 2, 2023).

4.8.2 Versions used

In the scope of this research, we employed the OMI QA4ECV (Quality Assurance for Essential Climate Variables) NO_2 product (Boersma et al., 2018a), encompassing data from May 2017 to November 2019 (see chapter 5). Additionally, we utilized both reprocessed (RPRO; v0102) and offline (OFFL; v0102 and v0103) data products from TROPOMI during the same period. For the timeframe spanning from November 15th to July 1st, 2021, our research made use of the NO_2 product from TROPOMI, sourced from the S5P-PAL product (see chapter 6). The abbreviation stands for Sentinel-5P Product Algorithm Laboratory for NO_2 (`https://data-portal.s5p-pal.com/`, last accessed on June 2, 2023).

The QA4ECV NO_2 OMI version 1.1 data product originates from the Level 1 UV-Vis spectral measurements obtained by the OMI spectrometer, as illustrated in Figure 4.1. These data consist of vertical columns for the troposphere, stratosphere, and total NO_2. It distinguishes itself from previous products like Dutch OMI NO_2 (DOMINO) data products

[8] These data may include internal temperature, voltage and current of electrical systems, activity of cooling systems, battery charge, transmission and reception data, and status of onboard computers.

[9] see fo example : Tilstra et al. (2020) conducted a validation of the radiometric calibration of the TROPOMI instrument. This was achieved by comparing the reflectance measured during flight with radiative transfer calculations.

of KNMI[10] and NASA's Standard Product (SP) NO_2 due to adjustments made in the retrieval algorithm. Table 4.1 precisely outlines the parameters used in the fitting for this QA4ECV product. These distinctions encompass distribution methods, stratospheric separation approaches, uncertainty levels, and alignment with other measurement sources, defining the unique characteristics of each dataset. For further information on this product, preliminary evaluations and errors, readers can consult Marchenko et al. (2015); Boersma et al. (2018a); Compernolle et al. (2020); Pinardi et al. (2020).

The other products used in this research are simply based on updates and continuous improvements. The OFFL and RPRO products, each with distinct identifiers and DOIs[11], provide comprehensive information on tropospheric columns, precision estimates, and quality values, catering to various research applications and needs. The data used were filtered based on recommendations in the ATBD (van Geffen et al., 2020a; TROPOMI HCHO ATBD, 2021; De Smedt et al., 2021) to use pixels with a quality value (QA value > 0.75 for NO_2 and QA value > 0.5 for H_2CO. The table 4.3 provides some information regarding the differences between these various versions.

[10]The Royal Netherlands Meteorological Institute
[11]DOI: Digital Object Identifier

Table 4.3: Data Release Information for different TROPOMI data Versions used (`https://sentinel.esa.int/documents/247904/3541451/Sentinel-5P-Nitrogen-Dioxide-Level-2-Product-Readme-File`)

Version	**Active since**	**Active until**	**Changes made**
01.00.02	OFFL: orbit 3661, 2018-06-28	Orbit 3847, 2018-07-11	Initial operational version
01.01.00	OFFL: orbit 3848, 2018-07-11	Orbit 5235, 2018-10-17	Update of surface albedo database
01.02.00	OFFL: orbit 5236, 2018-10-17	Orbit 5832, 2018-11-28	Implementation of a "destriping" algorithm to remove biases, improved retrieval for high Solar Zenith Angles and polar regions, enhanced algorithm for thermal tropopause level computation leading to a more realistic distribution of pressures, addition of a new variable, and improved definition of `qa_value` for high-quality retrievals over snow and ice.
01.03.00	OFFL: orbit 7425, 2019-03-20	Orbit 7999, 2019-04-30	The cloud retrieval algorithm (FRESCO−S) has undergone modifications, accompanied by enhancements in refining the definition of the `qa_value`.
01.02.02	RPRO: orbit 2818, 2018-04-30	Orbit 5235, 2018-10-17	No modifications compared to the preceding version.
S5P-PAL	RPRO: 2018-04	2021-11	S5P-PAL is a reprocessing of the NO_2 dataset using the L2 processor following a version change in December 2020, introducing a discontinuity in the time series. To ensure data consistency, the latest operational processor was used to reprocess data from the beginning of the mission until mid-November 2021.

Chapter 5

FIRST GROUND-BASED DOAS MEASUREMENTS OF NO_2 AT KINSHASA AND COMPARISONS WITH SATELLITE OBSERVATIONS

The following chapter is based on the first article related to this thesis. The sections and subsections related to this chapter follow exactly the published manuscript, referenced as follows:

Yombo Phaka, R., Merlaud, A., Pinardi, G., Mahieu, E., Hendrick, F.,Friedrich, M. M., Fayt, C., Van Roozendael, M., Djibi, B. L., Bopili Mbotia Lepiba, R., Phuku Phuati, E., and Mbungu Tsumbu, J.-P. (2021). First GroundBased Doas Measurements of NO_2 at Kinshasa and Comparisons With Satellite Observations. Journal of Atmospheric and Oceanic Technology, (2):1291–1304. https://doi.org/10.1175/JTECH-D-20-0195.1

Abstract

We present the first ground-based remote sensing measurements of NO_2 made in Kinshasa. They were performed from 2017 to 2019. The motivation of making observations on air pollution in Kinshasa comes from its geographical location, its demography, its climatic conditions and the many different sources of NO_2 existing in its surroundings. A method for recovering the vertical density of the NO_2 tropospheric column (VCDtropo) based on the Differential Optical Absorption Spectroscopy (DOAS) applied to observations at the zenith and 35° elevation angle is described. The mean value of VCDtropo observed in Kinshasa is 3×10^{15} molecules cm^{-2}. We further present first comparisons with the OMI and TROPOMI satellite observations. When comparing OMI data with our observations and using a linear regression analysis, we find a slope of 0.34 and a correlation coefficient of 0.50 for 51 days of coincidences over 2017−2019. Similar comparisons with TROPOMI for 44 days show a slope of 0.41 and a correlation coefficient of 0.72. This study opens up

perspectives for further air quality related studies in Kinshasa and central Africa.

5.1 INTRODUCTION

NO_2 (nitrogen dioxide) is a trace gas that plays an important role in the atmosphere Crutzen (1979); Brewer et al. (1973). NO_2 is a powerful oxidizing agent, which upon reaction with OH, produces nitric acid, a corrosive substance whose toxic effect destroys the environment Molina and Molina (2004); Chan and Coauthors (2010). NO_2 is also involved in the formation of tropospheric ozone Solomon (1999), one of the main components of smog. NO_2 concentrations vary from one region to another, depending on the magnitude of its different sources, such as biomass fires, road traffic, and lightning, and influence of transport. The detection and real-time monitoring of NO_2 is important for the diagnosis of air quality, especially in urban areas. According to the World Health Organization (WHO) guidelines, the yearly annual concentration of NO_2 must not exceed 40 $\mu g/m^3$ WHO (2006). Long-term exposure to concentrations above this threshold leads to respiratory and cardiovascular diseases.

Recent studies show that Africa is being overtaken by the problem of air pollution Knippertz et al. (2015). According to a study published by the Organisation for Economic Co-operation and Development (Roy, 2016), the number of premature deaths related to air pollution in Africa increased by 36% between 1990 and 2013. Research also shows that air quality in urban areas in Africa, defined in particular by black carbon, organic carbon, CO, NO_x ($NO+NO_2$), SO_2 and non-methane hydrocarbon concentrations, is expected to deteriorate rapidly in the coming decade, with concentrations of NO_2, aerosols and other combustion products anticipated to be on the rise Liousse et al. (2014).

Kinshasa (4.32° S, 15.18° E) is the capital of the Democratic Republic of Congo (DRC) and the third most populated city in Africa (12 millions) and it could reach 30 millions inhabitants by 2030 (UN, 2016). Up to very recently, there were no continuous measurements of air pollution performed from the ground in this city (Katoto and Coauthors, 2019) and the few observations in terms of NO_2 pollution available are those measured by satellite instruments.

Fig. 5.1 shows the different seasonal situations of NO_2 tropospheric pollution around DRC from 2018 to 2019, as seen by the TROPOMI instrument. A seasonal cycle of NO_2 pollution can be observed in this area, with a pollution spot always present and visible from the satellite during the whole period of the year in Kinshasa. Although not visible on the various frames of Fig. 5.1 given the size of the selected area, Kinshasa is most of the time showing vertical column density (VCD) in the upper range of the scale, i.e. above 2×10^{15} molecules cm^{-2}. The highest values of NO_2 for the whole observation area are observed between the months of June and August, corresponding to the dry season.

During the dry seasons, the peasant population living around Kinshasa and in almost all provinces of the DRC burns the savannah and forest in order to prepare the land for cultivation, producing pollutant emissions in atmosphere. Additionally to those emissions, there are emissions of polluting species by industrial entities poorly equipped with fume washing systems, by diesel generators that compensate for the inadequacies of electricity distribution, by the combustion of waste piled up in open dumps, and also by road traffic which mainly involves old vehicles. The management and mitigation of a problem such as air pollution requires a good knowledge of the phenomenon, which varies from one

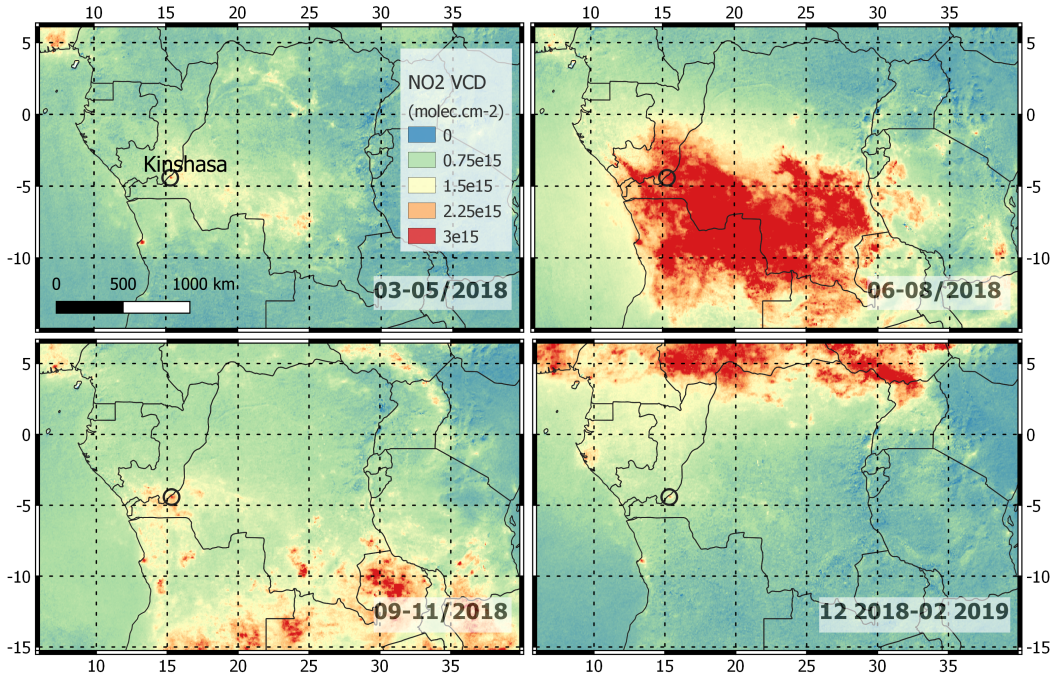

Figure 5.1: Maps of mean tropospheric NO_2 VCDs (from Royal Netherlands Meteorological Institute (KNMI)/European Space Agency (ESA) data processed at BIRA-IASB derived from TROPOMI observations over central Africa during the year 2018.

region to a another. Understanding the specific situation of Kinshasa first requires the collection of data to carry out studies, which are then used in support of the prevention and management of episodes of pollution peaks further aiming at informing in quasi real-time the population about the pollution levels.

In order to address the critical lack of data in this region, the Royal Belgian Institute for Space Aeronomy (BIRA-IASB) and the University of Kinshasa (UniKin) have set up a collaboration that led to the installation of an atmospheric remote sensing instrument in May 2017 on the UniKin site. This instrument, based on the Differential Optical Absorption Spectroscopy (DOAS) technique, is capable of continuous unattended operation.

DOAS instruments have been widely used for measuring NO_2 in the troposphere as well as in the stratosphere (Platt and Stutz, 2008). First used for stratospheric NO_2 measurements using scattered light observations at zenith Noxon (1975), more recent efforts have focused on tropospheric NO_2 in urban environment (Kramer et al., 2008; Gielen et al., 2017; Chen et al., 2009; Zhao et al., 2020; Ialongo et al., 2020; Friedrich et al., 2019).

This work presents NO_2 tropospheric vertical column densities retrieved from measurements made in Kinshasa between May 2017 and November 2019. It also compares the ground-based observations with NO_2 measurements made by two satellite instruments (OMI: Ozone Monitoring Instrument and TROPOMI: TROPOspheric Monitoring Instrument). This manuscript is organized as follows: section 2 provides a description of the observation site, the instrument, and the method used to analyze the measurements. Section 3 describes the algorithm used to obtain the tropospheric vertical columns of NO_2 and the approach for filtering out erroneous data. The interpretation and the discussion of the results are presented in section 4, with emphasis on comparisons between the ground-based

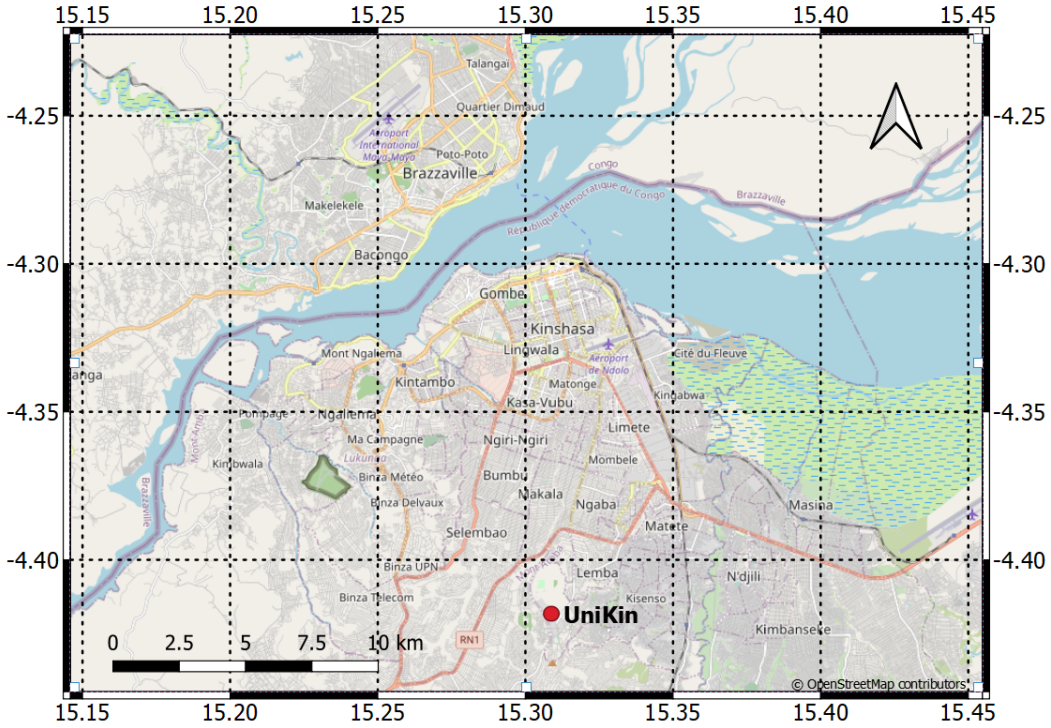

Figure 5.2: Map of Kinshasa with position of the UniKin site.

and satellite measurements.

5.2 SITE, INSTRUMENT, AND SPECTRAL ANALYSIS

5.2.1 Observation site

The city of Kinshasa extends over an area of 9,965 square kilometres along the southern bank of the Pool Malebo and constitutes a flat low surface at an average altitude of about 300 m a.s.l (Saint-Moulin, 2011). Situated between latitudes 4.30° and 4.50° South and between longitudes 15.14° and 15.32° East, the city of Kinshasa is bounded to the West and North by the Congo River forming the natural border with the Republic of Congo Brazzaville (see Fig. 5.2). Our observations were made at the UniKin (4.41° S, 15.31° E), 13 km from the river south of the city as indicated by the red dot on the Fig. 5.2. Kinshasa lies in a hot and humid tropical climate, with an average annual temperature of 25° C and an average annual rainfall of 1,400 mm. It rains in Kinshasa on average 112 days a year with a peak of 18 rainy days in April (**?**). The city has two seasons: a rainy and a dry season. The rainy period extends from mid-September to mid-May, with peaks of heavy rainfall in November and April. The dry season covers the period from mid-May to mid-September. The atmosphere of the city of Kinshasa is strongly influenced by clouds and aerosols, the abundance of which varies with the seasons.

Fig. 5.3 shows the time series of aerosol optical depth (AOD) in the vicinity of Kinshasa as observed by the Moderate-resolution Imaging Spectroradiometer (MODIS) instrument at 550 nm and converted to 477 nm using the Angstrom relationship. It shows that the values range from 0.1 to 1.5 with extreme values up to 2.5 (data from

https://giovanni.gsfc.nasa.gov/giovanni/). These observations indicate a cyclical presence of aerosols around Kinshasa, mainly due to forest fires as mentioned in the introduction. It can also be seen that the periods when maximum AOD values are observed correspond exactly to the periods when maximum NO_2 values are also observed by the satellite as seen in Fig. 5.1.

5.2.2 Instrumental set-up

The instrument used in this work is based on an Avantes ULS2048-XL spectrometer, covering the spectral range 280-550 nm at a spectral resolution of 0.7 nm full width at half maximum (FWHM). The spectrometer is of the Czerny-Turner type with a focal length of 75 mm, an input slit of 50 micrometer width, and a 1200 l/mm grating. An optical fiber of diameter 600 μm is connected to the UV-Vis spectrometer. The spectrometer is directly connected to a computer that controls the acquisition and record the spectra. We record after each minute of observations a spectrum representing intensity as a function of wavelength. From May 2017 to November 2017, measurements were carried out in the zenith sky geometry, pointing the telescope towards the zenith in 90 degree elevation angle. From July 2018 to November 2019, the instrument measured towards 35 degree elevation angle and 58 degree azimuth (NE). The gap in the observation period is caused by technical difficulties with the instrument, the change of observation strategy had to be implemented due to security issues. In addition to fixed geometry measurements, we also used an amateur telescope (Celestron Nexstar) Yombo et al. (2018) to perform experimental measurements in Multi-axis mode Hönninger et al. (2004). Table 5.1 lists the different observation situations for each period.

Table 5.1: *Observations set-up : Measurements at the zenith were interrupted due to insecurity at the observation site. Thus we were pushed to change the place of observation, which only offered the possibility to make the measurements at 35° elevation angle. Measurements in MAX-DOAS were made only for a few days because of the difficulties encountered in the field. The lack of electricity meant that measurements could not be taken every day.*

observation − period	*settings*
May 2017-November 2017	zenith measurements
2 October 2017	MAX-DOAS measurements with an amateur telescope(Nexstar)
December 2017-June 2018	No ground-based observations due to fiber breakage
July 2018-March 2019	measurements at 35° elevation and 58° NE azimuth
March 2019-November 2019	measurements removed from the database because of dust accumulation
November 2019	measurements resumed at 35° elevation and 58° NE azimuth

5.2.3 DOAS Analysis

The QDOAS software (Danckaert and Fayt, 2017) developed at BIRA-IASB is used to obtain differential slant column densities (DSCDs), which represent the difference between

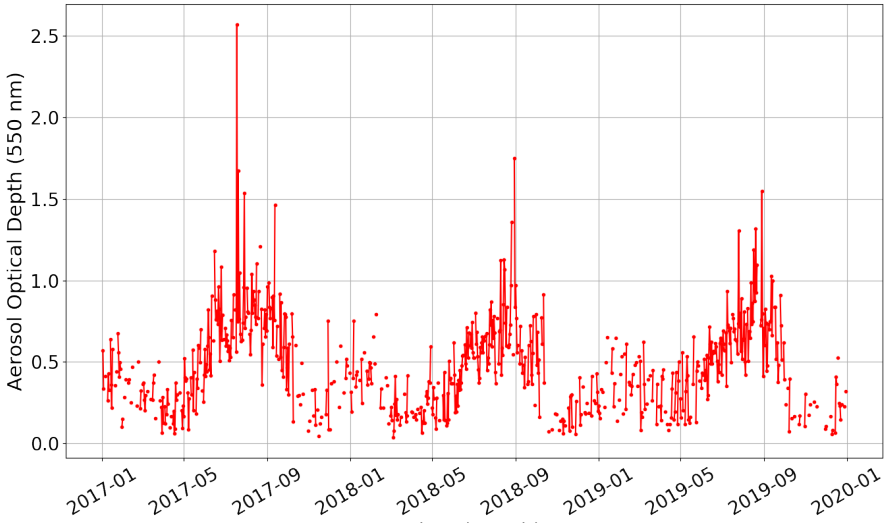

Figure 5.3: Time series of the monthly Aerosol Optical Depth (AOD) observed at 550 nm wavelength by the MODIS Terra instrument downloaded by : https://giovanni.gsfc.nasa.gov/giovanni/, for an area covering the city of Kinshasa [14-16°E, 3-5°S].

the slant column densities (SCDs, the integrated trace gas concentrations along the light path) of the measured and the reference spectra.

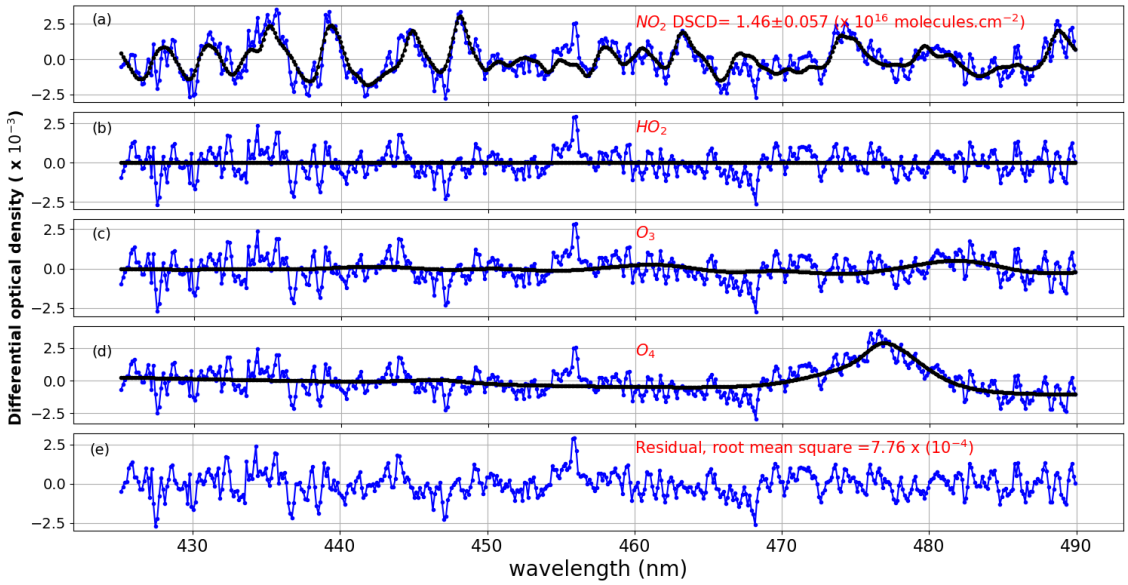

Figure 5.4: Example of a DOAS fit of a spectrum recorded on 1417 UTC 11 August 2017 (SZA= 51.62°). Black lines correspond to molecular cross-sections scaled to the detected absorptions in the measured spectrum (blue lines).

The DOAS fit was performed in a small wavelength window. In which the concerned absorber, in our case NO_2, shows strong and prominent absorption features. NO_2 has its strongest absorption lines in the 425-490 nm region. Here, other species such as O_3, H_2O and O_4 also show strong absorption, that need to be included in the QDOAS analysis.

The contributions of Rayleigh and Mie scattering that vary slowly with wavelength are removed by introducing a polynomial of degree 5. In addition to the elastic (Rayleigh, Mie) contributions, we added a synthetic Ring spectrum to correct for the "filling-in" effect on Fraunhofer lines, known as the Ring effect, which originates from the Raman rotational scattering of oxygen and nitrogen molecules (Chance and Spurr, 1997). QDOAS settings and cross-sections adopted for the analysis are listed in Table 6.1.

Fig. 5.4 shows a typical DOAS result for NO_2. The analyzed spectrum is of 1417 UTC 11 August 2017 (SZA= 51.62°) and the reference spectrum comes from the MAX-DOAS observations of 2 October 2017. The first four panels show the absorptions of NO_2 (panel a), water vapor (panel b), ozone (panel c), the collision complex O_2-O_2 called O_4 (panel d), as optical densities relative to the reference spectrum. The last panel displays the fit residuals. Black lines correspond to molecular cross-sections scaled to the detected absorptions in the measured spectrum. The calculated contributions refers to the NO_2 cross section (as function of wavelength) multiplied by the retrieved NO_2 DSCD; the latter is also given in the panel a and is $(1.46 \pm 0.057) \times 10^{16}$ molecules cm^{-2}.

5.3 NO_2 VERTICAL COLUMN RETRIEVALS

The method used to convert DSCDs to tropospheric vertical column densities (VCD_{tropo}) is an adaptation of the ones explained by Tack et al. (2015); Constantin et al. (2013); Chen et al. (2009). The conversion from a total slant column density (SCD) to a total vertical column density is performed using the air mass factor (AMF) as shown in equation 1 :

$$VCD = \frac{SCD}{AMF} \tag{5.1}$$

VCD represents a geophysical quantity that can be used for comparison with other measurements, such as those from satellites. AMF represents the proportionality factor between the slant column density and the vertical column density. It depends on the parameters influencing the transfer of the solar radiation through the atmosphere, i.e. pressure, temperature, aerosols, clouds, surface albedo, vertical profiles of important absorbers and the profile of the measured absorber (Hönninger et al., 2004). We have calculated the AMFs used in this work with a Radiative Transfer Model (RTM) as described in section 3.c. The SCD can be obtained from retrieved DSCDs by adding the NO_2 contribution of the reference spectrum ($SCD_{residual}$), used in the fit of the retrieved DSCDs, according to:

$$SCD = DSCD + SCD_{\text{residual}} \tag{5.2}$$

To determine the tropospheric slant column density (SCD_{tropo}), the stratospheric slant column density (SCD_{strato}) is subtracted from the SCD:

$$SCD_{\text{tropo}} = SCD - SCD_{\text{strato}} \tag{5.3}$$

In light of Equation 1, we calculate the VCD_{tropo} directly, dividing the SCD_{tropo} by the tropospheric air mass factors AMF_{tropo}:

$$VCD_{\text{tropo}} = \frac{DSCD - SCD_{\text{strato}} + SCD_{\text{residual}}}{AMF_{\text{tropo}}} \tag{5.4}$$

The determination of the unknown components ($SCD_{residual}$, SCD_{strato}, AMF_{tropo}) is discussed in the following subsections.

5.3.1 Determination of the stratospheric column density

The stratospheric NO_2 column can be retrieved during the twilight period, when the photon light path becomes larger in the stratosphere than in the troposphere (e.g Van Roozendael and Hendrick (2012)). In our case however, due to the low sensitivity of the instrument, our measurements do not reach solar zenith angle (SZA) near 90° (Figure 5.5, blue dots). Therefore we calculated the NO_2 SCD_{strato} using the model UVspec/DISORT RTM Mayer and Kylling (2005) coupled with the photochemical box-model PSCBOX (Errera and Fonteyn (2001); see also Hendrick and Coauthors (2004) and Tack et al. (2015)).

Simulations of SCD_{strato} were done for the first and the 15th of each month of our study period. Figure 5.5 (black dots), shows an example of the modeled stratospheric slant columns for 15 August 2018. The figure also shows the measured DSCDs for these days (blue dots). The daily behaviour of these columns is explained by the geometry of the measurements. This "U" behavior is related to the optical path in the atmosphere which increases at sunrise and sunset. The effect is particularly visible for NO_2 because this molecule is also present in the stratosphere where the geometrical enhancement is very important when the sun reaches (and exceeds) the horizon.

In practice, we interpolate in this modeled SCD_{strato}^{model} look-up table for the days of interest and normalize by the measured OMI NO_2 stratospheric VCD (VCD_{strato}^{OMI}) using the following equation:

$$SCD_{\text{strato}}^{norm} = VCD_{strato}^{OMI} * \frac{SCD_{\text{strato}}^{model}}{VCD_{\text{strato}}^{model}} \tag{5.5}$$

where VCD_{strato}^{model} is the modeled stratospheric NO_2 at the OMI overpass time.

Finally, as we retrieve the NO_2 absorption in our spectra with a cross section recorded at 298 K, this cross section is underestimated for the stratospheric NO_2. This leads to an enhancement of the stratospheric NO_2 signal in our measured DSCDs. We correct this by multiplying the modeled stratospheric NO_2 by 1.2, a factor corresponding to the factor between the NO_2 DSCDs retrieved at 220 K (typical temperature of the stratosphere) and 298 K Vandaele et al. (1998). Fig. 5.5 (cyan dots) illustrates SCD_{strato}^{norm} obtained for 15 August 2018.

5.3.2 Determination of the residual NO_2 column in the reference spectrum

The DOAS analysis requires the use of a reference spectrum. Ideally, this reference spectrum would represent the light of the sun before entering in the earth atmosphere. However, with ground-based measurements like ours, this is not possible. The reference spectrum thus contains a residual absorption that must be quantified independently of the DOAS analysis.

In our case, we used a reference spectrum recorded with a low-cost MAX-DOAS system, under clear-sky conditions from 1202 UTC 2 October 2017 at zenith. Since we also measured spectra at 30° during this MAX-DOAS acquisition, we can retrieve the reference tropospheric column under a geometric approximation (Hönninger et al., 2004). We esti-

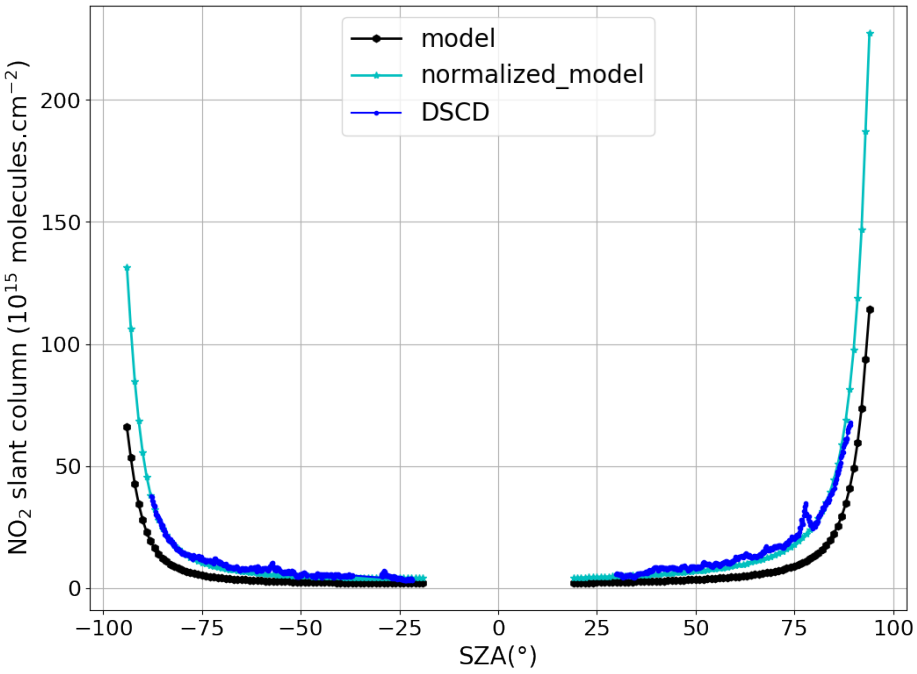

Figure 5.5: In black dots : example of the the stratospheric column density calculated using the UVspec/DISORT RTM coupled with a photochemical box-model PSCBOX for 15 August 2018. In blue : illustration of the DSCDs measurements of 15 August 2018 and in cyan dots, an example of the standardization of the model's SCD_{strato} by OMI observations. The negative values of SZA, correspond to the morning time while the positive ones are related to the evening time.

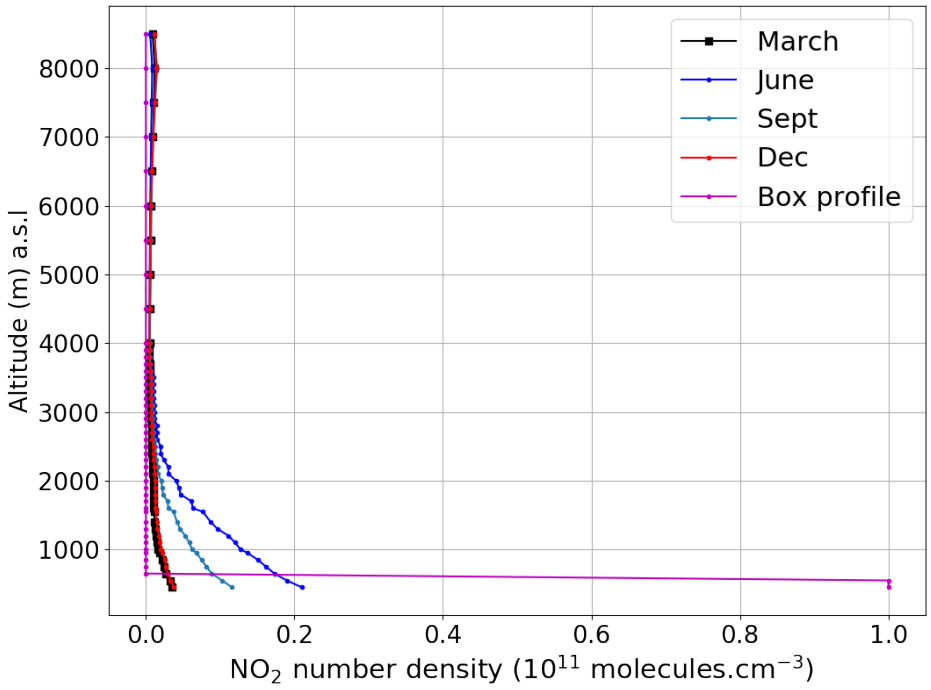

Figure 5.6: Mean monthly profiles of NO_2 extracted from the GEOS-Chem simulation during the year 2018 and a box profile. Note that the surface is 400 m above sea level.

mated the stratospheric contribution to the reference column from the model simulations explained in section 5.3 5.3.1. The total value of this residual column is estimated to be 0.65 $\times$ 10^{16} molecules cm^{-2}, as the sum of the tropospheric contribution (0.5 $\times$ 10^{16} molecules cm^{-2} obtained from MAX-DOAS measurements) and the stratospheric contribution (0.15 $\times$ 10^{16} molecules cm^{-2} obtained from model simulations). To analyze observations made at 35°, we changed the reference spectrum to a 35° spectrum from 1202 UTC 14 August 2018. The residual column was adapted, by adding the offset of 0.3 $\times$ 10^{16} molecules cm^{-2} coming from the difference between DOAS analyses made with the two reference spectra. Note that we changed the reference spectrum to reduce the effect of spectrometer instabilities and improve the DOAS analysis.

5.3.3 Tropospheric air mass factor

Tropospheric AMF calculations were performed using the VLIDORT RTM (Spurr, 2013). As mentioned above, the AMF calculation is intrinsically dependent on the site's observation conditions and the profile of the concerned absorber. Thus it is interesting to perform several tests to arrive at realistic parameters for the calculation of this AMF. The NO_2 profiles were retrieved from a GEOS-Chem 3-D Chemistry Transport Model full chemistry simulation, using version 12.0.2 driven by MERRA-2 meteorological fields (Bey et al. (2001); see also http://wiki.seas.harvard.edu/geos-chem/index.php/GEOS-Chem 12). Our simulation covers the period from 2017 to 2019. The temperature and pressure profiles used in VLIDORT come from global meteorological reanalysis of the European Centre for Medium-Range Weather Forecasts (ECMWF), taken over the 20-year period.

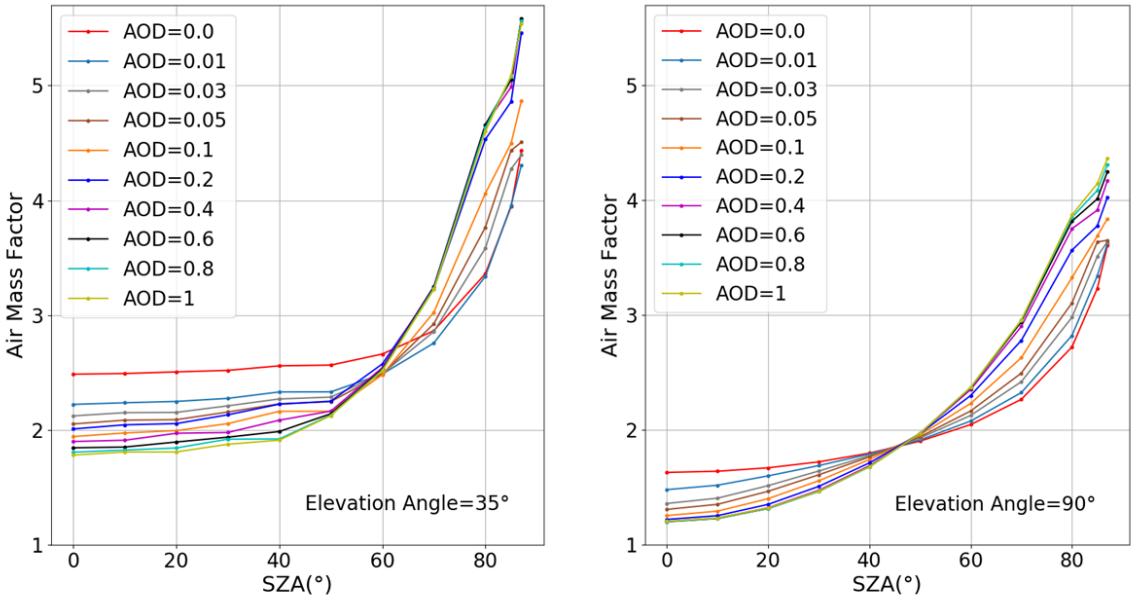

Figure 5.7: Sensitivity test of Tropospheric AMF with SZA and AOD variation.

VLIDORT takes the total layer extinction and total layer single scattering albedo as well as total layer phase function moments and returns the intensity (among other things that can be configured). The total layer input parameters are calculated from the contributions of the gas, air and aerosols. For this, we choose a trace gas concentration (for trace gas absorption), air density and wavelength (for Rayleigh scattering contribution) and aerosol properties such as single scattering albedo and asymmetry parameter with the Henyey–Greenstein phase function to calculate the aerosol phase function moments. The geophysical parameters used in the VLIDORT simulations are described in Table 5.2.

Figure 5.6 shows selected monthly averages of the NO_2 profile extracted from the GEOS-Chem simulation (2018) and a simple box model corresponding to a highly concentrated NO_2 200 m thick layer above the surface. The box profile helped us to evaluate the error in the calculation of the tropospheric AMF as explained in the subsection 5.4 5.4.2. In Fig. 5.6, GEOS-Chem profiles show that in the lower troposphere (between surface and 3 km) the highest NO_2 values are obtained for the months of June to September. This period corresponds to the dry season, when forest fires are often observed around Kinshasa (see Fig. 5.3).

The boundary layer height (BLH) above Kinshasa exhibits daily variations with a sharp increase at 6 UT, a maximum every day at noon UT and a sharp decrease from 15 UT. The minimum BLH happens in June (900 m at noon UT), while the maximum is reached in September (1300 m)(Copernicus Climate Change Service (C3S), 2017).

When performing sensitivity tests, we find that the calculated AMFs vary strongly with the SZA, the AOD and the NO_2 profile. On the other hand, they depend weakly on the change in temperature (T) and pressure (P) profiles. On this basis, we use constant T and P profiles in VLIDORT. The box profile has a considerable influence on the AMF found, that is why we use it in the subsection 5.4 5.4.2, to estimate the error in this

AMF calculation. The sensitivity test also showed that AMFs calculated under Kinshasa conditions are less dependent on the change in GEOS-Chem profile during the year. We have therefore set a unique GEOS-Chem profile in VLIDORT. Fig. 5.7 illustrates the sensitivity tests performed on AMFs (90° and 35°) as a function of SZA and for different AODs. We obtain realistic AMFs for Kinshasa conditions by interpolation through the tropospheric NO_2 AMF look-up table created at AOD values measured by the MODIS instrument.

Table 5.2: Parameters and Settings for Cloud Variability Study in Kinshasa

Parameter	**Setting**
Surface albedo	0.06
Wavelength	477 nm
Pressure and temperature profile	Standard atmosphere
A priori profile	Linearly decreasing profile from 0.3 ppb at 0 km to 0.01 ppb at 4 km
Aerosol profile	Box profile from the surface to 550m above ground
Aerosol extinction	0.0, 0.1, 0.3, 0.5, 1, offset
Asymmetry parameter	0.68

5.4 RESULTS AND DISCUSSION

In this section, we present the retrieved tropospheric NO_2 VCDs. Data recorded under dark or heavy cloud conditions are filtered out from the analysis. An uncertainty budget is described and we finally present a comparative study between our retrieved NO_2 VCDs and observations made by two satellite instruments (OMI and TROPOMI).

5.4.1 NO_2 Tropospheric vertical column

Fig. 5.8 illustrates our NO_2 VCDtropo retrievals. Panels (a) and (b) show the VCDtropo for 24 August and 11 October 2017 with the corresponding DSCDs. The DSCDs follow a "U" shape related to the optical path during the day. The AMF corrects this "U" shape for the VCDtropo, which range for these two days between 1 and $12\times\ 10^{15}$ molecules cm^{-2}. Panels (c) and (d) show the VCDtropo for August 2017 and October 2017, which belong to the dry and the wet season, respectively. Blue dots indicate the individual VCDtropo retrievals while the red lines are the daily averages. Although we retrieve the highest individual VCDtropo in early October, the daily averages are generally lower in October than in August.

5.4.2 Error estimation

The main sources of uncertainty in VCDs are related to each component used in Eq. (5.4). The uncertainty on the tropospheric VCD (σ_{VCD}) can be calculated as follows:

$$\sigma_{VCD}^2 = (\frac{\sigma_{DSCD}}{AMF_{tropo}})^2 + (\frac{\sigma_{SCDstrato}}{AMF_{tropo}})^2 + (\frac{\sigma_{SCDresiduel}}{AMF_{tropo}})^2 + (\frac{SCD_{tropo} * \sigma_{AMF_{tropo}}}{AMF_{tropo}^2})^2 \quad (5.6)$$

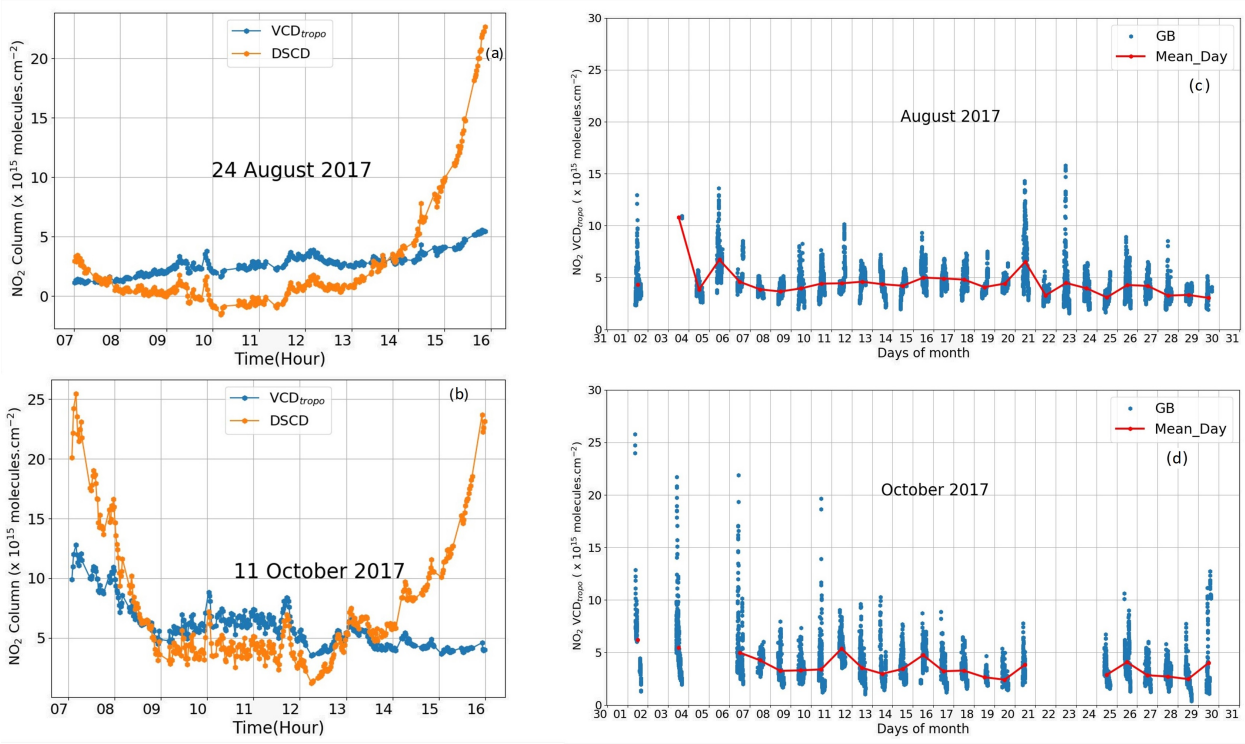

Figure 5.8: Examples of ground-based DOAS measurements of NO_2 in Kinshasa. Panels (a) and (b) show the VCDtropo (in blue) and DSCDs (in orange) for 24 August 2017 and 11 October 2017, respectively. Panels (c) and (d) show the VCDtropo for August and October, respectively. The red dots in panels (c) and (d) show the daily averages.

In Eq. (5.6), each error contribution has a different source, independent of the other terms. Therefore, there is no correlation between these different sources. The four contributions of Eq. (5.6) are respectively :

Table 5.3: *Error budget on recovered tropospheric NO_2 VCD. Relative (in %) and absolute errors (in molecules cm^{-2}) are given. sigma(90) and sigma(35) indicates the two error values obtained at 90° and 35°, terms used in Eq.* (5.6)*. VCD_{90} and VCD_{35} are respectively the propagation of these errors on the vertical column. The largest contribution comes from the error on tropospheric AMF, followed by the error on residual column. Relative error values were found by normalizing by a typical tropospheric vertical column of 3 $\times$ 10^{15} molecules cm^{-2} (mean value of tropospheric VCD as measured in Kinshasa).*

$Error source$	sigma(90), sigma(35)	VCD_{90}	VCD_{35}
DSCD	0.8 , 0.5 ($\times$ 10^{15})	11% (0.39)	6% (0.20)
SCD_{residuel}	1.3 , 1.8 ($\times$ 10^{15})	18% (0.63)	21% (0.75)
SCD_{strato}	0.5 , 0.5 ($\times$ 10^{15})	5% (0.2)	5% (0.2)
AMF_{tropo}	0.3 , 0.1	12% (0.42)	3% (0.13)
VCD	-	25% (0.89)	23% (0.81)

(a) The error on the DOAS fitting (σ_{DSCD}). This error has two contributions, the random error (caused by noise in spectral measurements) and a systematic error, related to the error on the effective cross-section of the NO_2. We estimated a random error to be 0.5 $\times$ 10^{15} molecules cm^{-2} by taking the mean of all the error values of the slant columns of NO_2 as analyzed with QDOAS. The systematic error was estimated at 3% in accordance with the study made by Vandaele et al. (1998).

(b) The error on the stratospheric SCD ($\sigma_{SCDstrato}$) is the uncertainty on the stratospheric slant column simulated by the RTM UVspec/DISORT coupled to the photochemical model PSCBOX. This error source is discussed in Tack et al. (2015) and references therein. Conservative estimates of the errors on the photochemical and RT components of the stratospheric NO_2 SCD simulation reach 20 and 10%, respectively. By adding both error components in quadrature, this leads to a total error of 22% on the SCD model (or 0.5 $\times$ 10^{15} molecules cm^{-2} based on the simulated NO_2 SCD_{strato} mean value around OMI overpass time over Kinshasa).

(c) The error on the residual amount of NO_2 in the reference spectra $SCD_{residual}$. We estimated the residual slant column error by propagating the error across all components used to estimate the residual column. This error has been estimated at 1.3 $\times$ 10^{15} molecules cm^{-2} for zenith measurements and 1.8 $\times$ 10^{15} molecules cm^{-2} for 35° measurements, as 20% of the $SCD_{residual}$ value used for the measurements in each case.

(d) Errors in the calculation of the tropospheric AMF are related to uncertainties in the input parameters used in the VLIDORT RTM. In Chen et al. (2009), an extensive sensitivity test was performed considering various input parameters in radiative transfer simulations. The influence of parameters such as aerosol and NO_2 layer height, AOD and NO_2 profile, surface albedo, etc. was tested. Based on this sensitivity analysis, the uncertainty on the AMF was estimated to be in the range of 10%-20% for SZA between 20 and 85 degrees. By considering the difference between AMFs calculated with profiles extracted from GEOS-Chem and those calculated with a simple box profile, we estimated the uncertainty on the tropospheric AMF used in this study to be of about 0.35 for the AMF calculated at 90° and 0.15 for those calculated at 35° (mean values taken at overpass).

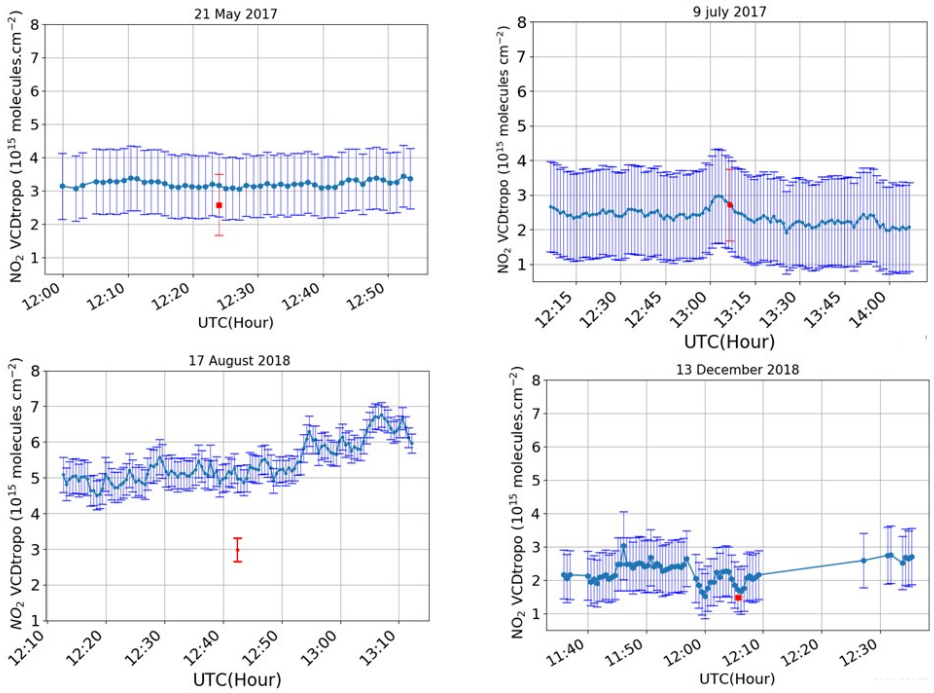

Figure 5.9: Comparison of tropospheric NO_2 VCDs (in blue) obtained from DSCDs measured at Kinshasa with OMI observations (in red)" and corresponding error bars.

The use of a box profile is justified by the fact that in polluted regions, the bulk of the NO_2 concentration is generally close to the surface.

The error budget presented in Table 5.3 indicates that the main source of error is tropospheric AMF. Calculations show that, for all measurements, the median of uncertainty on the tropospheric NO_2 VCD is 25% for zenith measurements and 23% for 35° measurements.

5.4.3 Comparaison with satellite observations

The Ozone Monitoring Instrument (OMI) is a nadir imaging spectrometer operating in two spectral bands (UV: 270-380 nm and Visible: 350-500 nm) on board the AURA satellite (Levelt et al., 2006). The size of its ground pixels varies from 13 × 24 km^2 at nadir to 28 × 150 km^2 at the swath edges. We show comparisons between our ground-based measurements and the OMI QA4ECV NO_2 product (Boersma et al., 2018b). For this comparison, we consider only pixels whose geographical center is located within 50 km of the observation site, having a cloud radiance fraction $< 50\%$ and an AMF ratio $(\mathrm{AMF}_{tropospheric}/\mathrm{AMF}_{geometric}) > 0.2$ as recommended by Boersma and Coauthors (2017); Boersma et al. (2018b). Fig. 5.9 illustrates the retrieved VCD_{tropo} for 4 days, under clear sky conditions. We have chosen 4 representative days of each season of the year (May and December for the rainy season and July and August for the dry season) and in different observation geometry (zenith in 2017, 35° in 2018). The values of VCD_{tropo} are averaged (+/- 30 min, usually around 50 measurements) around the time of the OMI overpass. Ground-based (GB) values vary between 2×10^{15} molecules cm^{-2} and 7×10^{15} molecules cm^{-2}, and we can observe the same type of seasonality but with differences in absolute value in particular visible on 17 August for example. The high GB values of 17 August

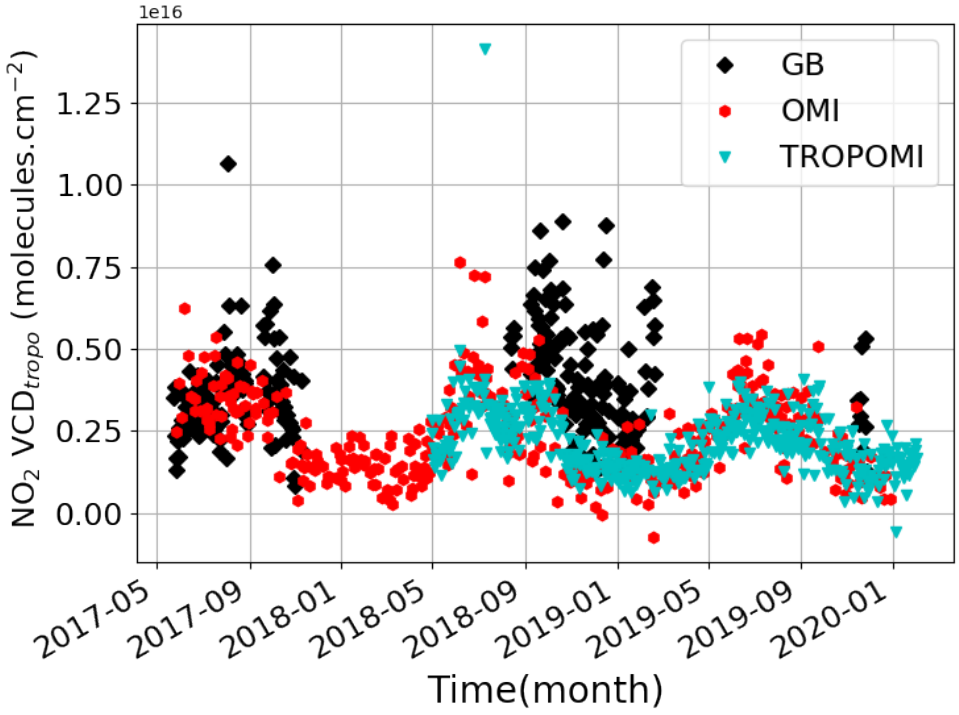

Figure 5.10: A comparison of the daily average of the tropospheric vertical column of NO_2 measured in Kinshasa (black dots) against OMI (red dots) and TROPOMI (blue dots) satellite observations between 2017 and 2019. Kinshasa measurements are averaged (+/- 30 minutes) around the OMI satellite overpass.

could be associated with a high AOD value (close to 1) observed on that day (see Fig. 5.3). The highest NO_2 values are observed on days of the dry season while the lowest NO_2 values are observed on days of the rainy season, as illustrated in Fig. 5.1. Similar to OMI, the TROPOspheric Monitoring Instrument (TROPOMI) is a nadir imaging spectrometer on board the Sentinel-5 Precursor satellite, launched on October 13, 2017. It measures the sunlight reflected in the ultraviolet, visible, near infrared and shortwave infrared spectral ranges Veefkind et al. (2012). With a swath width of 2600 km, it can cover the entire planet in a single day with a pixel size of 7 $\times$ 3.5 km^2 at true nadir in the UV/Vis/Near Infrared bands. The spatial resolution of TROPOMI has been further improved on 6 August 2019 with a pixel size of 5.5 $\times$ 3.5 km^2. Only TROPOMI ground pixels associated with a quality value (qa_{value} >0.75) have been selected in our study. Following recommendations by Verhoelst et al. (2021), we used reprocessed (RPRO, v0102) and the off-line (OFFL, v0102 and v0103) data products. The TROPOMI and OMI overpasses over Kinshasa occur around 1230 UTC (1330 LT). Comparisons with GB data are made using daily satellite values averaged over all selected pixels within a radius of 20 and 50 km (TROPOMI and OMI respectively) around Kinshasa.

In Figure 5.10, we show the time series of all GB measurements and satellite observations for 2017 to 2019 periods (see Table 5.1). The agreement between GB and OMI observations seems better in 2017 than in other periods of the study. This may be related to the fact that we used a different reference spectrum in the QDOAS analysis of the spectra recorded in 2018−2019. This second reference spectrum adds a bias of approximately 1 $\times$ 10^{15}

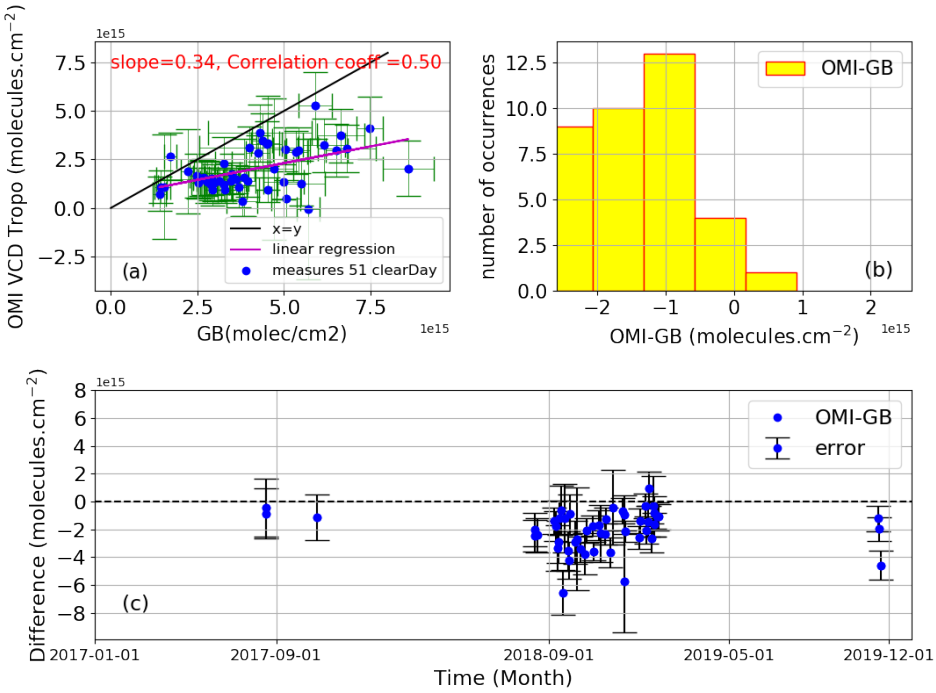

Figure 5.11: (a) Linear regression analysis chart between the NO_2 tropospheric vertical columns retrieved (+/- 30 min) around OMI observations for 51 clear days of observations. (b) Histogram of the bias between OMI and GB. (c) Time-series of difference between SAT and GB. The green bars in panel (a) represent the uncertainty of GB and OMI, and the black error bars in panel (c) represent the combined error on the differences between GB and OMI in molecules cm^{-2}.

molecules cm^{-2} in the calculation of VCDtropo. But it should be noted that all the GB measurements (black points) are included here, before selecting the coincident points with the satellite observations, and before flux filtering. Another point that may explain the difference in agreement between the two periods is the change in measurement geometry, from the zenith to measurements at 35° elevation in the direction of the city. The satellite measurements are always averaged within a circle of 50 or 20 km radius. So the satellite measurements are more representative of the sensitivity of the zenith measurements than the off-axis sensitivity towards the city.

Fig. 5.11 and Fig. 5.12 summarize the results of our comparisons. Upper panels show the linear regressions for the two cases. These are characterised by a correlation coefficient R of 0.50 and 0.72, and linear regression slopes of 0.34 and 0.41, for the OMI and TROPOMI datasets, respectively. Absolute differences (SAT-GB in $\times$ 10^{15} molecules cm^{-2}) and relative differences ((SAT-GB)/GB, in percent) were calculated for each case. For both datasets, the median bias is approximately -1.7 $\times$ 10^{15} molecules cm^{-2} (-46%). We calculated the bias error as the quadratic sum of GB and SAT errors plotted in the panel c of Fig. 5.11 and Fig. 5.12. For the comparison between OMI-GB and TROPOMI-GB, the mean values of these errors are 1.8 $\times$ 10^{15} molecules cm^{-2} and 0.9 $\times$ 10^{15} molecules cm^{-2},

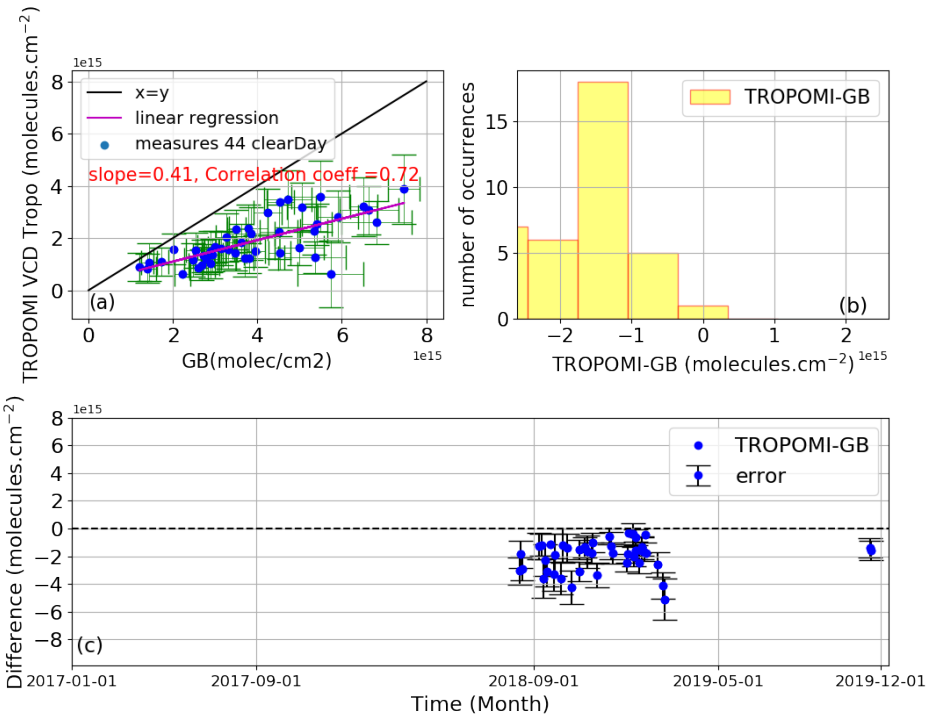

Figure 5.12: (a) Linear regression analysis chart between the NO_2 tropospheric vertical columns retrieved (+/- 30 min) around TROPOMI observations for 44 clear days of observations. (b) Histogram of the bias between TROPOMI and GB. (c) Time-series of difference between SAT and GB. The green bars in panel (a) represent the uncertainty of GB and TROPOMI, and the black error bars in panel (c) represent the combined error on the differences between GB and TROPOMI in molecules cm^{-2}.

respectively. The number of coincidence points for the two cases is slightly different, 51 for OMI and 44 for TROPOMI. The comparison results are obtained by removing the tropospheric VCD values of low-flux signal spectra (fluxes at 425 nm ¡ 120000 for the 2017 period and fluxes at 425 nm ¡ 30000 for 2018-2019). The change in the flux filtering threshold is related to the fact that the observations made in 2018-2019 were strongly influenced by dust compared to those made in 2017 and because of the change in the elevation angle in 2018. We also note that the current GB result does not change significantly when using AMFs calculated with a box profile discussed in subsection 5.3 5.3.3. The test shows a median bias of the order of -1.8 $\times$ 10^{15} molecules cm^{-2}, giving us good confidence in our GB VCDtropo retrievals.

Note that there is fewer coincidence points during the dry season. This is linked to the high aerosol load in the dry season, which leads to low ratios AMFtropospheric/AMFgeometric, the lowest ratios being filtered out as described above. In the dry season, aerosols partly screen the surface. This strengthens the value of ground-based measurements in this area.

5.4.4 Discussion

In this subsection, we discuss the reasons for the bias observed between OMI and TROPOMI data with respect to GB. The comparisons show negative biases of approximately -46% between the two satellite instruments and GB. This negative bias may be related to the low sensitivity of satellite instruments near-surface. The typical averaging kernels as illustrated by Eskes and Boersma (2003), figure 1, show that there is very little sensitivity below about 1 km, and thus the satellite retrieval strongly rely on the selected a priori profile.

For comparisons with OMI observations, a similar negative bias has been reported in urban areas Pinardi et al. (2020) and more specifically for the African cities of Bujumbura and Nairobi Gielen et al. (2017); Compernolle et al. (2020). This negative bias can be explained by several factors, such as the low sensitivity of satellite instruments near the surface as mentioned above, the lack of knowledge of the NO_2 a priori profile used in the AMF calculation, the coarse spatial resolution of OMI and the systematic uncertainties in the stratospheric column estimation.

Several studies have analysed the impact of algorithmic differences on the uncertainty of the NO_2 column, which can be as high as 42%, mainly due to the uncertainties in the AMFs due to different parameters such as surface albedo, a priori profile and cloud parameters Lorente et al. (2017).

Pinardi et al. (2020) showed that the relatively coarse spatial resolution of OMI (13×24 km^2 at best) affect the comparisons due to the smoothing of localised urban sources. The OMI pixels can be large compared to the size of the ground-based observation zone, including areas surrounding the observation site. The horizontal variability of NO_2 within the chosen radius of 50 km should also be considered. This may also contribute to the apparent bias found in our results. Variability of about $\pm 1 \times 10^{15}$ molecules cm^{-2} are found between the pixels in the selected radius.

Systematic uncertainties in the estimation of the stratospheric column could also contribute to this observed underestimation, given the set of small NO_2 tropospheric signals observed in African cities studied by Pinardi et al. (2020). In Kinshasa and its surroundings, values of the stratospheric vertical column approached 1.7×10^{15} molecules cm^{-2} on average compared to an average value of 3.7×10^{15} molecules cm^{-2} of the total NO_2 column. The stratospheric column of the satellite being of the same order as the tropospheric column, this may well lead to larger uncertainties in the recovery of the tropospheric column.

For comparisons with TROPOMI observations, we do not have many points of coincidence with the ground data (about 50 points, most of them in 2018). Altought the GB measurements of 2019 were filtered out because of dust accumulation on the instrument's observation window, the results indicate a relatively fair level of agreement (R = 0.72 and 0.41 of slope). Verhoelst et al. (2021) conducted a study based on the comparison of TROPOMI with the results of about 20 MAX-DOAS ground observation sites. The results of these comparisons show a negative bias of -23 to -37% in average under clean to moderate polluted conditions and large negative biases reaching about -51% in heavily polluted areas (ground-based tropospheric columns larger than 15×10^{15} molecules cm^{-2}). In our case, the results of comparisons between TROPOMI and GB for Kinshasa indicate a negative bias of -46%, thus approaching the threshold of high polluted areas

found by Verhoelst et al. (2021).

The apparent disagreements observed between TROPOMI and ground networks have been discussed in details by Verhoelst et al. (2021). These disagreements result from errors in the retrieval of S5p tropospheric columns due to uncertainties in the a priori profile in the TM5-MP chemical transport model (horizontally coarse $1^\circ \times 1^\circ$). Ialongo et al. (2020) and Zhao et al. (2020) showed that by using high resolution profiles based on the regional forecast model instead of the a priori coarse NO_2 profiles used in the TM5 model, an improvement in agreement between TROPOMI and ground data was achieved. Another factor is the treatment of clouds (see Verhoelst et al. (2021)). The presence of clouds and dust most of the year in Kinshasa greatly influences the observations, and the comparisons we present could be further improved by applying more advanced cloud filtering techniques, such as described in Gielen and Coauthors (2014).

Another way to improve the comparisons would be using measured NO_2 profiles from Kinshasa. Dimitropoulou et al. (2020) shows in their study on TROPOMI validation with MAX-DOAS data that the use of a vertical NO_2 profile derived from ground measurements at the observation site significantly reduces the systematic underestimation of TROPOMI data. In November 2019, we have installed a new MAX-DOAS instrument on the roof of the Faculty of Science at UniKin, that will allow us to monitor the NO_2 profile in Kinshasa, offering perspectives for improving the comparison in the near future.

5.5 CONCLUSION

This work aims at presenting the new atmospheric observation site in Kinshasa. The city, located in the center of the African continent, is characterized by an explosive demography and a strong presence of various sources of atmospheric pollutants. In Kinshasa and its surroundings, agricultural activities leading to forest fires, biomass fires, and embers used for cooking are among the sources of air pollution. Very little research on air pollution and ground-based observations exist, while this is of great importance for the understanding of the atmosphere above this site and for the improvement of the accuracy of satellites and models. Since May 2017, we have installed a lowcost optical remote sensing instrument above the Faculty of Sciences of the University of Kinshasa. The measurements made with this instrument, which has been operating for two years, have allowed us to start a preliminary study of the Kinshasa atmosphere, also making a comparison with two satellite instruments (OMI and TROPOMI).

We began measuring in the zenithal direction from May 2017 until November 2017. The security situation forced a change in the location of the instrument, which offered the possibility to take measurements only at an elevation angle of 35° from June 2018 to November 2019. The instability of the electricity at the observation site did not allow us to take measurements every day. Dust was also one of the problems we encountered during the observation period. Especially during the dry season, we observe the deposition of dust layers on the instrument's observation window. This dust problem makes the data unusable at times, as was the case for several days of 2019.

Using the QDOAS software, we analyzed the recorded spectra and constituted a database of DSCDs of NO_2 and trace gases. In this work, we focused on tropospheric NO_2 column retrieval. Such measurements were performed for the first time in the city of Kinshasa used them to validate tropopheric NO_2 measurements by OMI and TROPOMI satellite

instruments. The mean value of VCDtropo observed in Kinshasa is 3×10^{15} molecules cm^{-2}. Comparisons with OMI observations over 51 clear days give a slope of 0.34 and a correlation coefficient of 0.50. The systematic bias between OMI and ground-based data can be related to the unknown NO_2 profile in Kinshasa and also to the coarse horizontal resolution of the OMI instrument. With only 44 days coincident between GB and TROPOMI, we observe a slope of 0.41 and a correlation coefficient of 0.72. The correlation is better with TROPOMI which can be understood by the better resolution of TROPOMI and thus spatial matching between ground-based and space-borne measurements. The negative bias is a robust finding of the study as it is observed in both OMI and TROPOMI. Altought this is a common feature in other satellite versus GB measurements comparisons, this motivates further investigations. These comparisons are preliminary. Indeed, more data will be needed to confirm our first comparisons while we foresee that in-depth data filtering dealing with a larger number of coincidences and GB profile data availability will help to improve the comparisons with satellite measurements.

At the time of closing this paper, it is worth noting that a MaxDOAS instrument has been installed in Kinshasa since November 2019. This opens interesting prospects for the near future, since this instrument can provide very useful information such as the profiles of the main absorbers (NO_2, H_2CO). This will strengthen forthcoming studies addressing the precise assessment air quality in Kinshasa and central Africa, making use of an improved DOAS instrument and exploiting a Chemistry Transport Model.

Chapter 6

GROUND-BASED MULTI-AXIS DIFFERENTIAL OPTICAL ABSORPTION SPECTROSCOPY (MAX-DOAS) OBSERVATIONS OF NO_2 AND H_2CO AT KINSHASA AND COMPARISONS WITH TROPOMI OBSERVATIONS

The following chapter is entirely based on and reflects the exact content of the article accepted for publication in the AMT journal, titled : Ground-based MAX-DOAS observations of NO_2 and H_2CO at Kinshasa and comparisons with TROPOMI observations Rodriguez Yombo Phaka, Alexis Merlaud, Gaia Pinardi, Martina M. Friedrich, Michel Van Roozendael, Jean-François Müller, Jenny Stavrakou, Isabelle De Smedt, François Hendrick, Ermioni Dimitropoulou, Richard Bopili Mbotia Lepiba, Edmond Phuku Phuati, Buenimio Lomami Djibi, Lars Jacob, Caroline Fayt, Jean-Perre Mbungu Tsumbu, and Emmanuel Mahieu, Atmos. Meas. Tech., https://doi.org/10.5194/amt-16-5029-2023 , 2023

Abstract

We present a database of MAX-DOAS (Multi-AXis Differential Optical Absorption Spectroscopy) ground-based observations of NO_2 and H_2CO tropospheric vertical column densities (VCD_{tropo}) performed for the first time in the city of Kinshasa. These measurements were conducted between November 2019 and July 2021 and processed using the standardized inversion tools developed in the ESA FRM4DOAS (Fiducial Reference Measurements for Ground-Based DOAS Air-Quality Observations) project. The retrieved geophysical

quantities are used to validate column observations from the TROPOspheric Monitoring Instrument (TROPOMI) over Kinshasa. In the validation, we experiment three different comparison cases of increasing complexity. In the first case, a direct comparison between MAX-DOAS observations (hourly average of MAX-DOAS VCD_{tropo} at overpass) and TROPOMI shows an underestimation of TROPOMI with a median bias of -38% for NO_2 and -39% for H_2CO based on monthly comparison. The second case takes into account the different vertical sensitivities of the two instruments and the a priori profile. We note significant changes of the median bias for both compounds: -12% for NO_2 and +11% for H_2CO. The third case builds on the second case by considering also the direction of sight of the MAX-DOAS. For this third case, we find a median bias of +44% for NO_2 and a median bias of +4% for H_2CO. However this case is impacted by low sampling and is considered as less reliable. The findings from this study underscore the significance of employing a realistic a priori profile in TROPOMI column extraction, particularly within heavily polluted urban zones like Kinshasa. The investigation also highlights the necessity for prudence when integrating the MAX-DOAS line of sight due to the noise generated during subsampling and the limited horizontal sensitivity of MAX-DOAS observations. Importantly, the study further reveals the pronounced pollution levels of NO_2, H_2CO, and aerosols in both the city of Kinshasa and its adjacent regions, underscoring the imperative for consistent monitoring and effective regulatory measures by local authorities.

6.1 INTRODUCTION

The population explosion in Africa is a growing source of environmental problems. In particular, many African cities are increasingly affected by air pollution, so that air quality in African urban areas is expected to deteriorate in the coming decades with a strong impact on human health (Liousse et al., 2014). NO_x (sum of NO and NO_2) and formaldehyde (H_2CO) are important markers of this pollution. These compounds are also strongly emitted by fires and the biosphere; H_2CO is also considered an excellent marker of biogenic volatile organic compounds (VOCs) emissions (Stavrakou et al., 2009b; Bauwens et al., 2016). In the presence of VOCs, high NO_2 concentrations lead to increased formation of O_3 and aerosols (Crutzen, 1979). H_2CO plays a primary role on the oxidative capacity of the atmosphere and affects the global CO balance (e.g., Fortems-Cheiney et al., 2012; Cheng et al., 2018). The VOCs and NO_2 react in a non-linear manner to form O_3 in the atmosphere (eg., Seinfeld and Pandis (1998)).

At the global scale, the main sources of NO_x are combustion processes associated with traffic, industrial activities, and home heating whereas H_2CO is formed during the atmospheric oxidation of methane and non-methane volatile organic compounds (NMVOCs) of biogenic, pyrogenic, and anthropogenic sources origin (Seinfeld and Pandis, 1998). In tropical regions, particularly in Central Africa, major sources impacting NO_x and H_2CO include the seasonal biomass burning, the use of charcoal in cooking, and road traffic, generally dominated by old smoke emitting vehicles (Marais and Wiedinmyer, 2016a). At present, relatively few studies have addressed NO_2 and H_2CO sources in Central Africa, and in-situ measurements are generally lacking in tropical regions. Although nadir-looking UV-visible spaceborne sensors (e.g. TROPOMI) do sample this region, current satellite datasets present biases with respect to independent measurements. For example, TROPOMI H_2CO columns tend to systematically underestimate ground-based infrared remote-sensing data in polluted regions (Vigouroux et al., 2020). Regarding tropospheric NO_2, columns validation studies indicate moderate underestimations at polluted mid-

latitudes sites (e.g. Dimitropoulou et al. (2020); Zhao et al. (2020); Tack et al. (2021); Verhoelst et al. (2021); Poraicu et al. (2023)). However, satellite measurements are poorly characterized in tropical regions.

The Democratic Republic of Congo (DRC), a country in the heart of the Congo Basin, has multiple sources of air pollutants. Alone, it accounts for 54% of the Congo Basin rainforest, affected by deforestation due to expansion of agriculture and increasing demand for firewood (Mayaux et al., 2013). The associated emissions can be observed from space by satellite. For example, De Smedt et al. (2015) found that H_2CO column hotspots associated with vegetation fires in the region are among the highest in the world. Measurements in Bujumbura (Burundi) using the MAX-DOAS (Multi-AXis Differential Optical Absorption Spectroscopy) technique, have shown that the local atmospheric composition is influenced by biogenic VOC emissions from the DRC (Gielen et al., 2014), even though this site is relatively far away from emission sources.

Kinshasa, the capital of the DRC, a large and rapidly expanding megacity of 12 million inhabitants in 2016 expected to reach 20 million by 2030 (UN, 2016), is not spared by air pollution problems (McFarlane et al., 2021). It experiences a rapid increase in the number of motorcycles, a fleet dominated by old vehicles, poorly managed roads largely unpaved and, much like other large cities in Central Africa, poor quality fuel. It is also surrounded by the vast forested areas of the Congo Basin and most of its population uses charcoal for cooking. A recent study by Vohra et al. (2022), based on space-based observations has shown that several large African megacities, including Kinshasa, are experiencing significant annual increases in NO_2 due to emerging anthropogenic sources. It can also be seen that Kinshasa city center, where most activities take place (traffic, markets, businesses, etc), is more affected than other parts of the city. In spite of the reported pollution increases, the lack of routine monitoring impedes the development of efficient policies aiming to improve air quality.

In May 2017, a single-axis DOAS (Differential Optical Absorption Spectroscopy) system was installed on the roof of the Faculty of Sciences of the University of Kinshasa (UniKin) as part of a collaboration with the Belgian Institute for Space Aeronomy (BIRA-IASB). Based on measurements obtained from this instrument operated from 5 May 2017 to 1 November 2019, Yombo Phaka et al. (2021) identified the presence of a clear annual cycle in NO_2 concentrations with higher values during the dry season. A good correlation was found with satellite measurements, although the latter seemed to be biased low compared to the ground based-measurements. In November 2019, the single-axis instrument was replaced by a new MAX-DOAS (Multi-AXis DOAS) system built at BIRA-IASB, significantly increasing the information content of the measurements. The geophysical quantities extracted from these measurements are tropospheric column densities (VCD_{tropo}) and vertical profiles of NO_2 and H_2CO, as well as aerosol optical depths (AODs) and extinction profiles.

We present MAX-DOAS measurements conducted from November 2019 to July 2021. Vertical columns of NO_2 and H_2CO are used to validate co-located measurements from the TROPOMI instrument on board the Sentinel-5P (S5P) satellite and the AOD measured by the MAX-DOAS instrument is compared with MODIS satellite data. This manuscript is subdivided into 4 sections: Section 2 presents the observation site, the retrieval methodology and input parameters; Section 3 presents the resulting dataset as well as comparisons of TROPOMI with MAX-DOAS; Section 4 discusses the differences between the datasets, and the final section presents the conclusions.

6.2 OBSERVATIONS AND DATA SETS

6.2.1 Site description and instrumental setup

Figure 6.1 presents the MAX-DOAS instrument installed on the roof of the Faculty of Science of the University of Kinshasa (UniKin: -4.42° S, 15.31° E, 315 m a.s.l.) and its surroundings. On clear sky days during the dry season, the Lumumba tower is visible at 5.7 km from the site. During the wet season, Brazzaville is visible at about 16 km from the site. The reduction in visibility observed in the dry season is due to the presence of aerosols. The UniKin site is located about 5 km from downtown Kinshasa and about 10 km from the Congo River. More details on the city of Kinshasa and its characteristics are described in Yombo Phaka et al. (2021).

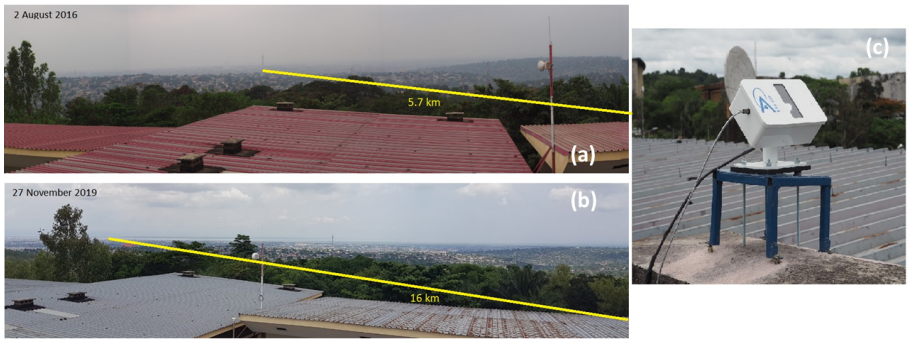

Figure 6.1: The MAX-DOAS instrument as installed on the roof of the Faculty of Science of the University of Kinshasa (panel c). The yellow lines (panels a and b) point respectively to the Lumumba tower, visible at 5.7 km from the site, and the city of Brazzaville, visible at about 16 km on clear sky days.

The MAX-DOAS is an upgrade of the single-axis DOAS instrument described in more detail in our previous study (Yombo Phaka et al., 2021). The spectrometer is an Avantes ULS2048-XL with a spectral range of 280-550 nm and a spectral resolution of 0.7 nm (Full Width at Half Maximum), Light enters the spectrometer through a lens connected to an optical fiber 600 μm in diameter. The upgrade first consisted in installing this spectrometer and a single-board computer (PC-104) in a box, which is air-cooled with a fan and equiped with a temperature sensor. This box is located under the roof of UniKin. Secondly and more importantly, we added an optical head on the roof, to perform elevation scans. This optical head is based on a home-made box of dimensions 22×14×8 cm^3 mounted on a pod at 45° and pointing 5° West of the North, i.e. towards the city. Light enters the box through a fused silica window and hits a flat elliptical mirror of minor axis 26.97 mm coated with enhanced aluminum. This mirror is attached to a HITEC servomotor (HS-7985MG) and scans between the horizon and zenith at multiple angles above the horizon (0°, 1°, 2°, 3°, 4°, 5°, 6°, 7°, 8°, 15°, 30°, 45°, 88°). The mirror reflects the light to a fused silica plano-convex lens of 25 mm diameter and 50 mm focal length, which focuses the light on the optical fiber. In each mirror position, we accumulate light for 50 seconds leading to a total scan time in about 10 minutes.

6.2.2 Retrieval methodology

The retrieval of NO_2 and H_2CO tropospheric vertical columns densities is performed using tools developed as part of the FRM$_4$DOAS (`https://frm4doas.aeronomie.be/`). FRM$_4$DOAS is an international project funded by the European Space Agency (ESA) and aims at harmonizing and standardizing the data retrieval from MAX-DOAS instruments operated within the NDACC. It incorporates community-based retrieval algorithms into a fully traceable, automated and quality controlled processing environment.

Spectra recorded by the instruments are delivered in NetCDF[1]4 format to a BIRA-IASB hosted ftp server. The automated analysis steps which are performed depend on the type of measurement (zenith only or MAX-DOAS) and on the spectral coverage of the instrument and are predefined for each instrument. However, the processing always starts with the production of dSCDs applying the QDOAS analysis tool (Danckaert and Fayt, 2017). The settings for QDOAS depend on the further processing, tropospheric or stratospheric retrieval (stratospheric NO_2 or total ozone column), as well as on instrument specifications and are described in the FRM$_4$DOAS ATBD (FRM4DOAS ATBD, 2017).

For the specific case of the MAX-DOAS retrievals in Kinshasa, we use three fitting windows: one for the retrieval of NO_2 dSCDs and the oxygen-collision complex O_2-O_2 denoted by O_4 dSCDs (in the visible spectral range), one for the retrieval of H_2CO (in the UV), and one for O_4 dSCDs in the UV range. Details of the retrieval settings are summarized in Table 6.1. Note that for the two fitting windows in the UV range, we also fit empirical spectral structures to correct for observed artifacts at low elevation angle (see Supplement material).

Figure 6.2 illustrates typical QDOAS fits in the four windows, for a spectrum recorded on 20 February 2020 at 09:10 UTC. In each panel, the blue line shows the measured differential optical densities as a function of wavelength and the black curve shows the molecular cross-sections scaled to the measured data. From the DOAS fits, the FRM$_4$DOAS system implements two MAX-DOAS retrieval agorithms: MAPA (Beirle et al., 2019), which is based on a parametrization of the retrieval profile shape and a Monte-Carlo approach for the inversion and MMF (Friedrich et al., 2019), an optimal estimation-based algorithm using the radiative transfer code VLIDORT (Spurr, 2013) as forward model. Both inversion algorithms have been extensively tested and validated using synthetic (Frieß et al., 2019) and real data (Tirpitz et al. (2021), Karagkiozidis et al. (2022)).

In the framework of FRM$_4$DOAS, the current strategy is to use both codes to produce independent profile and column data sets. For operational delivery, only MMF data selected for their consistency with corresponding MAPA results are retained. These results are submitted to the NDACC/RD repository[2] and to the ESA EVDC data base (`https://evdc.esa.int/search/`). Both MMF and MAPA codes implement a two-step retrieval approach for trace gas profile retrieval. In the first step, the aerosol profile is determined based on a set of O_4 dSCDs. In the second step, the retrieved aerosol profile is used to constrain the radiative transfer simulations needed for the trace gas retrieval. This implies that O_4 dSCDs must be determined in the visible wavelength region for NO_2 and in the UV for H_2CO retrieval. Note that, in this work, we only considered MMF due to inconsistencies in the MAPA aerosol retrievals for our Kinshasa spectra.

[1]NetCDF, which stands for Network Common Data Form, is a set of software libraries and self-describing, machine-independent data formats that support the creation, access, and sharing of array-oriented scientific data.

[2]`https://www-air.larc.nasa.gov/missions/ndacc/data.html?RapidDelivery=rd-list`

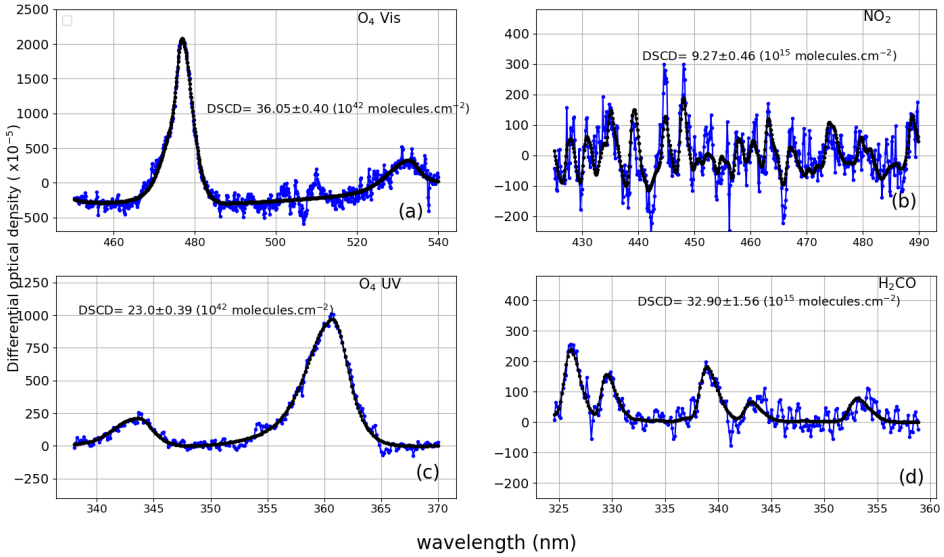

Figure 6.2: Example of QDOAS slant column retrievals for O_4 in the visible (panel a), NO_2 (panel b), O_4 in the ultraviolet (panel c) and H_2CO (panel d) for 20 February 2020 at 09h10 (Elevation viewing angle = 5°). Black lines correspond to molecular cross sections scaled to the detected absorptions and blue dots represent the measured signal.

Currently, in FRM$_4$DOAS, MAPA is mainly used as a quality check, but it does not provide averaging kernels. Due to a sampling effect, using MAPA as a quality check for H_2CO introduces a bias in the statistics. Higher VCDs are more likely to be flagged out, leading to discrepancies between MAPA and MMF. When assessing Aerosol Optical Depths (AODs), it becomes evident that MMF-produced AODs closely align with MODIS AODs, while MAPA-derived AODs consistently surpass both MMF and MODIS. We therefore opted to exclude MAPA from this study. Consistency is maintained by applying the same flagging criteria to NO_2. Only MMF values for which the quality assurance (QA) is lower than 2 were used. Three conditions should be met to establish this flagging (QA < 2). Firstly, scans with a degree of freedom (dof) below 1.3 are excluded. Secondly, all scans with an average root-mean-square (RMS) (between measured and simulated dSCDs) larger than 4 times the QDOAS estimated dSCD error are excluded. Furthermore, due to lack of good a priori knowledge for the aerosols, two aerosol retrievals are performed (differing by a factor 10 in AOD). If the retrieved aerosol profile agrees well, only one trace gas retrieval is performed and no extra test is applied. If however the retrieved aerosol profile differs more than 10% (as average partial AOD in each layer), the trace gas profile is performed with both aerosol profiles and all scans for which the retrieved VCD differs more than 10% are flagged as invalid.

Table 6.1: Main QDOAS analytical parameters for the retrieval of NO_2, O_4Vis, H_2CO, and O_4UV DSCD

Parameters	NO_2/O_4Vis	H_2CO	O_4UV
Fitting interval	425-490nm	325-360nm	338-370nm
Calibration	Chance and Kurucz (2010a)		
NO_2	Vandaele et al. (1996), 220K and 298K		
O_3	Serdyuchenko et al. (2014), 223K and 243K, preshifted by 0.003 nm		
H_2O	Rothman et al. (2010), 293K	-	-
O_4	Thalman and Volkamer (2013a), 293K (and 203K for NO_2/O_4Vis)		
H_2CO	-	Meller and Moortgat (2000), 293K	
Ring effect	Chance and Spurr (1997)		
Polynomial order	5		
Offset order	2	1	1

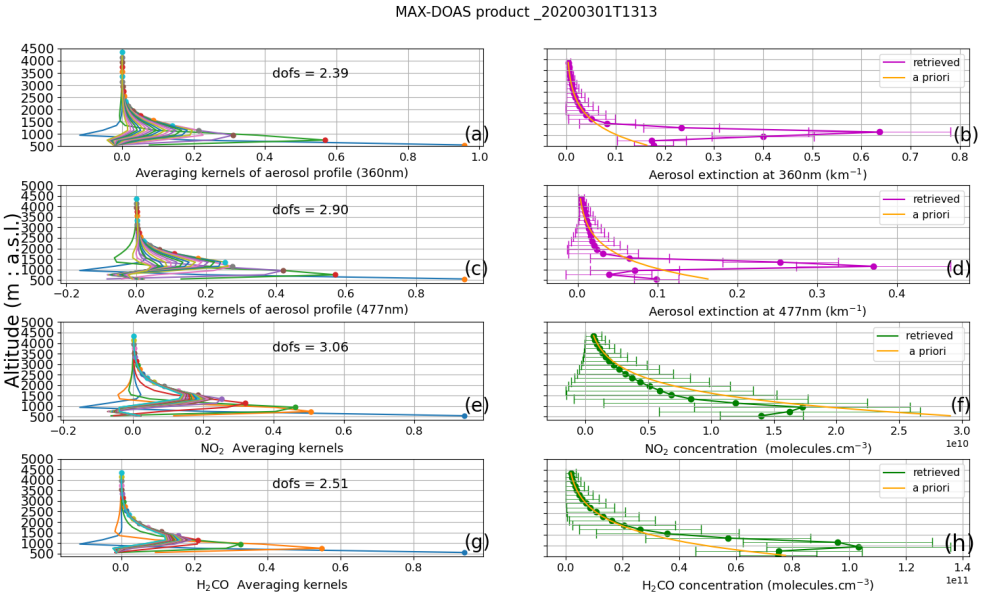

Figure 6.3: Example of FRM$_4$DOAS products around 13h13 UTC of 1 March 2020. The NO_2 and H_2CO profiles are represented in panels (f) and (h), respectively. Panels (e) and (g) show the corresponding Averaging Kernels (AKs), which are produced as part of the optical estimation inversion process and provide a measure of the vertical sensitivity of the measurements. Likewise, extinction profiles at 360 nm and 477 nm are represented in panels (b) and (d) and corresponding AKs are given in panels (a) and (c). The orange curves in the right subpanels are the a priori profiles. The horizontal bars represent the uncertainty on the retrieved profiles and, next to AKs, we also display values of the dofs (degree of freedom for signal).

Table 6.2: MMF retrieval settings for NO_2 and H_2CO observation in Kinshasa

Parameters	NO_2 Settings	H_2CO Settings
Surface albedo	0.06	0.06
Angström exponent	1	1
Wavelengths	477 nm	360 nm
Pressure and temperature profile	climatology from ECMWF 1995–2016	
A priori profile	exponential decay with a scale height of 1km	
Covariance a priori	diagonal elements as x_a^2, correlation length of 0.2 km	
VCD_{tropo} apriori	3×10^{15} molecules cm^{-2}	8×10^{15} molecules cm^{-2}
Single aerosol scattering albedo	0.92	0.92
Aerosol optical depth apriori	0.18	0.18
Asymmetry parameter	0.68	0.68
Height grid	200 m spacing up to 4 km	

Tables 6.2 summarizes the main settings used for the NO_2 and H_2CO retrievals based on MMF. Note that regarding aerosol parameters (single scattering albedo and phase function moments) and surface albedo the same default settings were used in both molecules. For the meteorological input parameters, the FRM_4DOAS retrieval chain uses an interpolation of a monthly climatology at each station, extracted from global meteorological reanalysis of the European Centre for Medium-Range Weather Forecasts (ECMWF) from 1995 to 2016 produced by Max Planck Institute for Chemistry (MPIC). An example of retrieval scan including the measurement for 1 March 2020 at 13:13 UTC is displayed in Fig. 6.3. Vertical concentration profiles (Fig. 6.3 b, d, f and h) retrieved by MMF and corresponding averaging kernels (AKs) (Fig. 6.3 a, c, e and g) are displayed. Inserts the AK panels, we show the degree of freedom for signal (dof) and the error bars included in the profile concentration plots show the total errors, including random error components such as smoothing and noise error from the inversion, as well as systematic uncertainties due to absorption cross section; namely 3% for NO_2 (Vandaele et al., 1998), 9% for H_2CO (Pinardi et al., 2013) and 20% for aerosol properties (Wagner et al., 2009). A priori profiles are represented next to retrieved profiles. The AKs indicate that the inversions are sensitive from the surface up to about 2.5 km.

6.2.3 TROPOMI data

TROPOMI is a nadir imaging spectrometer that measures reflected sunlight in the ultraviolet, visible, near-infrared, and shortwave infrared spectral ranges (Veefkind et al., 2012). The TROPOMI overpasses over Kinshasa occur around 12:30 UTC (13:30 LT). Its spatial resolution at nadir is 5.5 km × 3.5 km. TROPOMI data used in this work are based on the S5P-PAL, which stands for Sentinel-5P Products Algorithm Laboratory product for NO_2 (https://data-portal.s5p-pal.com/) and the off-line (OFFL: v2.1.4 and v2.2.1) for H_2CO. The NO_2 product from S5P-PAL is reprocessed with the same processor as version 2.3.1, covering the period from 1 May 2018 to 14 November 2021. For more technical details on the two products used, the reader is referred to the Algorithm Theoretical Basis Document (ATBD), available at http://www.tropomi.eu/data-products/ (last access: 25 May 2023) . We selected only those pixels associated with a quality value (qa-value > 0.75 for NO_2 and qa-value > 0.5 for H_2CO) following the recommendations of van Geffen et al. (2022a) and De Smedt et al. (2021).

This TROPOMI data set has been exploited in this work in three ways. Firstly, we apply the oversampling technique to this data set in order to provide information on the horizontal distribution of the two target compounds around the measuring site (see next paragraph). Secondly, direct comparisons between the standard TROPOMI product and ground-based measurements are performed. Thirdly, comparisons are performed that take into account differences in the vertical sensitivity of the MAX-DOAS and TROPOMI instruments (see Sect 6.2.5). Note that for these comparisons with ground measurements, only pixels within a radius of 20 km around the observation site were selected. The choice of 20 km was made for three main reasons: (1) consistency with the horizontal sensitivity of the MAX-DOAS instrument, which generally varies between 3 and 20 km depending on visibility conditions, as shown in Fig. 6.1, (2) reduction of random uncertainty in TROPOMI data, especially for H_2CO, as tested by Vigouroux et al. (2020), (3) consistency with Yombo Phaka et al. (2021), a study similar to this one and also other studies such as Pinardi et al. (2020); Irie et al. (2008), having tested these selection criteria for the case of NO_2.

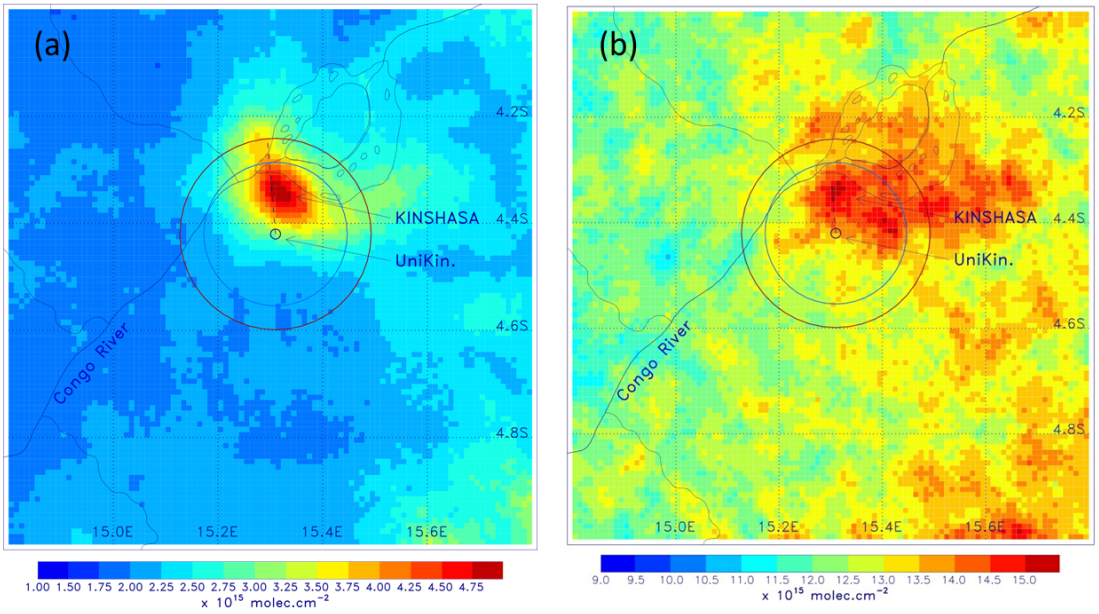

Figure 6.4: Distribution of oversampled NO_2 (panel a) and H_2CO (panel b) TROPOMI tropospheric columns in the station area (4°-5° S, 14.8°-15.8° E), from January 2020 to June 2021. The blue and brown circles represent the 15 km and 20 km radius circles around the station, respectively. The vertical black dashed line represents the pointing direction of the MAX-DOAS instrument.

The oversampling technique consists in long-term averaging of the satellite data on a very fine spatial grid, 0.01°x0.01° ($\sim$ 1x1 km^2), in a small domain around the station (4°-5° S, 14.8°-15.8° E). In this way, a high signal-to-noise ratio is achieved at high spatial resolution, at the expense of temporal resolution. We use TROPOMI data between January 2020 and June 2021, i.e. roughly the period of the MAX-DOAS measurements at Kinshasa. The technique takes advantage of the variable offset and geometry of the satellite measurement from day to day. This technique has been previously applied to SO_2 and NO_2 (de Foy et al., 2009; McLinden et al., 2012) and H_2CO (e.g., Zhu et al. (2014)) from OMI. We oversample both H_2CO and NO_2 vertical columns from TROPOMI. The column measurement for a given TROPOMI pixel is assumed to apply to a circle defined by the center of the pixel and a radius of 3.5 km. In this way, each 0.01° x 0.01° pixel accumulates $\sim$200 measurements

over the considered time period.

The resulting distributions on Fig. 6.4 show clear hot spots over the city of Kinshasa, with maximum values of $\sim$4.75 $\times$ 10^{15} molecules cm^{-2} and $\sim$16.0 $\times$ 10^{15} molecules cm^{-2} for NO_2 and H_2CO, respectively. Although the instrument is located outside the most polluted area, the instrument points towards downtown Kinshasa, where NO_2 and H_2CO levels are highest. These values are even higher when viewed in the direction of the MAX-DOAS, i.e. to the north of the city, precisely in downtown Kinshasa.

6.2.4 GEOS-Chem model output

We use a standard full chemistry simulation performed with the Goddard Earth Observing System chemistry (GEOS-Chem) model. GEOS-Chem is a 3D chemistry model that calculates local variations in atmospheric concentrations due to emissions, chemistry and deposition. The GEOS-Chem model has seen multiple applications across various regions of Africa (Lunt et al. (2019), Marais et al. (2019), and Bockarie et al. (2020)). We use version 12.0.2 (https://doi.org/10.5281/zenodo.1455215) runs implementing MERRA-2 assimilated meteorological fields at a horizontal resolution of 2° $\times$ 2.5° (latitude/longitude) on a vertical grid of 72 levels, up to 0.01 hPa (about 80 km). Emission inventories are taken into account using the Harvard Emission Component (HEMCO; Keller et al. (2014)) version 2.1.008 available in this version of the model. Our simulation includes EDGAR v4.3 for fossil fuel emissions, EMEP and NEI2011 for regional anthropogenic emissions, GFED v4 for fire emissions, MEGAN v2.1 for biogenic emissions, and RETRO for Non-Methane Volatile Organic Compounds (COVNM) emissions. In particular, the Diffuse and Inefficient Combustion Emissions in Africa (DICE-Africa) inventory is implemented to provide African anthropogenic emissions as in Marais and Wiedinmyer (2016a). DICE-Africa includes emissions from domestic and commercial use of wood from forests, household combustion of harvest residues, charcoal production and use, gas flaring, adhoc oil refining (Niger Delta only), kerosene use, diesel/petrol generators, and vehicles (including motorcycles). We use in the present study global multi-year simulations initiated in 2010, meaning that the years investigated here are unaffected by the initial conditions. The model outputs are saved every 2 hours.

6.2.5 Intercomparison methodology

Three different cases are explored in this study to compare the TROPOMI observations to those of MAX-DOAS.

Case 1: We select all TROPOMI pixels within a radius of 20 km around the observation site and compare the average column over the valid pixels to the average MAX-DOAS column around the overpass time.

Case 2: We recalculate the values of TROPOMI VCD_{tropo} selected in case 1, using the median of the MAX-DOAS daily median profiles according to Eq. (6.1) and Eq. (6.2) following Dimitropoulou et al. (2020). This recalculation is necessary to account for the different vertical sensitivity and a priori profile shapes of the TROPOMI and MAX-DOAS retrievals.

$$VCD^{smoothed}_{\text{MAX-DOAS}} = \sum_i \text{AVK}_i^{SP5} * C_{me}^{\text{MAX-DOAS}} \tag{6.1}$$

$$VCD^{recal}_{\text{SP5}} = VCD_{\text{SP5}} * \frac{VCD_{\text{MAX-DOAS}}}{VCD^{smoothed}_{\text{MAX-DOAS}}} \tag{6.2}$$

where $\text{VCD}^{smoothed}_{\text{MAX-DOAS}}$ represents the smoothed MAX-DOAS columns, AVK^{SP5} are the averaging Kernel of TROPOMI, $C_{me}^{\text{MAX-DOAS}}$ are the median profiles of the MAX-DOAS (in partial columns) discussed further below. We use the daily median profiles of MAX-DOAS to perform these transformations, in accordance with Dimitropoulou et al. (2020). $\text{VCD}^{recal}_{\text{SP5}}$ is the recalculated TROPOMI column using the MAX-DOAS profile as a priori. The index i denotes summation on the different layers.

Case 3: We proceed as in the previous case, but select only the pixels that lie in the azimuth direction of the instrument (355°). Previous studies have used this approach, exploiting the availability of measurements in different azimuth directions (Chen et al., 2009; Irie et al., 2008; Ma et al., 2013; Dimitropoulou et al., 2020). We then apply the transformation of case 2 to these selected pixels. The selection of TROPOMI pixels in the MAX-DOAS viewing direction is performed in three steps illustrated on Fig. 6.5. First, a horizontal profile (0 to 10 km) is created, consisting of 20 equally spaced points (distance of 0.5 km), starting from UniKin (4.42° S, 15.31° E) and oriented in the viewing direction of the instrument (355°). Second, geographical coordinates are assigned to each of the points. Finally, among the pixels lying within 20km of the observation site (24 in Fig. 6.5 a), only a few pixels cross the created line (3 pixels in Fig. 6.5b). Those are the pixels selected for the test within the MAX-DOAS line of sight.

In all three studied cases, the selected MAX-DOAS measurements are hourly averages at the overpass time. Numerical results of daily and monthly averages are also presented for each case. Absolute median differences (SAT-GB expressed in 10^{15} molecules cm^{-2}), relative median differences ((SAT-GB)/GB, in %), and least-squares linear regression statistics were calculated for each case. The results obtained for NO_2 and H_2CO are summarized in Sect. 6.3.2.

Figure 6.6 illustrates the daily median retrieved MAX-DOAS profiles (green dots) of NO_2 and H_2CO for 8 June and 15 November 2020, one day in the dry season and one day in the rainy season, respectively. The daily median profile of TM5 (orange curves) and GEOS-Chem for each molecule (red curves) is also shown for these two days. TM5 is a global chemistry transport model that is used to derive the a priori vertical profiles of NO_2 and H_2CO in TROPOMI product retrievals with a horizontal resolution of 1° x 1° (Williams et al., 2017). The horizontal bars represent the standard deviations related to each case. On panel a, the NO_2 profiles recovered by MAX-DOAS are found to be reasonably close to those of the two models. This behaviour is typical of all MAX-DOAS daily median NO_2 profiles during the dry season (see Fig. 6.15). The MAX-DOAS profile seems to fit fairly well with the TM5 and GEOS-Chem profiles for the dry season. However, during the rainy season, on panel c, as on all the other days (see Fig. 6.15), both models underestimate the MAX-DOAS profile for all altitudes. Regarding H_2CO, TM5 is found to overestimate the MAX-DOAS profile in the wet season. Most importantly, the TM5 profile during both seasons shows a fairly significant contribution in the upper troposphere, above 3 km, not found in the MAX-DOAS profile (see Fig. 6.15). This large difference in vertical profile

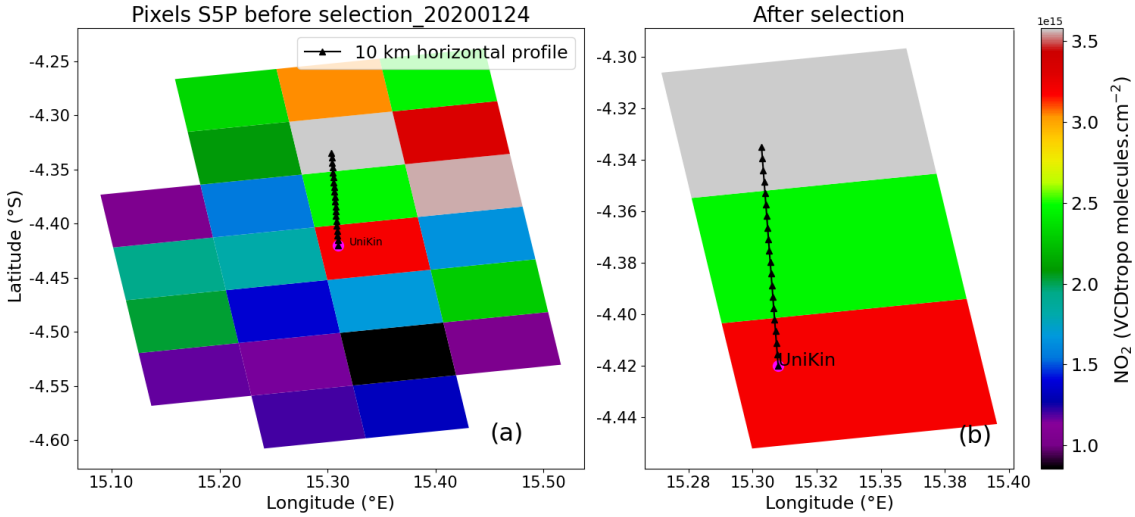

Figure 6.5: Illustration of the approach taking into account the pixels along the MAX-DOAS viewing direction. Panel (a) shows all the pixels selected within a 20 km radius of the UniKin and panel (b) shows the pixels selected along the viewing direction shown as a black line.

can seriously impact the recalculation of TROPOMI columns performed in case 2 and have impact the comparisons presented in Section 6.3.2.

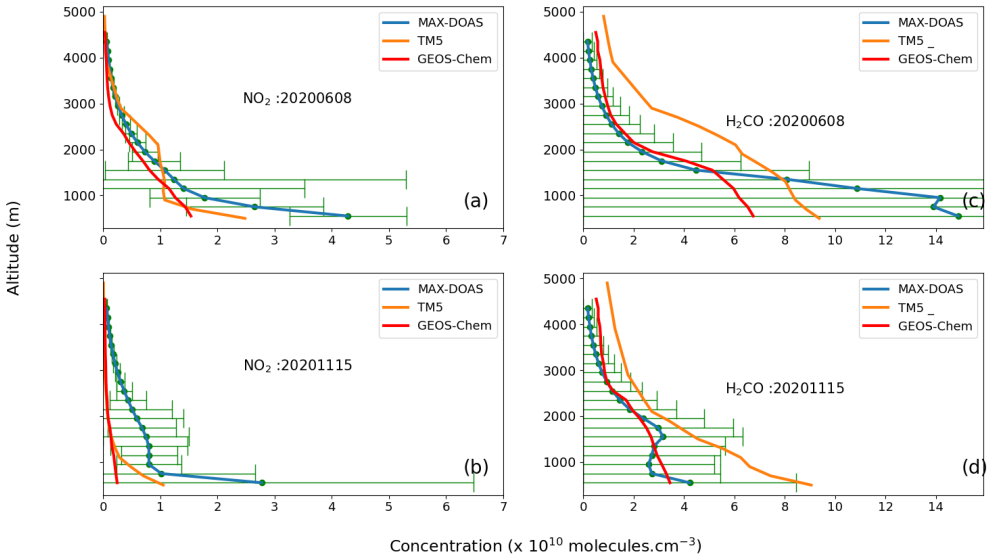

Figure 6.6: MAX-DOAS, TM5 and GEOS-Chem median profiles of NO_2 (panels: a, b) and H_2CO (panels : c ,d). The error bars represent the standard deviation. The daily MAX-DOAS medians profiles shown in green dots are illustrated by the type of profile used to recalculate the tropospheric vertical column densities according to Eq.(1) and Eq. (2).

6.3 RESULTS

The following section provides a description of the MAX-DOAS database of NO_2 and H_2CO VCD_{tropo} and Aerosols Optical Depth (AOD) and presents the results of comparisons made between model and satellite. In Sect. 6.3.1, we show the tropospheric columns and AODs time-series and the trace gases diurnal and seasonal variations. In Sect. 6.3.2, we present the MAX-DOAS and TROPOMI comparisons according to the three cases described in Sect. 6.2.5.

6.3.1 Overview of the MAX-DOAS database

Figure 6.7 shows the VCD_{tropo} of NO_2 and H_2CO (panels b, d) and the AOD (panels a, c). In each panel, the red curve represents the monthly average of the geophysical quantity displayed while the other curve connects the daily averages. AOD is retrieved in the visible (477 nm : panel a) and in ultraviolet (360 nm : panel c). The absence of measurements in November 2020 is due to a technical problem. The other gaps visible especially in panel c and d for H_2CO and AOD are due to data removed from our database, not having satisfied the MMF selection criteria.

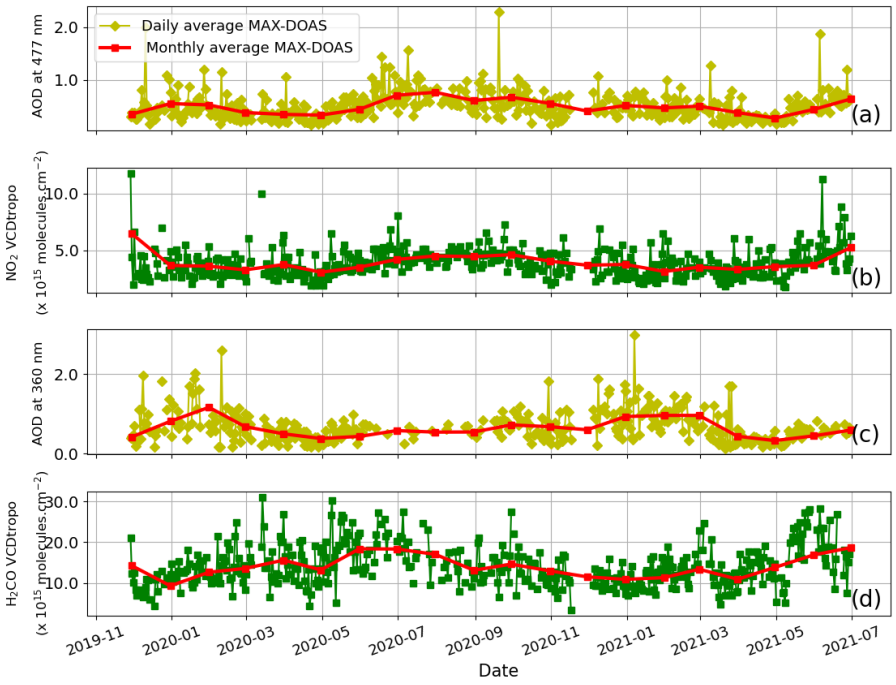

Figure 6.7: MAX-DOAS aerosol optical depth (AOD) measured at 477 nm (panel a) and 360 nm (panel c) and VCD_{tropo} of NO_2 (panel b) and H_2CO (panel d) measured between November 2019 and July 2021. In each panel, both daily and monthly averages are displayed.

During the study period, the daily averages of the tropospheric vertical NO_2 columns vary between 1.8×10^{15} and 11.8×10^{15} molecules cm^{-2} while the tropospheric vertical H_2CO columns range vary between 3.5×10^{15} molecules cm^{-2} and 31×10^{15} molecules cm^{-2},

with higher values measured during the dry seasons.

The AOD daily averages observed at 360 nm vary between 0.1 and 2.9 and are generally higher than the AOD observed at 477 nm varying between 0.1 and 2.2, due to increased scattering by aerosols at short wavelengths. Larger AOD values are also observed during the dry season, as for NO_2 and H_2CO, as illustrated by the decrease in visibility shown in Fig. 6.1 (panels a, b). This AOD increase can be explained by the accumulation of dust in the atmosphere over Kinshasa in the dry season due to the lack of cleaning effect of precipitation. This increase of AOD during the dry season is also confirmed by the Moderate Resolution Imaging Spectroradiometer (MODIS) AOD measurements. Figure 6.16 provide a good correspondence between the MODIS AODs at 550 nm and those of MAX-DOAS observed at 477 nm.

Figure 6.8 shows the mean diurnal variations of NO_2 and H_2CO VCD_{tropo}, calculated for all ground-based (GB) measurements. Three different periods are shown in these figures. The first period, from 1 January to 14 May, covers the short dry season, characterised by little rainfall. The second period, from 15 May to 14 September, covers the long dry season, when there is virtually no rainfall. The third period runs from 15 September to 31 December, covering the long rainy season.

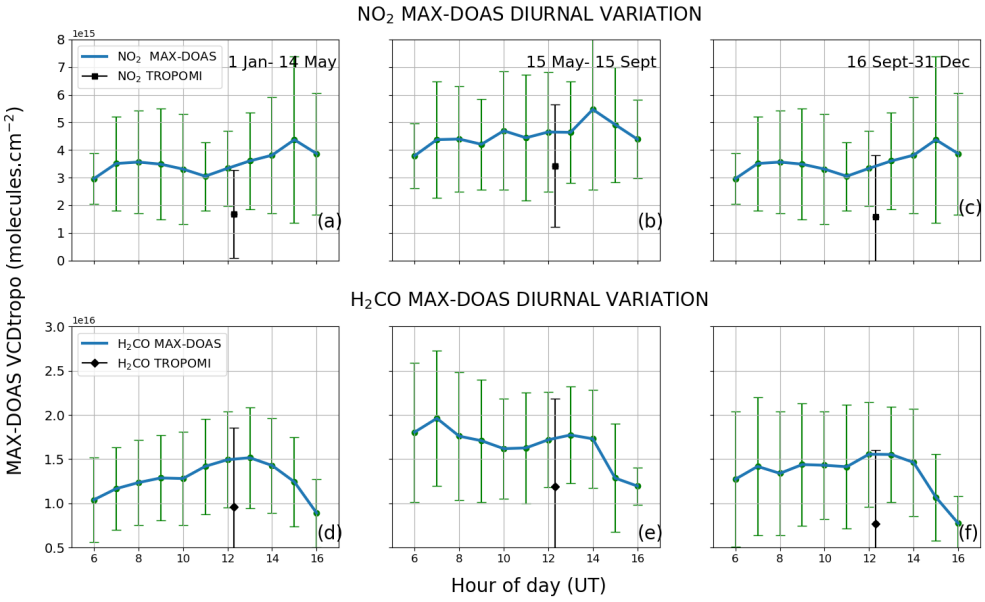

Figure 6.8: Mean diurnal variations of NO_2 VCD_{tropo} (panels a, b, c) and H_2CO (panels d, e, f) observed by the MAX-DOAS instrument (blue dots) and by TROPOMI (black dots) over the city of Kinshasa between November 2019 and July 2021. The error bars represent the (1-σ) standard deviation of VCDtropo computed for each hour within the specified period.

Regarding NO_2 VCD_{tropo}, we note a weak diurnal increase of similar amplitude during the 3 periods mentioned above. In the case of H_2CO VCD_{tropo}, the diurnal variation (also similar during the 3 periods) seems to be characterised by a maximum around noon in good agreement with Stavrakou et al. (2015). This behavior could be related to the diurnal pattern of biogenic emissions and fires. Isoprene emissions are favored by light and warm conditions (Guenther et al., 2006). Most of the fires occur around noon (70%) and 13:00 (22%), as reported by Cizungu et al. (2021) at the Luki Biosphere Reserve (5.5° S,

Table 6.3: Statistics summary for the MAX-DOAS and TROPOMI NO_2 comparisons.

Parameters (daily average/monthly average)	Case 1	Case 2	Case 3
Number of coincidences	198 / 19	198 / 19	90 / 19
Slope (s)	0.18 / 0.67	0.21 / 0.64	0.42 / 0.77
correlation coefficient (R)	0.32 / 0.71	0.30 / 0.68	0.43 / 0.48
intercept ($\times 10^{15}$ molecules cm^{-2})	1.61 / -0.21	2.76 / 1.15	3.87 / 2.74
bias (%)	-38 / -39	-2 / -12	41 / 44
bias ($\times 10^{15}$ molecules cm^{-2})	-1.26 / -1.69	-0.09 / -0.39	1.54 / 1.66

Case 1 : Direct comparison, all pixels
Case 2 : Recalculated TROPOMI, all pixels
Case 3 : Recalculated TROPOMI, azimuth-based selection

13.3° E), close to Kinshasa. The warmer and drier weather from noon onward is favoring the occurrence of fires and their spread. This would affect the H_2CO production with some delay, due to the VOCs oxidation. Oxidation of biogenic VOCs such as isoprene and monoterpenes leads to H_2CO typically after a few hours (Marais et al., 2012). For pyrogenic VOCs, their lifetime is highly variable, from a few hours to several days (Stavrakou et al., 2009b).

6.3.2 Intercomparison MAX-DOAS versus TROPOMI

Table 6.3 summarizes the results from the comparisons in three cases. The direct comparisons between TROPOMI and MAX-DOAS observations (case 1, see Fig. 6.9) yields poor agreement. We note low slopes (s) of 0.18 and 0.67 for the daily and monthly comparisons, respectively, and correlation coefficients (R) of 0.32 and 0.71. The corresponding intercepts are large, in the order of -1.26 $\times$ 10^{15} molecules cm^{-2} (daily) and -0.21 $\times$ 10^{15} molecules cm^{-2} (monthly), showing a strong contribution of the additive component. High negative median bias are also associated with these results, of the order of -1.2 $\times$ 10^{15} molecules cm^{-2} (-37.57%) and -1.69 $\times$ 10^{15} molecules cm^{-2} (-39.16%) for the daily and monthly comparisons, showing a strong underestimation of the TROPOMI observations relative to the MAX-DOAS observations. It should be noted that similar results were obtained using zenith measurements at the same site for NO_2 (Yombo Phaka et al., 2021). An underestimation of TROPOMI NO_2 observations was also frequently reported over large cities, e.g. by Griffin et al. (2019); Ialongo et al. (2020); Zhao et al. (2020); Marais et al. (2021b); Cai et al. (2022); Verhoelst et al. (2021) using NDACC ZSL-DOAS, MAX-DOAS and Pandonia global networks.

Moving to case 2, results are improved by making use of the MAX-DOAS profile shape information. Despite the relatively similar profile shapes of TM5 and MAX-DOAS (Fig. 6.6a, Fig. 6.15b), the impact of using the MAX-DOAS profiles as a priori in TROPOMI column retrieval appears to be significant. The agreement between the two data sets improves considerably compared to the first case, particularly in terms of reducing the median bias, while the slopes and correlation coefficients have maintained nearly identical values. We find a slope of 0.21 and 0.64 for daily and monthly comparisons respectively, and with correlation coefficients of 0.30 and 0.68 (see Fig. 6.10). On the other hand, there is high additive component at the intercept, 2.76 $\times$ 10^{15} molecules cm^{-2} and 1.15 $\times$ 10^{15} molecules cm^{-2} is noted for the daily and monthly comparisons. Negative median bias are also associated with these results, of the order of -0.09 $\times$ 10^{15} molecules cm^{-2} (-2.33%) and -0.39 $\times$ 10^{15} molecules cm^{-2} (-11.49%) for the daily and monthly comparisons, respectively. These results show the large impact of the a priori in the TROPOMI validation process

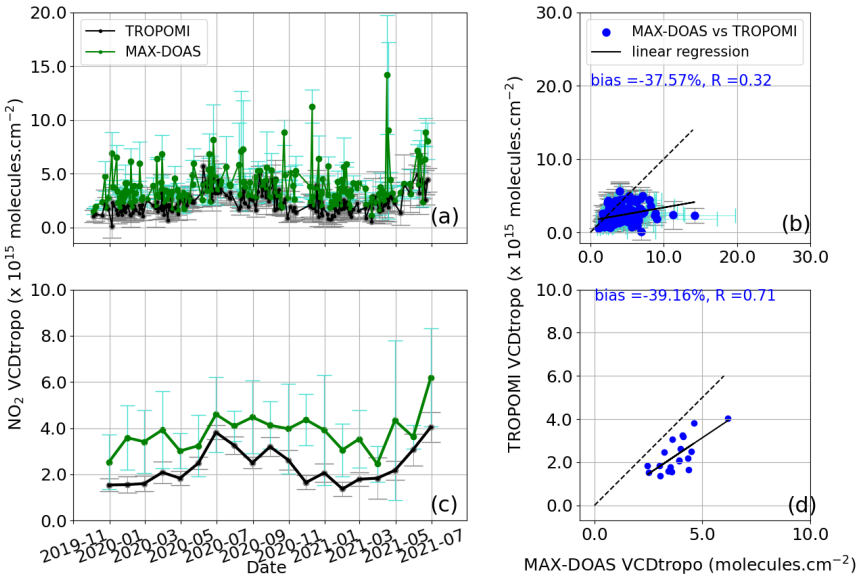

Figure 6.9: CASE 1 : NO_2 comparison of daily (panel a) and monthly (panel c) tropospheric vertical column densities of MAX-DOAS (green dots) and TROPOMI (black dots) over Kinshasa from 1 November 2019 to 1 July 2021. The MAX-DOAS is the hourly average coicidence day of TROPOMI satellite overpass. Error bars are (1-σ) standard deviations. (panel b and d): least-squares linear regressions between the two datasets.

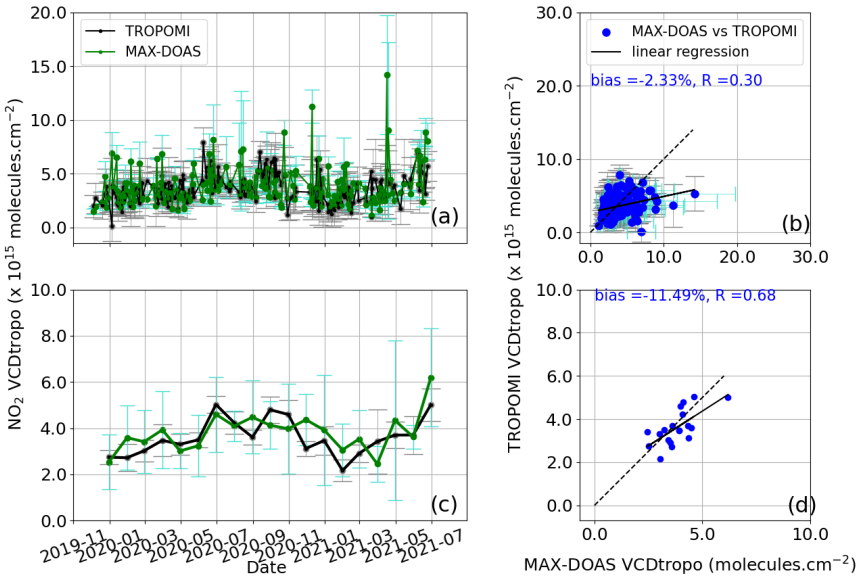

Figure 6.10: CASE 2 : NO_2 comparison of daily (panel a) and monthly (panel c) tropospheric vertical column densities of MAX-DOAS (green dots) and TROPOMI (black dots) over Kinshasa from 1 November 2019 to 1 July 2021. The MAX-DOAS is the hourly average coicidence day of TROPOMI satellite overpass. The individual TROPOMI points are those obtained from formulas 1 and 2 as described in the second case. Error bars are (1-σ) standard deviations. (panel b and d): least-squares linear regressions between the two datasets.

and confirms results from previous studies (e.g. Dimitropoulou et al. (2020)).

The comparison in case 3, for which only TROPOMI pixels lying in the MAX-DOAS viewing direction are selected is the most complex approach, since it takes into account the ground-based observation direction and the impact of the a priori profile shape on the TROPOMI retrieval (see Fig. 6.13 in the appendix). Although this case is potentially more realistic than case 2, as it addresses the spatial heterogeneity of the target compound in a more refined way, it implies a sharp reduction of the number of points making up the comparison sample. The number of TROPOMI data used for each co-location with MAX-DOAS measurements is reduced by about a factor of 0.15 on average (see Fig. 6.5), in comparison with case 2. The number of days with valid data is also reduced from 198 to 90. Therefore, given the noise in the TROPOMI column data, the regression of case 3 should be considered with caution. Furthermore, as seen on Fig. 6.4, the NO_2 field shows a steep gradient along the line of sight between UniKin and a distance of 10 km. The case 3 assumes a uniform sensitivity of MAX-DOAS along the 10 km of the line of sight, even though the instrument is likely more sensitive to shorter distances, where NO_2 columns are lower. We note an increase relative to case 2 of the TROPOMI bias to around 40% for daily and monthly comparisons. The possible causes explaining these differences are discussed in section 6.4.

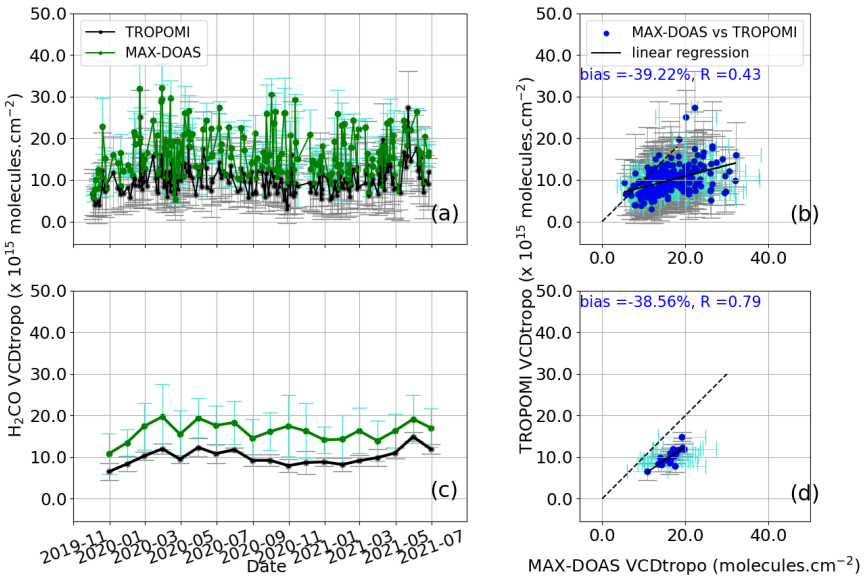

Figure 6.11: CASE 1 : H_2CO comparison of daily (panel a) and monthly (panel c) tropospheric vertical column densities of MAX-DOAS (green dots) and TROPOMI (black dots) over Kinshasa from 1 November 2019 to 1 July 2021. The MAX-DOAS is the hourly average coicidence day of TROPOMI satellite overpass. Error bars are (1-σ) standard deviations. (panel b and d): least-squares linear regressions between the two datasets.

Table 7.2 summarizes the results summary for H_2CO. As for NO_2, the direct comparison (case 1: Fig. 6.11) shows a strong median bias between TROPOMI and MAX-DOAS of around -5.91 x 10^{15} (-39%) (s =0.26, R = 0.43) for daily averages and -6.00 x 10^{15} (-39%) (s =0.68, R = 0.79) for monthly averages. TROPOMI is therefore underestimated. These results (daily comparisons) are close to those presented in De Smedt et al. (2021), for the polluted sites of UNAM in Mexico and Xianghe in China. We note an underestimation

Table 6.4: Statistics summary for the MAX-DOAS and TROPOMI H_2CO comparisons.

Parameters (daily average/monthly average)	Case 1	Case 2	Case 3
Number of coincidences	208 / 19	208 / 19	102 / 19
Slope (s)	0.26 / 0.68	0.30 / 1.00	0.37 / 0.90
correlation coefficient (R)	0.43 / 0.79	0.20 / 0.73	0.25 / 0.55
intercept ($\times$ 10^{15} molecules cm^{-2})	-5.71 / -1.06	12.89 / 1.50	12.61 / 3.15
bias (%)	-39 / -39	0.05 / 11	5 / 4
bias ($\times$ 10^{15} molecules cm^{-2})	-5.91 / -6.09	0.01 / 1.89	1.00 / 0.69

Case 1 : Direct comparison, all pixels
Case 2 : Recalculated TROPOMI, all pixels
Case 3 : Recalculated TROPOMI, azimuth-based selection

of TROPOMI compared to the ground measurements, with H_2CO levels ranging from 1 to 25 x 10^{15} molecules cm^{-2}. Chan et al. (2020a) and De Smedt et al. (2021) have also reported this underestimation in the case of large cities characterized by high pollution. The high H_2CO column levels (between 10 and 20 x 10^{15} molecules cm^{-2} on monthly average) characterize Kinshasa as a highly polluted area (columns higher than 8 x 10^{15} molecules cm^{-2}) according to the methodology of Vigouroux et al. (2020), who validated TROPOMI H_2CO using an extensive network of ground-based Fourier-transform infrared (FTIR) stations. In the same study, an average of 8.4 and 28 x 10^{15} molecules cm^{-2} were observed at the Paramaribo and Porto Velho stations, which are a highly polluted equatorial region in the same way as Kinshasa. Also in that study, we note a correlation coefficient of 0.9 between TROPOMI and the FTIR instrument of the Porto Velho station, value close to the one found in Kinshasa between TROPOMI and MAX-DOAS in case 1 (monthly comparison).

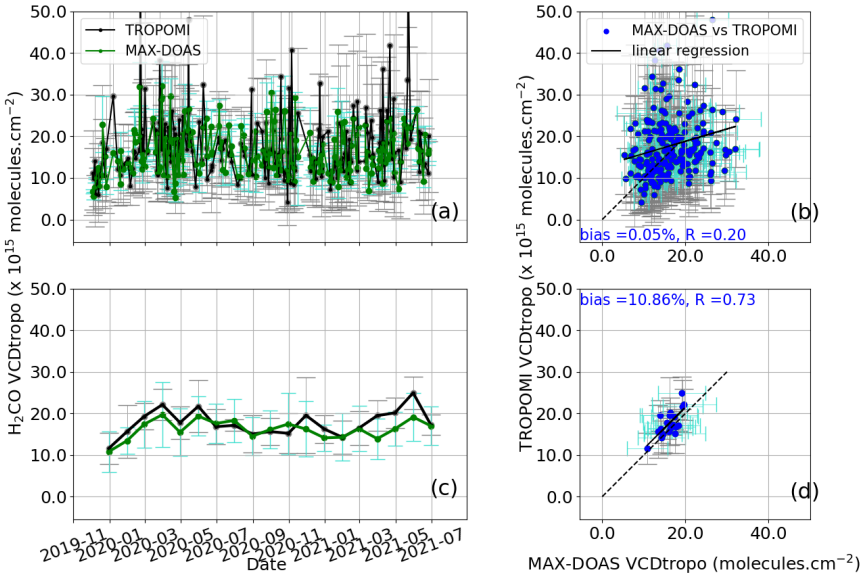

Figure 6.12: CASE 2 : H_2CO comparison of daily (panel a) and monthly (panel c) tropospheric vertical column densities of MAX-DOAS (green dots) and TROPOMI (black dots) over Kinshasa from 1 November 2019 to 1 July 2021. The MAX-DOAS is the hourly average coicidence day of TROPOMI satellite overpass. The individual TROPOMI points are those obtained from formulas 1 and 2 as described in the second case. Error bars are (1-σ) standard deviations. (panel b and d): least-squares linear regressions between the two datasets.

For case 2 (Fig. 6.12), when taking the MAX-DOAS median profile as a priori, the median bias is highly reduced around 0.01×10^{15} (0.05%) (s =0.30, R = 0.20) for daily averages and 1.89×10^{15} molecules cm^{-2} (11%) (s =1.00, R = 0.73) for monthly averages. These results demonstrate the impact of applying the change of a priori as in the case of NO_2. Those results are in agreement with those of De Smedt et al. (2021), who found that the negative bias of TROPOMI H_2CO against MAX-DOAS data at highly polluted sites (Mexico City and Xianghe) was reduced when substituting the TM5 profiles with the MAX-DOAS profiles in the TROPOMI product. The effect was weaker for less polluted sites such as Uccle (De Smedt et al., 2021). In section 6.4, we investigate the possible causes of this significant decrease in bias.

The third case (Fig. 6.14 in the appendix), shows an improved agreement between the two datasets, despite a sharp reduction in the number of points included in the comparative sampling. Slopes and correlation coefficients are s = 0.37 and R = 0.25 for daily comparisons; s=0.90 and R=0.55 for monthly comparisons. The median bias is estimated at about 5% for both daily and monthly comparisons, which represents a strong improvement on case 2. We discuss these differences in section 6.4.

6.4 DISCUSSION

The main conclusions of the comparisons between TROPOMI and MAX-DOAS data are as follows. First, there is a general underestimation of TROPOMI NO_2 and H_2CO columns in comparison to the ground-based observations, when the differences in vertical sensitivity and a priori profile shapes are not taken into account. Once those are considered in the comparison, there is a substantial improvement of the comparison statistics, especially, a strong impact on the reduction of the median difference between TROPOMI and MAX-DOAS. The comparison using selected TROPOMI pixels along the line of sight of the MAX-DOAS instrument shows a substantial increase in the TROPOMI averages, especially for NO_2, in line with the strong heterogeneity of the target compounds shown on Fig. 6.4. However, this approach is more strongly affected by the TROPOMI noise, and likely overestimates the influence of the very polluted city center, located 5-10 km from the station.

The general underestimation of TROPOMI compared to MAX-DOAS observations (case 1), can be partly understood by the limitation of nadir-viewing satellites to capture the high pollution lying near the ground (averaging kernels often below one for the first kilometers close to the ground), as is often the case in large cities. Kinshasa and its surroundings, with its high population density, intense road traffic and the common use of embers from wood burnt in the forest, is highly polluted. Figure 6.4 shows elevated concentrations of both molecules in downtown Kinshasa, located to the north of the measuring station, aligned with the viewing direction of the instrument. The southern part of the 20 km radius around the site is less polluted than the northern part, which may contribute to the underestimation of TROPOMI column averages in this radius. Furthermore, satellite retrieval heavily relies on choices made for the a priori profile. The a priori profile used in the inversion of the initial TROPOMI product is based the TM5 global model, featuring coarse horizontal resolution of 1° x 1° (Williams et al., 2017), which contrasts the fine horizontal resolution of TROPOMI (3.5×5.5 km^2) and leads to biased comparisons. Accounting for sensitivity through TROPOMI averaging kernels in conjunction with the MAX-DOAS profile (case 2) allowed us to deduce a correction factor. This factor is em-

ployed to update the initial TROPOMI product and notably mitigate the bias between TROPOMI and MAX-DOAS. The correction has a significantly more noticeable impact on H_2CO compared to NO_2 . This difference is attributed to the weaker vertical sensitivity near the surface in the UV range (H_2CO) as opposed to the Visible range (NO_2). Consequently, the influence of MAX-DOAS profiles is more substantial for H_2CO than for NO_2.

Additional uncertainties stem from clouds and aerosols present practically the whole year in this region, affecting the accuracy of the satellite retrievals in the troposphere (e.g., Boersma et al., 2004; Koelemeijer et al., 2001; Heckel et al., 2011; Leitão et al., 2010; McLinden et al., 2014). As seen in Fig. 6.7, AOD values can reach values up to 3 in the dry season. Although the TROPOMI dataset selected in our study has been filtered to remove the high cloudiness scenes ($QA \geq 0.75$ for NO_2 and $QA \geq 0.5$ for H_2CO), it should be noted that this filtering does not totally eliminate all the scenes affected by clouds and aerosols. Lorente et al. (2017) estimates that the a priori, combined with the surface albedo and cloud parameters can lead to uncertainties of up to the 47 % in the inversion of the TROPOMI data sets.

Considering only TROPOMI pixels intersecting the MAX-DOAS view (case 3) leads to elevated VCDs due to spatial variation of NO_2 and H_2CO around Kinshasa. The northward-oriented pixels (Fig. 6.4) show higher concentrations, further amplified by applying transformation of equation 1, explaining pronounced NO_2 biases. MAX-DOAS observations are heavily impacted by visibility, notably the Kinshasa with strong aerosol influence, reducing effective horizontal probing distance. This contributes to lower MAX-DOAS VCDs in case 3. Reduced pixel count (Fig. 6.5) also diminishes statistical data points, adding to TROPOMI sampling noise.

6.5 CONCLUSIONS

We present NO_2 and H_2CO MAX-DOAS measurements from an instrument installed at the University of Kinshasa in November 2019. Measurements in Africa are scarce, and we use them in order to validate the TROPOMI tropospheric columns. This work complements the first DOAS NO_2 observations made in this region between 2017 and 2019. The measurments obtained with the first instrument demonstrated a good agreement between TROPOMI and ground-based measurements, with a negative median bias of the order of -25% (Yombo Phaka et al., 2021). The present work aims at understanding and reducing the comparison bias by using the additional information provided by the new MAX-DOAS instrument (line-of-sight and retrieval of the gases vertical profiles). Measurements from the MAX-DOAS instrument for the period from November 2019 to July 2021 were analyzed and inverted within the harmonized FRM4DOAS project facilities. The annual cycle of NO_2 and H_2CO present highest tropospheric column levels during the dry season (mid-May to mid-September). The MAX-DOAS columns of NO_2 varied between 1.8 and 11.8 $\times$ 10^{15} molecules cm^{-2}, while that of H_2CO varied between 3.5 and 31 $\times$ 10^{15} molecules cm^{-2}. These MAX-DOAS measurements are then compared to the TROPOMI observations.

The TROPOMI validation exercise was carried out following 3 steps: (1) a standard comparison involving an average of all pixels within a radius of 20 km around the observation site and an hourly average of VCD_{tropo} MAX-DOAS at overpass S5p, (2) recalculating

the TROPOMI product using the MAX-DOAS profile as a priori, (3) selecting only the TROPOMI pixels within the MAX-DOAS line of sight and recalculating their VCDtropo as in the second case. The result of Case 1, complementing the previous exercise carried out at the same site, for NO_2, confirms that TROPOMI columns are underestimated, with a median bias of around -38%. When using the MAX-DOAS profile as a priori in the TROPOMI calculation, a significant improvement in the agreement between the two datasets is observed. The differences between the two datasets are substantially reduced, about -2% ($s = 0.21$, $R = 0.30$) for daily averages and -12% ($s = 0.64$, $R = 0.68$) for monthly averages. For H_2CO, based on case 1, we find a median bias of -39% ($s = 0.26$, $R = 0.43$) for daily averages and -39% ($s = 0.68$, $R = 0.79$) for monthly averages. In case 2, we find a strong bias reduction of around 0.05% (s =0.30, $R = 0.20$) for daily averages and 11% (s =1.00, $R = 0.73$) for monthly averages.

The third case, although potentially more realistic as it optimizes the spatial overlap of the comparison (by only selecting S5p pixels in the MAX-DOAS observation direction), shows less relevant statistical results than the other two, due to the small sample size. Given the horizontal distribution of the two compounds, TROPOMI VCDs are very high in the direction of downtown Kinshasa, leading to strong biases in the comparison results.

Our study demonstrates and confirms the impact of using MAX-DOAS profiles as a priori in the retrieval of TROPOMI columns. Indeed, due to the satellite low sensitivity near the surface, biases can manifest significantly in conditions of highly polluted large cities like Kinshasa, potentially resulting in an underestimation of satellite observations. However, this tendency is markedly mitigated when a correction is applied by considering profiles actually measured by the ground-based instrument.

Consequently, our recommendation is to implement this transformation, particularly in settings of highly polluted urban areas like Kinshasa. Nonetheless, caution should be exercised in the incorporation of the MAX-DOAS line of sight due to the introduced noise during downsampling, as observed in this study. This work also shows that the city of Kinshasa and its surroundings are very polluted in terms of NO_2, H_2CO and aerosols, thus requiring regular monitoring and control by the authorities.

6.6 APPENDIX

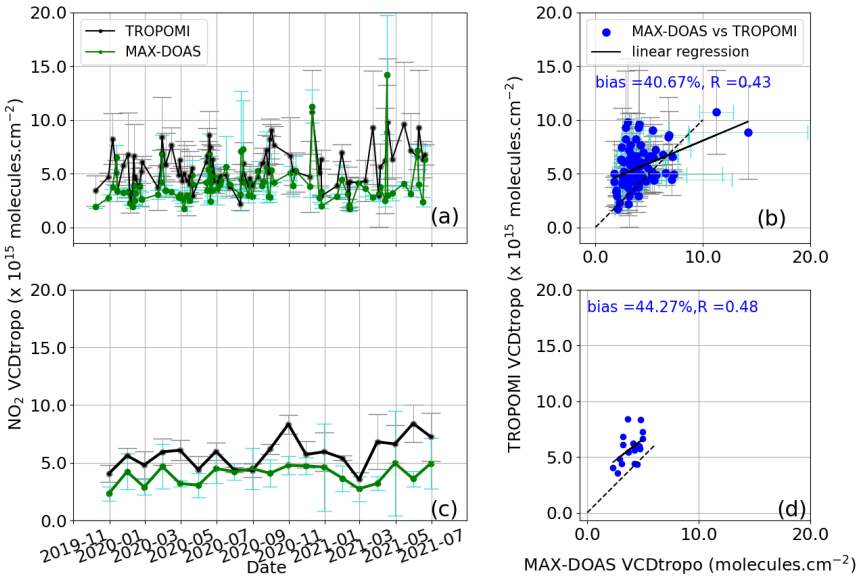

Figure 6.13: CASE 3 : NO_2 comparison of daily (panel a) and monthly (panel c) tropospheric vertical column densities of MAX-DOAS (green dots) and TROPOMI (black dots) over Kinshasa from 1 November 2019 to 01 July 2021. The MAX-DOAS is the hourly average coincidence day of TROPOMI satellite overpass. The individual TROPOMI points are those obtained from formulas 1 and 2. Error bars are (1-σ) standard deviations. Panel b and panel d are results of least-squares linear regressions between the two datasets, and provide the corresponding statistics.

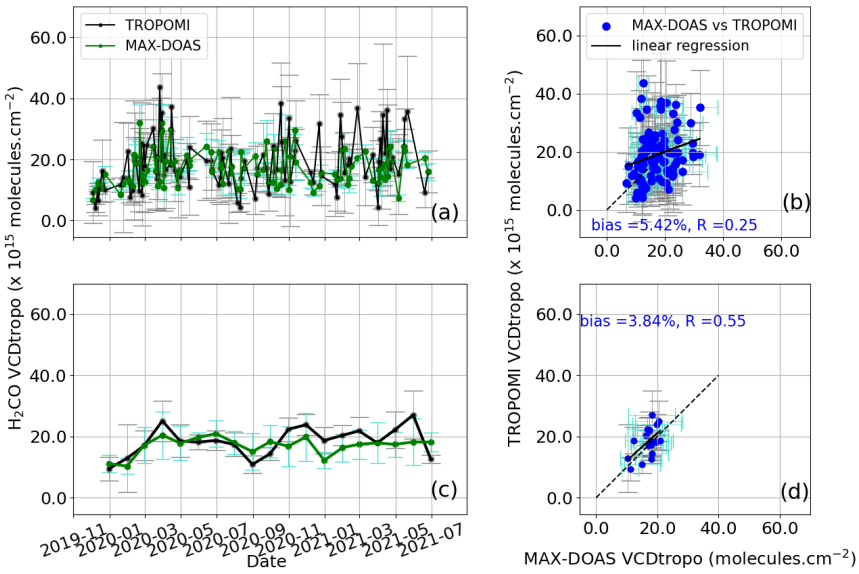

Figure 6.14: CASE 3 : H_2CO Comparison of daily (panel a) and monthly (panel c) tropospheric vertical column densities of MAX-DOAS (green dots) and TROPOMI (black dots) over Kinshasa from November 1, 2019 to July 01, 2021. The MAX-DOAS is the hourly average coincidence day of TROPOMI satellite overpass. The individual TROPOMI points are those obtained from formulas 1 and 2. Error bars are (1-σ) standard deviations. Panel b and panel d show the results of least-squares linear regressions between the two datasets.

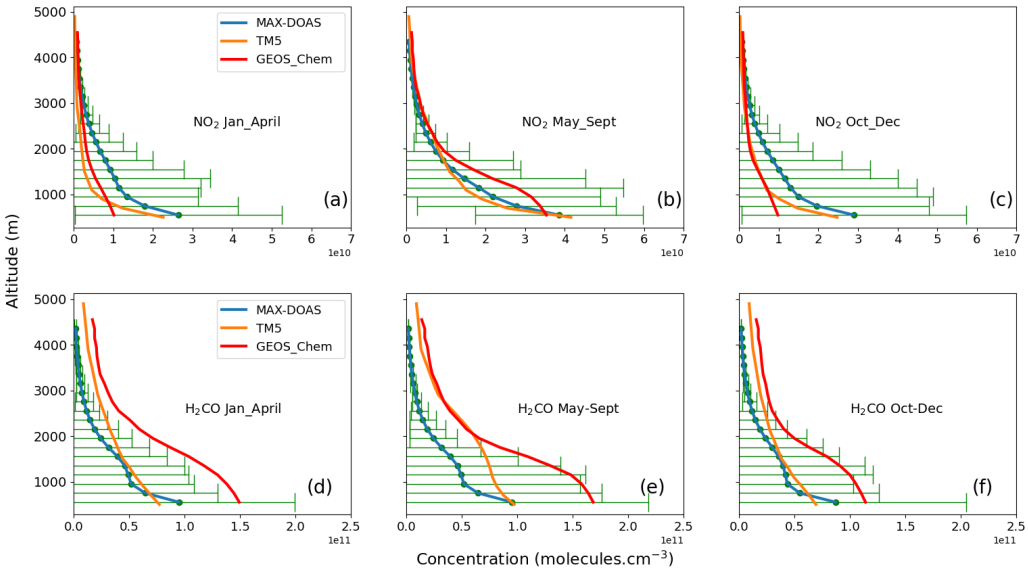

Figure 6.15: MAX-DOAS, TM5 and GEOS-Chem median profiles of NO_2 (panels: a, b, c) and H_2CO (panels : d, e, f). The error bars represent the standard deviation.

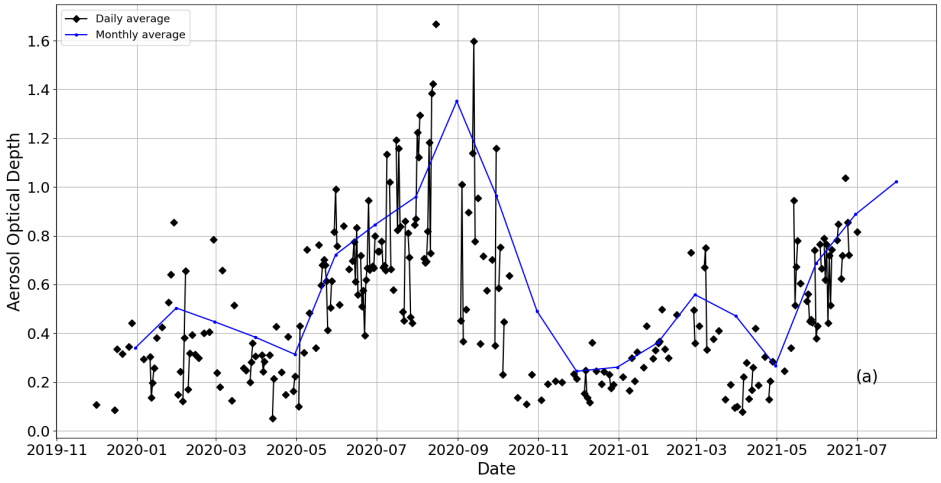

Figure 6.16: Time series of the monthly aerosol optical depth (AOD) observed at 550 nm wavelength by the MODIS Terra instrument downloaded from https://giovanni.gsfc.nasa.gov/giovanni/ for an area covering the city of Kinshasa (3–5°S, 14–16°E).

Chapter 7

GODDARD EARTH OBSERVING SYSTEM CHEMISTRY MODEL (GEOS-Chem)

The present chapter provides some details of the underlying theory of the Chemistry Transport Model (CTM) used in this study to generate NO_2 and H_2CO profiles, which have been essential for calculating AMFs required for converting dSCDs into VCDs, for all measurements taken in Kinshasa between 2017 and 2019 (see section 5.3.3). Subsequently, we present simulations of the two molecules and compare them to data from the TROPOMI and MAX-DOAS instruments. The aim of this analysis is to assess the performance of this model in the African region under consideration, with the ambition of drawing conclusions regarding potential emissions responsible for the observed pollution. It is important to note that GEOS-Chem exists in various versions [1], that can be operated with different horizontal and vertical resolutions, including a growing number of treated molecules. This model is therefore in constant evolution. For our thesis, we chose version 12.0.2 because it was available, functional, and operational in the GIRPAS laboratory. We provide a summary of the general descriptions of GEOS-Chem's operation, irrespective of versions, along with a link to the specific version used. The results of a standard and dedicated simulations conducted for the Kinshasa region and its surroundings are presented from Section 7.7 onward.

7.1 GENERAL CONSIDERATIONS

CTMs are used to study and understand processes or phenomena involving several parameters that are generally non-linear and interact with each other. Air pollution is one of these phenomena involving several parameters or non-linear mechanisms such as meteorology, turbulence, chemistry and transport.

The study of pollution therefore calls for mathematical modelling concepts allowing the

[1] `https://wiki.seas.harvard.edu/geos-chem/index.php/GEOS-Chem_versions`, last accessed on November 29, 2023

physical representation of this complex phenomenon. The existing models are generally based on non-linear partial derivative systems whose analytical solutions are not known. On this basis, numerical solutions are used to transform the physical continuous equations into discrete problems solved on defined computational domains called meshes. In summary, modelling starts with the mathematical equation of the phenomenon (conservation equations in general), the discretization of this equation by the elaboration of a mesh, the resolution of this discrete equation (often linear), the computer transcription and then the numerical simulation and the exploitation of the results.

According to the approaches used, two main families of models can be distinguished. The so-called Eulerian models, using the Eulerian approach and the so-called Lagrangian models using the Lagrangian approach. The Eulerian approach consists of considering a point in space in which the air masses passing through this point will be studied. Numerically speaking, this consists of discretizing the space in the form of a grid covering the area under study, applying a simulation of all the processes involved, i.e. transport, emissions, chemical reactions and others, in each of its grid points. These types of models can therefore be used to calculate, for example, import/export balances for pollutants in each grid cell. The Lagrangian approach consists of studying air masses whose transport and various changes in individual composition are simulated. As one of the objectives of this work is to estimate the emissions of the pollution observed in our study area, we have used the GEOS-Chem model, which is part of the Eulerian model family whose calculation time depends strongly on the resolution of the grid used. We run this global chemistry-transport model with a resolution of 2° × 2.5° (latitude/longitude) (see Figure 7.1, version 12.0.2).

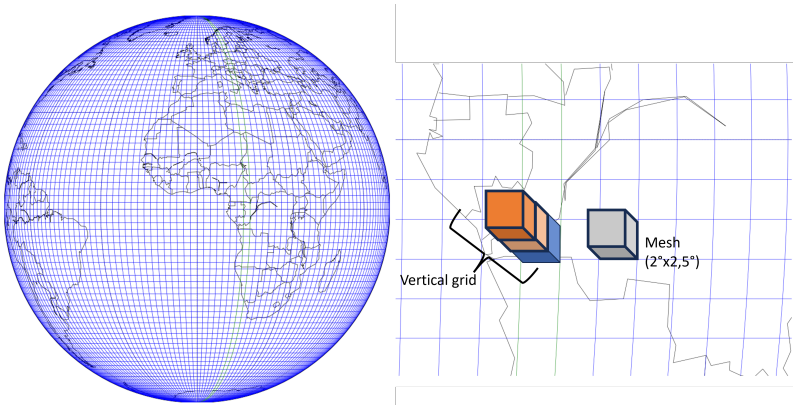

Figure 7.1: On the left, a representation of the Earth's globe overlaid with a grid of (2° x 2.5°) spacing. On the right side, an illustration depicting the GEOS-Chem mesh and vertical grid over Kinshasa area and its surroundings.

In addition to its availability in the Groupe Infra-Rouge de Physique Atmosphérique et Solaire (GIRPAS) lab where we carried out our research, the choice of GEOS-Chem is justified by the fact that this model is freely available, well documented (web pages, wiki, mailing lists) and above all easy to use. Widely used by atmospheric chemists and physicists around the world (more than 150 groups: `http://geos-chem.org`), GEOS-Chem thus presents an efficient modelling resource usable on a wide range of computer platforms with shared memory parallel systems (OpenMP) (Eastham et al., 2018). GEOS-Chem has the ability to perform simulations of oxidants, aerosols in the troposphere and stratosphere and provide balances of various gases. Another important aspect in our study is the possibility to use in GEOS-Chem the DICE-Africa emission inventory, a recent regional inventory, including the emissions of several sources of pollution existing in Africa other

times missing in the global inventories[2]. It should be noted that this model is managed by a support team based at Harvard and supervised by an international steering committee.

In the following sections, we give the general ideas of the conservation equations used by GEOS-Chem, the theories of the different processes involved in the simulation (chemistry, transport, deposition, turbulence), the different inputs needed to make these simulations successful (meteorological parameters, emission inventories) and the description of the result extraction tool used in this thesis. We will not go into the details of the computer code running this simulation, which can be consulted in `https://www.acom.ucar.edu/webt/geos-chem/2018/GC_Code_Structure_BMY_NCAR_v3.pdf`

7.2 GEOS-Chem DESCRIPTION

As mentioned in the previous section, the CTMs are computer codes that allow the solution of physical equations modelling the phenomenon by numerical methods (algorithms). GEOS-Chem proceeds to the solution of the general Eulerian form of the three-dimensional continuity equations (equation 7.1), looking for the concentrations of simulated chemical species (Fritz et al., 2022).

$$\frac{\partial n}{\partial t} = - \bigtriangledown (n_{\mathrm{i}} U) + P_{\mathrm{i}}(n) - L_{\mathrm{i}}(n) \qquad i \in [1, m] \tag{7.1}$$

Where $n = (n_1, ...n_m)^{T}$ [3] is the number density vector representing the concentrations of the m species, U is the wind vector (including sub-grid components parameterized as turbulent diffusion and convection), and $P_{\mathrm{i}}(n)$ and $L_{\mathrm{i}}(n)$ are the local production and loss rates of species i including terms to describe chemical reactions, aerosol microphysics, emissions, precipitation scavenging, and dry deposition. In GEOS-Chem, as in all 3-D CTMs, equation 7.1 is solved by operator splitting to separately and successively apply concentration updates over finite time steps from a transport operator (equation 7.2) and the operator coupling the continuity equations between species through chemical kinetics and aerosol physics (equation 7.3).

$$\frac{\partial n_{\mathrm{i}}}{\partial t} = - \bigtriangledown (n_{\mathrm{i}} U) \qquad i \in [1, m] \tag{7.2}$$

$$\frac{d n_{\mathrm{i}}}{d t} = P_{\mathrm{i}}(n) - L_{\mathrm{i}}(n) \qquad i \in [1, m] \tag{7.3}$$

The numerical solution of these equations is performed in a cubic mesh, taking into account all the physical and chemical processes contributing to the evolution of the molecules whose concentration is to be determined. In the following sections, we present the basic ideas of the concepts explaining the processes involved. The specifics of their algorithms, as implemented in GEOS-Chem, are outlined in the dedicated references (`https://github.com/geoschem/geos-chem`, last accessed on November 29, 2023).

In the resolution of the aforementioned three-dimensional equations, we observe the need for meteorological parameters such as wind speed, which is directly integrated into the

[2] Fuelwood for energy, charcoal production and use, and gasoline and diesel for motorcycles, cars, and generators
[3] The symbol T as an exponent indicates the transposition of the matrix n

equations, along with many other meteorological parameters involved in various ways. To address this, there are three configuration modes allowing GEOS-Chem to use these meteorological variable inputs, referred to as meteorological fields.

The first mode, also known as the standard mode described by Bey et al. (2001), is the offline mode. In this setup, the model does not simulate atmospheric dynamics itself. Instead, it utilizes meteorological variables generated by simulations of the Goddard Earth Observing System (GEOS) from the Global Modeling and Assimilation Office (GMAO) at NASA, assimilating meteorological observations (Fritz et al., 2022). The second mode is the real-time mode (GEOS-Chem forward processing), where simulation outputs are provided quasi-real-time, offering global-scale data at a native horizontal resolution of $0.25° \times 0.3125°$. There is also the option to regrid to a coarser resolution (through conservative repositioning of meteorological fields). To achieve this, the GEOS Earth system model is coupled with the GEOS-Chem tropospheric-stratospheric unified chemistry extension (UCX) to represent composition from the surface to the top of the GEOS atmosphere (0.01 hPa). The third mode, known as the online mode and introduced by Long et al. (2015), enables the utilization of GEOS-Chem as a chemical module within Earth System Models (ESMs), with its initial application to the GEOS ESM. In this configuration, GEOS-Chem focuses solely on the local terms of the continuity equation.

In this work, we used the full-chemistry GEOS-Chem offline mode, version 12.0.2 (`https://doi.org/10.5281/zenodo.1455215`) runs implementing MERRA-2 assimilated meteorological fields. The following section gives descriptions of the fields used.

7.3 TRANSPORT AND DEPOSITION

7.3.1 Transport

Variations in wind speed and direction play a crucial role in processes like the dilution and transport of air pollutants, defining the dynamics of the Earth's atmosphere (see 2.2.2). On a smaller scale, the mixing of air masses facilitates pollutant dilution, while on a larger scale, it ensures their transportation. The effectiveness of the transport mechanism relies heavily on factors such as wind speed, sunshine, temperature, and atmospheric stability. These parameters must be accurately modeled due to their significant influence on pollutant concentration levels. For instance, pollutant dispersion increases with higher wind speed and turbulence. Sunshine contributes to soil and surface heating, initiating convection phenomena responsible for both vertical and horizontal movements. The collective impact of these factors determines the duration during which pollutants remain in the atmosphere, the distance they travel from their emission source via wind transport, and the extent to which they are removed. This transport occurs through horizontal (advective process) and vertical (convective process) movements, combined and expressed in Equation 7.2.

In GEOS-Chem, the advection equation is solved using the algorithm of Lin and Rood (1996) and convection is calculated from the convective mass fluxes in the meteorological archive, as described by Wu et al. (2007)

7.3.2 Deposition

Atmospheric deposition serves as a primary mechanism for the settling of pollutants onto land and water surfaces. This process is intricately linked to meteorological factors (temperature, precipitation, humidity, and wind), the physico-chemical properties of the deposited particles (size, reactivity), and the characteristics of the receiving surfaces. Wet deposition, governed by precipitation, and dry deposition, occurring through gravitational sedimentation or diffusion followed by turbulent transfer, absorption by plants, or adsorption onto surfaces, represent distinct processes leading to observed deposition.

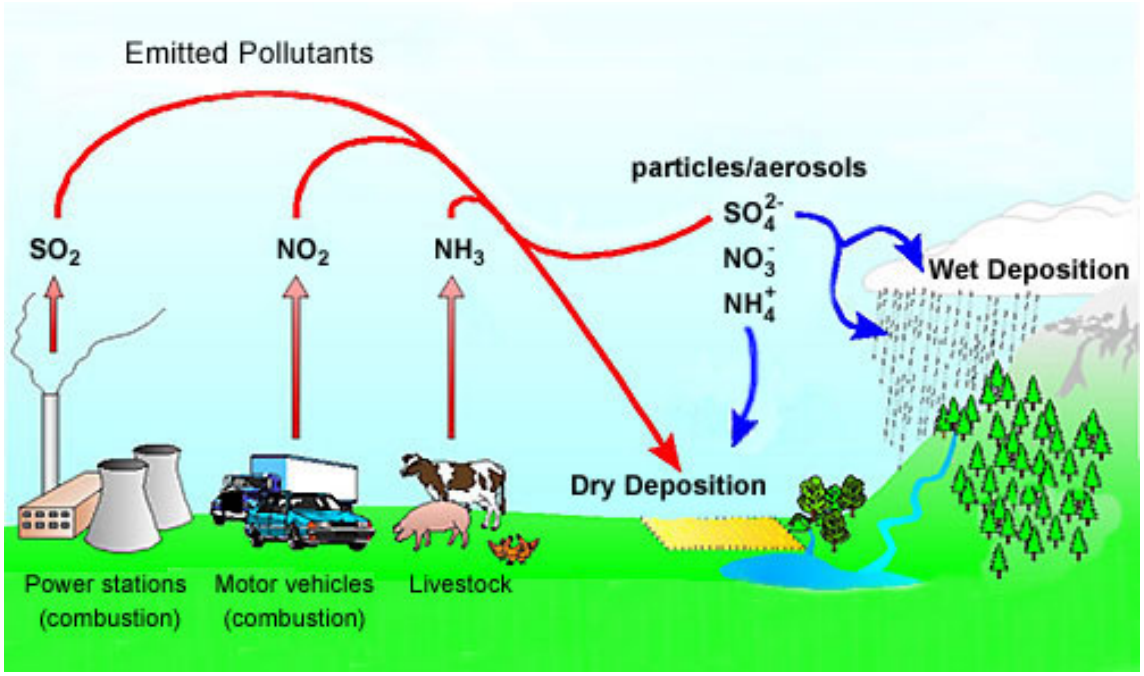

Figure 7.2: Pollutant emission and deposition processes `https://www.apis.ac.uk/starters-guide-air-pollution-and-pollution-sources`

A. Wet deposition scheme

Wet deposition encompasses processes associated with precipitation (rain[4], snow[5], hail[6]) and covert wet deposition, which involves the impact of cloud droplets on elevated surfaces or the settling of fog droplets (Seigneur, 2018). Among these, raindrops, due to their ability to absorb larger quantities of pollutants, play a more dominant role in the precipitation process. During precipitation events, gaseous or particulate pollutants become entrapped by cloud or raindrops. Gaseous pollutants, being soluble in water, are captured through dissolution in the aqueous phase, while particulate pollutants are intercepted when they collide with these water droplets. This trapping mechanism enables pollutants to descend to the surface and involves two primary processes: "rain-out," which entails the entrainment of pollutants present in the atmosphere at the time of water droplet formation, and

[4]Rain: Rain is liquid precipitation that falls from clouds in the form of water droplets. It is the most common type of precipitation.

[5]Snow: Snow consists of ice crystals that form in the atmosphere and fall to the ground. Snowflakes are intricate ice structures with a variety of shapes.

[6]Hail: Hail is a type of precipitation that occurs in severe thunderstorms. It consists of balls or lumps of ice that can vary in size from small pellets to large stones.

"wash-out," involving the leaching of the atmosphere by water droplets beneath the clouds. The latter occurs through either the fixation of free ions on the droplet surfaces or adsorption. The comprehensive processes related to wet deposition considered in GEOS-Chem are depicted in Figure 7.3.

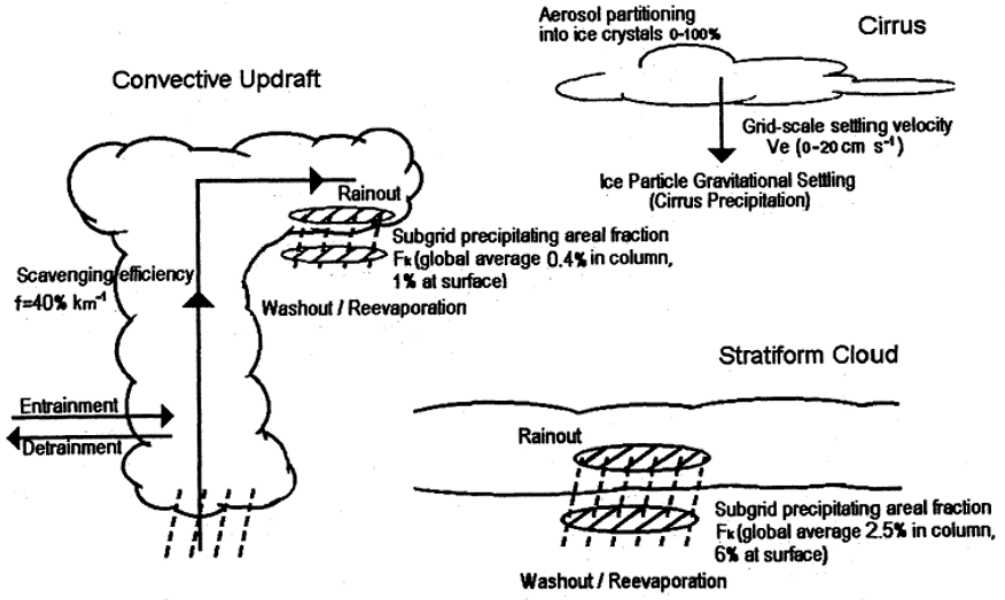

Figure 7.3: The diagram for water-soluble aerosols wet deposition process as treated in GEOS-Chem (Liu et al., 2001).

GEOS-Chem exploits the mathematical expressions of Hernri's law (equation 7.4), which details the dissolution process of gases in a liquid. The constants involved in this expression for all species concerned can be found in `https://wiki.seas.harvard.edu/geos-chem/index.php/Wet_deposition` (last accessed on November 30, 203).

$$K_{\mathrm{H}} = \frac{K_0 + exp((C_{\mathrm{R}}) * (\frac{1}{T} - \frac{1}{298.15}) * R * T}{AMT} \tag{7.4}$$

with K_{H} as the Henry's law solubility constant, in M[7] atm^{-1}, C_{R} is the Henry's law volatility constant, T is the temperature in K, R is the universal gas constant = 8.3144621 J K^{-1} mol^{-1}, ATM is the reference pressure at STP (Standard Temperature and Pressure) = 101.325 mPa, and 298.15 is the reference temperature (in K) at STP.

B. Dry deposition scheme

Three primary mechanisms govern dry deposition: sedimentation, inertial or interception impacts, and diffusion (Wesely and Hicks, 2000). Sedimentation and inertial impacts are primarily associated with particles, while diffusion is pertinent to gaseous pollutants. These three processes, defining dry deposition, are generally considered in comprehensive modeling. For instance, Zhang et al. (2003) provide parameterizations employed by various models for simulating the dry deposition of gaseous pollutants and particles in

[7] 1 M = 1 mol/dm^3

urban environments. In GEOS-Chem, dry deposition fluxes are derived using the serial aerodynamic resistance scheme, a method developed by Wesely (1989) and implemented by Wang et al. (1998).

7.4 METEOROGICAL FIELDS AND GRID RESOLUTION

7.4.1 Meterogical fields

Meteorological fields are essential inputs for the effective operation of CTMs. These fields furnish parameters such as temperature, pressure, humidity, and wind speed, which play a crucial role in the physico-chemical reactions of the pollutant species simulated within a specific grid cell (refer to Section 7.4.2). In practical terms, these meteorological parameters are obtained through various measuring instruments such as probes, balloons, satellites, and ground stations, strategically placed across the globe. However, vast areas of the Earth and atmosphere lack coverage from these instruments. The challenge arises from the desire to have knowledge of these parameters throughout the atmosphere, a goal hindered by technological limitations and associated costs.

To address this limitation, meteorologists and oceanographers employ a mathematical tool called assimilation. Assimilation involves optimally combining observations retrieved from different instruments (probes, satellites) with existing scientific theoretical knowledge of the atmosphere. This approach not only aids in forecasting but also enables the approximation of meteorological parameters in regions not covered by direct measurements. The objective is to provide reasonably short-term forecasts of their evolution. Examples of assimilation data sources include the European Centre for Medium-Range Weather Forecasts (ECMWF) and the Global Modeling and Assimilation Office (Global Modeling and Assimilation Office (GMAO)) (`https://gmao.gsfc.nasa.gov/field_campaigns/`, last accessed on November 29, 2023).

In this thesis, temperature and pressure profiles utilized in Chapter 5 and 6 (AMF calculation) are derived from ECMWF data. Additionally, all simulations conducted with the GEOS-Chem model utilize meteorological field data from the Modern-Era Retrospective analysis for Research and Applications, Version 2 (MERRA-2), provided by GMAO (Bey et al., 2001).

MERRA-2 provides a comprehensive database of global meteorological parameters, derived from assimilation systems that combine *era* satellite observations (hyperspectral radiance and microwave), GPS radio occultation data, and the geophysical information content of the ozone profile `https://gmao.gsfc.nasa.gov/pubs/docs/McCarty885.pdf`. MERRA-2 adopts a cube-sphere discretization with an approximate horizontal resolution of $0.5^\circ \times 0.625^\circ$ and 72 hybrid-static levels from the surface to 0.01 hPa (Gelaro et al., 2017).

7.4.2 Grid resolution

As previously mentioned, the functioning of any model relies on the concept of discretization within the working domain, enabling the numerical solution of the problem or its implementation on a computing machine. This discretization occurs both horizontally and vertically, resulting in cubic meshes, as illustrated in Figure 7.4, organized

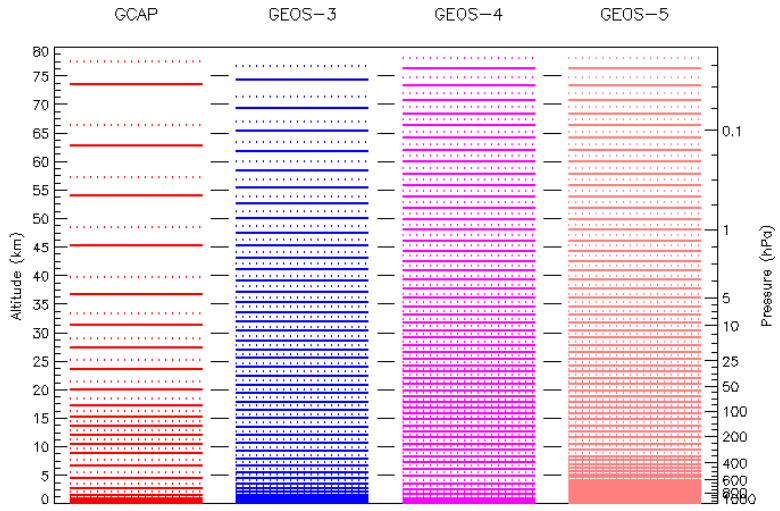

Figure 7.4: GEOS-Chem vertical grid (`http://wiki.seas.harvard.edu/geos-chem/index.php/GEOS-Chem_vertical_grids`, last accessed on November 29, 2023). The GEOS-5 vertical grid was used in this study.

into vertical grids. GEOS-Chem is characterized by various grid configurations with distinct mesh sizes across different versions. In this study, we utilized version 12.0.2 (`https://doi.org/10.5281/zenodo.1455215`, last accessed on November 29, 2023), featuring a horizontal resolution of 2° x 2.5° (Figure 7.1) and a vertical resolution, as depicted in the right side of Figure 7.4, comprising 72 levels up to 0.01 hPa (approximately 80 km). The initial layers of grids near the surface exhibit finer resolution compared to the upper layers, allowing for heightened sensitivity in the lower troposphere.

7.5 CHEMISTRY

The GEOS-Chem model supports various patterns of chemical reactions in both the troposphere and the stratosphere. The v12.0 GEOS-Chem mechanism incorporates 228 species (Shen et al., 2020). Table 7.5 organizes these species into boxes based on their chemical characteristics. For a comprehensive view of the chemistry mechanisms associated with each chemical species processed in GEOS-Chem, interested individuals can refer to the extension files accessible at (`https://wiki.seas.harvard.edu/geos-chem/index.php/GEOS-Chem_chemistry_mechanisms`). These files contain open access codes known as Kinetic PreProcessor (KPP).

7.5.1 Chemical kinetics

Theoretical description of kinetic implications at the microscopic or molecular level is generally necessary to establish the chemical evolution of a given species in a reactive environment. The primary objective is to ascertain the rates at which the elements (i.e., chemical species) involved in the system are either formed or consumed. To illustrate, consider a chemical reaction of the form 7.5. In this context, the rates of formation (represented by S_{e3} and S_{e4}) and transformation (in the case of S_{e1} and S_{e2}) are governed by the principles of the law of mass action, as highlighted by Ayari (1995).

Block	Type of species[b]	Number of species	Species
1	Aromatics	21	CH2I2, LBRO2H, LBRO2N, LTRO2H, LTRO2N, SO4H2, IMAE, BENZ, TOLU, TRO2, BRO2, CH2CI2, IMAO3, RA3P, RP, PP, IPMN, GLYX, A3O2, PO2, R4N1
2	Organic nitrates	7	INDIOL, SO4H1, PPN, IONITA, N, RCO3, R4N2
3	Isoprene, terpenes	30	CH2ICl, LISOPOH, LISOPNO3, MONITA, OCS, CHBr3, CHCl3, HCFC22, PRPN, HPALD, HONIT, RIPB, RIPA, LIMO, MONITS, ISOPNB, CH3CHOO, MVKN, PRN1, MONITU, CH2OO, PROPNN, ISOP, OLND, OLNN, HC5OO, ISN1, HC5, RIO2, INO2
4	Alkanes, alkenes, acetone	12	MSA, MAP, ETP, SO4, ATOOH, C2H6, ATO2, ACTA, ACET, ETO2, PRPE, ALD2
5	Higher alkanes, methyl ethyl ketone	14	CH3I, RB3P, CH3Cl, ALK4, R4P, C3H8, EOH, B3O2, KO2, MGLY, R4O2, HAC, RCHO, MEK
6	Halocarbons, isoprene products	55	CH2IBr, ISN1OA, ISN1OG, LVOCOA, LVOC, PYAC, SOAMG, DHDN, CH3CCl3, H1301, H2402, PMNN, CCl4, CFC11, CFC12, CFC113, CFC114, CFC115, H1211, IEPOXD, CH2Br2, HCFC123, HCFC141b, HCFC142b, CH3Br, DHPCARP, IAP, HPC52O2, MOBA, ISNP, MAOP, MRP, RIPD, ETHLN, ISNOHOO, NPMN, MOBAOO, DIBOO, ISNOOB, INPN, MACRNO2, MVKOO, GAOO, MGLYOO, MGLOO, MAN2, ISNOOA, ISOPNDO2, MACROO, MACRN, MAOPO2, LIMO2, ISOPNBO2, ISOPND, NMAO3
7	Secondary organic aerosol	25	LXRO2H, LXRO2N, SOAGX, SOAIE, SOAME, DHDC, IEPOXA, IEPOXB, XRO2, XYLE, PIP, HC187, VRP, DHMOB, MTPA, MTPO, ROH, IEPOXOO, HCOOH, PIO2, GLYC, VRO2, MRO2, MACR, MVK
8	Sulfur, peroxyacetyl nitrate	15	CO2, N2O, DMS, HNO4, HNO2, PAN, MP, H, CH4, H2O2, MCO3, SO2, CO, O1D, O
9	Oxidants	12	MPN, N2O5, HNO3, CH2O, MO2, O3, NO, HO2, NO3, NO2, H2O, OH
10	Iodine reservoirs	13	AERI, ISALA, ISALC, I2O4, I2O3, IBr, INO, HI, ICl, ClNO2, BrSALC, BrSALA, I2
11	Bromine and chlorine inorganic species	11	ClOO, BrCl, Br2, BrNO3, HOBr, HOCl, ClNO3, Cl, HBr, ClO, HCl
12	Bromine and iodine radicals	13	I2O2, BrNO2, Cl2O2, IONO, OIO, OClO, HOI, IONO2, Cl2, I, IO, BrO, Br

Figure 7.5: The names of 228 species processed in GEOS-Chem. Table taken from Shen et al. (2020), constructed from `http://wiki.seas.harvard.edu/geos-chem/index.php/Species_in_GEOS-Chem`.

$$S_{e1} + S_{e2} \longrightarrow S_{e3} + S_{e4} \tag{7.5}$$

$$\frac{d[S_{e1}]}{dt} = \frac{d[S_{e2}]}{dt} = -\frac{d[S_{e3}]}{dt} = -\frac{d[S_{e4}]}{dt} \tag{7.6}$$

The rate of disappearance of S_{e1} can therefore be calculated by the equation **??**, and thanks to the relation 7.6, we can calculate the rate of production of S_{e3} and at the same time the rates of S_{e2} and S_{e4}.

$$\frac{d[S_{e1}]}{dt} = -A \cdot \exp\left(-\frac{E_a}{RT}\right)[S_{e1}]^{n_{e1}}[S_{e2}]^{n_{e2}} \tag{7.7}$$

where n_{e1} and n_{e2} are stoichiometric coefficients, R is the universal gas constant in (cal/mol-K), T is the temperature in K, A is the frequency factor in

7.5.2 Radiation

The determination of the kinetics involved in photolysis reactions of specific molecules necessitates an understanding of the solar radiation that instigates these reactions. Therefore, radiation modeling becomes imperative in CTM. The sunlight emanating from the sun, comprising photons with energy dependent on wavelength, undergoes both scattering and absorption by atmospheric gases. Notably, certain wavelength ranges of this radiation do not penetrate the Earth's surface due to factors such as the absorption of radiation by oxygen and nitrogen molecules below 100 nm, and the partial absorption by ozone between 100 and 200 nm. Consequently, the solar radiation that effectively reaches the Earth's surface is predominantly in wavelengths exceeding 300 nm.

Solar radiation reaching the Earth's surface undergoes transmission or reflection, where transmission contributes to planetary heating and reflection, characterized by the albedo, has the opposite impact, varying across surfaces and influencing planetary energy exchange and climate.

IPCC (2001) defines a radiative forcing as a change in the radiation budget assessed at the top of the troposphere. A positive radiative forcing implies a global warming of the troposphere, while a negative radiative forcing cools it (Menegoz, 2009). GEOS-Chem performs radiative forcing calculations, using the optional RRTMG module described in Heald et al. (2014).

The Fast-JX code by Bian and Prather (2002) is used in GEOS-Chem to calculate the photolysis frequencies of chemical reactions involved in the troposphere and stratosphere. Aerosol extinction is also supported in GEOS-Chem and its description can be found Latimer and Martin (2019). The fractional optical thicknesses of clouds are also taken into account in GEOS-Chem and are described by Liu et al. (2009).

7.5.3 Emissions

Any CTM needs emission inventories as input to be able to computationally estimate the concentration of a given species at a given location. Emission inventories therefore constitute a documentation of the evolution of emissions of an air pollutant and its precursors (Seigneur, 2018). It is therefore a database cataloging the quantity of a pollutant emitted by a given process in a given geographical space and during a given period. Several research teams around the world are working to provide databases of global, continental, regional or even local emission inventories. The equation 7.8 (Seigneur, 2018) is a basic form used in the quantification of most pollutant emissions.

$$S_{\mathrm{ij}} = FE_{\mathrm{ij}} * A_{\mathrm{j}} \tag{7.8}$$

Where S_{ij} is the emission rate of pollutant (or precursor) i from source j (in grams per second), E_{ij} is the emission factor of pollutant i and A_{j} indicates the activity of the source (in units of activity per second).

It should be noted that each emission inventory is realized on a grid determined by its designers. In GEOS-Chem, there is a module called Harmonized Emissions Component (HEMCO) (version 2.1.008 available in this version of the model, Keller et al. (2014))

Table 7.1: Annual Global Emission Inventory for this Study (Tg/year. 1 Tg = 10×10^{12} g = 1 Million Tons)

Sources	**NO_x**	**COV**	**Inventory**
Anthropogenic emissions			
Electricity and Heat Production	31	0.7	EDGAR
Petroleum Refineries - Manufacture of Solid Fuels	0.9	2.1	DICE Africa
Other industrial sources	19.2	64.4	EDGAR
Waste and wastewater treatment	0.2	2.6	DICE Africa
Residential, commercial and institutional	6.2	36	EDGAR
Agriculture	6	4.4	RETRO
Road transport	27	25.4	EMEP and DICE Africa
Air transport	2.9	0.1	EMEP and NEI2011
Maritime transport	17	1.2	EDGAR
Others transports	1.9	0.2	DICE Africa
Subtotal of anthropic sources	112	136	-
Biomass Fires	25	251	GFED
Natural sources	53	1000	MEGAN
Subtotal of biomass burning and natural emission	78	136	-
Total	**190**	**1387**	**-**

VOCs excluding methane

NO_x emissions are expressed as NO_2

which allows to facilitate the incorporation of the inventories in GEOS-Chem without modifying its source code. This module also gives the possibility to apply scale factors, to overlay and to mask certain geographical areas available in the inventories. The emission inventories included in our simulation incorporate various datasets, including : Emissions Database for Global Atmospheric Research (EDGARD v4.3 :(Janssens-Maenhout et al., 2019)) for fossil fuel emissions, European Monitoring and Evaluation Programme (EMEP) and National Emissions Inventory 2011 (NEI2011) for regional anthropogenic emissions, Global Fire Emissions Database (GFED v4)[8] for fire emissions, Model of Emissions of Gases and Aerosols from Nature (MEGAN v2.1)[9] for biogenic emissions, and RETRO for Non-Methane Volatile Organic Compounds (COVNM) emissions. Notably, we have employed the Diffuse and Inefficient Combustion Emissions in Africa (DICE-Africa) inventory to account for anthropogenic emissions in Africa, as documented by (Marais and

[8]GFED (Global Fire Emissions Database): GFED is a widely-used global database that provides estimates of biomass burning emissions, including emissions from wildfires and agricultural fires, contributing valuable data for atmospheric and environmental research (`http://globalfiredata.org/`).

[9]MEGAN is a modeling tool used to quantify natural emissions of gases and aerosols, accounting for sources like biogenic emissions from vegetation, soil emissions, and emissions from natural events like volcanic eruptions, contributing to our understanding of atmospheric chemistry and air quality.

Wiedinmyer, 2016a). DICE-Africa is recognized as one of the most comprehensive and reliable emission inventories available, offering extensive and high-quality information on various sources across Africa. It encompasses emissions stemming from activities such as wood use in domestic and commercial settings, household combustion of harvest residues, charcoal production and consumption, gas flaring, limited oil refining (Niger Delta only), kerosene usage, diesel/petrol generators, and vehicles, including motorcycles. Table 7.1 displays the global values in Tg extracted from the above-mentioned inventories, which were used in the GEOS-Chem simulations presented in the subsequent sections.

7.6 GEOS-Chem for KINSHASA SIMULATION

The following section presents the GEOS-Chem simulations conducted at GIRPAS as part of this thesis. To assess the GEOS-Chem model's performance in simulating NO_2 and H_2CO concentrations in our study area. We conducted three specific simulations for our study. The first simulation did not include any biomass burning emission inventory, the second one incorporated the Global Fire Emissions Database (GFED) biomass burning inventory (named full simulation), and the third, a shorter simulation, integrated the Fire Emission Estimate for Research (FEER) biomass burning inventory. These diverse experiments allowed us to evaluate the efficiency and influence of these inventories within our study region. In this context, we employed multi-year global simulations commencing in 2010. This approach ensures that the years under investigation remain unaffected by the initial conditions. We saved the model outputs at intervals of 2 hours.

The GEOS-Chem model was deployed within the computational infrastructure of the GIRPAS laboratory, boasting a storage capacity of 100 terabytes dedicated to GEOS-Chem and a processing speed of 2.3 GHz[10], distributed across 32 cores. The input files utilized, including weather data and emission inventories, were detailed in the previous sections. The HEMCO module, as outlined in Section 7.5.3, facilitated the configuration of emission inventories and the application of scaling factors for the four simulations. Approximately three months were required to complete a 19-month simulation spanning from November 2019 to July 2021.

The model outputs, in the format of binary punch (bpch)[11] files, necessitated a separate code for data extraction.

7.6.1 Mass conservative extraction tools

The model generates bpch files that contain essential information such as mixing ratios and air density. The extraction process, tailored to the geographical coordinates of our Kinshasa observation station (Lat, Lon), a user-defined vertical grid, and terrain topography. To facilitate a comparison with ground-based instruments and the TROPOMI satellite, it became necessary to extract the data on the vertical grids specific to these instruments. To ensure that no information is lost during this extraction process onto a different grid than the model's predefined one, it is imperative to employ a transfer scheme that adheres

[10] AMD opteron processor : `https://www.techpowerup.com/cpu-specs/opteron-6376.c1295`

[11] "bpch" is an abbreviation for "binary punch" files: output files generated by certain atmospheric chemistry models, typically in binary format, containing chemical and atmospheric data describing the concentrations of various chemical components, meteorological variables, transport data, etc., at different altitudes and geographical locations in the atmosphere.

to mass conservation principles (Figure 7.6). To accomplish this, we employ a regridding scheme based on a theoretical framework such as the one developed by Langerock et al. (2015).

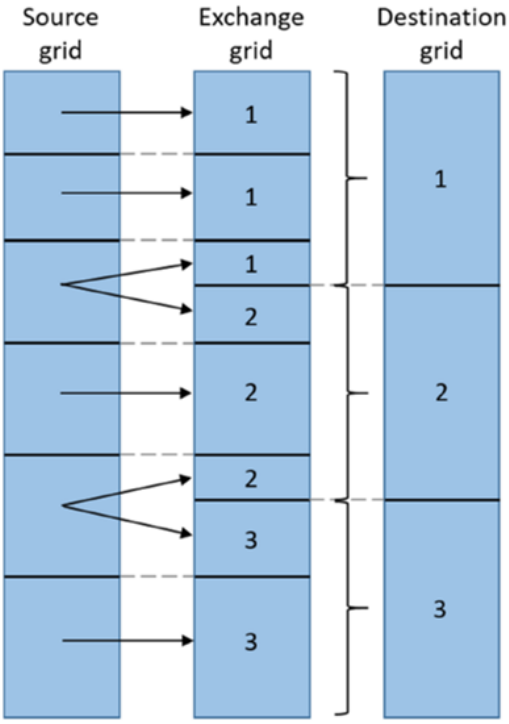

Figure 7.6: The regridding scheme employed to extract customized informations from Prignon (2021).

7.6.2 Data Smoothing

The following subsection presents the outcomes of the comparisons between GEOS-Chem model simulations and TROPOMI, as well as MAX-DOAS observations, aiming to assess the performance of the GEOS-Chem simulation over Kinshasa. These model outputs are initially extracted on the vertical grid specific to each dataset (TROPOMI and MAX-DOAS). Subsequently, they undergo a smoothing process using the respective AK corresponding to each dataset, following the formalism described by Rogers and Connor (2003) as outlined in Equation Eq.7.9 for MAX-DOAS comparisons and Equation Eq.7.10 as specified in the TROPOMI user manual (Eskes et al., 2021) for TROPOMI comparisons.

$$x_{\text{smooth}} = x_{\text{a}} + AK(x_{\text{m}} - x_{\text{a}}) \tag{7.9}$$

$$X^{smoothed}_{\text{GEOS-Chem}} = \sum_{i} AK^{SP5}_{\text{i}} * X_{\text{g}} \tag{7.10}$$

In this context, x_m represents the model profile, x_a corresponds to the a priori profile of the target compound (NO_2 or H_2CO), and AK is the Averaging Kernel matrix for MAX-DOAS related to the target compound. Finally, x_{smooth} denotes the resulting smoothed profile. This procedure ensures that the smoothed profile, derived from the model dataset,

is aligned with the same observational conditions as the MAX-DOAS measurement, which has a vertical resolution limited to approximately 4 km. In equation 7.10 used for the comparison between the model and the satellite, $X^{smoothed}_{\text{GEOS-Chem}}$ represents the smoothed GEOS-Chem profile, AK^{SP5} are the TROPOMI averaging Kernels and X_g the regridded GEOS-Chem profile.

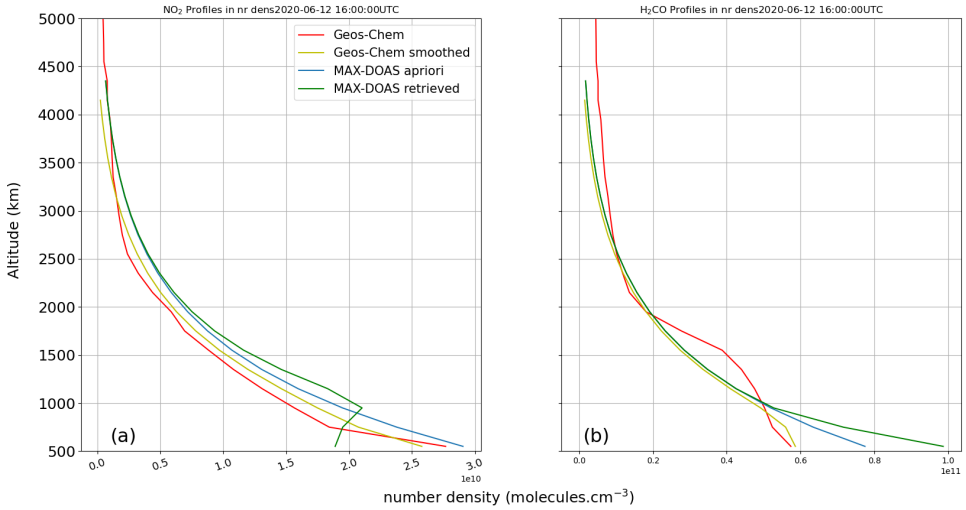

Figure 7.7: Illustration of typical GEOS-Chem profiles extracted after simulations without smoothing and with smoothing. Panels a and b depict the profiles of NO_2 and H_2CO, respectively.

The figure 7.7 provides a comparison of the NO_2 and H_2CO profiles simulated by the GEOS-Chem model, along with profiles measured by MAX-DOAS and its a priori profile for August 5th at 16:00. An notable characteristic of all these profiles is their exponential decrease, with initially high values in the lower layers of the atmosphere. However, it is essential to highlight a significant difference between the profiles measured by MAX-DOAS and those simulated by the model. The MAX-DOAS instrument has limited vertical resolution, ceasing at approximately 4 km in altitude, which means that beyond this altitude, MAX-DOAS measurements are unavailable, posing a challenge in terms of obtaining information on the free troposphere.

On the other hand, the GEOS-Chem model's profiles extend up to 80 km, providing a complete vertical coverage of the atmosphere. Our extractions were made on a vertical grid up to 16 km. In order to account for these differences in resolutions, we applied the transformations 7.9. When applying smoothing to the model profiles, we observe a loss of information. For example, in the case of NO_2, we observe a decrease in concentration from 3 x 10^{15} molecules cm^{-2} to 2.6 x 10^{15} molecules cm^{-2} for the vertical column. Similarly, in the case of H_2CO, the loss of information results in a decrease from 9 10^{15} molecules cm^{-2} to 7 x 10^{15} molecules cm^{-2} in terms of the total tropospheric column. Additionally, it is worth noting the substantial difference in horizontal resolutions. The model has a coarse resolution of 2° x 2.5°, unlike MAX-DOAS, whose horizontal sensitivity ranges from approximately 3 km to 7 km depending on visibility conditions. These limitations have thus confined the comparisons solely to TROPOMI and GEOS-Chem. For illustrative purposes, comparisons between MAX-DOAS and GEOS-Chem are provided in the appendix. In the following sections, we exclusively present comparisons between GEOS-Chem and TROPOMI because it is straightforward to extract TROPOMI data on the GEOS-Chem

grid. To achieve this, the GEOS-Chem profiles underwent a smoothing process as per Equation 7.10.

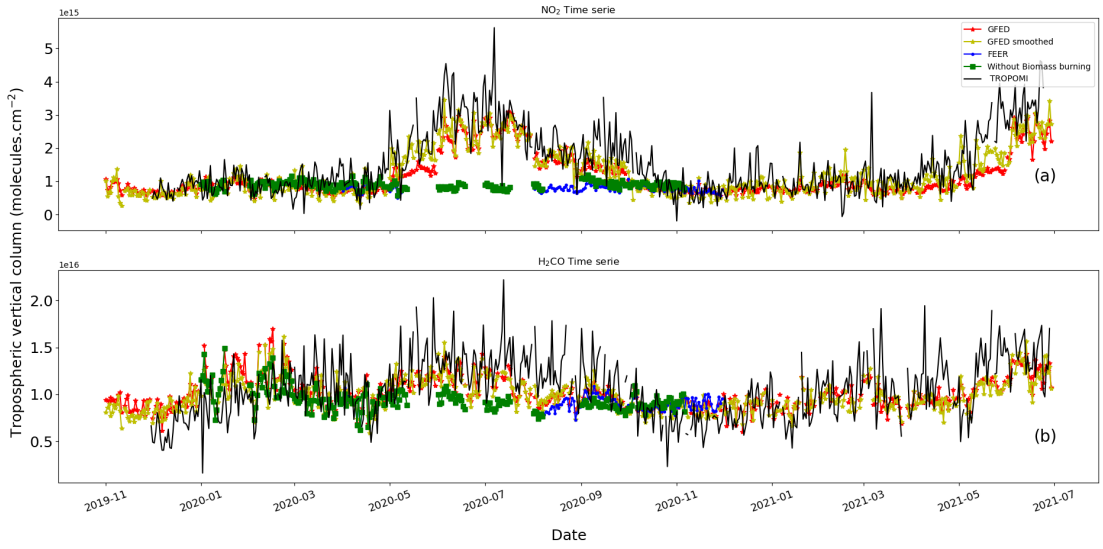

Figure 7.8: Multimonths time series comparisons for 2019/11 to 2021/06 illustrating the variations in test differences using the GEOS-Chem model. The tests involve the use of the GFED emission inventory (red), tests conducted without biomass burning (green), data smoothed with AK S5P (yellow), and TROPOMI observation data (black)

7.6.3 Intercomparison of GEOS-Chem with TROPOMI

Figure 7.8 a, b presents daily time series of average tropospheric vertical columns between 10:00 and 14:00 for NO_2 (panel a) and H_2CO (panel b). The black curve represents TROPOMI observations extracted within region (3−5°E, 13−16°S), based on the GEOS-Chem grid for the study area. In red and yellow, we have the unsmoothed and smoothed full GEOS-Chem simulations, respectively. The green lines represent GEOS-Chem simulations excluding biomass burning emissions, while the blue lines correspond to short simulations that include the FEER biomass burning emission inventory.

An immediate observation is the excellent reproduction of the seasonal cycle by both TROPOMI and the full GEOS-Chem simulation. The highest values are observed during the dry season, which is strongly marked by forest fires in this region. While the trend remains flat throughout the study period for simulations without forest fires. During the rainy periods, we can see that for NO_2, the impact of forest fires is less pronounced as both complete simulations and simulations without forest fires follow similar trends. The significant change is only evident during the dry season between May and September (Figure 7.8 panel a). However, for H_2CO, the impact of forest fires is clearly visible and present throughout the year, with a clear amplification during the dry season. Looking at Figure 7.9, we can see that the impact of these forest fire emissions reaches altitudes of up to 10 km for H_2CO and up to 5 km for NO_2. Simulations that include FEER biomass burning emissions, although conducted over a shorter period, do not appear to reproduce the observed seasonality seen in the full simulation. Therefore, the full simulation is more representative of TROPOMI observations than the other two scenarios. This is further emphasized in Table 7.2, which presents the statistical results of these comparisons.

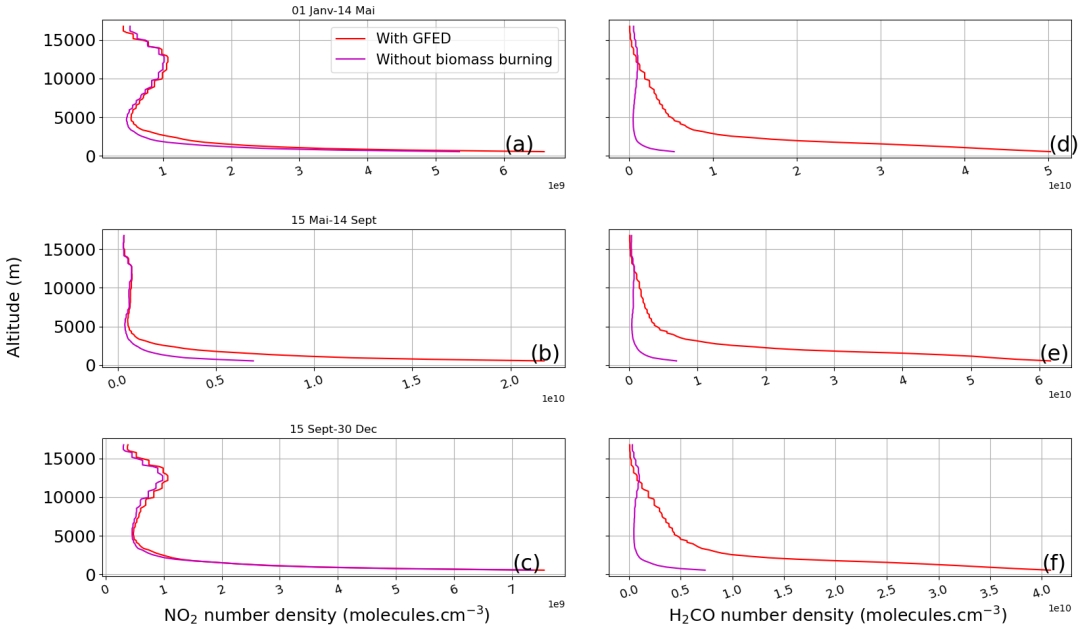

Figure 7.9: Average vertical profiles of NO_2 and H_2CO number density, simulated by GEOS-Chem, over the Kinshasa area and its surrounding (3−5°E, 13−16°S) regions. These simulations cover the period from November 2019 to July 2021, coinciding with TROPOMI's observations during the local time window of 13-14 hours in various seasons. The red and blue lines represent the profiles obtained with and without biomass burning simulations, respectively. The biomass burning inventory utilized in this analysis is derived from GFED.

Table 7.2: Statistics summary for the GEOS-Chem and TROPOMI daily average comparisons.

Parameters (NO_2/H_2CO)	WBB	BB
Number of coincidences	572 / 577	572 / 577
Slope (s)	-1.66 / 0.04	1.07 / 0.90
correlation coefficient (R)	-0.18 / 0.02	0.80 / 0.50
intercept ($\times 10^{15}$ molecules cm^{-2})	3.03 / 1.82	10.45 / 1.82
bias (%)	80.90 / 15.45	13.82 / 5.63
bias ($\times 10^{15}$ molecules cm^{-2})	0.35 / 0.95	0.07 / 0.25

WBB : Without biomass burning
BB : With biomass burning

These statistical results illustrate the good performance of the GEOS-Chem model in reproducing TROPOMI NO_2 observations, although its performance for H_2CO is somewhat weaker. The biases between the two datasets are also relatively low, with a 14% bias for NO_2 and a 6% bias for H_2CO.

The relatively weaker performance of GEOS-Chem, particularly observed for H_2CO, and the overall low biases observed in the comparisons with TROPOMI data may be attributed to several factors related to the accuracy of GEOS-Chem. This accuracy is generally influenced by various factors, including emission inventory uncertainties, the model's chemistry pertaining to the studied molecules, and meteorological conditions (Marais et al., 2021a).

Emission inventories, as used in our case, often have different spatial resolutions that are lower than that of the model, which can introduce uncertainties in our simulations. It has been noted that aerosols resulting from biomass burning emissions are inadequately defined in both global and regional models, further increasing uncertainties in understanding their impacts Pan et al. (2020). Additionally, the choice of biomass burning emission inventory has a noticeable impact on our simulations.

In our specific case, the use of the GFED emission inventory proved to be highly beneficial, enabling the reproduction of the seasonal cycles of both molecules in this region. This also revealed that while anthropogenic emissions are present, their influence appears to be less significant compared to biomass burning emissions. Indeed, in Africa as a whole, as indicated by studies such as Opio et al. (2022), biomass burning is often a significant source of both of these molecules. The latest report from CCAC (2023), which provides recent information on Africa, also emphasizes this source. For instance, Kinshasa is close to the Luki Biosphere Reserve (5.5°S, 13.3°E), where studies have confirmed biomass burning emissions occurring frequently during the dry season (Cizungu et al., 2021).

7.7 CHAPTER PARTIAL CONCLUSION

In summary, this chapter introduced the GEOS-Chem model, a chemistry and transport model that allowed us to generate NO_2 and H_2CO profiles used to calculate air mass factors. These air mass factors were then used to convert dSCDs from May 2017 to November 2019. Furthermore, we used GEOS-Chem simulations to assess the model's performance in the Kinshasa region and its surroundings.

Given the horizontal resolution of MAX-DOAS typically ranging between 3 km and 7 km depending on visibility conditions, we did not present direct comparisons between GEOS-Chem tropospheric columns and MAX-DOAS. Instead, we compared GEOS-Chem to TROPOMI observations, extracting them at the resolution of the GEOS-Chem grid covering the study area.

The results of these comparisons showed good agreement between GEOS-Chem and TROPOMI, especially for NO_2, with reasonably acceptable agreement for H_2CO. These findings demonstrate the performance of GEOS-Chem in this region. Additionally, GEOS-Chem simulations without the inclusion of biomass burning emissions showed a flat trend, confirming the importance of considering this inventory and suggesting that the impact of biomass burning is predominant compared to other sources.

Chapter 8

CONCLUSIONS AND PERSPECTIVES

8.1 FINAL CONCLUSIONS

The research described in this thesis has focused on three main themes: (1) Contribution to the development of the KinAERO instrument and its complete installation, as well as maintenance, in the city of Kinshasa since May 2017. (2) Valorisation of the observations from this instrument to carry out initial validation exercises of data from the TROPOMI satellite instrument. (3) Evaluation of the performance of the GEOS-Chem chemistry and transport model in Kinshasa and its surrounding areas.

8.1.1 On the instrument

Kinshasa, like many major cities in Central Africa, lacks adequate measurement systems for conducting in-depth studies of the atmosphere above this region. The KinAERO instrument, installed in Kinshasa, represents a crucial first step towards establishing an initial database for profiles and vertical columns of NO_2, H_2CO, and AOD in this area.

This instrument is based on the principle of DOAS, which enables the recording of UV-Visible spectra of light scattered by air molecules. Two versions of the instrument have been employed. The initial version consisted in a commercial Avantes spectrometer covering the spectral range from 280-550 nm, connected to a 600 μm optical fiber. The spectrometer was directly linked to a computer, allowing for spectrum recording and control of a commercial motorized module, coupled with the system to perform measurements at various elevation angles. This first version of the instrument was developed at the BIRA-IASB, tested, and validated through comparison with BIRA-IASB's MAX-DOAS measurements, which served as a source of inspiration. Subsequently, the instrument was transported and installed in Kinshasa in May 2017, operating until November 2019. Challenges were encountered in conducting measurements at multiple elevation angles due to the need to place the heavy Nexstar instrument on the rooftop, limiting the capability to obtain multiple multi-angle measurements.

As a result, a second version of the instrument was developed to facilitate measurements at various elevation angles automatically. This second version has been operational from

November 2019 to the present day. The data provided by this instrument consists of spectra of light scattered in the air, recorded at 2048 wavelength points, with recordings made every minute. Since May 2017, we have built a robust database of high-quality data, paving the way for atmospheric studies in this region that, until now, lacked significant data.

8.1.2 On measurements : 2017-2019

The initial spectra recorded between May 2017 and November 2019 underwent a comprehensive spectral analysis using the QDOAS program to derive the dSCDs of NO_2. These dSCDs were subsequently converted into vertical columns using air mass factors. These factors were calculated using a radiative transfer model with profile inputs from the GEOS-Chem model. Multiple Python codes were developed for this purpose to facilitate the conversion of dSCDs into VCDs.

These VCDs were then compared to observations from the OMI and TROPOMI satellite instruments. The initial findings revealed that the city of Kinshasa and its surrounding areas are heavily affected by NO_2 pollution, with elevated tropospheric vertical column densities reaching approximately $3\times\ 10^{15}$ molecules cm^{-2}. These high values were observed during the dry season, which is characterized by forest fires for agricultural land preparation.

The results of the satellite comparisons indicated that the satellites underestimate NO_2 columns, exhibiting a bias of approximately -25% compared to ground-based measurements. The analysis and interpretation of these results highlighted the limited vertical sensitivity of satellites to near-surface layers and the use of unrealistic profiles in satellite data retrieval. This motivated the installation of a new instrument capable of performing automated measurements at multiple elevation angles, thereby obtaining information on atmospheric profiles.

8.1.3 On measurements : 2019-2021

The second part of the data used in this thesis relies on spectra recorded at various elevation angles by the second version of the instrument. The analysis of these spectra was conducted using the recently developed tool FRM4DOAS at IASB. This tool serves as a framework for standardizing the processing of measurements from MAX-DOAS network stations distributed worldwide. We aimed to integrate the measurements from Kinshasa into this automated pipeline to consider them as an integral part of the stations used in the satellite instrument validation process.

This framework employs the initial steps we had previously used to analyze our early measurements, including the determination of dSCDs, air mass factor calculations, and vertical column determinations. The significant advantage of spectra at multiple elevation angles is that they allow for the acquisition of dSCDs at various elevations, thereby opening the possibility of obtaining profiles through inversion techniques. The framework used also enables the generation of these profiles using inversion algorithms such as the MMF.

We, therefore, extracted profiles of NO_2 and H_2CO by utilizing aerosol extinction via O_4 dSCDs in the visible and UV-Visible spectral ranges. These profiles proved highly valuable

in the second phase of data analysis as they allowed us to recalculate the fundamental products of TROPOMI, namely NO_2 and H_2CO VCDs, to correct errors resulting from the use of unrealistic a priori assumptions in satellite product retrieval. To achieve these corrections, we developed several Python algorithms leveraging TROPOMI's averaging kernels and the profiles.

This step was of paramount importance because, compared to the first phase where corrections could not be made due to the lack of profiles, the second phase yielded significantly improved comparison results with the satellite. Biases were substantially reduced between ground-based and satellite measurements. In fact, for our study, validation results indicated biases of approximately -12% for NO_2 and 11% for H_2CO. The seasonal cycle is clearly visible in the observations of this second instrument, categorizing Kinshasa and its surroundings as regions heavily polluted with NO_2 and H_2CO, with elevated values primarily observed during the dry season.

8.1.4 On the GEOS-Chem model

The GEOS-Chem model was initially employed to generate NO_2 profiles, which were subsequently used in the calculation of air mass factors during the initial data analysis of MAX-DOAS observations. Following this, we compared its simulations in terms of VCDs with TROPOMI observations to assess its performance in this region. Both datasets exhibited a good agreement, particularly for the two molecules. We did not directly compare GEOS-Chem with MAX-DOAS due to the significant difference in spatial resolution. However, its comparison with TROPOMI allowed us to observe that biomass burning emissions have a significant impact on the reproduction of NO_2 and H_2CO VCDs in this region. Performance tests revealed that during the rainy seasons, the impact of these biomass burning emissions was less pronounced for NO_2 compared to the dry season when it became more evident. As for H_2CO, the influence of biomass burning was clearly visible throughout the study period.

8.2 FINAL REMARK AND OUTLOOK

8.2.1 Final remark

These research efforts have made a substantial contribution to the scientific literature. Firstly, they have facilitated the establishment of an effective database for NO_2, H_2CO and AOD in the Kinshasa city and its surroundings. This region holds great significance in the validation of satellite instruments due to its central geographical location within the Congo Basin. The data collected have corroborated the high levels of NO_2 and H_2CO pollution previously reported in satellite-based studies. Moreover, these findings not only confirmed ground-level pollution but also revealed that it exceeded previous satellite-based estimates. The study demonstrated that by utilizing realistic measured profiles as a priori information, satellite observations aligned better with ground-based measurements. This approach thus enabled the initiation of a preliminary validation exercise for satellite observations in this region. Regarding the utilization of the GEOS-Chem model, our research highlighted the substantial impact of biomass burning emissions on the replication of NO_2 and H_2CO signals recorded in this region.

8.2.2 Outlook

The perspectives of this thesis offer a promising glimpse into numerous future research possibilities and enhancements to our understanding of the atmosphere in the region. Here are some of the avenues to explore:

Continuity of MAX-DOAS Measurements in Kinshasa : Although the dataset utilized in this thesis, derived from measurements obtained by the MAX-DOAS instrument, was limited in 2021, it is noteworthy that the instrument remains functional. We continue to record a series of high-quality data, consistently expanding the produced database. Future studies can further exploit this dataset. Additionally, it is worth mentioning that AOD data were underutilized in this work, suggesting the potential for in-depth exploration of this aspect in future research.

Expansion of the MAX-DOAS Network: An essential step forward would be to expand the MAX-DOAS network by installing more instruments in other cities within the country. This expansion would strengthen the database for the entire nation. As an example, in the eastern part of the DRC, where the volcano is located, the installation of a MAX-DOAS could greatly contribute to the study of SO_2 emissions during volcanic eruptions. Even in cities like Kimpese and Lukala, where cement-related activities are present, the installation of such an instrument would help monitor emissions resulting from these industrial activities. The Congo Flux Project, initiated in 2012, facilitated the installation of instruments on the Yangambi Tower right in the heart of the Congolese forest. However, the current focus of the mission is primarily on measuring greenhouse gases. The installation of a MAX-DOAS instrument to measure trace gases affecting the troposphere and air quality could also make a significant contribution to understanding the atmosphere in this region. Furthermore, extending the network on a Central African scale would be an intriguing prospect. It would allow for studies on other gases.

Improvement of GEOS-Chem Model Resolution: Although the GEOS-Chem model has been a valuable tool in this thesis, its use with a relatively limited resolution has hindered direct comparisons with MAX-DOAS observations. Therefore, it would be desirable to deepen this study by conducting simulations at a finer resolution. This would allow to better exploit information on emissions in Kinshasa. Currently, results regarding the impact of biomass burning emissions have been obtained at a relatively coarse resolution (2° x 2.5°), and a finer resolution would enable a more accurate representation of local processes. One key to the success of such a study would be to maintain collaborations with the BIRA-IASB, which possesses a regional-scale Chemistry and Transport Model called MAGRITTE[1] (Model of Atmospheric composition at Global and Regional scales using Inversion Techniques). By combining in-situ data from Kinshasa with simulations from this model, it would be possible to extract relevant information regarding Kinshasa's own emissions.

Surface Air Quality Monitoring: Given the absence of a surface air quality monitoring network in the region, it would be prudent to delve deeper into this study. This time, the use of models at a resolution suitable for a city's scale could be considered. The objective would be to estimate surface concentrations using techniques such as machine learning, combining TROPOMI data and information from the models (study example :(Chan et al., 2021)). This approach would provide a more precise

[1]MAGRITTE model code and data, https://doi.org/10.18758/71021042, 2018

picture of air quality in Kinshasa and contribute to improving environmental monitoring in the region. It would be advisable to encourage and further develop the relationships established with the Lamont Laboratory at Columbia University. They have already begun installing low-cost instruments at various intersections in Kinshasa to measure PM (McFarlane et al., 2021), and their MODULAIR gas instrument is currently installed on the roof of the University of Kinshasa, in the same location as the MAX-DOAS instrument used in this thesis (see 2.13). Ideally, this collaboration would allow us to leverage the initial surface data provided by this small network to improve and deepen the assessment of air quality in the city of Kinshasa.

APPENDIX

A Contributions to the scientific literature

A.1 Peer-reviewed

Yombo Phaka, R., Merlaud, A., Pinardi, G., Friedrich, M. M., Hendrick, F., Müller, J.-F., Stavrakou, J., De Smedt, I., Dimitropoulou, E., Bopili Mbotia Lepiba, R., Phuku Phuati, E., Djibi, B. L., Jacob, L., Fayt, C., Van Roozendael, M., Mbungu Tsumbu, J.-P. and Mahieu, E. (2023). Ground-based MAX-DOAS observations of NO_2 and H_2CO at Kinshasa and comparisons with TROPOMI observations. Atmospheric Measurement Techniques. doi:10.5194/amt-2022-327 `https://hdl.handle.net/2268/307125`

Yombo Phaka, R., Merlaud, A., Pinardi, G., Mahieu, E., Hendrick, F., Friedrich, M., Fayt, C., Van Roozendael, M.,Lomami Djibi, B., Boplili Mbotia Lepiba, R., Phuku Phuati, E. and Mbungu Tsumbu, J.-P. (2021). First Groundbased DOAS Measurements of NO_2 at Kinshasa and Comparisons with Satellite Observations. Journal of Atmospheric and Oceanic Technology. doi:10.1175/JTECH-D-20-0195.1 `https://hdl.handle.net/2268/259955`

A.2 Popular science

Yombo Phaka, R., Holenu Mangenda, H., Vuni Simbu, A., Bakambana Ndambi, R., Bopili Mbotia Lepiba, R., and Aloni Komanda, J. (10 February 2022). Suivi de la qualité de l'air dans la ville de Kinshasa par les mesures mobiles du NO_2 en differents points Géographiques. «Environment, Ingénierie and Développement (EID), 86. doi:10.46298/eid.2022.8379 `https://hdl.handle.net/2268/266165`

A.3 Oral presentations and posters

Yombo Phaka, R. and Mahieu, E. (13 December 2021). Ground-based MAX-DOAS observation of NO_2 and H_2CO over Kinshasa and comparisons with GEOS-Chem model data and TROPOMI observation. Poster session presented at American Geophysical Union (AGU) 2021 fall meeting. `https://hdl.handle.net/2268/266163`

Yombo Phaka, R. (03 April 2019). PROGRAMME DE RECHERCHE ATMOSPHERIQUE A KINSHASA. Paper presented at séminaire doctoral. `https://hdl.handle.net/2268/`

234187

Pinardi, G., Alexis, M., Martina, F., Caroline, F., Lars, J., Michel, V. R., Henri, C., Bernard, H., Caroline, V.,Benjamin, B., Yombo Phaka, R. and Mahieu, E. (2019). First results from the KinAero MAXDOAS instrument. Paper presented at EGU General Assembly 2019, Vienna, Austria.https://hdl.handle.net/2268/234193

Yombo Phaka, R. (October 2019). POLLUTION ATMOSPHERIQUE A KINSHASA (PREMIERES MESURES, PREMIERS RESULTATS). Paper presented at ISWI-MAGHREB-AFRIQUE DE L'OUEST (IMAO)/Ecole de Météorologie de l'Espace IMAO 2019, THIES, Senegal. https://hdl.handle.net/2268/247159

B A few instrumental configurations

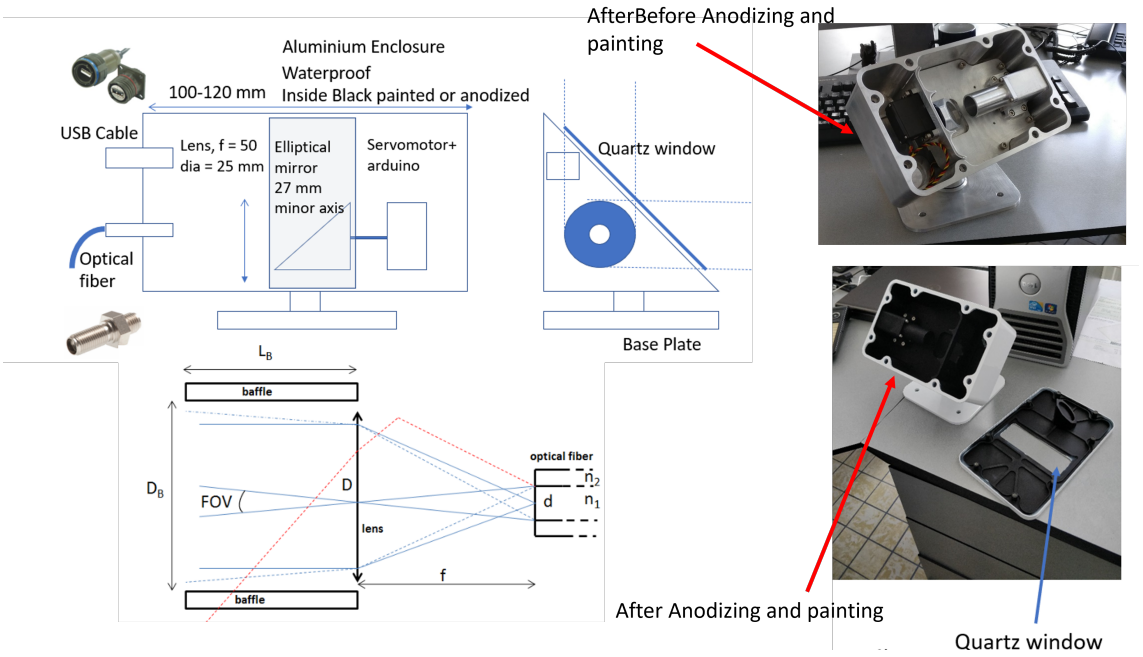

Figure B1: Optical head with arduino and scanner (Field of view calc : 0.66°).

C Comparison of KinAERO's and the IASB's MAX-DOAS DSCDs

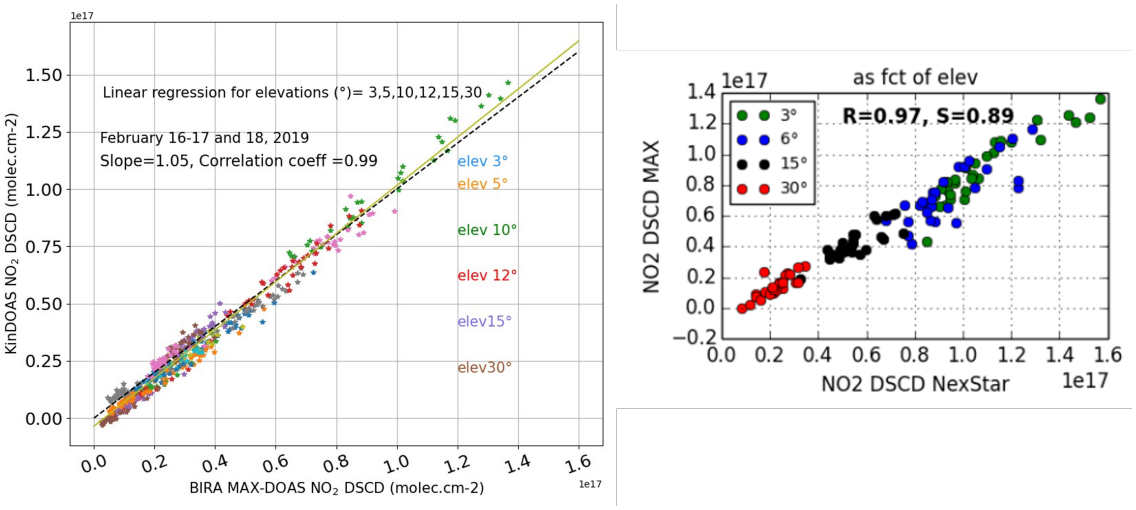

Figure C2: Relationship regression plot between the dSCDs of the MAX-DOAS instrument installed at BIRA-IASB and the Kinshasa instrument. Test carried out after development of the Kinshasa instrument.

D Kinshasa MAX-DOAS observations versus GEOS-Chem

D.1 Diurnal variation

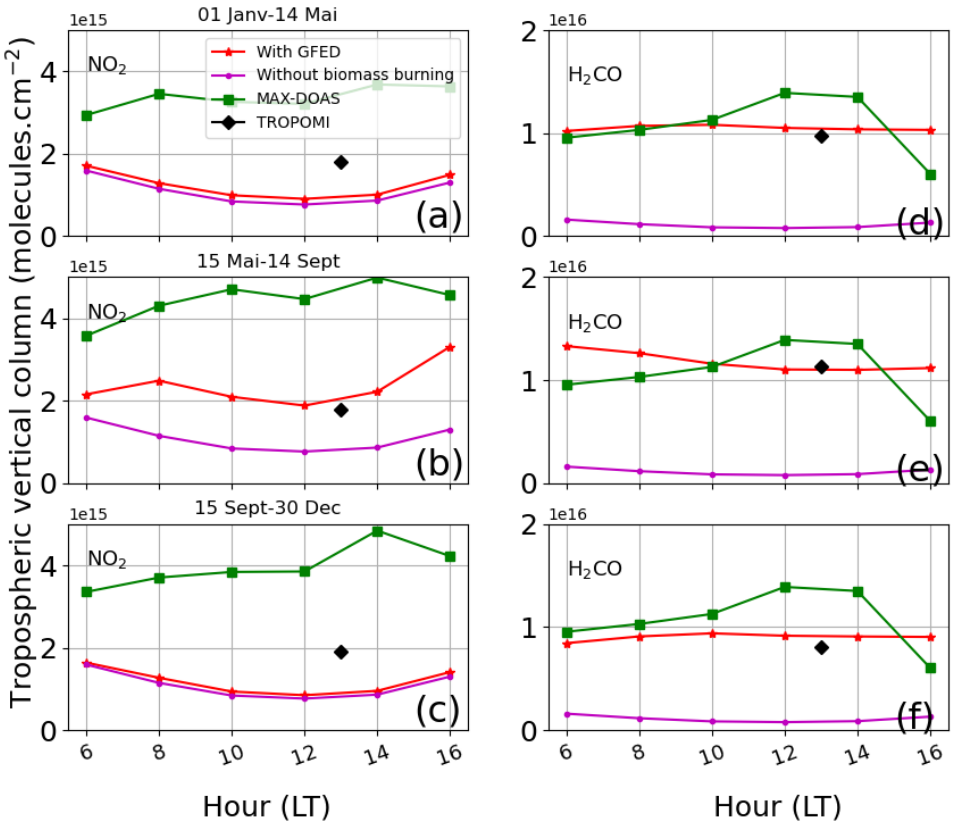

Figure D3: diurnal variation GB versus GEOS-Chem

E Correction of angular-dependent artefact in KinAero UV spectra

E.1 Problem overview

Checking on the quality of the H_2CO fitting results, we noticed that fitting residuals systematically degraded for low elevation angles. This problem was prominently observed in the UV spectral range where H_2CO is retrieved, but was essentially absent in the visible part of the spectrum used for NO_2 retrieval. The Figure E4 below, panel (a) illustrates the observed dependency. After further inspection, we noticed that the increased residual structure was systematic in nature (i.e. always of the same shape) which points to an instrumental issue. The exact reason for it could not be identified, but it might be related to an angular dependence of the spectral reflectivity of the mirror used to collect the sky light on the fiber optic (possibly connected to polarization effects). In any case we attempted to design an empirical correction to reduce the impact of these spectral features on H_2CO and O_4 retrievals. The approach adopted is described below.

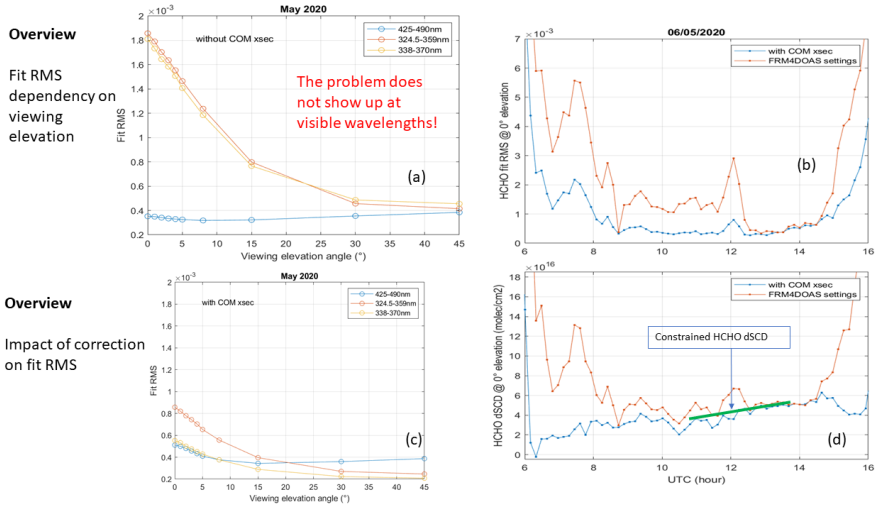

Figure E4: Eliminating H_2CO contamination in COM Cross-section.

E.2 Empirical correction

The idea of the correction is to introduce an additional vector in the DOAS fit, that effectively accounts for the systematic spectral features. This new effective cross-section was empirically constructed from measured residuals (see Figure E5) on a day showing a large variability in the effect (see Figure E4, panel b). To minimize the risk of introducing a systematic bias on the retrieved H_2CO, we constrained the H_2CO differential slant column (dSCD) in the DOAS fit applied to construct the COM residual cross-section using values extracted from surrounding measurements less affected by the artefact (see Figure E4 panels c and d). The resulting COM cross-section was then introduced in the fit for all other measurements resulting in (1) a large improvement of the fit residuals (see Figure E4, panel b), (2) a much smoother diurnal variation of the H_2CO dSCD (see Figure E4 panel d), and (3) the elimination of the correlation between H_2CO dSCDs and fit residuals (see Figure E5, panels c and d). The same procedure was applied in the spectral range used for O_4 retrieval. The impact of the correction on retrieved H_2CO and O_4 dSCDs is illustrated in Figure E7 and Figure E6. The use of these corrected dSCDs in the profiling algorithm MMF resulted in a significant improvement of the stability of the inversion (i.e. the number of rejected profiles was largely reduced), which further validates the approach.

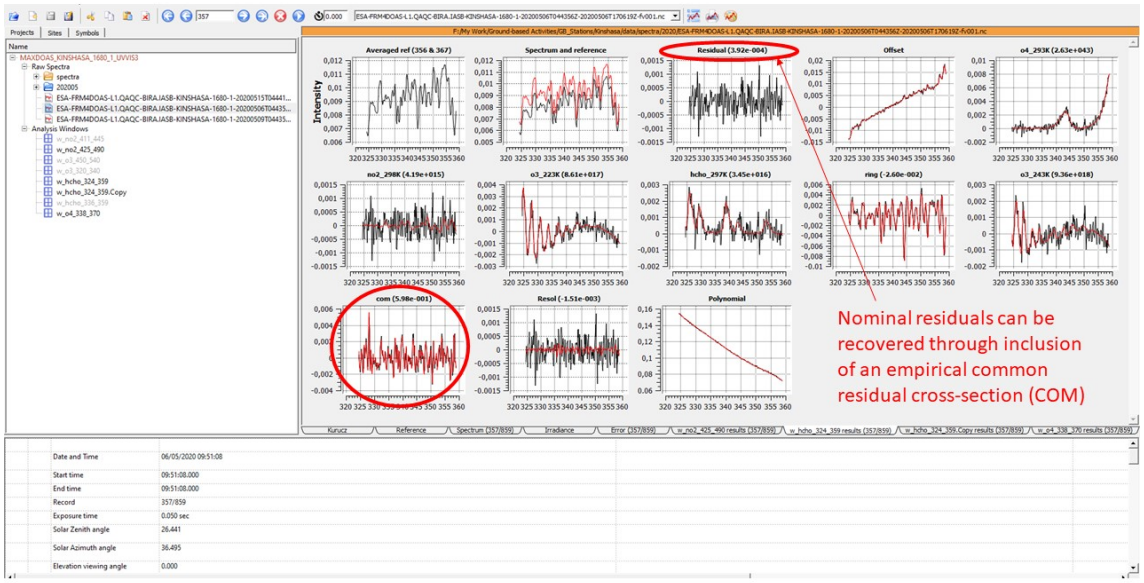

Figure E5: Recovery of Nominal Residuals via empirical Inclusion of a Common Residual Cross-section (COM).

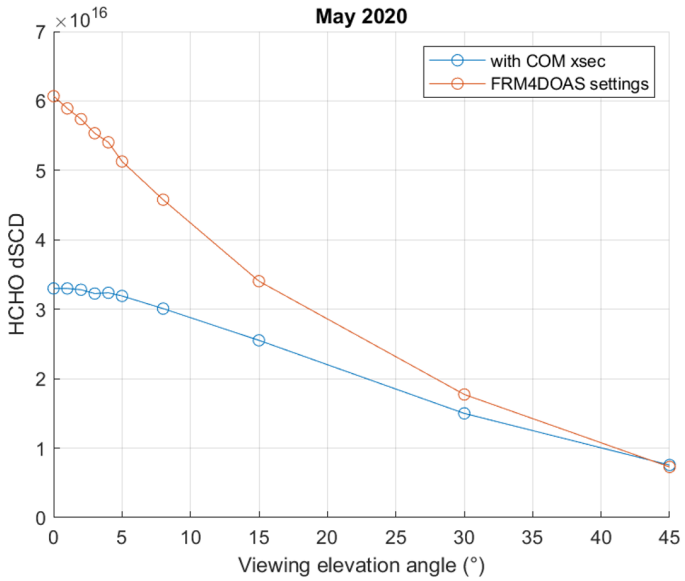

Figure E6: Impact of correction on H_2CO dSCDs. dSCDs reduced by approx. 45% at lowest elevation angles.

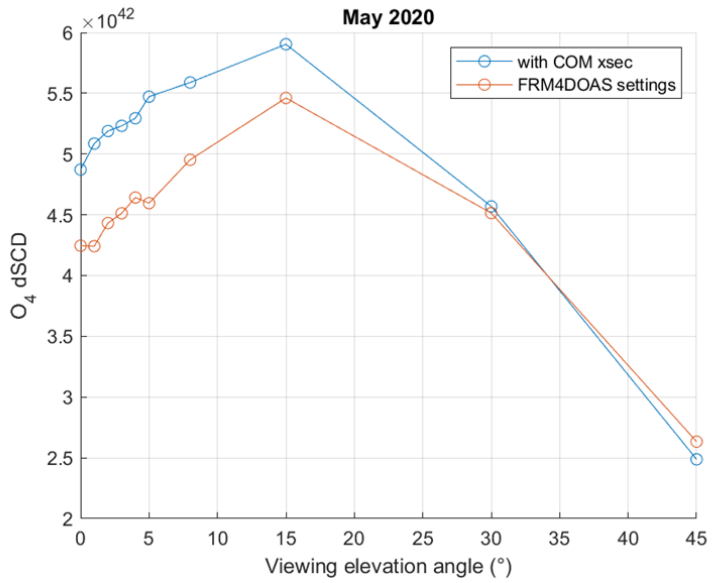

Figure E7: Impact of correction on O_4 dSCDs. Effect opposite to H_2CO, and of reduced amplitude (approx. 20% at lowest elevations)

Bibliography

Amegah, A.: Global Health Risk Factors: Air Pollution. In: Haring, R., Kickbusch, I., Ganten, D., Moeti, M. (eds) Handbook of Global Health, Springer, https://doi.org/https://doi.org/10.1007/978-3-030-05325-3_38-1, 2020.

Anderson, G., Clough, S., Kneizys, F., Chetwynd, J., and Shettle, E.: AFGL Atmospheric Constituent Profiles (0-120 km), p. 46, 1986.

Aneja, V. P., Schlesinger, W. H., and Erisman, J. W.: Effects of agriculture upon the air quality and climate: research, policy, and regulations, Environ Sci Technol, 43, 4234–4240, 2009.

Ayari, M. A.: Implantation d'un modèle de cinétique chimique dans un code d'éléments finis, Master's thesis, École Polytechnique de Montréal, URL `https://publications.polymtl.ca/9234/`, 1995.

Babatola, S. S.: Global burden of diseases attributable to air pollution, J Public Health Afr, 9, 813, 2018.

Bauer, S. E., Im, U., Mezuman, K., and Gao, C. Y.: Desert Dust, Industrialization, and Agricultural Fires: Health Impacts of Outdoor Air Pollution in Africa, Journal of Geophysical Research: Atmospheres, 124, 4104–4120, https://doi.org/https://doi.org/10.1029/2018JD029336, 2019.

Bauwens, M., Stavrakou, T., Müller, J.-F., De Smedt, I., Van Roozendael, M., van der Werf, G. R., Wiedinmyer, C., Kaiser, J. W., Sindelarova, K., and Guenther, A.: Nine years of global hydrocarbon emissions based on source inversion of OMI formaldehyde observations, Atmospheric Chemistry and Physics, 16, 10 133–10 158, https://doi.org/10.5194/acp-16-10133-2016, 2016.

Beirle, S., Dörner, S., Donner, S., Remmers, J., Wang, Y., and Wagner, T.: The Mainz profile algorithm (MAPA), Atmos. Meas. Tech., 12, 1785–1806, https://doi.org/10.5194/amt-12-1785-2019, 2019.

Benbrahim-Tallaa, L., Baan, R. A., Grosse, Y., Lauby-Secretan, B., El Ghissassi, F., Bouvard, V., Guha, N., Loomis, D., Straif, K., and International Agency for Research on Cancer Monograph Working Group: Carcinogenicity of diesel-engine and gasoline-engine exhausts and some nitroarenes, Lancet Oncol, 13, 663–664, 2012.

Bey, I., Jacob, D. J., Yantosca, R. M., Logan, J. A., Field, B. D., Fiore, A. M., Li, Q., Liu, H. Y., Mickley, L. J., and Schultz, M. G.: Global modeling of tropospheric chemistry with assimilated meteorology: Model description and evaluation, Journal of Geophysical Research Atmospheres, 106, 23 073–23 095, https://doi.org/10.1029/2001JD000807, 2001.

Bian, H. and Prather, M.: Fast-J2: Accurate simulation of stratospheric photolysis in global chemical models, Journal of Atmospheric Chemistry, 41, 281–296, 2002.

Bockarie, A. S., Marais, E. A., and MacKenzie, A. R.: Air Pollution and Climate Forcing of the Charcoal Industry in Africa, Environmental Science & Technology, 54, 13 429–13 438, https://doi.org/10.1021/acs.est.0c03754, 2020.

Boersma, K. F. and Coauthors: QA4ECV Product Specification Document for the QA4ECV NO2 ECV Precursor Product, Atmospheric Measurement Techniques, 11, 1–32, https://doi.org/10.5194/amt-11-1-2018, 2017.

Boersma, K. F., Eskes, H. J., and Brinksma, E. J.: Error analysis for tropospheric NO2 retrieval from space, Journal of Geophysical Research: Atmospheres, 109, https://doi.org/10.1029/2003jd003962, 2004.

Boersma, K. F., Eskes, H. J., Richter, A., De Smedt, I., Lorente, A., Beirle, S., van Geffen, J. H. G. M., Zara, M., Peters, E., Van Roozendael, M., Wagner, T., Maasakkers, J. D., van der A, R. J., Nightingale, J., De Rudder, A., Irie, H., Pinardi, G., Lambert, J.-C., and Compernolle, S. C.: Improving algorithms and uncertainty estimates for satellite NO_2 retrievals: results from the quality assurance for the essential climate variables (QA4ECV) project, Atmospheric Measurement Techniques, 11, 6651–6678, https://doi.org/10.5194/amt-11-6651-2018, 2018a.

Boersma, K. F., Eskes, H. J., Richter, A., De Smedt, I., Lorente, A., Beirle, S., van Geffen, J. H. G. M., Zara, M., Peters, E., Van Roozendael, M., Wagner, T., Maasakkers, J. D., van der A, R. J., Nightingale, J., De Rudder, A., Irie, H., Pinardi, G., Lambert, J.-C., and Compernolle, S. C.: Improving algorithms and uncertainty estimates for satellite NO2 retrievals: results from the quality assurance for the essential climate variables (QA4ECV) project, Atmospheric Measurement Techniques, 11, 6651–6678, https://doi.org/10.5194/amt-11-6651-2018, © Author(s) 2018. This work is distributed under the Creative Commons Attribution 4.0 License., 2018b.

Bogumil, K., Orphal, J., and Burrows, J. P.: Temperature dependent absorption cross sections of O3, NO2, and other atmospheric trace gases measured with the SCIAMACHY spectrometer, in: Looking down to Earth in the New Millennium, Proceedings of the ERS-ENVISAT Symposium, ESA publication SP-461, Gothenburg, Sweden, 2000.

Bornman, M. S., Aneck-Hahn, N. H., de Jager, C., Wagenaar, G. M., Bouwman, H., Barnhoorn, I. E. J., Patrick, S. M., Vandenberg, L. N., Kortenkamp, A., Blumberg, B., Kimmins, S., Jegou, B., Auger, J., DiGangi, J., and Heindel, J. J.: Endocrine Disruptors and Health Effects in Africa: A Call for Action, Environ Health Perspect, 125, 085 005, 2017.

Boucher, O.: Aérosols atmosphériques - Propriétés et impacts climatiques, Springer Verlag, Paris, 2012.

Brewer, A. W., Mcelroy, C. T., and Kerr, J. B.: Nitrogen Dioxide Concentrations in the Atmosphere, Nature, 246, 129–133, 1973.

Brink, A.: Mapping land cover dynamics with Copernicus, World Heritage Review, 98, 32–37, https://doi.org/10.18356/27887138-2021-98-4, 2021.

Cahalan, R. F., Ridgway, W., Wiscombe, W. J., Bell, T. L., and Snider, J. B.: The Albedo of Fractal Stratocumulus Clouds, Journal of Atmospheric Sciences, 51, 2434 – 2455, https://doi.org/https://doi.org/10.1175/1520-0469(1994)051⟨2434:TAOFSC⟩2.0.CO;2, 1994.

Cai, K., Li, S., Lai, J., Xia, Y., Wang, Y., Hu, X., and Li, A.: Evaluation of TROPOMI and OMI Tropospheric NO2 Products Using Measurements from MAX-DOAS and State-Controlled Stations in the Jiangsu Province of China, Atmosphere, 13, 886, https://doi.org/10.3390/atmos13060886, 2022.

CCAC: Full Report: Integrated Assessment of Air Pollution and Climate Change for Sustainable Development in Africa, Tech. rep., Climate and Clean Air Coalition (CCAC), URL `https://www.ccacoalition.org/resources/`, 2023.

Chailleux, Y.: Observation satellitaire de la pollution à l'ozone par synergie multispectrale à trois bandes Ultraviolet+Visible+Infrarouge, Theses, Université Paris-Est, URL `https://theses.hal.science/tel-02066124`, 2018.

Chan, A. W. and Coauthors: Role of Aldehyde Chemistry and NOx Concentrations in Secondary Organic Aerosol Formation, Atmospheric Chemistry and Physics, 10, 7169–7188, https://doi.org/10.5194/acp-10-716, 2010.

Chan, K. L., Wiegner, M., Geffen, J. V., Smedt, I. D., Alberti, C., Cheng, Z., Ye, S., and Wenig, M.: MAX-DOAS measurements of tropospheric NO2and HCHO in Munich and the comparison to OMI and TROPOMI satellite observations, Atmos. Meas. Tech., 13, 4499–4520, https://doi.org/10.5194/amt-13-4499-2020, 2020a.

Chan, K. L., Wiegner, M., van Geffen, J., De Smedt, I., Alberti, C., Cheng, Z., Ye, S., and Wenig, M.: MAX-DOAS measurements of tropospheric NO_2 and HCHO in Munich and the comparison to OMI and TROPOMI satellite observations, Atmospheric Measurement Techniques, 13, 4499–4520, https://doi.org/10.5194/amt-13-4499-2020, 2020b.

Chan, K. L., Khorsandi, E., Liu, S., Baier, F., and Valks, P.: Estimation of Surface NO2 Concentrations over Germany from TROPOMI Satellite Observations Using a Machine Learning Method, Remote Sensing, 13, https://doi.org/10.3390/rs13050969, 2021.

Chance, K. and Kurucz, R. L.: An improved high-resolution solar reference spectrum for earth's atmosphere measurements in the ultraviolet, visible, and near infrared, Journal of Quantitative Spectroscopy and Radiative Transfer, 111, 1289–1295, https://doi.org/10.1016/j.jqsrt.2010.01.036, 2010a.

Chance, K. V. and Kurucz, R. L.: An improved high-resolution solar reference spectrum for earth's atmosphere measurements in the ultraviolet, visible, and near infrared, J. Quant. Spectrosc. Radiat. Transfer, 111, 1289–1295, 2010b.

Chance, K. V. and Spurr, R. J. D.: Ring effect studies: Rayleigh scattering, including molecular parameters for rotational Raman scattering, and the Fraunhofer spectrum, Applied Optics, 36, 5224–5230, 1997.

Chandrasekhar, S.: Radiative transfer, 1960.

Chen, D., Zhou, B., Beirle, S., Chen, L. M., and Wagner, T.: Tropospheric NO_2 column densities deduced from zenith-sky DOAS measurements in Shanghai, China, and their application to satellite validation, Atmospheric Chemistry and Physics, 9, 3641–3662, https://doi.org/10.5194/acp-9-3641-2009, 2009.

Cheng, Y., Wang, Y., Zhang, Y., Crawford, J. H., Diskin, G. S., Weinheimer, A. J., and Fried, A.: Estimator of Surface Ozone Using Formaldehyde and Carbon Monoxide Concentrations Over the Eastern United States in Summer, Journal of Geophysical Research: Atmospheres, 123, 7642–7655, https://doi.org/https://doi.org/10.1029/2018JD028452, 2018.

Chimot, J., Vlemmix, T., Veefkind, J. P., de Haan, J. F., and Levelt, P. F.: Impact of aerosols on the OMI tropospheric NO_2 retrievals over industrialized regions: how accurate is the aerosol correction of cloud-free scenes via a simple cloud model?, Atmospheric Measurement Techniques, 9, 359–382, https://doi.org/10.5194/amt-9-359-2016, 2016.

Cizungu, N. C., Tshibasu, E., Lutete, E., Mushagalusa, C. A., Mugumaarhahama, Y., Ganza, D., Karume, K., Michel, B., Lumbuenamo, R., and Bogaert, J.: Fire risk assessment, spatiotemporal clustering and hotspot analysis in the Luki biosphere reserve region, western DR Congo, Trees, Forests and People, 5, 100 104, https://doi.org/ https://doi.org/10.1016/j.tfp.2021.100104, 2021.

Clemer, K., Van Roozendael, M., Fayt, C., Hendrick, F., Hermans, C., Pinardi, G., Spurr, R., Wang, P., and De Mazière, M.: Multiple wavelength retrieval of tropospheric aerosol optical properties from MAXDOAS measurements in Beijing, Atmospheric Measurement Techniques, 3, 863–878, https://doi.org/10.5194/amt-3-863-2010, 2010.

Compernolle, S., Verhoelst, T., Pinardi, G., Granville, J., Hubert, D., Keppens, A., Niemeijer, S., Rino, B., Bais, A., Beirle, S., Boersma, K., Burrows, J., De Smedt, I., Eskes, H., Goutail, F., Hendrick, F., Lorente, A., Pazmino, A., Piters, A., and Lambert, J.-C.: Validation of Aura-OMI QA4ECV NO2 Climate Data Records with ground-based DOAS networks: role of measurement and comparison uncertainties, Atmospheric Chemistry and Physics, 20, https://doi.org/10.5194/acp-20-8017-2020, 2020.

Constantin, D. E., Merlaud, A., Roozendael, M. V., Voiculescu, M., Fayt, C., Hendrick, F., Pinardi, G., and Georgescu, L.: Measurements of tropospheric NO2, Sensors, 13, 3922–3940, https://doi.org/10.3390/s130303922, 2013.

Copernicus Climate Change Service (C3S): ERA5: Fifth generation of ECMWF atmospheric reanalyses of the global climate, accessed 24 September 2019, 2017.

Crutzen, P. J.: The The role of No and NO2 in the chemistry of the troposphere and stratosphere, Ann. Rev. Earth Planet. Sci, 7, 443–72, URL `www.annualreviews.org`, 1979.

Damian, V., Sandu, A., Damian, M., Potra, F., and Carmichael, G.: The kinetic preprocessor KPP - A software environment for solving chemical kinetics, Computers and Chemical Engineering, 26(11), 1567–1579, https://doi.org/10.1016/S0098-1354(02)00128-X, 2002.

Danckaert, T. and Fayt, C.: QDOAS Software user manual, September, Royal Belgian Institute for Space Aeronomy (BIRA), Brussel, 2017.

de Foy, B., Krotkov, N. A., Bei, N., Herndon, S. C., Huey, L. G., Martínez, A.-P., Ruiz-Suárez, L. G., Wood, E. C., Zavala, M., and Molina, L. T.: Hit from both sides: tracking industrial and volcanic plumes in Mexico City with surface measurements and OMI SO_2 retrievals during the MILAGRO field campaign, Atmospheric Chemistry and Physics, 9, 9599–9617, https://doi.org/10.5194/acp-9-9599-2009, 2009.

de Graaf, M., Sihler, H., Tilstra, L. G., and Stammes, P.: How big is an OMI pixel?, Atmospheric Measurement Techniques, 9, 3607–3618, https://doi.org/10.5194/amt-9-3607-2016, 2016.

de Haan, J. F., Bosma, P. B., and Hovenier, J. W.: The adding method for multiple scattering calculations of polarized light, , 183, 371–391, 1987.

De Smedt, I., Stavrakou, T., Hendrick, F., Danckaert, T., Vlemmix, T., Pinardi, G., Theys, N., Lerot, C., Gielen, C., Vigouroux, C., Hermans, C., Fayt, C., Veefkind, P., Müller, J.-F., and Van Roozendael, M.: Diurnal, seasonal and long-term variations of global formaldehyde columns inferred from combined OMI and GOME-2 observations, Atmospheric Chemistry and Physics, 15, 12 519–12 545, https://doi.org/10.5194/acp-15-12519-2015, 2015.

De Smedt, I., Theys, N., Yu, H., Danckaert, T., Lerot, C., Compernolle, S., Van Roozendael, M., Richter, A., Hilboll, A., Peters, E., Pedergnana, M., Loyola, D., Beirle, S., Wagner, T., Eskes, H., van Geffen, J., Boersma, K. F., and Veefkind, P.: Algorithm theoretical baseline for formaldehyde retrievals from S5P TROPOMI and from the QA4ECV project, Atmospheric Measurement Techniques, 11, 2395–2426, https://doi.org/10.5194/amt-11-2395-2018, 2018.

De Smedt, I., Pinardi, G., Vigouroux, C., Compernolle, S., Bais, A., Benavent, N., Boersma, F., Chan, K.-L., Donner, S., Eichmann, K.-U., Hedelt, P., Hendrick, F., Irie, H., Kumar, V., Lambert, J.-C., Langerock, B., Lerot, C., Liu, C., Loyola, D., Piters, A., Richter, A., Rivera Cárdenas, C., Romahn, F., Ryan, R. G., Sinha, V., Theys, N., Vlietinck, J., Wagner, T., Wang, T., Yu, H., and Van Roozendael, M.: Comparative assessment of TROPOMI and OMI formaldehyde observations and validation against MAX-DOAS network column measurements, Atmospheric Chemistry and Physics, 21, 12 561–12 593, https://doi.org/10.5194/acp-21-12561-2021, 2021.

de Vries, W.: Impacts of nitrogen emissions on ecosystems and human health: A mini review, Current Opinion in Environmental Science Health, 21, 100 249, https://doi.org/https://doi.org/10.1016/j.coesh.2021.100249, 2021.

Dee, D. P., Uppala, S. M., Simmons, A. J., Berrisford, P., Poli, P., Kobayashi, S., Andrae, U., Balmaseda, M. A., Balsamo, G., Bauer, P., Bechtold, P., Beljaars, A. C. M., van de Berg, L., Bidlot, J., Bormann, N., Delsol, C., Dragani, R., Fuentes, M., Geer, A. J., Haimberger, L., Healy, S. B., Hersbach, H., Hólm, E. V., Isaksen, L., Kållberg, P., Köhler, M., Matricardi, M., McNally, A. P., Monge-Sanz, B. M., Morcrette, J.-J., Park, B.-K., Peubey, C., de Rosnay, P., Tavolato, C., Thépaut, J.-N., and Vitart, F.: The ERA-Interim reanalysis: configuration and performance of the data assimilation system, Quarterly Journal of the Royal Meteorological Society, 137, 553–597, https://doi.org/https://doi.org/10.1002/qj.828, 2011.

Dentener, F., van Weele, M., Krol, M., Houweling, S., and van Velthoven, P.: Trends and inter-annual variability of methane emissions derived from 1979-1993 global CTM simulations, Atmospheric Chemistry and Physics, 3, 73–88, https://doi.org/10.5194/acp-3-73-2003, 2003.

Dimitropoulou, E., Hendrick, F., Pinardi, G., Friedrich, M. M., Merlaud, A., Tack, F., Longueville, H. D., Fayt, C., Hermans, C., Laffineur, Q., Fierens, F., and Roozendael, M. V.: Validation of TROPOMI tropospheric NO2 columns using dual-scan multi-axis differential optical absorption spectroscopy (MAX-DOAS) measurements in Uccle, Brussels, Atmos. Meas. Tech., 13, 5165–5191, https://doi.org/10.5194/amt-13-5165-2020, 2020.

Dobber, M., Voors, R., Dirksen, R., Kleipool, Q., and Levelt, P.: The high-resolution solar reference spectrum between 250 and 550 nm and its application to measurements with the Ozone Monitoring Instrument, Solar Physics, 249, 281–291, https://doi.org/10.1007/s11207-008-9187-7, 2008.

Dornelles, K., Roriz, M., Roriz, V., and Caram, R.: Thermal performance of white solar-reflective paints for coll roofs and the influence on the thermal comfort and building energy use in hot climates, https://doi.org/10.13140/RG.2.1.1745.5843, 2011.

Eastham, S. D., Long, M. S., Keller, C. A., Lundgren, E., Yantosca, R. M., Zhuang, J., Li, C., Lee, C. J., Yannetti, M., Auer, B. M., Clune, T. L., Kouatchou, J., Putman, W. M., Thompson, M. A., Trayanov, A. L., Molod, A. M., Martin, R. V., and Jacob, D. J.: GEOS-Chem High Performance (GCHP v11-02c): a next-generation implementation of the GEOS-Chem chemical transport model for massively parallel applications, Geoscientific Model Development, 11, 2941–2953, https://doi.org/10.5194/gmd-11-2941-2018, 2018.

Edner, H., Ragnarson, P., Spannare, S., and Svanberg, S.: Differential Optical-absorption Spectroscopy (DOAS) System For Urban Atmospheric-pollution Monitoring, Optical Society of America. Journal B: Optical Physics, 32, 327–333, https://doi.org/10.1364/AO.32.000327, 1993.

Engelbrecht, J. P., Swanepoel, L., Chow, J. C., Watson, J. G., and Egami, R. T.: PM2.5 and PM10 concentrations from the Qalabotjha low-smoke fuels macro-scale experiment in South Africa, Environ Monit Assess, 69, 1–15, 2001.

Errera, Q. and Fonteyn, D.: Four-dimensional variational chemical assimilation of CRISTA stratospheric measurements, Journal of Geophysical Research: Atmospheres, 106, 12 253–12 265, https://doi.org/https://doi.org/10.1029/2001JD900010, 2001.

Eskes, H., van Geffen, J., Boersma, F., Eichmann, K.-U., Apituley, A., Pedergnana, M., Sneep, M., Veefkind, J. P., and Loyola, D.: Sentinel-5 Precursor/TROPOMI Level 2 Product User Manual: Nitrogen Dioxide, Tech. rep., 2021.

Eskes, H. J. and Boersma, K. F.: Averaging kernels for DOAS total-column satellite retrievals, Atmospheric Chemistry and Physics, 3, 1285–1291, https://doi.org/10.5194/acp-3-1285-2003, 2003.

Ferreira, V. M.: Inversion de spectres infrarouges en émission thermique de la basse atmosphère terrestre enregistrés sous ballon par transformée de Fourier en visée au nadir : préparation de la mission spatiale IASI, Theses, Université Pierre et Marie Curie - Paris VI, URL `https://theses.hal.science/tel-00009090`, 2005.

Ferrel, W.: Atmospheric circulation, Encyclopædia Britannica, URL `https://www.britannica.com/science/Ferrel-cell`, 2010.

Fisher, S., Bellinger, D. C., Cropper, M. L., Kumar, P., Binagwaho, A., Koudenoukpo, J. B., Park, Y., Taghian, G., and Landrigan, P. J.: Air pollution and development in Africa: impacts on health, the economy, and human capital, Lancet Planet Health, 5, e681–e688, URL `https://www.thelancet.com/journals/lanplh/article\/PIIS2542-5196(21)00201-1/fulltext`, 2021.

Fleischmann, O. C., Hartmann, M., Burrows, J. P., and Orphal, J.: New ultraviolet absorption cross-sections of BrO at atmospheric temperatures measured by time-windowing Fourier transform spectroscopy, Journal of Photochemistry and Photobiology A: Chemistry, 168, 117–132, https://doi.org/https://doi.org/10.1016/j.jphotochem.2004.03.026, 2004.

Fortems-Cheiney, A., Chevallier, F., Pison, I., Bousquet, P., Saunois, M., Szopa, S., Cressot, C., Kurosu, T. P., Chance, K., and Fried, A.: The formaldehyde budget as seen by

a global-scale multi-constraint and multi-species inversion system, Atmos. Chem. Phys., 12, 6699–6721, https://doi.org/10.5194/acp-12-6699-2012, 2012.

Freire, M., Lall, S., and Leipziger, D.: Africa's Urbanization: Challenges and Opportunities, Tech. rep., The Growth Dialogue, Washington, DC 20052, URL http://growthdialogue.org/growthdialog/wp-content/uploads/2017/09/Working-Paper-Africa-Urbanization.pdf, 2014.

Friedrich, M., Rivera, C., Stremme, W., Ojeda, Z., Arellano, J., Bezanilla, A., García-Reynoso, J. A., and Grutter, M.: NO2 vertical profiles and column densities from MAX-DOAS measurements in Mexico City, Atmos. Meas. Tech., 12, 2545–2565, https://doi.org/10.5194/amt-12-2545-2019, 2019.

Frieß, U., Beirle, S., Alvarado Bonilla, L., Bösch, T., Friedrich, M. M., Hendrick, F., Piters, A., Richter, A., van Roozendael, M., Rozanov, V. V., Spinei, E., Tirpitz, J.-L., Vlemmix, T., Wagner, T., and Wang, Y.: Intercomparison of MAX-DOAS vertical profile retrieval algorithms: studies using synthetic data, Atmos. Meas. Tech., 12, 2155–2181, https://doi.org/10.5194/amt-12-2155-2019, 2019.

Frieß, U., Monks, P., Remedios, J., Rozanov, A., Sinreich, R., Wagner, T., and Platt, U.: MAX-DOAS O4 measurements: A new technique to derive information on atmospheric aerosols: 2. Modeling studies, Journal of Geophysical Research, 111, https://doi.org/10.1029/2005JD006618, 2006.

Frisvad, J. R. and Kragh, H.: On Ludvig Lorenz and his 1890 treatise on light scattering by spheres, The European Physical Journal H, 44, 137–160, https://doi.org/10.1140/epjh/e2019-100022-y, 2019.

Fritz, T. M., Eastham, S. D., Emmons, L. K., Lin, H., Lundgren, E. W., Goldhaber, S., Barrett, S. R. H., and Jacob, D. J.: Implementation and evaluation of the GEOS-Chem chemistry module version 13.1.2 within the Community Earth System Model v2.1, EGUsphere, 2022, 1–54, https://doi.org/10.5194/egusphere-2022-226, 2022.

FRM4DOAS ATBD, A.: Fiducial Reference Measurements for Ground-Based DOAS Air-Quality Observations Deliverable D3 : MAXDOAS Instruments Review, Tech. Rep. 4000118181, 2017.

Fuglestvedt, J. S., Berntsen, T. K., Isaksen, I. S., Mao, H., Liang, X.-Z., and Wang, W.-C.: Climatic forcing of nitrogen oxides through changes in tropospheric ozone and methane; global 3D model studies, Atmospheric Environment, 33, 961–977, https://doi.org/https://doi.org/10.1016/S1352-2310(98)00217-9, 1999.

Galle, B., Johansson, M., Rivera, C., Zhang, Y., Kihlman, M., Kern, C., Lehmann, T., Platt, U., Arellano, S., and Hidalgo, S.: Network for Observation of Volcanic and Atmospheric Change (NOVAC)—A global network for volcanic gas monitoring: Network layout and instrument description, Journal of Geophysical Research: Atmospheres, 115, https://doi.org/https://doi.org/10.1029/2009JD011823, 2010.

Gelaro, R., McCarty, W., Suárez, M. J., Todling, R., Molod, A., Takacs, L., Randles, C. A., Darmenov, A., Bosilovich, M. G., Reichle, R., Wargan, K., Coy, L., Cullather, R., Draper, C., Akella, S., Buchard, V., Conaty, A., da Silva, A. M., Gu, W., Kim, G.-K., Koster, R., Lucchesi, R., Merkova, D., Nielsen, J. E., Partyka, G., Pawson, S., Putman, W., Rienecker, M., Schubert, S. D., Sienkiewicz, M., and Zhao, B.: The Modern-Era Retrospective Analysis for Research and Applications, Version 2 (MERRA-2), Journal

of Climate, 30, 5419 – 5454, https://doi.org/https://doi.org/10.1175/JCLI-D-16-0758.1, 2017.

Giannini, A., Biasutti, M., Held, I. M., and Sobel, A. H.: A global perspective on African climate, Climatic Change, 90, 359–383, 2008.

Gielen, C. and Coauthors: A simple and versatile cloud-screening method for MAX-DOAS retrievals, Atmospheric Measurement Techniques, 7, 3509–3527, https://doi.org/10.5194/amt-7-3509-2014, 2014.

Gielen, C., Roozendael, M. V., Hendrick, F., Pinardi, G., Vlemmix, T., Bock, V. D., Backer, H. D., Fayt, C., Hermans, C., Gillotay, D., and Wang, P.: A simple and versatile cloud-screening method for MAX-DOAS retrievals, Atmos. Meas. Tech., 7, 3509–3527, https://doi.org/10.5194/amt-7-3509-2014, 2014.

Gielen, C., Hendrick, F., Pinardi, G., De Smedt, I., Fayt, C., Hermans, C., Stavrakou, T., Bauwens, M., Müller, J.-F., Ndenzako, E., Nzohabonayo, P., Akimana, R., Niyonzima, S., Van Roozendael, M., and De Mazière, M.: Characterisation of Central-African aerosol and trace-gas emissions based on MAX-DOAS measurements and model simulations over Bujumbura, Burundi, Atmospheric Chemistry and Physics Discussions, 2017, 1–41, https://doi.org/10.5194/acp-2016-1104, 2017.

Godfrey, S. and Tunhuma, F.: The Climate Crisis: Climate Change Impacts, Trends and Vulnerabilities of Children in Sub Sahara Africa., Tech. rep., United Nations Children's Fund Eastern and Southern Africa Regional Office, Nairobi., URL `https://www.unicef.org/esa/media/7061/file/UNICEF-The-Climate-Crisis-2020.pdf`., 2020.

Griffin, D., Zhao, X., McLinden, C. A., Boersma, F., Bourassa, A., Dammers, E., Degenstein, D., Eskes, H., Fehr, L., Fioletov, V., Hayden, K., Kharol, S. K., Li, S. M., Makar, P., Martin, R. V., Mihele, C., Mittermeier, R. L., Krotkov, N., Sneep, M., Lamsal, L. N., ter Linden, M., van Geffen, J., Veefkind, P., and Wolde, M.: High-Resolution Mapping of Nitrogen Dioxide With TROPOMI: First Results and Validation Over the Canadian Oil Sands, Geophysical Research Letters, 46, 1049–1060, https://doi.org/10.1029/2018GL081095, 2019.

Guenther, A., Karl, T., Harley, P., Wiedinmyer, C., Palmer, P. I., and Geron, C.: Estimates of global terrestrial isoprene emissions using MEGAN (Model of Emissions of Gases and Aerosols from Nature), Atmospheric Chemistry and Physics, 6, 3181–3210, URL `https://hal.science/hal-00295995`, 2006.

Hardy, K., Buckley, S., Collins, M. J., Estalrrich, A., Brothwell, D., Copeland, L., García-Tabernero, A., García-Vargas, S., de la Rasilla, M., Lalueza-Fox, C., Huguet, R., Bastir, M., Santamaría, D., Madella, M., Wilson, J., Cortés, A. F., and Rosas, A.: Neanderthal medics? Evidence for food, cooking, and medicinal plants entrapped in dental calculus, Naturwissenschaften, 99, 617–626, 2012.

Hartmann, J., West, A. J., Renforth, P., Köhler, P., De La Rocha, C. L., Wolf-Gladrow, D. A., Dürr, H. H., and Scheffran, J.: Enhanced chemical weathering as a geoengineering strategy to reduce atmospheric carbon dioxide, supply nutrients, and mitigate ocean acidification, Reviews of Geophysics, 51, 113–149, https://doi.org/https://doi.org/10.1002/rog.20004, 2013.

Heald, C., Ridley, D., Kroll, J., Barrett, S., Cady-Pereira, K., Alvarado, M., and Holmes, C.: Contrasting the direct radiative effect and direct radiative forcing of

aerosols, Atmospheric Chemistry and Physics, 14, 5513–5527, https://doi.org/10.5194/acp-14-5513-2014, 2014.

Heckel, A., Kim, S. W., Frost, G. J., Richter, A., Trainer, M., and Burrows, J. P.: Influence of low spatial resolution a priori data on tropospheric NO 2 satellite retrievals, Atmos. Meas. Tech., 4, 1805–1820, https://doi.org/10.5194/amt-4-1805-2011, 2011.

Hendrick, F. and Coauthors: Retrieval of nitrogen dioxide stratospheric profiles from ground-based zenith-sky UVvisible observations: Validation of the technique through correlative comparisons, Atmospheric Chemistry and Physics, 4, 2867–2904, https://doi.org/10.5194/acpd-4-2867-2004, 2004.

Hendrick, F., Mahieu, E., Bodeker, G. E., Boersma, K. F., Chipperfield, M. P., De Mazière, M., De Smedt, I., Demoulin, P., Fayt, C., Hermans, C., Kreher, K., Lejeune, B., Pinardi, G., Servais, C., Stübi, R., Van der A, R., Vernier, J.-P., and Van Roozendael, M.: Analysis of stratospheric NO_2 trends above Jungfraujoch using ground-based UV-visible, FTIR, and satellite nadir observations, Atmos. Chem. Phys., 12, 8851–8864, 2012.

Hendrick, F., Müller, J.-F., Clémer, K., Wang, P., De Mazière, M., Fayt, C., Gielen, C., Hermans, C., Ma, J. Z., Pinardi, G., Stavrakou, T., Vlemmix, T., and Van Roozendael, M.: Four years of ground-based MAX-DOAS observations of HONO and NO_2 in the Beijing area, Atmospheric Chemistry and Physics, 14, 765–781, https://doi.org/10.5194/acp-14-765-2014, 2014.

Hermans, C. and Coauthors: Absorption Cross-Section of the Collision-Induced Bands of Oxygen from the UV to the NIR, in: Weakly Interacting Molecular Pairs: Unconventional Absorbers of Radiation in the Atmosphere, edited by Camy-Peyret, C. and Vigasin, A. A., vol. 27 of *NATO Science Series IV*, pp. 193–202, Springer, 2003.

Hess, M., Koepke, P., and Schult, I.: Optical properties of Aerosols and Clouds: The Software Package OPAC, Bulletin of the American Meteorological Society, 79, 831–844, https://doi.org/10.1175/1520-0477(1998)079⟨0831:OPOAAC⟩2.0.CO;2, 1998.

Hide, R.: Optics of the Atmosphere: Scattering by Molecules and Particles, vol. 28, IOP Publishing Ltd, https://doi.org/10.1088/0031-9112/28/11/025, 1977.

Hönninger, G., von Friedeburg, C., and Platt, U.: Multi axis differential optical absorption spectroscopy (MAX-DOAS), Atmospheric Chemistry and Physics, 4, 231–254, https://doi.org/10.5194/acp-4-231-2004, 2004.

Ialongo, I., Virta, H., Eskes, H., Hovila, J., and Douros, J.: Comparison of TROPOMI/Sentinel-5 Precursor NO2 observations with ground-based measurements in Helsinki, Atmos. Meas. Tech., 13, 205–218, https://doi.org/10.5194/amt-13-205-2020, 2020.

IEA: Africa Energy Outlook, Tech. rep., International Energy Agency, URL `https://iea.blob.core.windows.net/assets/2f7b6170-d616-4dd7-a7ca-a65a3a332fc1/Africa_Energy_Outlook_2019.pdf`, 2019.

IHME: Global Burden of Disease Study 2013 (GBD 2013) – Results by Risk Factor – Country Level, URL `http://vizhub.healthdata.org/gbd-compare/`, 2015.

IHME: The State of Air Quality and Health Impacts in Africa. A Report from the State of Global Air Initiative. Boston, MA, Tech. rep., Health Effects Institute. 2022, URL `https://issuu.com/ihme/docs/soga-africa-report`, 2022.

IPCC: The Scientific Basis. Contribution of Working Group I to the Third Assessment Report of the Intergovernmental Panel on Climate Change [Houghton, J.T., et al. (eds.), Tech. rep., Cambridge University Press, Cambridge, United Kingdom and New York, NY, USA, 2001.

IPCC: Climate Change 2022: Impacts, Adaptation, and Vulnerability. Contribution of Working Group II to the Sixth Assessment Report of the Intergovernmental Panel on Climate Change, Tech. rep., Intergovernmental Panel on Climate Change, URL `https://www.ipcc.ch/report/ar6/wg2/.`, 2021.

Irie, H., Kanaya, Y., Akimoto, H., Tanimoto, H., Wang, Z., Gleason, J. F., and Bucsela, E. J.: Validation of OMI tropospheric NO_2 column data using MAX-DOAS measurements deep inside the North China Plain in June 2006: Mount Tai Experiment 2006, Atmospheric Chemistry and Physics, 8, 6577–6586, https://doi.org/10.5194/acp-8-6577-2008, 2008.

Jacob, D.: Introduction to Atmospheric Chemistry, Princeton University Press, 1999.

Jacob, D. and Winner, D.: Effect of climate change on air quality, Atmospheric Environment, 43, 51–63, 2009.

Janssens-Maenhout, G., Crippa, M., Guizzardi, D., Muntean, M., Schaaf, E., Dentener, F., Bergamaschi, P., Pagliari, V., Olivier, J. G. J., Peters, J. A. H. W., van Aardenne, J. A., Monni, S., Doering, U., Petrescu, A. M. R., Solazzo, E., and Oreggioni, G. D.: EDGAR v4.3.2 Global Atlas of the three major greenhouse gas emissions for the period 1970–2012, Earth System Science Data, 11, 959–1002, https://doi.org/10.5194/essd-11-959-2019, 2019.

John P. Burrows, Peter Borrell, U. P.: The Remote Sensing of Tropospheric Composition from Space, vol. 3, pp. 1–65, Springer Berlin Heidelberg, https://doi.org/https://doi.org/10.1007/978-3-642-14791-3,2011, 2011.

Karagkiozidis, D., Friedrich, M. M., Beirle, S., Bais, A., Hendrick, F., Voudouri, K. A., Fountoulakis, I., Karanikolas, A., Tzoumaka, P., Van Roozendael, M., Balis, D., and Wagner, T.: Retrieval of tropospheric aerosol, NO_2, and HCHO vertical profiles from MAX-DOAS observations over Thessaloniki, Greece: intercomparison and validation of two inversion algorithms, Atmos. Meas. Tech., 15, 1269–1301, https://doi.org/10.5194/amt-15-1269-2022, 2022.

Karekezi, S.: Renewables in Africa – Meeting the Energy Needs of the Poor, Energy Policy, 30, special Issue – Africa: Improving Modern Energy Services for the Poor, 2002.

Katoto, P. D. and Coauthors: Ambient air pollution and health in sub-Saharan Africa: Current evidence, perspectives and a call to action, Environmental Research, 173, 174–188, https://doi.org/10.1016/j.envres.2019.03.029, 2019.

Keller, C. A., Long, M. S., Yantosca, R. M., Da Silva, A. M., Pawson, S., and Jacob, D. J.: HEMCO v1.0: A versatile, ESMF-compliant component for calculating emissions in atmospheric models, Geoscientific Model Development, 7, 1409–1417, https://doi.org/10.5194/gmd-7-1409-2014, 2014.

Kleipool, Q. L., Dobber, M. R., de Haan, J. F., and Levelt, P. F.: Earth surface reflectance climatology from 3 years of OMI data, Journal of Geophysical Research: Atmospheres, 113, https://doi.org/https://doi.org/10.1029/2008JD010290, 2008.

Knippertz, P., Evans, M., Field, P., Fink, A., Liousse, C., and Marsham, J.: The possible role of local air pollution in climate change in West Africa, Nature Climate Change, 5, URL https://www.nature.com/natureclimatechange, 2015.

Koelemeijer, R. B., Stammes, P., Hovenier, J. W., and Haan, J. F. D.: A fast method for retrieval of cloud parameters using oxygen a band measurements from the Global Ozone Monitoring Experiment, Journal of Geophysical Research Atmospheres, 106, 3475–3490, https://doi.org/10.1029/2000JD900657, 2001.

Kramer, L. J., Leigh, R. J., Remedios, J. J., and Monks, P. S.: Comparison of OMI and ground-based in situ and MAXDOAS measurements of tropospheric nitrogen dioxide in an urban area, J. Geophys. Res., 113, D16S39, https://doi.org/10.1029/2007JD009168, 2008.

Lamoulie, A.: Cartographie de flammes par deux techniques optiques : imagerie spectrale multiplex et spectroscopie par diode laser, Ph.D. thesis, Université Pierre et Marie Curie - Paris VI, 1998.

Lamy, K.: Projection Climatique du Rayonnement Ultraviolet au cours du 21ème siècle : impact de différents scénarios climatiques, Ph.D. thesis, 2018.

Langerock, B., De Mazière, M., Hendrick, F., Vigouroux, C., Desmet, F., Dils, B., and Niemeijer, S.: Description of algorithms for co-locating and comparing gridded model data with remote-sensing observations, GEOScientific Model Development, 8, 911–921, 2015.

Laszlo, I., Stamnes, K., Wiscombe, W., and Tsay, S.-C.: The Discrete Ordinate Algorithm, DISORT for Radiative Transfer, pp. 3–65, https://doi.org/10.1007/978-3-662-49538-4_1, 2016.

Latimer, R. N. C. and Martin, R. V.: Interpretation of measured aerosol mass scattering efficiency over North America using a chemical transport model, Atmospheric Chemistry and Physics, 19, 2635–2653, https://doi.org/10.5194/acp-19-2635-2019, 2019.

Leitão, J., Richter, A., Vrekoussis, M., Kokhanovsky, A., Zhang, Q. J., Beekmann, M., and Burrows, J. P.: On the improvement of NO_2 satellite retrievals: aerosol impact on the airmass factors, Atmos. Meas. Tech, 3, 475–493, URL https://www.atmos-meas-tech.net/3/475/2010/, 2010.

Levelt, P., van den Oord, G., Dobber, M., Malkki, A., Visser, H., de Vries, J., Stammes, P., Lundell, J., and Saari, H.: The ozone monitoring instrument, IEEE Transactions on Geoscience and Remote Sensing, 44, 1093–1101, https://doi.org/10.1109/TGRS.2006.872333, 2006.

Likens, G. E. and Bormann, F. H.: Acid rain: a serious regional environmental problem, Science, 184, 1176–1179, 1974.

Lin, H., Long, M. S., Sander, R., Sandu, A., Yantosca, R. M., Estrada, L. A., Shen, L., and Jacob, D. J.: An Adaptive Auto-Reduction Solver for Speeding Up Integration of Chemical Kinetics in Atmospheric Chemistry Models: Implementation and Evaluation in the Kinetic Pre-Processor (KPP) Version 3.0.0, Journal of Advances in Modeling Earth Systems, 15, e2022MS003 293, https://doi.org/https://doi.org/10.1029/2022MS003293, e2022MS003293 2022MS003293, 2023.

Lin, S.-J. and Rood, R. B.: Multidimensional Flux-Form Semi-Lagrangian Transport Schemes, Monthly weather review, 124, 12 046–2070, https://doi.org/https://doi.org/10.1175/1520-0493(1996)124⟨2046:MFFSLT⟩2.0.CO;2, 1996.

Liou, K.-N.: An Introduction to Atmospheric Radiation, vol. 84, Elsevier, 2002.

Liousse, C., Assamoi, E., Criqui, P., Granier, C., and Rosset, R.: Explosive growth in African combustion emissions from 2005 to 2030, Environ. Res. Lett, 9, https://doi.org/10.1088/1748-9326/9/3/035003, 2014.

Liu, H., Jacob, D., Bey, I., and Yantosca, R.: Constraints from 210Pb and 7Be on wet deposition and transport in a global three-dimensional chemical tracer model driven by assimilated meteorological fields, Journal of Geophysical Research: Atmospheres, 106, https://doi.org/10.1029/2000JD900839, 2001.

Liu, Y., Schichtel, B. A., and Koutrakis, P.: Estimating particle sulfate concentrations using MISR retrieved aerosol properties, IEEE Journal of Selected Topics in Applied Earth Observations and Remote Sensing, 2, 176–184, 2009.

Long, M. S., Yantosca, R., Nielsen, J. E., Keller, C. A., da Silva, A., Sulprizio, M. P., Pawson, S., and Jacob, D. J.: Development of a grid-independent GEOS-Chem chemical transport model (v9-02) as an atmospheric chemistry module for Earth system models, Geoscientific Model Development, 8, 595–602, https://doi.org/10.5194/gmd-8-595-2015, 2015.

Lorente, A., Boersma, K. F., Yu, H., Dörner, S., Hilboll, A., Richter, A., Liu, M., Lamsal, L. N., Barkley, M., Smedt, I. D., Roozendael, M. V., Wang, Y., Wagner, T., Beirle, S., Lin, J. T., Krotkov, N., Stammes, P., Wang, P., Eskes, H. J., and Krol, M.: Structural uncertainty in air mass factor calculation for NO2 and HCHO satellite retrievals, Atmos. Meas. Tech., 10, 759–782, https://doi.org/10.5194/amt-10-759-2017, 2017.

Loyola, D. G., Gimeno García, S., Lutz, R., Argyrouli, A., Romahn, F., Spurr, R. J. D., Pedergnana, M., Doicu, A., Molina García, V., and Schüssler, O.: The operational cloud retrieval algorithms from TROPOMI on board Sentinel-5 Precursor, Atmospheric Measurement Techniques, 11, 409–427, https://doi.org/10.5194/amt-11-409-2018, 2018.

Lunt, M., Palmer, P., Feng, L., Taylor, C., Boesch, H., and Parker, R.: An increase in methane emissions from tropical Africa between 2010 and 2016 inferred from satellite data, Atmospheric Chemistry and Physics Discussions, pp. 1–30, https://doi.org/10.5194/acp-2019-477, 2019.

Lutgens, K. and Tarbuck, E.: The Atmosphere. 8th Edition, Prentice-Hall, Upper Saddle River, NJ, 2001.

Ma, J. Z., Beirle, S., Jin, J. L., Shaiganfar, R., Yan, P., and Wagner, T.: Tropospheric NO2 vertical column densities over Beijing: Results of the first three years of ground-based MAX-DOAS measurements (2008-2011) and satellite validation, Atmos. Chem. Phys., 13, 1547–1567, https://doi.org/10.5194/acp-13-1547-2013, 2013.

Marais, E. A. and Wiedinmyer, C.: Air Quality Impact of Diffuse and Inefficient Combustion Emissions in Africa (DICE-Africa), Environmental Science and Technology, 50, 10 739–10 745, https://doi.org/10.1021/acs.est.6b02602, 2016a.

Marais, E. A. and Wiedinmyer, C.: Air Quality Impact of Diffuse and Inefficient Combustion Emissions in Africa (DICE-Africa), Environ. Sci. Technol., 50, 10 739–10 745, 2016b.

Marais, E. A., Jacob, D. J., Kurosu, T. P., Chance, K., Murphy, J. G., Reeves, C., Mills, G., Casadio, S., Millet, D. B., Barkley, M. P., Paulot, F., and Mao, J.: Isoprene emissions in Africa inferred from OMI observations of formaldehyde columns, Atmospheric Chemistry and Physics, 12, 6219–6235, https://doi.org/10.5194/acp-12-6219-2012, 2012.

Marais, E. A., Silvern, R. F., Vodonos, A., Dupin, E., Bockarie, A. S., Mickley, L. J., and Schwartz, J.: Air Quality and Health Impact of Future Fossil Fuel Use for Electricity Generation and Transport in Africa, Environmental Science & Technology, 53, 13 524–13 534, https://doi.org/10.1021/acs.est.9b04958, 2019.

Marais, E. A., Roberts, J. F., Ryan, R. G., Eskes, H., Boersma, K. F., Choi, S., Joiner, J., Abuhassan, N., Redondas, A., Grutter, M., Cede, A., Gomez, L., and Navarro-Comas, M.: New observations of NO_2 in the upper troposphere from TROPOMI, Atmospheric Measurement Techniques, 14, 2389–2408, https://doi.org/10.5194/amt-14-2389-2021, 2021a.

Marais, E. A., Roberts, J. F., Ryan, R. G., Eskes, H., Boersma, K. F., Choi, S., Joiner, J., Abuhassan, N., Redondas, A., Grutter, M., Cede, A., Gomez, L., and Navarro-Comas, M.: New observations of NO_2 in the upper troposphere from TROPOMI, Atmos. Meas. Tech., 14, 2389–2408, https://doi.org/10.5194/amt-14-2389-2021, 2021b.

Marchenko, S., Krotkov, N. A., Lamsal, L. N., Celarier, E. A., Swartz, W. H., and Bucsela, E. J.: Revising the slant column density retrieval of nitrogen dioxide observed by the Ozone Monitoring Instrument, J. Geophys. Res. Atmos., 120, 5670–5692, https://doi.org/10.1002/2014JD022913, 2015.

Marquard, L. C., Wagner, T., and Platt, U.: Improved air mass factor concepts for scattered radiation differential optical absorption spectroscopy of atmospheric species, Journal of Geophysical Research: Atmospheres, 105, 1315–1327, https://doi.org/https://doi.org/10.1029/1999JD900340, 2000.

Martin, A. and Barber, F.: Acid gases and acid in rain monitored for over 5 years in rural east-central England, Atmospheric Environment, 18, 1715–1724, 1984.

Martin, R. V., Chance, K., Jacob, D. J., Kurosu, T. P., Spurr, R. J. D., Bucsela, E. J., Gleason, J. F., Palmer, P. I., Bey, I., Fiore, A. M., Li, Q., Yantosca, R. M., and Koelemeijer, R.: An improved retrieval of tropospheric nitrogen dioxide from GOME, Journal of Geophysical Research, 107, 4437, URL `https://api.semanticscholar.org/CorpusID:17028624`, 2002.

Martínez-Alonso, S., Veefkind, J. P., Dix, B., Gaubert, B., Theys, N., Granier, C., Soulié, A., Darras, S., Eskes, H., Tang, W., Worden, H., de Gouw, J., and Levelt, P. F.: S-5P/TROPOMI-Derived NOx Emissions From Copper/Cobalt Mining and Other Industrial Activities in the Copperbelt (Democratic Republic of Congo and Zambia), Geophysical Research Letters, https://doi.org/10.1029/2023GL104109, 2023.

Mayaux, P., Pekel, J. F., Desclée, B., Donnay, F., Lupi, A., Achard, F., Clerici, M., Bodart, C., Brink, A., Nasi, R., and Belward, A.: State and evolution of the African rainforests between 1990 and 2010, Philosophical Transactions of the Royal Society B: Biological Sciences, 368, https://doi.org/10.1098/rstb.2012.0300, 2013.

Mayer, b.: Radiative transfer in the cloudy atmosphere, The European Physical Journal, 1, 75–99, https://doi.org/10.1140/epjconf/e2009-00912-1, 2009.

Mayer, B. and Kylling, A.: Technical note: The libRadtran software package for radiative transfer calculations - description and examples of use, Atmospheric Chemistry and Physics, 5, 1855–1877, https://doi.org/10.5194/acp-5-1855-2005, 2005.

Maître, H.: Du photon au pixel : L'appareil photographique numérique, ISTE, 2 edn., 2e édition revue et augmentée, 2016.

McFarlane, C., Isevulambire, P. K., Lumbuenamo, R. S., Ndinga, A. M. E., Dhammapala, R., Jin, X., McNeill, V. F., Malings, C., Subramanian, R., and Westervelt, D. M.: First measurements of ambient pm2.5 in kinshasa, democratic republic of congo and brazzaville, republic of congo using field-calibrated low-cost sensors, Aerosol and Air Quality Research, 21, https://doi.org/10.4209/aaqr.200619, 2021.

McLinden, C. A., Fioletov, V., Boersma, K. F., Krotkov, N., Sioris, C. E., Veefkind, J. P., and Yang, K.: Air quality over the Canadian oil sands: A first assessment using satellite observations, Geophysical Research Letters, 39, https://doi.org/https://doi.org/10.1029/2011GL050273, 2012.

McLinden, C. A., Fioletov, V., Boersma, K. F., Kharol, S. K., Krotkov, N., Lamsal, L., Makar, P. A., Martin, R. V., Veefkind, J. P., and Yang, K.: Improved satellite retrievals of NO2 and SO2 over the Canadian oil sands and comparisons with surface measurements, Atmos. Chem. Phys., 14, 3637–3656, https://doi.org/10.5194/acp-14-3637-2014, 2014.

Meftah, M., Sarkissian, A., Keckhut, P., and Hauchecorne, A.: The SOLAR-HRS New High-Resolution Solar Spectra for Disk-Integrated, Disk-Center, and Intermediate Cases, Remote Sensing, 15, https://doi.org/10.3390/rs15143560, 2023.

Meller, R. and Moortgat, G. K.: Temperature dependence of the absorption cross sections of formaldehyde between 223 and 323 K in the wavelength range 225-375 nm, J. Geophys. Res. Atmos., 105, 7089–7101, https://doi.org/10.1029/1999JD901074, 2000.

Menegoz, M.: Modélisation globale des interactions atmosphère-aérosols, Master's thesis, Université Toulouse III - Paul Sabatier, 2009.

Merlaud, A.: Development and use of compact instruments for tropospheric investigations based on optical spectroscopy from mobile platforms, Phd thesis, Université catholique de Louvain, Example City, CA, available at `https://uv-vis.aeronomie.be/publications/thesis/alexism_thesis.php`, 2013.

Mie, G.: Beiträge zur Optik trüber Medien, speziell kolloidaler Metallösungen, vol. 330, Annalen der Physik, 1908.

Molina, M. J. and Molina, L. T.: Megacities and Atmospheric Pollution, Journal of Air & Waste Management Association, 54, 644–680, https://doi.org/10.1080/10473289.2004.10470936, 2004.

Noxon, J. F.: Nitrogen dioxide in the stratosphere and troposphere measured by ground-based absorption spectroscopy, Science, 189, 547–549, 1975.

Odén, S.: Dagens Nyheter (Sweden), October 24, 1967., 1967.

Odén, S.: The acidification of air precipitation and its consequences in the natural environment. Ecology Committee Bulletin No. 1, Swedish Sciences Research Council, Stockholm, translation Consultants Ltd.: Arlington, VA, 1968.

OECD: The Cost of Air Pollution: Health Impacts of Road Transport, OECD Publishing, Paris, URL http://dx.doi.org/10.1787/9789264210448-en, 2014.

Opio, R., Mugume, I., Nakatumba-Nabende, J., Nanteza, J., Nimusiima, A., Mbogga, M., and Mugagga, F.: Evaluation of WRF-chem simulations of NO2 and CO from biomass burning over East Africa and its surrounding regions, Terrestrial, Atmospheric and Oceanic Sciences, 33, https://doi.org/10.1007/s44195-022-00029-9, 2022.

Pan, X., Ichoku, C., Chin, M., Bian, H., Darmenov, A., Colarco, P., Ellison, L., Kucsera, T., Da Silva, A., Wang, J., Oda, T., and Cui, G.: Six global biomass burning emission datasets: Intercomparison and application in one global aerosol model, Atmos. Chem. Phys., 20, 969–994, https://doi.org/10.5194/acp-20-969-2020, 2020.

Paton-Walsh, C., Emmerson, K. M., Garland, R. M., Keywood, M., Hoelzemann, J. J., Huneeus, N., Buchholz, R. R., Humphries, R. S., Altieri, K., Schmale, J., Wilson, S. R., Labuschagne, C., Kalisa, E., Fisher, J. A., Deutscher, N. M., van Zyl, P. G., Beukes, J. P., Joubert, W., Martin, L., Mkololo, T., Barbosa, C., de Fatima Andrade, M., Schofield, R., Mallet, M. D., Harvey, M. J., Formenti, P., Piketh, S. J., and Olivares, G.: Key challenges for tropospheric chemistry in the Southern Hemisphere, Elementa: Science of the Anthropocene, 10, 00 050, https://doi.org/10.1525/elementa.2021.00050, 2022.

Perliski, L. M. and Solomon, S.: On the evaluation of air mass factors for atmospheric near-ultraviolet and visible absorption spectroscopy, , 98, 10,363–10,374, https://doi.org/10.1029/93JD00465, 1993.

Petkova, E., Jack, D., Volavka-Close, N., and Kinney, P.: Particulate matter pollution in African cities, Air Quality, Atmosphere Health, 6, https://doi.org/10.1007/s11869-013-0199-6, 2013.

Petty, G. W.: A First Course in Atmospheric Radiation, Sundog Publishing, 2006.

Pinardi, G., Van Roozendael, M., Abuhassan, N., Adams, C., Cede, A., Clémer, K., Fayt, C., Frieß, U., Gil, M., Herman, J., Hermans, C., Hendrick, F., Irie, H., Merlaud, A., Navarro Comas, M., Peters, E., Piters, A. J. M., Puentedura, O., Richter, A., Schönhardt, A., Shaiganfar, R., Spinei, E., Strong, K., Takashima, H., Vrekoussis, M., Wagner, T., Wittrock, F., and Yilmaz, S.: MAX-DOAS formaldehyde slant column measurements during CINDI: intercomparison and analysis improvement, Atmos. Meas. Tech., 6, 167–185, https://doi.org/10.5194/amt-6-167-2013, 2013.

Pinardi, G., van Roozendael, M., Hendrick, F., Theys, N., Abuhassan, N., Bais, A., Boersma, F., Cede, A., Chong, J., Donner, S., Drosoglou, T., Dzhola, A., Eskes, H., Frieß, U., Granville, J., Herman, J. R., Holla, R., Hovila, J., Irie, H., Kanaya, Y., Karagkiozidis, D., Kouremeti, N., Lambert, J. C., Ma, J., Peters, E., Piters, A., Postylyakov, O., Richter, A., Remmers, J., Takashima, H., Tiefengraber, M., Valks, P., Vlemmix, T., Wagner, T., and Wittrock, F.: Validation of tropospheric NO2 column measurements of GOME-2A and OMI using MAX-DOAS and direct sun network observations, Atmos. Meas. Tech., 13, 6141–6174, https://doi.org/10.5194/amt-13-6141-2020, 2020.

Platt, U. and Perner, D.: Direct measurements of atmospheric CH2O, HNO2, O3, NO2, and SO2 by differential optical absorption in the near UV, Journal of Geophysical Research, 85, 7453–7458, URL https://api.semanticscholar.org/CorpusID:140572826, 1980.

Platt, U. and Stutz, J.: Differential Optical Absorption Spectroscopy (DOAS)—Principles and Applications, vol. 15, Springer, https://doi.org/10.1007/978-3-540-75776-4, 2008.

Platt, U., Perner, D., and Pätz, H. W.: Simultaneous measurement of atmospheric CH2O, O3, and NO2 by differential optical absorption, Journal of Geophysical Research, 84, 6329–6335, URL https://api.semanticscholar.org/CorpusID:128399413, 1979.

Platt, U., Perner, D., Winer, A. M., Harris, G. W., and Pitts Jr., J. N.: Detection of NO3 in the polluted troposphere by differential optical absorption, Geophysical Research Letters, 7, 89–92, https://doi.org/https://doi.org/10.1029/GL007i001p00089, 1980.

Pope, R. M. and Fry, E. S.: Absorption spectrum (380-700 nm) of pure water. II. Integrating cavity measurements, Appl. Opt., 36, 8710–8723, 1997.

Poraicu, C., Müller, J.-F., Stavrakou, T., Fonteyn, D., Tack, F., Deutsch, F., Laffineur, Q., Van Malderen, R., and Veldeman, N.: Cross-evaluating WRF-Chem v4.1.2, TROPOMI, APEX, and in situ NO_2 measurements over Antwerp, Belgium, Geoscientific Model Development, 16, 479–508, https://doi.org/10.5194/gmd-16-479-2023, 2023.

Prignon, M.: Stratospheric circulation changes: investigations using multidecadal observations and simulations of inorganic fluorine, Ph.D. thesis, Université de Liège, 2021.

Puk̄ite, J., Kühl, S., Deutschmann, T., Platt, U., and Wagner, T.: Extending differential optical absorption spectroscopy for limb measurements in the UV, Atmospheric Measurement Techniques, 3, 631–653, 2010.

Pörtner, H.-O., Roberts, D. C., Tignor, M. M. B., Poloczanska, E. S., Mintenbeck, K., Alegría, A., Craig, M., Langsdorf, S., Löschke, S., Möller, V., Okem, A., and (eds.), B. R.: Climate Change 2022: Impacts, Adaptation and Vulnerability. Contribution of Working Group II to the Sixth Assessment Report of the Intergovernmental Panel on Climate Change, Cambridge University Press, Cambridge, UK and New York, NY, USA, https://doi.org/10.1017/9781009325844, 2022.

Rayleigh, J.: On the Scattering of Light by Small Particles, URL https://books.google.be/books?id=YbNuMwEACAAJ, 1871.

Rich, S.: Ozone Damage to Plants, Annual Review of Phytopathology, 2, 253–266, https://doi.org/10.1146/annurev.py.02.090164.001345, 1964.

R.K. Pachauri and L.A. Meyer: Climate Change 2014: Synthesis Report, Tech. rep., Intergovernmental Panel on Climate Change (IPCC), Geneva, Switzerland, 2014.

Rodgers, C. D.: The Vertical Resolution of Remotely Sounded Temperature Profiles with a priori Statistics, Journal of Atmospheric Sciences, 33, 707 – 709, https://doi.org/https://doi.org/10.1175/1520-0469(1976)033⟨0707:TVRORS⟩2.0.CO;2, 1976.

Rodgers, C. D.: Inverse methods for atmospheric sounding - theory and practice, World Scientific Publishing Co. Pte. Ltd., 2000.

Rogers, C. and Connor, B.: Intercomparison of remote sounding instruments), Journal of Geophysical Research., 108, 4116–4129, https://doi.org/10.1029/2002JD002299, 2003.

Rothman, L., Gordon, I., Barber, R., Dothe, H., Gamache, R., Goldman, A., Perevalov, V., Tashkun, S., and Tennyson, J.: HITEMP, the high-temperature molecular spectroscopic database, Journal of Quantitative Spectroscopy and Radiative Transfer, 111, 2139–2150, https://doi.org/10.1016/j.jqsrt.2010.05.001, xVIth Symposium on High Resolution Molecular Spectroscopy (HighRus-2009), 2010.

Rothman, L. S., Gordon, I. E., Babikov, Y., Barbe, A., Chris Benner, D., Bernath, P. F., Birk, M., Bizzocchi, L., Boudon, V., Brown, L. R., Campargue, A., Chance, K., Cohen, E. A., Coudert, L. H., Devi, V. M., Drouin, B. J., Fayt, A., Flaud, J.-M., Gamache, R. R., Harrison, J. J., Hartmann, J.-M., Hill, C., Hodges, J. T., Jacquemart, D., Jolly, A., Lamouroux, J., Le Roy, R. J., Li, G., Long, D. A., Lyulin, O. M., Mackie, C. J., Massie, S. T., Mikhailenko, S., Müller, H. S. P., Naumenko, O. V., Nikitin, A. V., Orphal, J., Perevalov, V., Perrin, A., Polovtseva, E. R., Richard, C., Smith, M. A. H., Starikova, E., Sung, K., Tashkun, S., Tennyson, J., Toon, G. C., Tyuterev, V. G., and Wagn, G.: The HITRAN 2012 molecular spectroscopic database, Journal of Quantitative Spectroscopy and Radiative Transfer, 130, 4–50, https://doi.org/10.1016/j.jqsrt.2013.07.002, 2013.

Roy, R.: The Cost of Air Pollution in Africa, Tech. Rep. 333, OECD Development Center, 2016.

Roșu, A., Constantin, D., Voiculescu, M., Arseni, M., Roșu, B., Merlaud, A., Van Roozendael, M., and Georgescu, P.: Assessment of NO2 Pollution Level during the COVID-19 Lockdown in a Romanian City, Int J Environ Res Public Health, 18, 544, https://doi.org/10.3390/ijerph18020544, 2021.

Saint-Moulin, L.: Atlas de l'organisation administrative de la République démocratique du Congo, Centre d'études pour l'action sociale Doc., 2nd edn., 2011.

Saleem, A., Karimi, I. A., and Farooq, S.: Estimating NOx emissions of useful two-fuel blends from literature data, Fuel, 316, 123 213, https://doi.org/https://doi.org/10.1016/j.fuel.2022.123213, 2022.

Sandu, A., Verwer, J. G., Blom, J. G., Spee, E. J., Carmichael, G. R., and Potra, F. A.: Benchmarking stiff ode solvers for atmospheric chemistry problems II: Rosenbrock solvers, Atmospheric Environment, 31, 3459–3472, https://doi.org/10.1016/S1352-2310(97)83212-8, 1997.

Seigneur, C.: Pollution atmosphérique : Concept, théorie et applications, Belin Education, 2018.

Seinfeld, J. and Pandis, S.: Atmospheric Chemistry and Physics, from Air Pollution to Climate Change, Wiley−Interscience, 1997.

Seinfeld, J. and Pandis, S.: Atmospheric Chemistry and Physics: From Air Pollution to Climate Change, 1998.

Seinfeld, J. and Pandis, S.: Atmospheric Chemistry and Physics: From Air Pollution to Climate Change., September, John Wiley Sons, New York, 2006.

Serdyuchenko, A., Gorshelev, V., Weber, M., Chehade, W., and Burrows, J. P.: High spectral resolution ozone absorption cross-sections Part 2: Temperature dependence, Atmos. Meas. Tech., 7, 625–636, https://doi.org/10.5194/amt-7-625-2014, 2014.

Shen, L., Mickley, L., and Murray, L.: Strong influence of 200-2050 climate change on particulate matter in the United States: Results from a new statistical model, Atmospheric Chemistry and Physics, 17, 4355–4367, 2017.

Shen, L., Jacob, D. J., Santillana, M., Wang, X., and Chen, W.: An adaptive method for speeding up the numerical integration of chemical mechanisms in atmospheric chemistry models: application to GEOS-Chem version 12.0.0, Geoscientific Model Development, 13, 2475–2486, https://doi.org/10.5194/gmd-13-2475-2020, 2020.

Shindell, D. T., Faluvegi, G., Koch, D. M., Schmidt, G. A., Unger, N., and Bauer, S. E.: Improved Attribution of Climate Forcing to Emissions, Science, 326, 716–718, https://doi.org/10.1126/science.1174760, 2009.

Shukla, P., Skea, J., Slade, R., van Diemen, R., Haughey, E., and Malley, J.: Climate Change and Land: an IPCC special report on climate change, desertification, land degradation, sustainable land management, food security, and greenhouse gas fluxes in terrestrial ecosystems, Tech. rep., Climate Change and Land, URL `https://www.ipcc.ch/srccl/`, 2019.

Sillman, S., Logan, J. A., and Wofsy, S. C.: The sensitivity of ozone to nitrogen oxides and hydrocarbons in regional ozone episodes, Journal of Geophysical Research: Atmospheres, 95, 1837–1851, https://doi.org/https://doi.org/10.1029/JD095iD02p01837, 1990.

Solomon, S.: Stratospheric ozone depletion: A review of concepts and history, Reviews of Geophysics, 37, 275–316, https://doi.org/https://doi.org/10.1029/1999RG900008, 1999.

Solomon, S. C., Schmeltekopf, A. L., and Sanders, R. W.: On the interpretation of zenith sky absorption measurements, Journal of Geophysical Research, 92, 8311–8319, URL `https://api.semanticscholar.org/CorpusID:131265788`, 1987.

Spurr, R.: User ' s Guide VLIDORT Version 2.6, vol. 1183, RT Solutions, Inc., 2013.

Spurr, R. J., Kurosu, T. P., and Chance, K. V.: A linearized discrete ordinate radiative transfer model for atmospheric remote-sensing retrieval, Journal of Quantitative Spectroscopy and Radiative Transfer, 68, 689–735, https://doi.org/10.1016/S0022-4073(00)00055-8, 2001.

Stavrakou, T., Müller, J.-F., De Smedt, I., Van Roozendael, M., Kanakidou, M., Vrekoussis, M., Wittrock, F., Richter, A., and Burrows, J. P.: The continental source of glyoxal estimated by the synergistic use of spaceborne measurements and inverse modelling, Atmospheric Chemistry and Physics, 9, 8431–8446, https://doi.org/10.5194/acp-9-8431-2009, 2009a.

Stavrakou, T., Müller, J.-F., De Smedt, I., Van Roozendael, M., van der Werf, G. R., Giglio, L., and Guenther, A.: Evaluating the performance of pyrogenic and biogenic emission inventories against one decade of space-based formaldehyde columns, Atmospheric Chemistry and Physics, 9, 1037–1060, https://doi.org/10.5194/acp-9-1037-2009, 2009b.

Stavrakou, T., Müller, J.-F., De Smedt, I., Van Roozendael, M., van der Werf, G. R., Giglio, L., and Guenther, A.: Global emissions of non-methane hydrocarbons deduced from SCIAMACHY formaldehyde columns through 2003–2006, Atmospheric Chemistry and Physics, 9, 3663–3679, https://doi.org/10.5194/acp-9-3663-2009, 2009c.

Stavrakou, T., Müller, J.-F., Bauwens, M., De Smedt, I., Van Roozendael, M., De Mazière, M., Vigouroux, C., Hendrick, F., George, M., Clerbaux, C., Coheur, P.-F., and Guenther, A.: How consistent are top-down hydrocarbon emissions based on formaldehyde observations from GOME-2 and OMI?, Atmospheric Chemistry and Physics, 15, 11 861–11 884, https://doi.org/10.5194/acp-15-11861-2015, 2015.

Tack, F., Hendrick, F., Goutail, F., Fayt, C., Merlaud, A., Pinardi, G., Hermans, C., Pommereau, J.-P., and Van Roozendael, M.: Tropospheric nitrogen dioxide column retrieval from ground-based zenith–sky DOAS observations, Atmospheric Measurement Techniques, 8, 2417–2435, https://doi.org/10.5194/amt-8-2417-2015, 2015.

Tack, F., Merlaud, A., Iordache, M.-D., Pinardi, G., Dimitropoulou, E., Eskes, H., Bomans, B., Veefkind, P., and Roozendael, M. V.: Assessment of the TROPOMI tropospheric NO2 product based on airborne APEX observations, Atmos. Meas. Tech., 14, 615–646, https://doi.org/10.5194/amt-14-615-2021, 2021.

Thalman, R. and Volkamer, R.: Temperature dependent absorption cross-sections of O2–O2 collision pairs between 340 and 630 nm and at atmospherically relevant pressure, Phys. Chem. Chem. Phys., 15, 15 371–15 381, https://doi.org/10.1039/C3CP50968K, 2013a.

Thalman, R. and Volkamer, R.: Temperature dependent absorption cross-sections of O_2–O_2 collision pairs between 340 and 630 nm and at atmospherically relevant pressure, Physical Chemistry Chemical Physics, Issue 37, previous Article Next Article, 2013b.

Tilstra, L. G., de Graaf, M., Wang, P., and Stammes, P.: In-orbit Earth reflectance validation of TROPOMI on board the Sentinel-5 Precursor satellite, Atmospheric Measurement Techniques, 13, 4479–4497, https://doi.org/10.5194/amt-13-4479-2020, 2020.

Tirpitz, J.-L., Frieß, U., Hendrick, F., Alberti, C., Allaart, M., Apituley, A., Bais, A., Beirle, S., Berkhout, S., Bognar, K., Bösch, T., Bruchkouski, I., Cede, A., Chan, K. L., den Hoed, M., Donner, S., Drosoglou, T., Fayt, C., Friedrich, M. M., Frumau, A., Gast, L., Gielen, C., Gomez-Martín, L., Hao, N., Hensen, A., Henzing, B., Hermans, C., Jin, J., Kreher, K., Kuhn, J., Lampel, J., Li, A., Liu, C., Liu, H., Ma, J., Merlaud, A., Peters, E., Pinardi, G., Piters, A., Platt, U., Puentedura, O., Richter, A., Schmitt, S., Spinei, E., Stein Zweers, D., Strong, K., Swart, D., Tack, F., Tiefengraber, M., van der Hoff, R., van Roozendael, M., Vlemmix, T., Vonk, J., Wagner, T., Wang, Y., Wang, Z., Wenig, M., Wiegner, M., Wittrock, F., Xie, P., Xing, C., Xu, J., Yela, M., Zhang, C., and Zhao, X.: Intercomparison of MAX-DOAS vertical profile retrieval algorithms: studies on field data from the CINDI-2 campaign, Atmos. Meas. Tech., 14, 1–35, https://doi.org/10.5194/amt-14-1-2021, 2021.

TROPOMI HCHO ATBD: Sentinel-5P TROPOMI HCHO ATBD, Format Document 2.3.0, BIRA, Royal Netherlands Meteorological Institute, DLR, 2021.

UN: The World's cities in 2016: data booklet, United Nations, 2016.

UN: UN-Habitat and IHS-Erasmus University Rotterdam (2018) "The State of African Cities 2018: The geography of African investment.", Tech. rep., United Nations Human Settlements Programme (UN-Habitat)., URL `https://www.ccacoalition.org/resources/\full-report-integrated-assessment\-air-pollution-and-climate-change-sustainable-development-africa`, 2018.

UN: UNdata, United Nations, URL `https://data.un.org/.`, 2022.

UNCTD: Reaping the Potential Benefits of the African Continental Free Trade Area for Inclusive Growth. Economic Development in Africa Report 2021, Tech. rep., United Nations Conference on Trade and Development, URL `https://unctad.org/system/files/official-document/aldcafrica2021_en.pdf`, 2021.

UNEP: Integrated Waste Management in Africa: Focus on Circularity, Tech. rep., United Nations Environment Programme, 2020.

van Geffen, J., Boersma, K. F., Eskes, H., Sneep, M., ter Linden, M., Zara, M., and Veefkind, J. P.: S5P TROPOMI NO_2 slant column retrieval: method, stability, uncertainties and comparisons with OMI, Atmospheric Measurement Techniques, 13, 1315–1335, https://doi.org/10.5194/amt-13-1315-2020, 2020a.

van Geffen, J., Boersma, K. F., Eskes, H., Sneep, M., ter Linden, M., Zara, M., and Veefkind, J. P.: S5P TROPOMI NO2 slant column retrieval: method, stability, uncertainties and comparisons with OMI, Atmospheric Measurement Techniques, 13, 1315–1335, https://doi.org/10.5194/amt-13-1315-2020, 2020b.

van Geffen, J., Eskes, H., Compernolle, S., Pinardi, G., Verhoelst, T., Lambert, J.-C., Sneep, M., ter Linden, M., Ludewig, A., Boersma, K. F., and Veefkind, J. P.: Sentinel-5P TROPOMI NO_2 retrieval: impact of version v2.2 improvements and comparisons with OMI and ground-based data, Atmospheric Measurement Techniques, 15, 2037–2060, https://doi.org/10.5194/amt-15-2037-2022, 2022a.

Van Geffen, J. H. G. M., Boersma, K. F., Van Roozendael, M., Hendrick, F., Mahieu, E., De Smedt, I., M., S., and Veefkind, J. P.: Improved spectral fitting of nitrogen dioxide from OMI in the 405–465 nm window, Atmospheric Measurement Techniques, 8, 1685–1699, 2015.

van Geffen, J. H. G. M., Eskes, H. J., Boersma, K. F., and Veefkind, J. P.: TROPOMI ATBD tropospheric and total NO2 issue 2.4.0, Tech. Rep. S5P-KNMI-L2-0005-RP, KNMI, document approval record: This document was prepared by J.H.G.M. van Geffen, H.J. Eskes, K.F. Boersma and J.P. Veefkind. It was checked by S. Beirle, A. Richter, B. Sanders, 2022b.

Van Roozendael, M. and Hendrick, F.: Recommendations for NO_2 column retrieval from NDACC zenith-sky UV-VIS spectrometers, Tech. rep., Belgian Institute for Space Aeronomy (BIRA-IASB), 2012.

Vandaele, A., Hermans, C., Simon, P., Van Roozendael, M., Guilmot, J., Carleer, M., and Colin, R.: Fourier transform measurement of NO2 absorption cross-section in the visible range at room temperature, Journal of Atmospheric Chemistry, 25, 289–305, https://doi.org/10.1007/BF00053797, 1996.

Vandaele, A., Hermans, C., Simon, P., Carleer, M., Colin, R., Fally, S., Mérienne, M., Jenouvrier, A., and Coquart, B.: Measurements of the NO_2 absorption cross-section from 42,000 cm^{-1} to 10,000 cm^{-1} (238–1000 nm) at 220 K and 294 K, Journal of Quantitative Spectroscopy and Radiative Transfer, 59, 171–184, https://doi.org/10.1016/S0022-4073(97)00168-4, atmospheric Spectroscopy Applications 96, 1998.

Veefkind, J. P., Aben, I., McMullan, K., Förster, H., de Vries, J., Otter, G., Claas, J., Eskes, H. J., de Haan, J. F., Kleipool, Q., van Weele, M., Hasekamp, O., Hoogeveen, R., Landgraf, J., Snel, R., Tol, P., Ingmann, P., Voors, R., Kruizinga, B., Vink, R., Visser, H., and Levelt, P. F.: TROPOMI on the ESA Sentinel-5 Precursor: A GMES mission for global observations of the atmospheric composition for climate, air quality and ozone layer applications, Remote Sensing of Environment, 120, 70–83, https://doi.org/10.1016/j.rse.2011.09.027, 2012.

Veefkind, J. P., de Haan, J. F., Sneep, M., and Levelt, P. F.: Improvements to the OMI O_2–O_2 operational cloud algorithm and comparisons with ground-based radar–lidar observations, Atmospheric Measurement Techniques, 9, 6035–6049, https://doi.org/10.5194/amt-9-6035-2016, 2016.

Verhegghen, A., Mayaux, P., de Wasseige, C., and Defourny, P.: Mapping Congo Basin vegetation types from 300 m and 1 km multi-sensor time series for carbon stocks and forest areas estimation, Biogeosciences, 9, 5061–5079, https://doi.org/doi:10.5194/bg-9-5061-2012, 2012.

Verhoelst, T., Compernolle, S., Pinardi, G., Lambert, J. C., Eskes, H. J., Eichmann, K. U., Fjæraa, A. M., Granville, J., Niemeijer, S., Cede, A., Tiefengraber, M., Hendrick, F., Pazmiño, A., Bais, A., Bazureau, A., Folkert Boersma, K., Bognar, K., Dehn, A., Donner, S., Elokhov, A., Gebetsberger, M., Goutail, F., Grutter De La Mora, M., Gruzdev, A., Gratsea, M., Hansen, G. H., Irie, H., Jepsen, N., Kanaya, Y., Karagkiozidis, D., Kivi, R., Kreher, K., Levelt, P. F., Liu, C., Müller, M., Navarro Comas, M., Piters, A. J., Pommereau, J. P., Portafaix, T., Prados-Roman, C., Puentedura, O., Querel, R., Remmers, J., Richter, A., Rimmer, J., Cárdenas, C. R., De Miguel, L. S., Sinyakov, V. P., Stremme, W., Strong, K., Van Roozendael, M., Pepijn Veefkind, J., Wagner, T., Wittrock, F., Yela González, M., and Zehner, C.: Ground-based validation of the Copernicus Sentinel-5P TROPOMI NO2 measurements with the NDACC ZSL-DOAS, MAX-DOAS and Pandora global networks, Atmos. Meas. Tech., 14, 481–510, https://doi.org/10.5194/amt-14-481-2021, 2021.

Vigouroux, C., Langerock, B., Augusto Bauer Aquino, C., Blumenstock, T., Cheng, Z., De Mazière, M., De Smedt, I., Grutter, M., Hannigan, J. W., Jones, N., Kivi, R., Loyola, D., Lutsch, E., Mahieu, E., Makarova, M., Metzger, J. M., Morino, I., Murata, I., Nagahama, T., Notholt, J., Ortega, I., Palm, M., Pinardi, G., Röhling, A., Smale, D., Stremme, W., Strong, K., Sussmann, R., Té, Y., Van Roozendael, M., Wang, P., and Winkler, H.: TROPOMI-Sentinel-5 Precursor formaldehyde validation using an extensive network of ground-based Fourier-transform infrared stations, Atmos. Meas. Tech., 13, 3751–3767, https://doi.org/10.5194/amt-13-3751-2020, 2020.

Vohra, K., Marais, E., Bloss, W. J., Schwartz, J., Mickley, L. J., Van Damme, M., Lieven, C., and Coheur, P.-F.: Rapid rise in premature mortality due to anthropogenic air pollution in fast-growing tropical cities from 2005 to 2018, Science Advances, 8, eabm4435, https://doi.org/10.1126/sciadv.abm4435, 2022.

Wagner, T., Dix, B., Friedeburg, C. v., Frieß, U., Sanghavi, S., Sinreich, R., and Platt, U.: MAX-DOAS O4 measurements: A new technique to derive information on atmospheric aerosols—Principles and information content, Journal of Geophysical Research: Atmospheres, 109, https://doi.org/10.1029/2004JD004904, 2004.

Wagner, T., Deutschmann, T., and Platt, U.: Determination of aerosol properties from MAX-DOAS observations of the Ring effect, Atmos. Meas. Tech., 2, 495–512, https://doi.org/10.5194/amt-2-495-2009, 2009.

Wang, F., Gao, Q., Hu, L., Gao, N., Ge, T., Yu, J., and Liu, Y.: Risk of eye damage from the wavelength-dependent biologically effective UVB spectrum irradiances, PLoS One, 7, e52 259, 2012.

Wang, Y., Jacob, D. J., and Logan, J. A.: Parameterization of Surface Resistances to Gaseous Dry Deposition in Regional-Scale Numerical Models, Global Simulation of Tropospheric O3-NOx-Hydrocarbon Chemistry 1. Model Formulation, 10, 713–725, https://doi.org/10.1029/98JD00158, 1998.

Wang, Y., Lampel, J., Xie, P., Beirle, S., Li, A., Wu, D., and Wagner, T.: Ground-based MAX-DOAS observations of tropospheric aerosols, NO_2, SO_2 and HCHO in Wuxi, China, from 2011 to 2014, Atmospheric Chemistry and Physics, 17, 2189–2215, https://doi.org/10.5194/acp-17-2189-2017, 2017.

Webb, A. R., Kift, R., Thiel, S., and Blumthaler, M.: An empirical method for the conversion of spectral UV irradiance measurements to actinic flux data, Atmospheric

Environment, 36, 4397–4404, https://doi.org/https://doi.org/10.1016/S1352-2310(02)00319-9, 2002.

Wesely, M. L.: Parameterization of surface resistances to gaseous dry deposition in regional-scale numerical models, Atmospheric Environment, 23, 1293–1304, 1989.

Wesely, M. L. and Hicks, B. B.: A review of the current status of knowledge on dry deposition, Atmospheric Environment, 34, 2261–2282, https://doi.org/10.1016/S1352-2310(99)00467-7, 2000.

WHO: Air Quality Guidelines for Europe, Tech. rep., World Health Organization, 2006.

Williams, J. E., Folkert Boersma, K., Le Sager, P., and Verstraeten, W. W.: The high-resolution version of TM5-MP for optimized satellite retrievals: Description and validation, Geoscientific Model Development, 10, 721–750, https://doi.org/10.5194/gmd-10-721-2017, 2017.

Wu, S., Mickley, L. J., Jacob, D. J., Logan, J. A., Yantosca, R. M., and Rind, D.: Why are there large differences between models in global budgets of tropospheric ozone?, Journal of Geophysical Research: Atmospheres, 112, d05 302, https://doi.org/10.1029/2006JD007801, 2007.

Yombo, R., Pinardi, G., Merlaud, A., Fayt, C., Van Rozendael, M., and Mbungu, P.: DOAS measurements from Kinshasa: Context and first results, in: 20th EGU General Assembly, Vienna, Austria, eGU2018-6924, 2018.

Yombo Phaka, R., Merlaud, A., Pinardi, G., Mahieu, E., Hendrick, F., Friedrich, M. M., Fayt, C., Van Roozendael, M., Djibi, B. L., Bopili Mbotia Lepiba, R., Phuku Phuati, E., and Mbungu Tsumbu, J.-P.: First GroundBased Doas Measurements of No2 At Kinshasa and Comparisons With Satellite Observations, Journal of Atmospheric and Oceanic Technology, pp. 1291–1304, https://doi.org/10.1175/jtech-d-20-0195.1, 2021.

Zhang, L., Brook, J., and R, V.: A revised parameterization for gaseous dry deposition in air-quality models, Atmospheric Chemistry and Physics, 3, https://doi.org/10.5194/acpd-3-1777-2003, 2003.

Zhao, X., Griffin, D., Fioletov, V., McLinden, C., Cede, A., Tiefengraber, M., Müller, M., Bognar, K., Strong, K., Boersma, F., Eskes, H., Davies, J., Ogyu, A., and Lee, S. C.: Assessment of the quality of tropomi high-spatial-resolution no2 data products in the greater toronto area, Atmos. Meas. Tech., 13, 2131–2159, https://doi.org/10.5194/amt-13-2131-2020, 2020.

Zhu, L., Jacob, D. J., Mickley, L. J., Marais, E. A., Cohan, D. S., Yoshida, Y., Duncan, B. N., Abad, G. G., and Chance, K. V.: Anthropogenic emissions of highly reactive volatile organic compounds in eastern Texas inferred from oversampling of satellite (OMI) measurements of H_2CO columns, Environmental Research Letters, 9, 114 004, https://doi.org/10.1088/1748-9326/9/11/114004, 2014.